TABLE OF CONTENTS

LIST OF FIGURES . . . . vii 1/A12

LIST OF TABLES . . . . xiv 1/B5

NOMENCLATURE . . . . xv 1/B6

Chapter

I. INTRODUCTION 1 1/B12

1.1 Previous Work 2 1/B13

1.2 Asymmetric Jet Velocity Profile 9 1/C7

1.3 Objectives of the Thesis 11 1/C10

1.4 Outline of Thesis 12 1/C11

II. EXPERIMENTAL APPARATUS 15 1/C14

2.1 Description of the Wind Tunnel Components 15 1/C14
Heat exchanger
Blower system
Plenum chamber
Transition section
Test section

2.2 Description and Performance of the Wall Jet Flow System 27 1/D13
Air supply system
Wall jet assembly
Performance of the wall jet

III. INSTRUMENTATION 49 1/F12

3.1 Pitot Probes and Preston Tubes 49 1/F12

3.2 Hot-wire probes 51 1/G1
Slant-wire rotating mechanism
Traversing mechanism

3.3 Electronic Signal Processing 56 1/G6

3.4 Calibrations 56 1/G6

3.5 Uncertainties in the Measurements . . . 57 1/G7

IV. EXPERIMENTAL RESULTS FOR THE ZERO PRESSURE GRADIENT FLOW 59 1/G9

4.1 Flow Conditions 60 1/G10

4.2 Mean Flow Data 64 2/A5
Skin friction C_f
Mean velocity U
Integral parameters
Effect of the asymmetric jet velocity profile on the mean flow
Profile parameters

4.3 Turbulence Data 89 2/C5
Turbulence intensity u_t/U_∞
Turbulence intensities v_t/U_∞, w_t/U_∞ and shear stress $-\overline{uv}$
Effect of the asymmetric jet velocity profile on the turbulent quantities
Turbulent kinetic energy k
Correlation functions R_{uv} and a_1
Eddy viscosity ν_{eff}
Length scales L_{mix} and L_k
Production of turbulent kinetic energy
Spectra and dissipation measurements

V. EXPERIMENTAL RESULTS FOR THE ADVERSE PRESSURE GRADIENT FLOW 140 3/A8

5.1 Flow Conditions 141 3/A9

5.2 Mean Flow Data 147 3/B2
Skin friction C_f
Mean Velocity U
Integral parameters
Effect of the asymmetric jet velocity profile on the mean flow
Profile parameters

5.3 Turbulence Data 167 3/C12
Turbulence intensity u_t/U_∞
Turbulence intensities v_t/U_∞, w_t/U_∞ and the shear stress $-\overline{uv}$
Turbulent kinetic energy k
Correlation functions R_{uv} and a_1
Eddy viscosity
Mixing length L_{mix} and Prandtl-Kolmogorov length scale L_k
Production of turbulent kinetic energy

VI. PREDICTION METHOD 192 3/F1

6.1 Selection of the Prediction Method 192 3/F1

6.2 Description of the Theoretical Method 194 3/F3
Turbulence model
Computational procedure
Starting procedure

VII. COMPUTED RESULTS 205 3/F14

7.1 Prediction of the Zero Pressure Gradient Flow 206 3/G1
Computations using the experimental initial velocity and turbulence profiles
Computations using the automatic starting procedure

7.2 Predictions of the Adverse Pressure Gradient Flow 216 3/G11
Computations using experimental initial profiles of velocity and turbulence
Computations using the automatic starting procedure

7.3 Comparison of the Performance of Linear and Uniform Jet Velocity Profiles 232 4/B3
Selection of the parameter a
Starting turbulence profiles
Prediction results

VIII. CONCLUSIONS 249 4/C8

APPENDIX A. MEASUREMENTS ON A WALL JET BY BOWLES (1977) 252 4/C11

APPENDIX B. ESTIMATION OF THE FRICTIONAL LOSSES IN THE WALL JET NOZZLE 255 4/C14

APPENDIX C. MEASUREMENT OF THE TURBULENCE INTENSITIES AND THE REYNOLDS SHEAR STRESS 259 4/D4

APPENDIX D. NORMAL HOT-FILM DATA FOR THE ZERO PRESSURE GRADIENT FLOW 272 4/E4

APPENDIX E. SLANT-WIRE DATA FOR ZERO PRESSURE GRADIENT FLOW 279 4/E14

APPENDIX F. NORMAL HOT-FILM DATA FOR ADVERSE PRESSURE GRADIENT FLOW 286 4/F13

APPENDIX G. SLANT-WIRE DATA FOR ADVERSE PRESSURE GRADIENT FLOW 291 4/G9

LIST OF REFERENCES 294 4/G14

Item 830-H-14 NAS 1.26:3340

DEC 16 1980

NASA Contractor Report 3340

ORIGINAL

COMPLETED

Investigation of Blown Boundary Layers With an Improved Wall Jet System

K. R. Saripalli and R. L. Simpson

GRANT NSG-1548
NOVEMBER 1980

NASA

NASA Contractor Report 3340

Investigation of Blown Boundary Layers With an Improved Wall Jet System

K. R. Saripalli and R. L. Simpson
Southern Methodist University
Dallas, Texas

Prepared for
Langley Research Center
under Grant NSG-1548

National Aeronautics
and Space Administration

Scientific and Technical
Information Branch

1980

BLANK PAGE

BLANK PAGE

TABLE OF CONTENTS

LIST OF FIGURES vii

LIST OF TABLES xiv

NOMENCLATURE xv

Chapter

I. INTRODUCTION 1

1.1 Previous Work 2

1.2 Asymmetric Jet Velocity Profile 9

1.3 Objectives of the Thesis 11

1.4 Outline of Thesis 12

II. EXPERIMENTAL APPARATUS 15

2.1 Description of the Wind Tunnel Components 15
Heat exchanger
Blower system
Plenum chamber
Transition section
Test section

2.2 Description and Performance of the Wall Jet Flow System 27
Air supply system
Wall jet assembly
Performance of the wall jet

III. INSTRUMENTATION 49

3.1 Pitot Probes and Preston Tubes 49

3.2 Hot-wire probes 51
Slant-wire rotating mechanism
Traversing mechanism

3.3 Electronic Signal Processing 56

3.4 Calibrations 56

3.5 Uncertainties in the Measurements . . . 57

IV. EXPERIMENTAL RESULTS FOR THE ZERO PRESSURE GRADIENT FLOW 59

4.1 Flow Conditions 60

4.2 Mean Flow Data 54
  - Skin friction C_f
  - Mean velocity U
  - Integral parameters
  - Effect of the asymmetric jet velocity profile on the mean flow
  - Profile parameters

4.3 Turbulence Data 89
  - Turbulence intensity u_t/U_∞
  - Turbulence intensities v_t/U_∞, w_t/U_∞ and shear stress $-\overline{uv}$
  - Effect of the asymmetric jet velocity profile on the turbulent quantities
  - Turbulent kinetic energy k
  - Correlation functions R_{uv} and a_1
  - Eddy viscosity ν_{eff}
  - Length scales L_{mix} and L_k
  - Production of turbulent kinetic energy
  - Spectra and dissipation measurements

V. EXPERIMENTAL RESULTS FOR THE ADVERSE PRESSURE GRADIENT FLOW 140

5.1 Flow Conditions 141

5.2 Mean Flow Data 147
  - Skin friction C_f
  - Mean Velocity U
  - Integral parameters
  - Effect of the asymmetric jet velocity profile on the mean flow
  - Profile parameters

5.3 Turbulence Data 167
Turbulence intensity u_t/U_∞
Turbulence intensities v_t/U_∞, w_t/U_∞ and the shear stress $-\overline{uv}$
Turbulent kinetic energy k
Correlation functions R_{uv} and a_1
Eddy viscosity
Mixing length L_{mix} and Prandtl-Kolmogorov length scale L_k
Production of turbulent kinetic energy

VI. PREDICTION METHOD 192

6.1 Selection of the Prediction Method 192

6.2 Description of the Theoretical Method 194
Turbulence model
Computational procedure
Starting procedure

VII. COMPUTED RESULTS 205

7.1 Prediction of the Zero Pressure Gradient Flow 206
Computations using the experimental initial velocity and turbulence profiles
Computations using the automatic starting procedure

7.2 Predictions of the Adverse Pressure Gradient Flow 216
Computations using experimental initial profiles of velocity and turbulence
Computations using the automatic starting procedure

7.3 Comparison of the Performance of Linear and Uniform Jet Velocity Profiles 232
Selection of the parameter a
Starting turbulence profiles
Prediction results

VIII. CONCLUSIONS 249

APPENDIX A. MEASUREMENTS ON A WALL JET BY BOWLES (1977) 252

APPENDIX B. ESTIMATION OF THE FRICTIONAL LOSSES IN THE WALL JET NOZZLE 255

APPENDIX C. MEASUREMENT OF THE TURBULENCE INTENSITIES AND THE REYNOLDS SHEAR STRESS 259

APPENDIX D. NORMAL HOT-FILM DATA FOR THE ZERO PRESSURE GRADIENT FLOW 272

APPENDIX E. SLANT-WIRE DATA FOR ZERO PRESSURE GRADIENT FLOW 279

APPENDIX F. NORMAL HOT-FILM DATA FOR ADVERSE PRESSURE GRADIENT FLOW 286

APPENDIX G. SLANT-WIRE DATA FOR ADVERSE PRESSURE GRADIENT FLOW 291

LIST OF REFERENCES 294

LIST OF FIGURES

1.1 (a) Velocity Profile for a Simple Wall Jet . . . 4

1.1 (b) Velocity Profile for a Blown Boundary Layer 4

1.2 (a) Uniform Jet Velocity Profile 10

1.2 (b) Symmetrical Jet Velocity Profile 10

1.2 (c) Asymmetric Jet Velocity Profile 10

2.1 Schematic Arrangement of the Wind Tunnel 16

2.2 Perforated Top Wall in Position for the Adverse Pressure Gradient Flow . . . 25

2.3 A Single Cell of the Perforated Plate . . 26

2.4 Perforated End Plate to Span the End Section of the Tunnel 28

2.5 Wall Jet Assembly. 31

2.6 Poplar Wood Section "A" (Fig. 2.5) 33

2.7 Poplar Wood Section "B" (Fig. 2.5) 33

2.8 Extruded Aluminum End Piece 34

2.9 Wall Jet Baffle Plate 37

2.10 Flow Path Inside the Wall Jet Nozzle Around the Corner 38

2.11 Measured Velocity and Turbulence Profiles at the Slot (x/y_c=0.292) . . . 40

2.12 Square Brass Tube for Measuring the Wall Jet Exit Dynamic Pressure 45

3.1 Rectangular Mouth Boundary Layer Pitot (Total Head) Tube 50

3.2 Slant-Wire Rotating Mechanism With the Probe Mounted on It 53

3.3 Traversing Mechanism 55

4.1 Position of the Top Wall for the Zero Pressure Gradient Flow 62

4.2 Mean Velocity Profile in the Wall Co-ordinates at 21 cm Upstream of the Slot 65

4.3 (a) Variation of Skin Friction 65

4.3 (b) Variation of Skin Friction in Logarithmic Co-ordinates 67

4.3 (c) Variation of Skin Friction Coefficient C_{fm}. 67

4.4 (a-e) Mean Velocity Profiles 68

4.5 (a&b) Mean Velocity Profiles in the Wall Co-ordinates 75

4.5 (c) Streamline Pattern Around the Slot Lip . . 78

4.6 (a) Growth of the Boundary Layer Thickness . . 78

4.6 (b) Growth of the Displacement Thickness . . . 79

4.6 (c) Growth of the Momentum Thickness 79

4.6 (d) Variation of the Shape Factor 80

4.6 (e) Variation of the Momentum Thickness Reynolds Number Re_2 80

4.7 (a) Development of Y_{max} and Y_{half} 84

4.7 (b) Development of Y_{min} 84

4.8 (a) Variation of U_{max} and U_{min} 88

4.8 (b) Variation of $(U_{max} - U_{min})$ 88

4.9 (a-c) Distributions of the Turbulence Intensity u_t/U_∞ 90

4.10 (a&b) Distributions of u_t in the Wall Co-ordinates 93

4.11 (a&b) Distributions of the Turbulence Intensity v_t/U_∞ 97

4.12 (a&b) Distributions of the Turbulence Intensity w_t/U_∞ 99

4.13 (a&b) Distributions of the Shear Stress 102

4.14 (a&b) Distributions of the Turbulent-Kinetic Energy k 107

4.15 (a&b) Distributions of the Correlation Function R_{uv} 108

4.16 (a&b) Distributions of the Correlation Function a_1 110

4.17 (a-c) Distributions of the Eddy Viscosity . . . 112

4.18 (a-c) Distributions of the Prandtl Mixing Length L_{mix} 115

4.19 (a-c) Distributions of the Prandtl-Kolmogorov Length Scale L_k 117

4.20 (a-c) Distributions of the Shear Stress Production of Turbulent Kinetic Energy 120

4.21 (a&b) Spectra of $\overline{u^2}$ at x/y_c=0.292 and at Different y/y_c Locations 123

4.22 (a&b) Spectra of $\overline{u^2}$ Representing the Inner Layer at Different Stations 124

4.23 (a&b) Spectra of $\overline{u^2}$ Representing the Outer Layer at Different Stations 125

4.24 (a-c) Distributions of the Dissipation Rate . . 131

4.25 (a-c) Distributions of the Bursting Period . . 136

5.1 Position of the Top Wall for the Adverse Pressure Gradient Flow 143

5.2 Free-Stream Velocity Distribution . . . 146

5.3 (a) Variation of Skin Friction 146

5.3 (b) Variation of Skin Friction in Logarithmic Co-ordinates 148

5.3 (c) Variation of the Skin Friction Coefficient C_{fm} 148

5.4 (a-c) Mean Velocity Profiles 150

5.5 (a&b) Mean Velocity Profiles in the Wall Co-ordinates 155

5.6 (a) Growth of the Boundary Layer Thickness . . . 158

5.6 (b) Growth of the Displacement Thickness 158

5.6 (c) Growth of the Momentum Thickness 159

5.6 (d) Variation of the Shape Factor 159

5.6 (e) Variation of the Momentum Thickness Reynolds Number Re_2 160

5.7 (a) Development of Y_{max} and Y_{half} 165

5.7 (b) Development of Y_{min} 165

5.8 (a-c) Variation of U_{max}, U_{min} and $(U_{max}-U_{min})$ . . 168

5.9 (a-c) Distributions of the Turbulence Intensity u_t/U_∞ 171

5.10 (a&b) Distributions of u_t in Wall Co-ordinates . . 174

5.11 Distributions of the Turbulence Intensity v_t/U_∞ 178

5.12 Distributions of the Turbulence Intensity w_t/U_∞ 179

5.13 (a&b) Distributions of the Shear Stress 180

5.14 Variation of the Turbulent Kinetic Energy k. 183

5.15 Variation of the Correlation Function R_{uv} . 185

5.16 Variation of the Correlation Function a_1 . . 185

5.17 Distributions of the Eddy Viscosity 187

5.18 Distributions of the Prandtl Mixing Length L_{mix} 188

5.19 Distributions of the Prandtl-Kolmogorov Length Scale L_k 188

5.20 Distributions of the Shear Stress Production of Turbulent Kinetic Energy 190

6.1 Assumed Velocity Profile for the Automatic Starting Procedure 202

7.1 (a) Initial Profile of $-\overline{uv}$ for the Computations using Experimental Initial Profiles in the Case of Zero Pressure Gradient Flow . . . 207

7.1 (b) Predicted Development of the Displacement Thickness for the Zero Pressure Gradient Flow 210

7.1 (c) Predicted Development of the Momentum Thickness for the Zero Pressure Gradient Flow 211

7.1 (d) Predicted Variation of the Skin Friction for the Zero Pressure Gradient Flow 212

7.1 (e) Predicted Variation of the Profile Length Scales for the Zero Pressure Gradient Flow 213

7.1 (f) Predicted Variation of U_{max} and U_{min} for the Zero Pressure Gradient Flow 214

7.2 (a) Initial Profiles of $-\overline{uv}$ for the Computations Using the Experimental Initial Profiles in the Case of Adverse Pressure Gradient Flow . . . 218

7.2 (b) Predicted Development of the Displacement Thickness for the Adverse Pressure Gradient Flow . . . 219

7.2 (c) Predicted Development of the Momentum Thickness for the Adverse Pressure Gradient Flow . . . 220

7.2 (d) Predicted Variation of Skin Friction for the Adverse Pressure Gradient Flow 221

7.2 (e) Predicted Variation of U_{max} for the Adverse Pressure Gradient Flow . . . 222

7.2 (f) Predicted Variation of U_{min} for the Adverse Pressure Gradient Flow 223

7.2 (g) Predicted Variation Y_{min} for the Adverse Pressure Gradient Flow 224

7.2 (h) Predicted Development of the Profile Length Scales for the Adverse Pressure Gradient Flow 225

7.3 (a) Starting Velocity Profile for the Predictions with Uniform Jet Velocity Profile Using the Automatic Starting Procedure 234

7.3 (b) Starting Velocity Profile for the Predictions with Linear Jet Velocity Profile Using the Automatic Starting Procedure 234

7.3 (c) Comparison of Uniform and Linear Jet Velocity Profiles Without the Mixing Layer 235

7.4 (a) Predicted Velocity Profiles at x/y_c=100.3 for the Adverse Pressure Gradient Flow 239

7.4 (b) Predicted Development of the Displacement Thickness for the Adverse Pressure Gradient Flow 240

7.4 (c) Predicted Growth of the Momentum Thickness in the Case of Adverse Pressure Gradient Flow 241

7.4 (d) Predicted Variation of Skin Friction for the Adverse Pressure Gradient Flow . . 242

7.4 (e) Predicted Variation of U_{min} for the Adverse Pressure Gradient Flow 243

7.4 (f) Predicted Variation of Y_{min} for the Adverse Pressure Gradient Flow 244

7.4 (g) Predicted Variation of the Profile Length Scales for the Adverse Pressure Gradient Flow 245

A-1 Mean Velocity and Turbulence Profiles at the Exit of the Jet (Bowles) . . . 253

B.1 Close-up View of the Jet Nozzle 256

C.1 Geometry and Position of the Slant-Wire Probe 261

LIST OF TABLES

2.1 Variation of the Slot Height Along the Length of the Wall Jet 35

4.1 Variation of the Free Stream Velocity Measured with the Rake Hot-Wire Probe 61

4.2 Magnitude of N_0 F(n) at 1 KHz for the Spectra Presented in Figs. 4.21, 4.22, 4.23 . 126

D Normal Hot-Film Data of U/U_∞ and u_t/U_∞ for the Zero Pressure Gradient Flow 273

E Slant-Wire Data for the Zero Pressure Gradient Flow 280

F Normal Hot-Film Data of U/U_∞ and u_t/U_∞ for the Adverse Pressure Gradient Flow 287

G Slant-Wire Data for the Adverse Pressure Gradient Flow 292

NOMENCLATURE

a	Fraction of the slot height over which the jet velocity is uniform in the velocity profile of the automatic starting procedure (Fig. 6.1 (b)).
a_1	Correlation coefficient $-\overline{uv}/(u_t^2 + v_t^2 + w_t^2)$.
A, B	Constants in the equation 4.2 or in the equation C.4 of Appendix C.
C_f	Skin friction coefficient based on the free stream velocity $C_f = \tau_w(\frac{1}{2}\rho U_\infty^2)$.
C_{fm}	Skin friction coefficient based on the maximum velocity $C_{fm} = \tau_w/(\frac{1}{2}\rho U_{max}^2)$.
C_μ	A constant in the expression for the Prandtl-Kolmogorov length scale.
$F(n)$	Spectrum function of $\overline{u^2}$.
f	U/U_∞ in the equation 4.5.
H	Form factor or shape factor $\frac{\delta_1}{\delta_2}$.
k	Turbulent kinetic energy $\frac{1}{2}(\overline{u^2} + \overline{v^2} + \overline{w^2})$.
K	Constant in the equation (4.4).
K_1, K_2	Constants in the equation C.1 of Appendix C.

L_k	Prandtl-Kolmogorov length scale, $\nu_{eff}/(C_\mu\sqrt{k})$
L_{mix}	Mixing Length $[\nu_{eff}/(\lvert\partial U/\partial y\rvert)]^{\frac{1}{2}}$.
L_ε	Dissipation length scale $k^{3/2}/_\varepsilon$.
N_0	A constant of the spectrum analyser.
n	Exponent in the equation C.4 of Appendix C or the exponent in the power law velocity profile (Fig. 6.1) or the frequency in Hz.
n_b	Bursting frequency.
P	Mean pressure.
p	Pressure fluctuation.
R_e	Reynolds number.
Re_2	Momentum thickness Reynolds number $U_\infty\delta_2/\nu$.
Re_x	Reynolds number $U_\infty x/\nu$ (equation 4.3).
Re_λ	Turbulence Reynolds number $(\overline{u^2})^{\frac{1}{2}}\lambda/\nu$.
R_{uv}	Correlation coefficient $-\overline{uv}/(u_t v_t)$.
t	Time.
$\tilde{U}, \tilde{V}, \tilde{W}$	Instantaneous velocities in the x, y, z directions.
U, V, W	Mean velocity in the positive x, y, z directions.

u_t, v_t, w_t	RMS fluctuations $\sqrt{\overline{u^2}}$, $\sqrt{\overline{v^2}}$, $\sqrt{\overline{w^2}}$, respectively.
u, v, w	Velocity fluctuations in the x, y, z directions respectively.
$-\overline{uv}$	Reynolds shear stress.
$\overline{u^2}$, $\overline{v^2}$, $\overline{w^2}$	Reynolds normal stresses.
U_∞	Free-stream or external velocity.
U_J	Jet velocity.
U_{Jmax}	Maximum jet velocity (Fig. 7.3 (b) and (c)).
U_{Jave}	Jet velocity defined in Chapter 4, Section 4.2.5 (b).
U_{max}	Maximum velocity in the velocity profile (Fig. 1.1 (b)).
U_{min}	Minimum velocity in the velocity profile (Fig. 1.1 (b)).
U^+	U/U_τ
U_τ	Frictional velocity or the shear velocity $\sqrt{\frac{\tau_w}{\rho}}$.
x,y,z	Cartesian co-ordinates; x is the streamwise distance, with x = 0 at the slot; y is the distance normal to the bottom wall, with y = 0 at the surface of the bottom wall.
y_c	Slot height.
Y_{half}	Value of y where $U = \frac{(U_{max} + U_{min})}{2}$.

Y_{max}	Value of y where $U = U_{max}$.
Y_{min}	Value of y where $U = U_{min}$.
y^+	$U_\tau y/\nu$.

Greek Symbols

α	Constant used in the equation (4.5).
$\Delta(U/U_\tau)$	Strength of the wake component.
ΔR	Uncertainty in the value of R.
δ	Boundary layer thickness where $\frac{U}{U_\infty} = 0.99$.
δ_1	Displacement thickness $\int_0^\infty (1 - \frac{U}{U_\infty})\,dy$.
δ_2	Momentum thickness $\int_0^\infty \frac{U}{U_\infty}(1-U/U_\infty)\,dy$.
ε	Dissipation rate.
ξ	Co-ordinate defined in Fig. 6.1.
η	$U_\infty y/\nu$.
θ	Angle of rotation of the slant-wire probe (Appendix C, Fig. C.1).
λ	Microscale $(15\,\nu\,\overline{u^2}/\varepsilon)^{1/2}$.
ν	Kinematic viscosity.
ν_{eff}	Kinematic eddy viscosity or kinematic effective viscosity $\nu_{eff} = -\overline{uv}/(\partial U/\partial y)$.

ξ	Co-ordinate defined in Fig. 6.1.
ρ	Density.
ϕ	Angle of the slant wire (Appendix C, Fig. C.1).

Superscripts

overbar ($^{-}$)	Time average.

Subscripts

BL	Upstream boundary layer value.
J	Jet value.
ML	Mixing layer value.

Abbreviations Used in the Figures and Tables

CF	C_f
CF_m	C_{fm}
DELTA	δ
DELTA1	δ_1
DELTA2	δ_2
DUDY	$\partial(U/U_\infty)/\partial(y/\delta)$.
EDVIS	ν_{eff}
EPS	ε

LMIX	L_{mix}
LK	L_k
NU	ν
NB	n_b
PROD	$-\overline{uv}(\partial U/\partial y)$
RE2	Re_2
UINF	U_∞
UTAU	U_τ
$-\overline{UV}$	$-\overline{uv}$
UT	u_t
VT	v_t
WT	w_t
YC	y_c
YHALF	Y_{half}
YMAX	Y_{max}
YMIN	Y_{min}

CHAPTER I

INTRODUCTION

A tangential wall jet is the flow of high velocity fluid emanating from a narrow slot and blowing tangentially over a rigid wall. The flow of a wall jet mixing with an external moving stream has drawn considerable basic and applied interest in the past because it incorporates the characteristics of both a boundary layer and a free jet. Tangential wall jets are generally used in practice: (a) to control turbulent boundary layer separation on high lift aerofoils and thereby achieve a large increase in lift (Williams and Alexander, 1958), (b) to prevent separation and improve the pressure recovery in wide angle diffusers (Ramaprian, 1969; Nicoll and Ramaprian, 1970), (c) to cool a surface exposed to a stream of hot gas as in the case of combustion chambers and the exhaust nozzles of rocket motors (Samuel and Joubert, 1964; Seban, 1960; Papell and Trout, 1959), (d) to heat a surface exposed to cold temperatures (Wieghardt, 1946).

This thesis is concerned with the behavior of two-dimensional incompressible turbulent wall jets submerged in a boundary layer when they are used to prevent boundary layer separation on plane surfaces. The main motivation for studying this topic comes from the large increase in lift that can be obtained from high lift aerofoils if the flow can be kept attached to the aerofoil surface by the use of wall jets (Williams and Alexander, 1958). The effect of the jet from the blowing slot is to increase the kinetic energy of the flow in the boundary layer near the surface, thereby enabling it to advance into a high adverse pressure gradient region without separating.

1.1 Previous Work

Wall jets have been investigated quite extensively in the past. However, most work is concerned with the case where the ratio of jet velocity to free-stream velocity is large in the range of 2 to infinity and with a negligible upstream boundary layer at the slot. The reason for the concentration of effort on the higher velocity ratios is mainly because of the fact that the velocity profiles in such cases contain only a velocity maximum instead of also a minimum and the flow can be analyzed approximately by methods of velocity profile similarity. However, the useful range of velocity ratios lies between 1 and 2, since it is impractical to maintain higher velocity ratios, especially in supersonic flows. Even in the cases where the study of wall jets at low velocity ratios was attempted, the momentum deficit of the upstream boundary layer at the slot was small. In practical applications, however, the jet usually mixes with a thick upstream boundary layer that is approaching separation, giving rise to a velocity profile shown in Fig. 1.1(b) rather than that of a "simple" wall jet in Fig. 1.1(a). Therefore, the study of wall jets submerged in a thick upstream boundary layer is very useful. This class of flows will be referred to as "blown boundary layers" since the wall jet is submerged in a boundary layer.

1.1(a) Previous Work on Wall Jets With Upstream Boundary Layers

In describing the previous work, attention will be restricted to those authors who have considered a wall jet submerged in an upstream boundary layer, which was referred to earlier as "blown boundary layer." Irwin (1974) gives a fairly comprehensive description of the work in the literature on blown boundary layers.

Carriere, Eichelbrenner and Poisson-Quinton (1959) appear to have been the first to measure detailed mean velocity profiles downstream of the slot. They attempted to use an empirical integral method to predict the development of the flow. Thomas (1962, 1965) gave a crude empirical method of determining the blowing momentum required to prevent separation. Even though Thomas' empirical method is simple, it does not seem very sound as it is based on very little experimental evidence.

Bradshaw and Gee (1962) presented mean flow measurements in a blown boundary layer along with measurements in simple wall jets on curved and plane surfaces. They identified two essentially different modes of

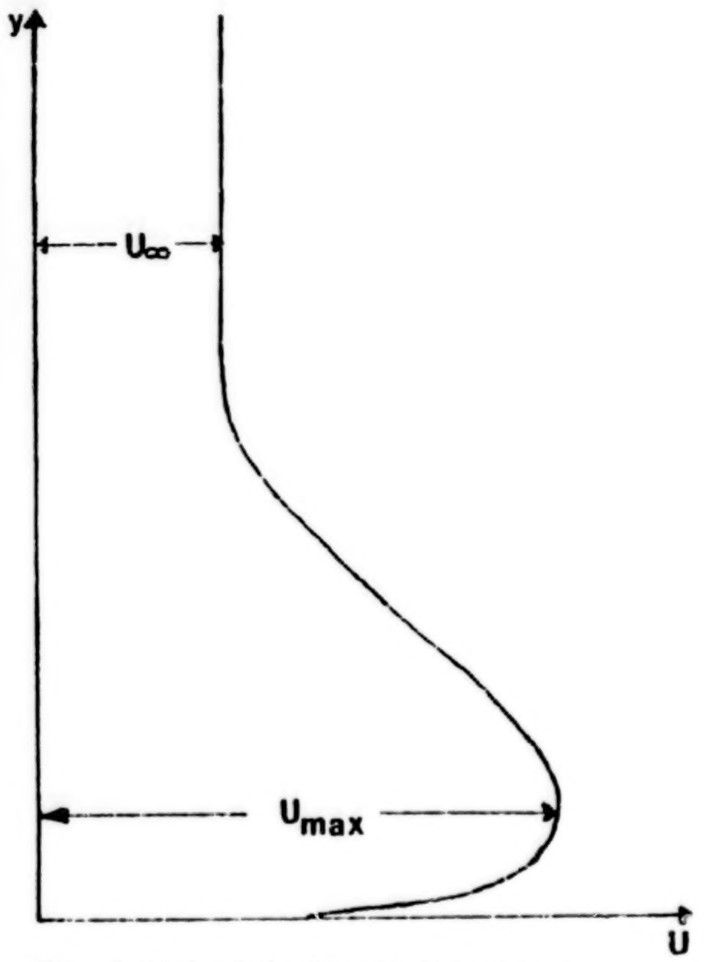

Fig. 1.1(a) Velocity Profile for a "Simple" Wall Jet

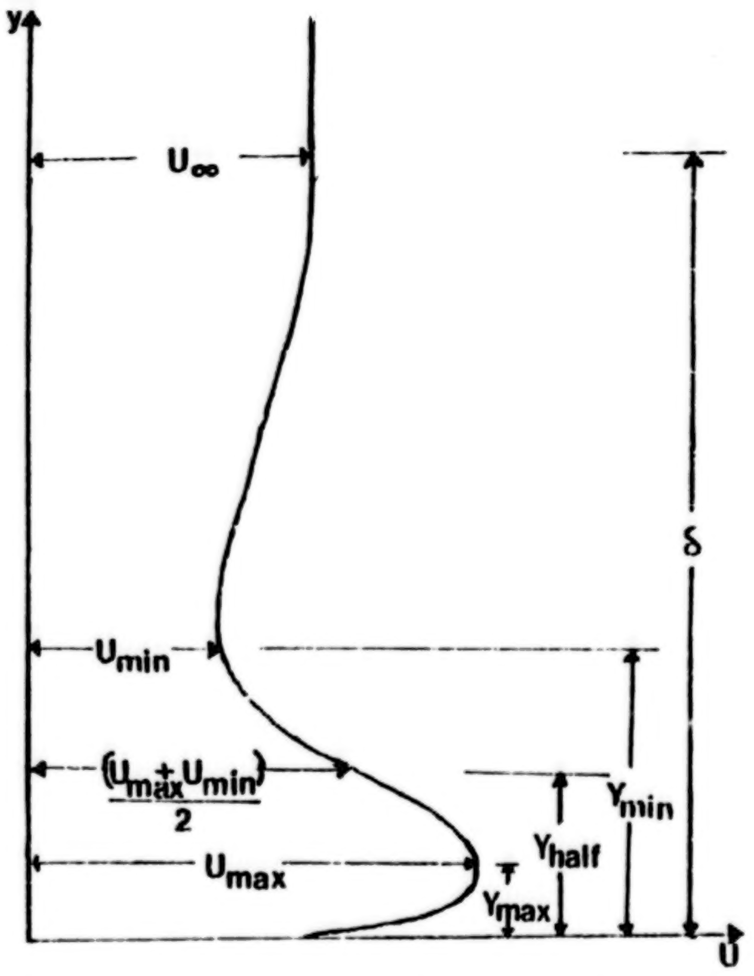
y
U∞
δ
Umin
(Umax+Umin)/2
Umax
Ymin
Yhalf
Ymax
U

Fig. 1.1(b) Velocity Profile for a Blown Boundary Layer "separation," one involving reversed flow at the wall, the other having reversed flow in the wake at the velocity minimum. McGahan (1965) carried out mean flow measurements in blown boundary layers on a cylinder with its axis aligned with the flow direction. The pressure gradient was adjusted by sticking paper strips on the outside of an outer concentric porous cylinder and by placing an end plate to block the flow, at the downstream end. McGahan proposed an integral calculation method for predicting the flow development when the upstream boundary layer was thick. It agreed with his data fairly well except near to the point of separation at the wall.

Gartshore and Newman (1969) described an integral calculation method for wall jets in arbitrary pressure gradients primarily for the use with small upstream boundary layers. However they did attempt to account for a large upstream boundary layer by changing the starting conditions properly. They also presented measurements of mean quantities for wall jets under zero and adverse pressure gradients with small upstream boundary layers.

Kind (1971) extended Gartshore and Newman's calculation method to deal with strongly curved wall jets developing in the presence of moderately thick upstream boundary layers. The upstream boundary layer was accounted for by using a revised method of starting and assuming that the stagnation pressure remains constant along streamlines outside the wall jet. He also presented mean flow measurements on wall jets on the cylindrical trailing edge of a circulation control airfoil.

Most of the above mentioned previous work on blown boundary layers was mainly concerned with high jet velocity ratios (greater than 2.0) and measurements of mean quantities under small upstream boundary layers.

Goradia and Colwell (1971) measured mean velocity profiles of several wall jets under adverse pressure gradients in a two-dimensional diffuser with low jet volicity ratios in the neighborhood of 1 to approximately 2. The velocity data were used to formulate empirical relationships between parameters such as the form factor H and energy form factor and to derive empirical expressions for the velocity profiles. The measurements were also utilized for the calculations of wall shear and shear distribution by numerical methods. English (1970) considered the flow over a slotted flap which is equivalent to considering a wall jet with the total head at the slot equal to that of the freestream. The measurements of mean velocity and shear stress were made under zero and adverse pressure gradients. The slot width was somewhat larger than that usually used for wall jets, so that a region of potential flow often exists in the flow from the slot over a large portion of the flap surface.

Kacker and Whitelaw (1968, 1971) investigated wall jets under a zero pressure gradient with the jet velocity ratios in the range of 0.75 and 2.74 and with a small upstream boundary layer. They made measurements of mean velocity, turbulence intensities, turbulent shear stress, and spectra. They derived the results of eddy viscosity, mixing length and Prandtl-Kolmogorov length scale from the measurements. However, the restriction to zero pressure gradient conditions limits the usefulness of the data. The upstream boundary layer was too small to have a very significant influence on the flow.

Ramaprian (1973, 1975) reported measurements on the wall of a conical diffuser with annular injection at the entrance and with the jet velocity ratios in the range of 1.27 to 2.38. Measurements of mean velocity, turbulence intensities, shear stress, and spectra were reported. He used Spalding and Patankar's (1967) method with a mixing length model for the prediction of his flows and the method yielded satisfactory predictions of the wall jet development. The empirical constants were adjusted to give best agreement with his data.

Irwin (1974) studied a number of blown boundary layers with adverse pressure gradients. Measurements of mean velocity, turbulence intensities, shear stress and spectra were made for the case of a self-preserving strong wall jet under an adverse pressure gradient flow with negligible upstream boundary layer. Another case he studied was that of a strong wall jet (jet velocity ratio ≈ 3.3) under an adverse pressure gradient with a small upstream boundary layer. The effect of the upstream boundary layer in this case persisted quite far downstream of the slot, but was eventually absorbed by the wall jet. Measurements of mean velocity, turbulence intensities and shear stress were reported in this case. Irwin also reported measurements of mean velocity on two strong wall jets (jet velocity ratio ≈ 3.3 and 2.5) with highly adverse pressure gradients and with large upstream boundary layers. Only one case of a wall jet under adverse pressure gradient conditions with a relatively smaller jet excess velocity (jet velocity ratio ≈1.65) and large upstream boundary layer was reported by Irwin. In this case, the wall jet was just sufficient to prevent separation, but no detailed measurements of turbulence were made. Irwin developed a theoretical prediction method applicable to blown boundary layers. It essentially uses the computing method of Spalding and Patankar (1967, 1969) and the turbulence model proposed by Launder, Reece and Rodi (1973) along with the modifications of the turbulence model to account for the effect of the wall on the turbulence and the streamline curvature. He reported good predictions of his measurements in blown boundary layers and also other different types of flows, which included isolated wall jets, normal boundary layers and curved wall jets.

The above mentioned previous work on blown boundary layers reveals that previous studies of wall jets under thick upstream boundary layers under zero and adverse pressure gradients are very limited. In some cases where attempts have been made, the data were generally limited to the mean quantities rather than detailed data on turbulence. Hence, there is a need for the study of wall jets under thick upstream boundary layers and with low jet velocity ratios, i.e., less than 2.

1.2 Asymmetric Jet Velocity Profile

Almost all of the previous investigators of wall jets have used a uniform jet velocity profile shown in Fig. 1.2(a) with negligible upper and lower wall boundary layers of the jet nozzle. In cases where the jet boundary layers were considerable, the velocity profile was symmetric about the centerline of the slot as shown in Fig. 1.2(b). However, it is interesting to see how the flow development is affected if the jet velocity profile is made asymmetric as shown in Fig. 1.2(c) instead of uniform or symmetric for a given value of the total jet momentum. For the same total jet momentum, an asymmetric profile will have higher maximum jet velocity than a symmetric profile. The idea of using an asymmetric velocity profile stems from the following arguments. In a practical situation, the upstream boundary layer at the slot is the one corresponding to a flow approaching separation and has a large deficit of momentum. Therefore, it is reasonable to state that a greater part of the jet momentum should be made available nearer to the slot lip than nearer to the wall to reduce the momentum deficit of the upstream boundary layer. However, one

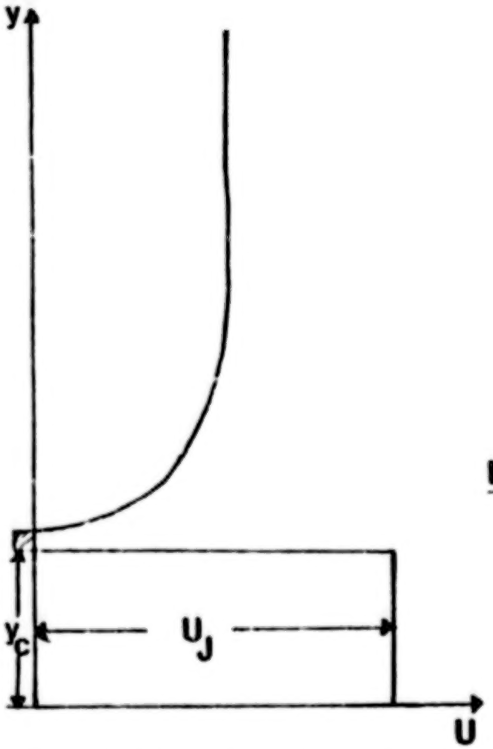

Fig. 1.2(a) Uniform Jet Velocity Profile

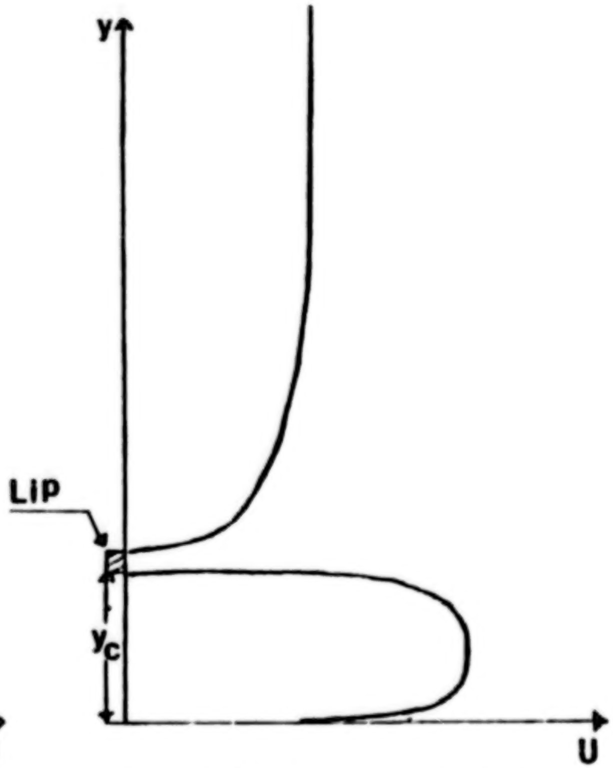

Fig. 1.2(b) Symmetrical Jet Velocity Profile

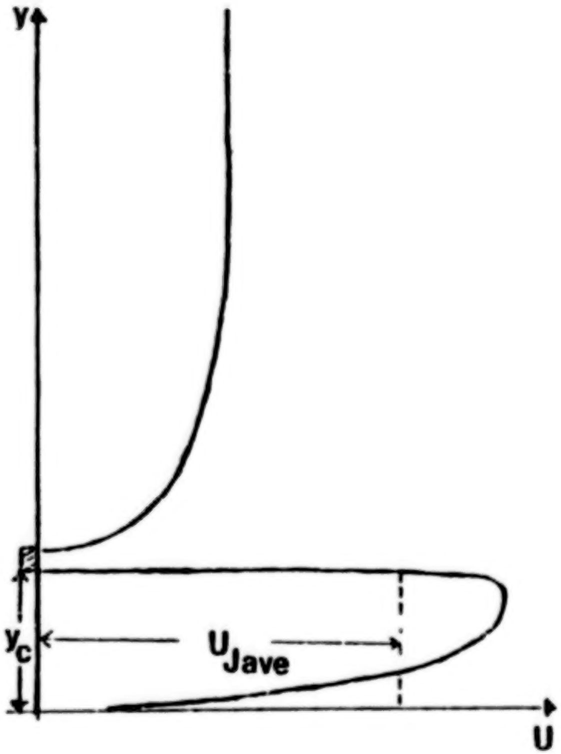

Fig. 1.2(c) Asymmetric Jet Velocity Profile

might argue that momentum is also needed near the wall to prevent separation there. But relatively more momentum is required near the slot lip than near the wall and the momentum of the jet in the lower half of the jet should be sufficient to prevent wall flow separation. In comparison, the symmetric jet velocity profile might be able to prevent separation at the bottom wall, but a large momentum deficit region might develop in the outer layer far downstream which might eventually lead to separation at the lower wall. Also, the asymmetric profile should result in less frictional losses at the wall as the velocity gradients are relatively smaller at the wall. Thus, the jet momentum is more effectively utilized in the case of an asymmetric jet velocity profile in reducing the momentum deficit of the upstream boundary layer instead of wasting it on wall friction.

1.3 Objectives of the Thesis

The objectives of the present work are as follows:

1. To obtain experimental data on low jet velocity ratio wall jets in thick upstream boundary layers advancing into zero and strong adverse streamwise pressure gradients.

2. To obtain detailed turbulence data on the type of wall jets considered here in order to aid in the future development of turbulence models and prediction methods and also to supplement the few existing sets of turbulence data for this type of flow.

3. To investigate the effectiveness of an asymmetric jet velocity profile, as compared to a uniform profile, in the control of separation and its influence on the development of the flow downstream of the slot.

4. To predict the present class of wall jets using an existing theoretical method for such flows and to investigate the effectiveness of an asymmetric jet velocity profile from a theoretical basis.

1.4 Outline of the Thesis

Chapter 2 describes the experimental apparatus. The constructional and performance details of the wind tunnel and the wall jet flow system are given as well as how the asymmetric jet velocity profile was produced at the slot. Chapter 3 is devoted to the description of the instrumentation used in obtaining the experimental data.

Chapter 4 gives the experimental results for the zero pressure gradient flow. A brief description of the flow conditions and the process of setting the zero pressure gradient are given. The effect of the asymmetric jet velocity profile on the flow development as indicated by different measured quantities is described. The turbulence data for the zero pressure gradient case were studied in more detail in order to be useful as an aid in developing turbulence models and prediction methods in the future. The spectral data were obtained only for the zero pressure gradient flow. The measured quantities included mean velocity, turbulence intensities, shear stress, spectra and skin friction. The derived quantities included, turbulent kinetic energy, eddy viscosity, Prandtl mixing length, Prandtl-Kolmogorov length scale, correlation coefficients, dissipation and production rates of turbulent kinetic energy and bursting periods.

Chapter 5 is devoted to the experimental results for the adverse pressure gradient flow. The flow conditions and the process of setting the adverse pressure gradient are given. Fewer turbulence data are presented as compared to the zero pressure gradient flow. The pressure gradient was adjusted to be representative of the practical situation on aerofoils and jet flaps. The effect of the asymmetric jet velocity profile on the flow development is described for the case of adverse pressure gradient flow.

Chapter 6 is concerned with the description of the prediction method used to predict the present flows. The prediction method developed by Irwin (1974) for blown boundary layers was used. Only the salient features of the method are given.

Chapter 7 deals with the computed results. The prediction results for the present flows are compared with the experimental data. A main distinction is made between the predictions using the experimental starting conditions and the predictions using the "automatic starting procedure" of Irwin. The former represents the experimental asymmetric jet velocity profile and the latter represents the uniform jet velocity profile. The advantages of an asymmetric profile over a uniform profile are discussed on a theoretical basis. Finally, the case of a linear jet velocity profile was taken to represent an ideal asymmetric profile, which had the greatest momentum near the slot top. Computations were made with the linear velocity profile and compared with the predictions using a uniform profile for the adverse pressure gradient flow.

Chapter 8 lists the conclusions of the thesis.

Use of trade names or names of manufacturers in this report does not constitute an official endorsement of such products or manufacturers, either expressed or implied, by the National Aeronautics and Space Administration.

CHAPTER II

EXPERIMENTAL APPARATUS

This chapter deals with the construction and performance details of the wind tunnel and the wall jet-flow system used in the present work. The function of the wind tunnel is to supply the test section with low turbulence air at a given velocity and temperature. The function of the wall jet is to supply the secondary air necessary for tangential flow injection at the wall.

Figure 2.1 shows the schematic of the wind tunnel including the wall jet system. The wind tunnel is an open circuit blower type tunnel and uses the ambient air. The important components of the wind tunnel include: the heat exchanger for temperature control, the blower, the plenum chamber, the contraction and the test section. The wall jet flow system consists of the wall jet assembly and the air supply system.

The different components of the wind tunnel are described below in the order that the flow passes through them, followed by a description of the wall jet flow system.

2.1 Description of the Wind Tunnel Components

2.1.1 Heat Exchanger

The first component in the path of the airflow is the heat exchanger. A passenger car radiator used for

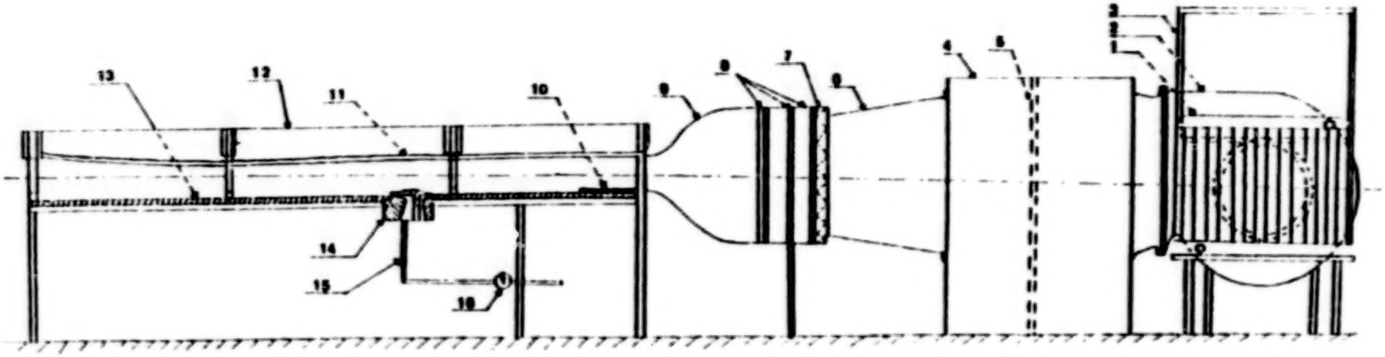

Fig. 2.1 Schematic Arrangement of the Wind Tunnel

1. Heat Exchanger
2. Blower
3. Damper
4. Plenum Chamber
5. Baffle
6. Contraction
7. Honeycomb
8. Screens
9. Contraction (4:1)
10. Roughness Element
11. Top Wall
12. Glass Side Walls
13. Bottom Wall
14. Wall Jet
15. Feed Line
16. Pressure Regulator

this purpose is a finned tube type with a frontal area of 60X48 cm. The heating or cooling of the ambient air was accomplished by allowing hot or cold water through the radiator. By suitably controlling the flow rate of water it was possible to control the temperature of the air in the test section within ±0.1°C at 25°C. The heat exchanger was mainly used to cool the air in the present experiments. The room air conditioning system, supported by two portable heaters each of 1000W capacity was used to heat the ambient air. By properly controlling the heat input to the heaters, it was possible to control the temperature of the air in the test section within ±0.1°C at 25°C.

2.1.2 Blower System

The next component in the air circuit is a FARR HP-2A class 2 type rear access air filter of 61X61X31 cm size enclosed in a box covered on all four sides. This filter is capable of removing dust and foreign particles down to 5 microns size and larger with a 95% efficiency. With less efficiency, it filters particles down to 2 microns size. A damper was placed between the heat exchanger and the filter to control the amount of air flow and hence the velocity of the air in the test section. The damper was made of a plexiglas sheet that slides in an aluminum frame mounted in the access space between the filter frame and the heat exchanger.

The air then enters the suction side of an Aerovent, BIA Aerofoil type, belt driven, centrifugal, general purpose blower. The blower is driven by a Reliance 1.49 KW, 1970 RPM, open, drip-proof motor. The blower can deliver $40m^3$/min of air at 6.6 cm H_2O static pressure. The blower wheel is 31 cm in diameter and has aerofoil type blades.

2.1.3 Plenum Chamber

The air delivered by the blower enters the plenum chamber. The primary function of the plenum chamber is to suppress any large scale fluctuations produced by the blower and to settle the air. The plenum chamber is made of 0.7 mm thick sheet metal and is 99 cm wide, 155 cm long, and 114 cm high. The plenum chamber is connected to the blower on the upstream side and to the ductwork on the downstream side through rubber sheets to avoid the transmission of vibrations from the blower to the downstream ductwork and finally to the test section. The inlet and outlet of the plenum chamber, dimensioned 55X55 cm and 53X53 cm respectively, were facing each other to start with. In this case, the air from the blower was entering directly into the downstream ductwork, unaffected by the plenum chamber. To eliminate this problem, a wooden baffle of 114X112X1.25 cm in size was placed inside the chamber between the inlet and the outlet. The baffle divides the plenum chamber into two equal compartments joined by about a 114X41 cm gap at each end of the baffle. The function of the baffle is to circumvent the air from the blower to the sides, thereby preventing the air from entering directly into the downstream duct work. The baffle plate fully covers the height of the plenum chamber.

2.1.4 Transition Section

The ductwork between the plenum chamber and the test section is classified as the transition section. It includes two contractions and a rectangular duct containing the screens and the honeycomb material. The purpose of the first contraction is two-fold:

1. It serves as a transition piece between the plenum chamber and the downstream sections, and

2. It increases the flow velocity and reduces the turbulence level.

The first contraction has the inlet and outlet dimensions of 53X53 cm and 39X23 cm respectively and is 46 cm in length. It is made of 0.7 mm thick sheet metal. The air after passing through the first contraction enters a rectangular duct also made of 0.7 mm thick sheet metal with dimensions, 46X28X39 cm. This rectangular duct houses the honeycomb material and three screens whose primary function is to reduce the turbulence level in the air stream. The screens and honeycomb were selected according to guidelines given by Bradshaw and Pankhurst (1964). The aluminum honeycomb is 3.2 mm in cell size and 4.3 cm in thickness. The honeycomb eliminates the large scale turbulence and swirl in the air stream. The scale of turbulence is further reduced by three screens in series. The first two aluminum screens are 16 (horizontal) X 18 (vertical) mesh screens with a wire diameter of 0.25 mm and an open area ratio 0.63. The third aluminum screen is a 32X32 square mesh screen with a wire diameter of 0.18 mm and an open area ratio 0.602. The screens are placed 14 cm apart to allow the turbulence in the wake of each screen to decay before the next screen is reached.

The next component in the transition section is a second contraction made of 0.7 mm thick sheet metal with inlet and outlet dimensions of 40X24 cm and 10.2X24 cm, respectively, giving a contraction ratio of nearly 4 to 1. This contraction was designed by Simpson and Wyatt (1972) according to the design method of Jordinson (1961). It further reduces the turbulence intensity of the air stream. Measurements made before the test section was installed indicated a very flat velocity profile at the outlet of the second contraction. The velocity was virtually constant in the spanwise direction. The turbulence intensity u_t/U_∞ was about 0.2% in the freestream of the test section.

2.1.5 Test Section

The test section is 24 cm wide and has a total length of 196 cm. The side walls are 6.4 mm thick float type plate glass 22 cm in height and 196 cm in length. The bottom wall is 1.9 cm thick hard "fin-form" plywood with a very smooth surface finish and is made of two parts. The first part is 58.5 cm in length and the second part is 128.3 cm. The 9.2 cm gap between them is filled by the wall jet, the constructional details of which are given later. The leveled bottom wall rests on a steel platform bolted to the concrete floor.

A piece of sandpaper 16.5 cm (length) X 24 cm (width) is glued to the bottom wall at the beginning of the test section immediately after the contraction outlet This sandpaper is a "NORTON CLOSEKOTE" silicon carbide floor sanding paper with 24 grit size (mesh number) and with an average particle size of the abrasive grain equal to 1.04 mm. Several other types of roughness elements such as, (a) 6.4 mm square rod, (b) 2.4 mm round rod, (c) a rectangular strip 12.7X3.2 mm and combinations of these were also tried before selecting the sandpaper. The purpose of the roughness element is to produce a thick turbulent boundary layer at the end of the first 58.5 cm of the test section. The velocity profile at 45 cm away from the beginning of the test section and at the center of the test section was measured with a rectangular mouth boundary layer total head pitot tube (Fig. 3.1), and with each of the above mentioned roughness elements in position. The present sandpaper roughness element was selected on the basis of maximum momentum thickness Reynolds number and maximum strength of the wake component (Coles, 1962) obtained from the measurements at 45 cm away from the beginning of the test section. The reason for having a large momentum thickness Reynolds number is because of the fact that the present wall jet experiments were planned to be carried out with large momentum deficit upstream boundary layer meeting the wall jet. Three brass rods of 1.6 mm diameter and of proper length are glued to the side and top edges of the contraction outlet. These tripping devices fix the point of transition on the top and side-wall boundary layers.

2.1.5(a) Top Wall for the Zero Pressure Gradient Studies

The top wall used for zero pressure gradient studies is a 9.5 mm thick plexiglas sheet with access holes at several stations to insert the measuring probes and can be adjusted to various positions. The edges of the top wall are sealed against the glass side walls by squeezing foam weather stripping in between them. The nominal height of the test section between the contraction outlet and the wall jet is 9.6 cm. The height of the remaining part of the test section can be adjusted by moving the upper wall to create a zero pressure gradient flow. The end section of the tunnel was kept open for zero pressure gradient studies.

2.1.5(b) Top Wall for the Adverse Pressure Gradient Studies

A considerable amount of effort has been spent in selecting the proper method for producing an adverse pressure gradient without inducing strong three-dimensional flow effects. Two of the possible methods were:

1. A test section with a solid top wall and an increasing cross-sectional area with an increasing static pressure, and

2. A test section with a perforated top wall which allows bleeding off of a portion of the flow in the test section thereby increasing the static pressure downstream. The second method was selected in view of the limitations on the size of the test section and the severity of the required pressure gradient. The pressure distribution in this method can be varied by suitably covering some of the perforations uniformly across the tunnel. The static pressure difference between the inside of the test section and the ambient atmosphere necessary to bleed the flow was created by a perforated plate attached to the end section of the tunnel. By properly covering portions of the end plate, the level of static pressure inside the tunnel can be varied.

A number of commercially available perforated sheets of different materials were considered for the top wall of the present application. A 3.4 mm thick "masonite" perforated sheet with an open area ratio 0.33 was finally selected for the present application. Figure 2.2 shows the perforated sheet in position. Figure 2.3 shows one single cell of the perforated plate with a scale in the inset. The cells are square in shape and are 19 mm in size (center to center). The perforated plate was cut to size in such a way that the test section width is spanned by 12 cells. Two aluminum angles (25X13X3 mm), one on each side were attached by screws to two rectangular (13X3 mm) aluminum strips lying above the aluminum angles with the perforated top wall sandwiched in between them. The aluminum angle is placed inside the flow in such a way that its longer side is perpendicular to the tunnel floor and runs all the way from the beginning to the end of the tunnel. This aluminum angle serves two purposes:

1. It acts as a reinforcement for the structurally fragile "masonite" top wall, and

2. It assists in side wall boundary layer control by acting as a baffle between the main flow and the side wall boundary layer.

The first 4½ cells on each side of the center of the tunnel at any given streamwise section were open

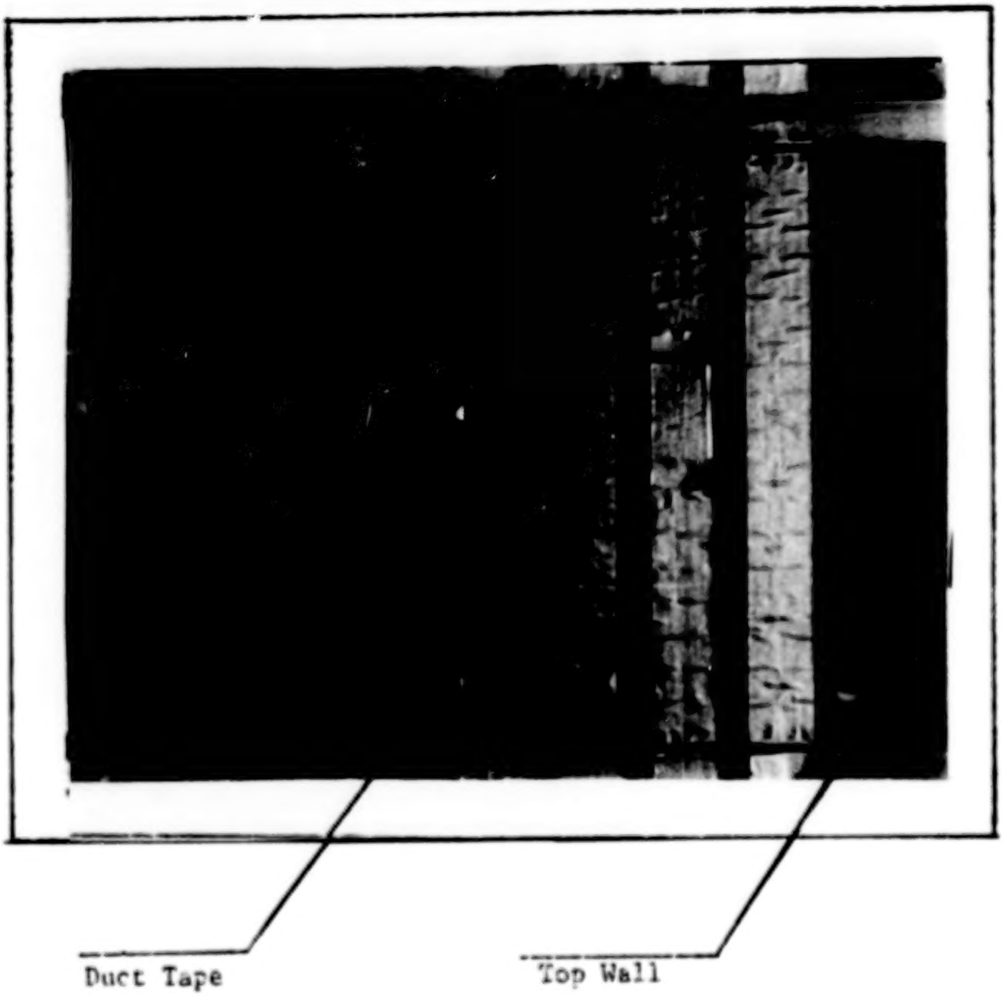
Duct Tape
Top Wall

Fig. 2.2 Perforated Top Wall in Position for the Adverse Pressure Gradient Flow

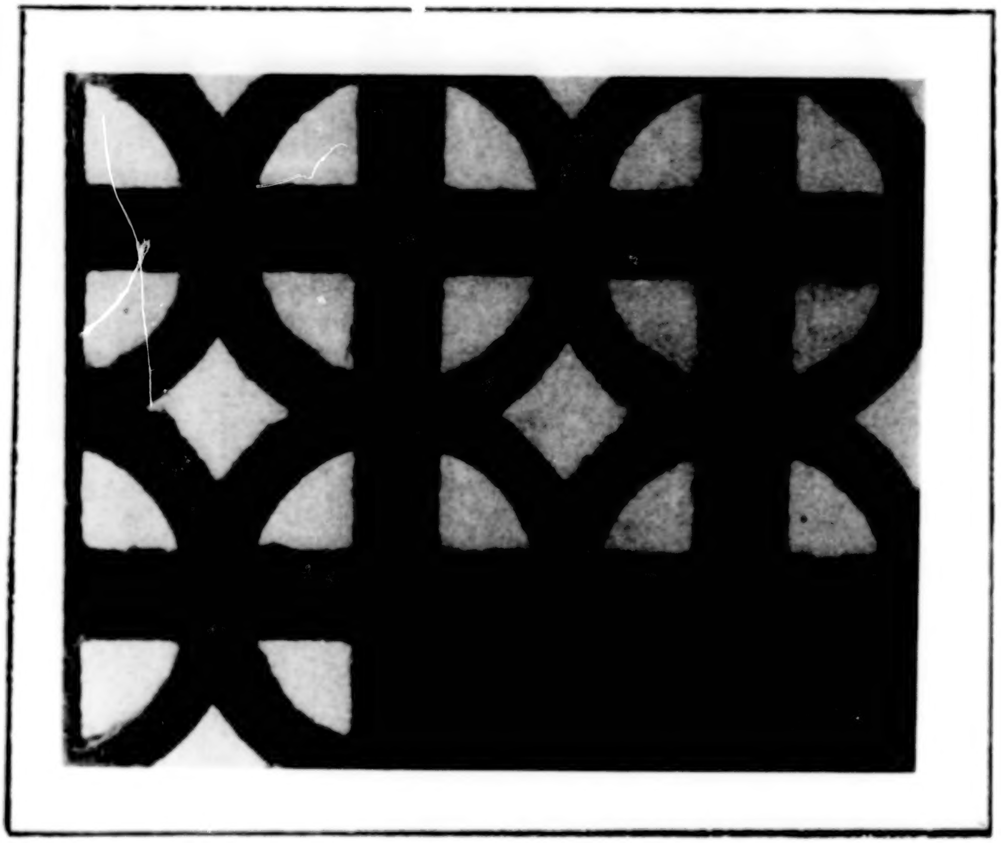

Fig. 2.3 A Single Cell of the Perforated Plate

for flow bleeding. The next half cell was covered with the aluminum angle. After the aluminum angle, one cell was available for sidewall boundary layer bleeding. Small plastic mouldings of a channel cross section with air tight rubber beading pressed into them were slipped on to the edges of the top wall. The top wall was then pushed into position with a slight pressure against the glass side walls to ensure proper sealing at the edges. The perforations in the top wall were also used to insert the various probes without further disturbing the flow.

The end plate of proper size to span the end section of the tunnel was cut from the same perforated sheet from which the top wall was made. The end plate contained six rows of cells. The static pressure level inside the tunnel was controlled by properly covering these cells with a commercially available duct tape. Fig. 2.4 shows the end plate.

2.2 Description and Performance of the Wall Jet Flow System

The wall jet flow system can be divided into two parts: the air supply system and the wall jet assembly, each of which is described below in detail followed by the details on the performance of the wall jet flow system.

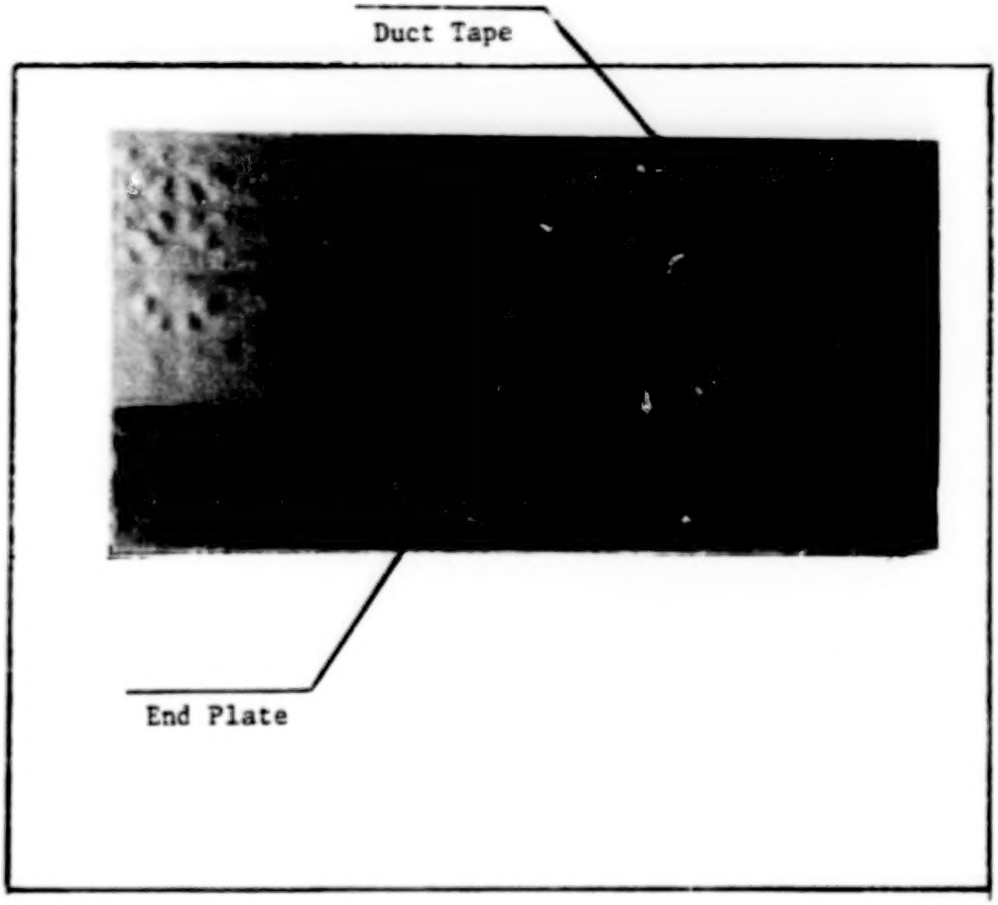
Duct Tape
End Plate

Fig. 2.4 Perforated End Plate to Span the End Section of the Tunnel

2.2.1 Air Supply System

The air supply to the wall jet is obtained from the compressed air supply available in the laboratory. The compressed air supply can provide filtered air at a maximum pressure of $2.76X10^6$ N/m^2 and at the flow rates suitable to the present requirements. This compressed air is fed to the wall jet through a 13 mm I.D. copper tube. A pressure regulator in the line regulates the input pressure to the wall jet so as to maintain a constant mass flow rate and it is located 178 cm upstream of the wall jet inlet along the copper tubing. The last 41 cm of the copper tubing has 25 mm I.D. to suit the inlet to the wall jet.

The temperature of the air entering the wall jet assembly was always found to be lower than the required level. Two electrical heating tapes were wrapped around the copper tubing between the pressure regulator and the wall jet inlet to heat the compressed air. These heating tapes, supplied by the Fischer Scientific Co., are 305X1.3 cm in size with a maximum attainable temperature of 249°C. The heating tapes operate on 115V supply and have a power output of 340 Watts. The electrical power input to the tapes is controlled by a 115V, 10A variable auto transformer. By properly adjusting the variable auto transformer, the temperature of the air coming out of the wall jet can be controlled to the required value within ± 0.3°C at 25°C. The temperature of the wall jet air was measured by a thermometer fitted into the copper tubing near to the wall jet assembly inlet with its bulb located in the flow. Because of the low residence time for the air, the heat losses between the point where the thermometer is located and the exit of the wall jet were found to be very small. This was indicated by the air temperature difference between the inlet and the exit of the wall jet assembly which was found to be of the order of 0.3°C. Because of the high mass flow rate of the mainstream as compared to the wall jet mass flow rate and both being at the same temperature (25°C), the above mentioned temperature difference should not cause any appreciable error in measurements.

2.2.2 Wall Jet Assembly

Fig. 2.5 shows the constructional details of the wall jet assembly. It is basically a 2-D nozzle intended to convert high pressure low velocity fluid to a low pressure high velocity fluid. The high velocity fluid is then injected into the main flow along the bottom wall of the tunnel.

A specially cut, varnished, poplar wood section forms one wall of the nozzle and a 12.7 mm thick aluminum divider plate forms the other wall. The flow passage between the aluminum divider plate and another poplar wood section similar in shape to the first one can be used as wall suction system to bleed the upstream boundary layer.

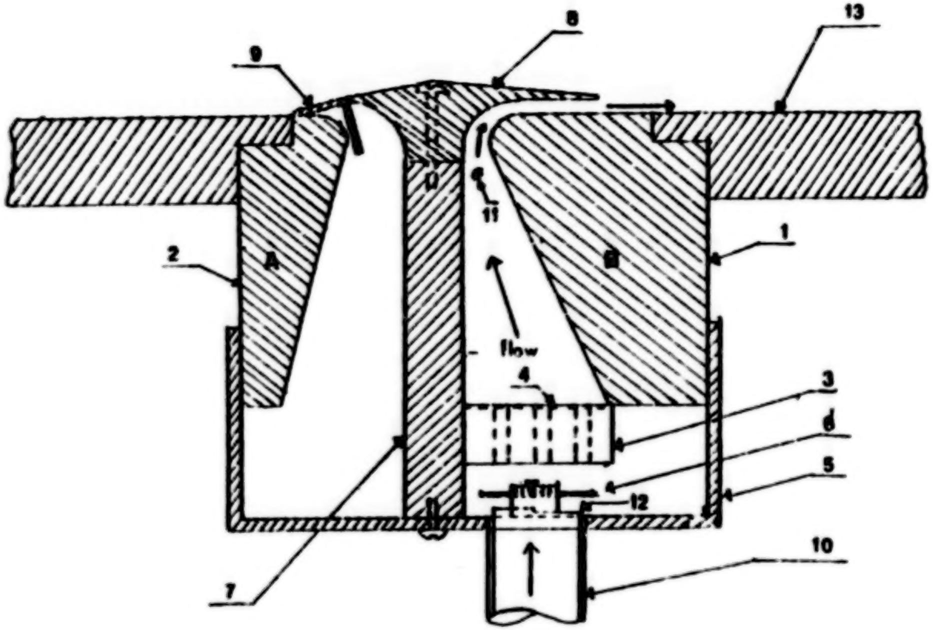

Fig. 2.5 Wall Jet Assembly

1. and 2. Poplar Wood Sections (B and A)
3. Honeycomb
4. Screen
5. Aluminum Box Sections
6. Baffle Plate
7. Aluminum Divider Plate
8. Extruded Aluminum End Piece
9. Aluminum Angle to Block the Flow
10. Feed Pipe
11. Static Pressure Tap (located 1.27 cm below the bottom surface of the tunnel)
12. Cylindrical Baffle made of steel sheet
13. Bottom surface of the tunnel

However, this flow passage has been blocked at its top by a 13X3X1.6 mm aluminum angle in place as shown in Fig. 2.5. The exact dimentions of the poplar wood sections are shown in Figs. 2.6 and 2.7. The poplar wood was chosen as it is less susceptible to moisture absorption and warpage.

A specially extruded aluminum end piece attached to the aluminum divider plate by screws from the top completes the nozzle shape. The dimensions of the extruded aluminum end piece are shown in Fig. 2.8. The primary purpose of this extruded piece is to turn the fluid leaving the bottom portion of the nozzle so that the fluid is injected into the main flow, parallel to the tunnel wall. This extrusion also serves as an extension of the nozzle as there is some reduction in the flow area when the flow passes underneath the extrusion. Shims are placed between the aluminum divider plate and the extruded end piece wherever necessary to insure a uniform opening at the wall jet exit along the length of the wall jet. Table 2.1 shows the jet exit gap or the "slot height" along the length of the wall jet which has a nominal value of 2.72 mm.

The wall jet assembly is held together by two 3 mm thick aluminum end plates on each side. The entire wall jet assembly is mounted inside a 2.6 mm thick aluminum box section with 114X45 mm outside dimensions and with the top face being removed. A threaded hole was

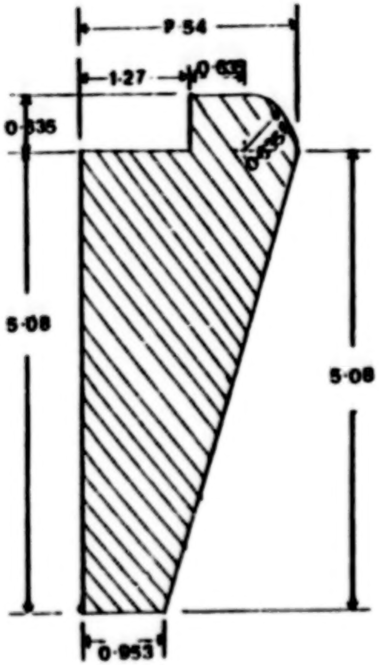
2·54
1·27
0·635
0·635
0·635R
5·08
5·08
0·953

Fig. 2.6 Poplar Wood Section "A" (Fig. 2.5)(All dimensions are in cm.)

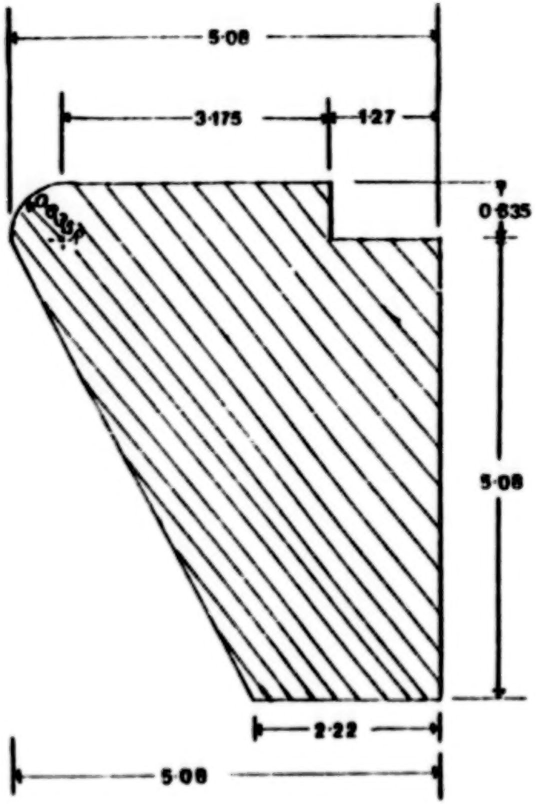
5·08
3·175
1·27
0·635R
0·635
5·08
2·22
5·08

Fig. 2.7 Poplar Wood Section "B" (Fig. 2.5)(All dimensions are in cm.)

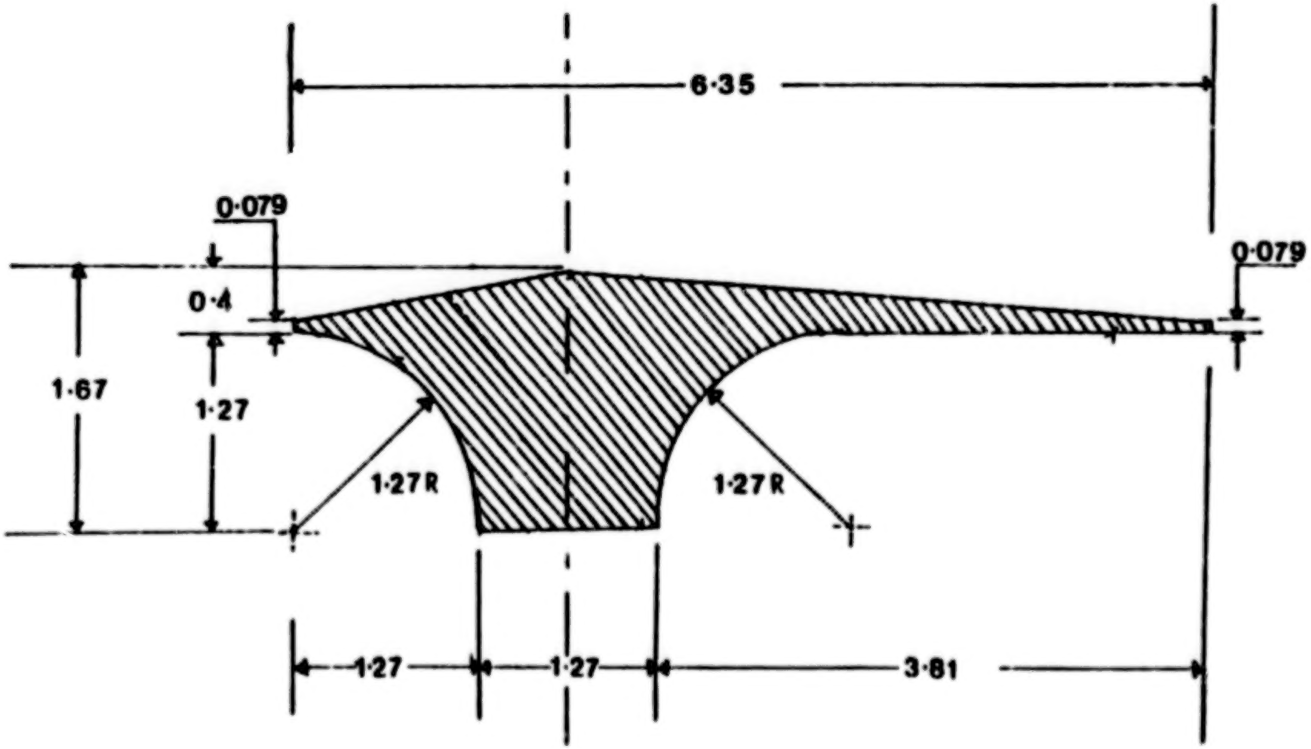
6·35
0·079
0·079
0·4
1·67
1·27
1·27R
1·27R
1·27
1·27
3·81

Fig. 2.8 Extruded Aluminum End Piece
(All dimensions are in cm.)

TABLE 2.1

VARIATION OF THE SLOT HEIGHT ALONG THE LENGTH OF THE WALL JET

Z (mm)	y_c (mm)
0.0	2.72
12.7	2.72
25.4	2.72
38.1	2.72
50.8	2.72
63.5	2.72
76.2	2.72
88.9	2.72
101.6	2.72
114.3	2.72
127.0	2.72
139.7	2.72
152.4	2.72
165.1	2.72
177.8	2.72
190.5	2.72
203.2	2.72
215.9	2.71
228.6	2.69
241.3	2.69

Z = Distance from the right end (looking downstream) of the wall jet

y_c = slot height

cut at the bottom of the aluminum box section on the wall jet nozzle side to receive the 25 mm I.D. copper tube supplying the air.

The air from the compressed air supply enters the wall jet assembly at its bottom. A baffle plate (Fig. 2.9) attached to the aluminum box section diverts the flow from the center to the ends, preventing the air from being blown directly into the nozzle. The air then passes through a 13 mm thick honeycomb with 3 mm cell size. After that, the air passes over a 30 square mesh steel screen with a wire diameter of 0.17 mm and an open area ratio 0.65. The honeycomb and screen act as resistance to the flow and help to distribute the flow uniformly over the entire cross-sectional area of the nozzle entrance.

2.2.3 Performance of the Wall Jet

The performance of the wall jet is described below from the view points of (a) the significant features of the present wall jet, and (b) the two-dimensional behavior of the flow coming out of the slot.

2.2.3(a) Significant Features of the Wall Jet

Fig. 2.10 shows the flow path inside the wall jet nozzle in the assembled position with a scale in the inset. The present wall jet design is unique in view of the few important considerations given below.

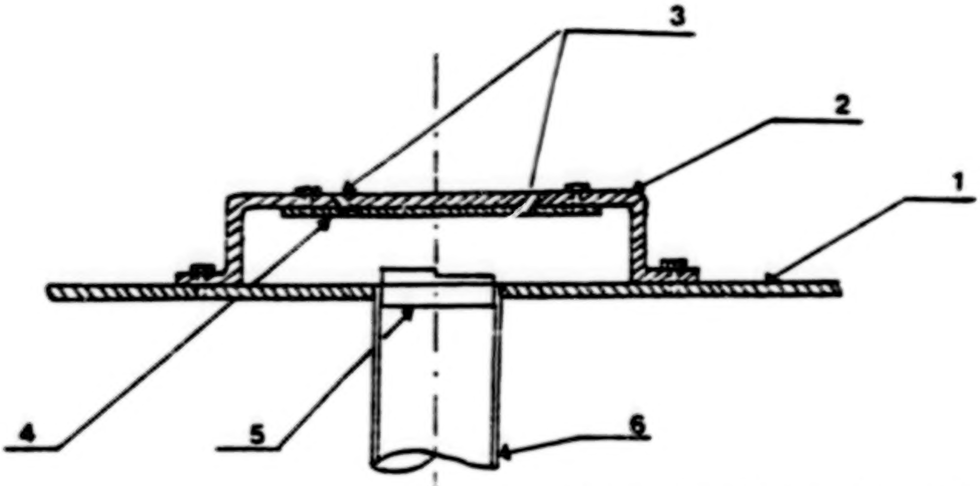

Front view facing the wall jet

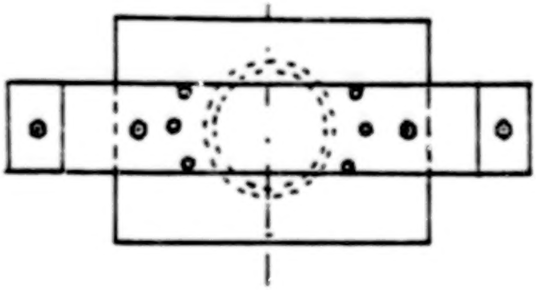

Top View

Fig. 2.9 Wall Jet Baffle Plate

1. Aluminum Box Section
2. Baffle Holding Piece
3. Inclined Holes
4. Baffle Plate
5. Cylindrical baffle made of steel sheet
6. Feed Tube

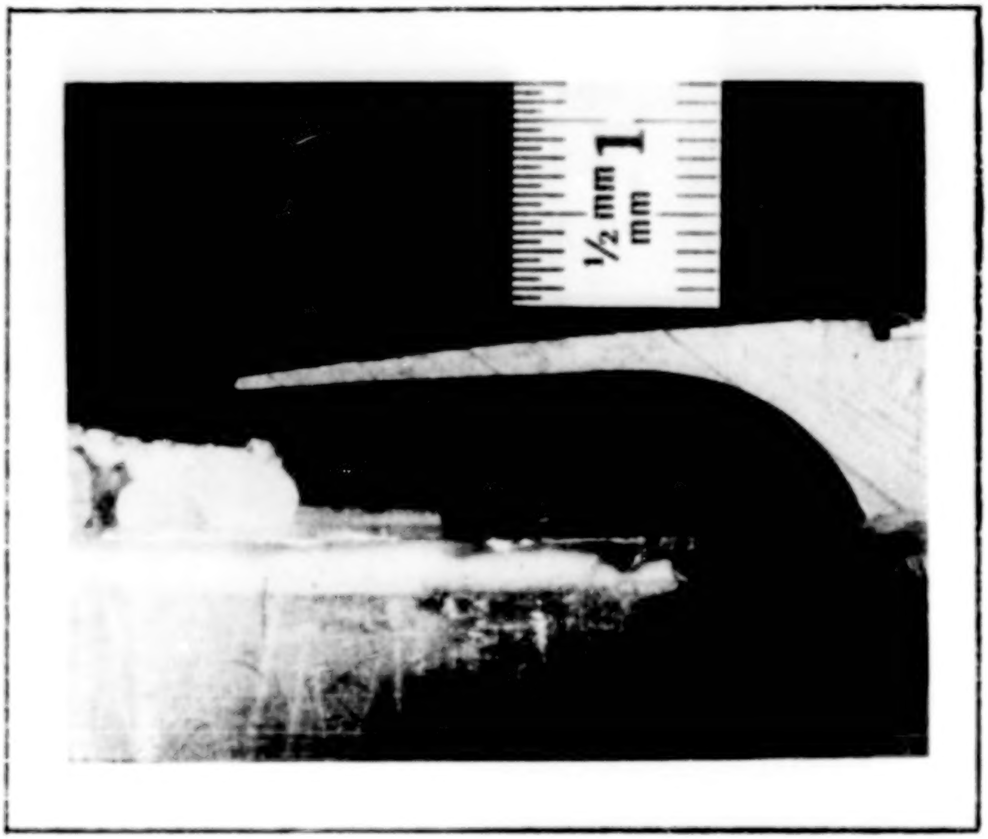

Fig. 2.10 Flow Path Inside the Wall Jet Nozzle Around the Corner

This wall jet design produces an asymmetric mean velocity profile at the exit of the nozzle with a relatively larger amount of momentum concentrated in the top portion of the slot than in the bottom portion. Fig. 2.11 shows the velocity and turbulence profiles measured with a hot wire at $x/y_c = 0.292$. It can be seen here that the u_t profile is typical of a two-dimensional turbulent channel flow. The advantages of having an asymmetric mean velocity profile at the nozzle exit are spelled out in several places in this work. It is one of the objectives of this work to investigate the effect of an asymmetric jet velocity profile on the downstream development of the wall jet flow.

The asymmetric mean velocity profile at the exit of the nozzle is produced in the following way. The flow takes a steep 90° turn as it passes from the vertical section of the nozzle to the horizontal section. In this process the flow experiences a strong pressure gradient normal to the streamlines as the streamlines are curved around the corner with the static pressure decreasing as one moves away from the bottom surface of the nozzle. The fluid near the bottom surface of the nozzle experiences more deceleration than the fluid near the top surface of the nozzle because the static pressure is greater near the bottom surface than at the top. Hence the bottom wall boundary layer is much thicker than the

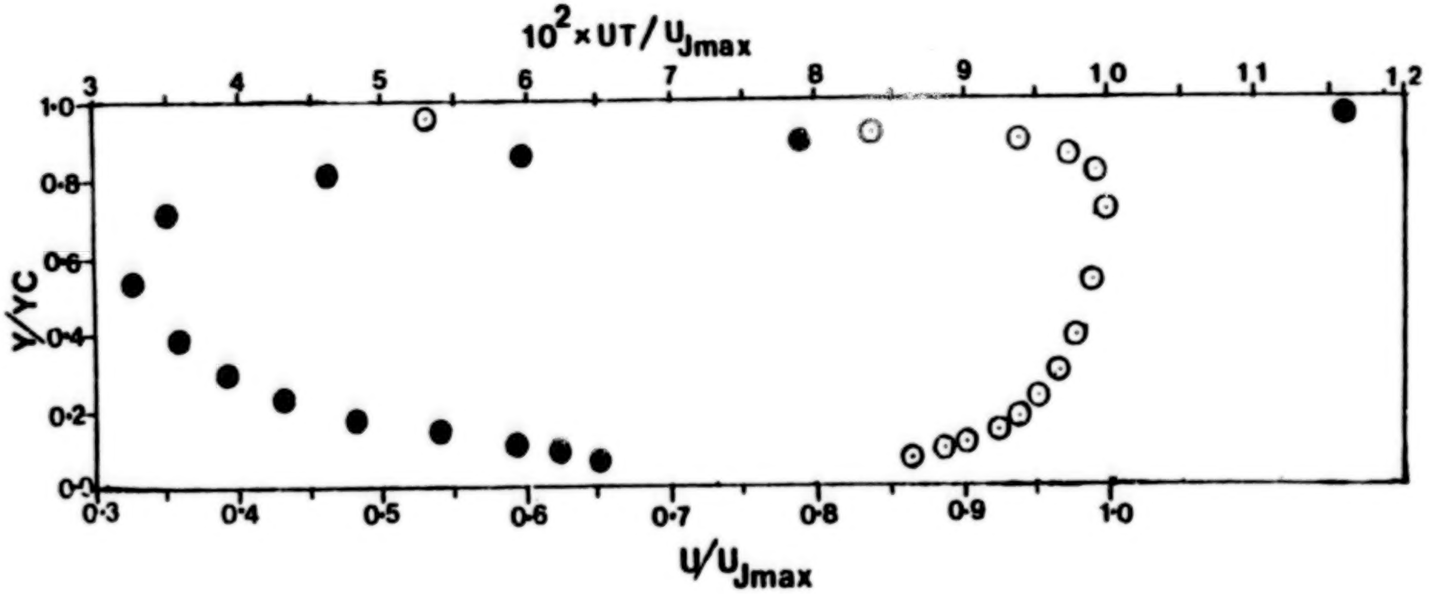

Fig. 2.11 Measured Velocity and Turbulence Profiles at the Slot ($x/y_c = 0.292$)

⊙ Velocity Profile (U/U_{Jmax})

● Turbulence Profile (u_t/U_{Jmax})

top wall boundary layer, thereby resulting in an asymmetric velocity profile at the exit.

Here there is a possibility that the flow might separate near the small radius round corner of the bottom wall because of the strong flow curvature. This was prevented by gradually decreasing the cross-sectional area of the nozzle around the corner by a ratio of approximately 2.5:1. The reduction in the flow area keeps the flow from separating. To support this fact, flow visualization studies have been made around the bottom round corner of the nozzle. The bottom wooden surface was first coated with a thin layer of wax. Water was sprayed in the form of a fine mist around the corner and along the length of the nozzle. The jet was turned on with operating velocities typical of our experiments. If separation occurs around the corner, water droplets should have remained there without being carried away by the flow. However, all the water droplets were carried away by the flow, indicating that the flow was not separating around the corner.

Here it should be mentioned that Bowles (1977) took measurements of the exit mean velocity and turbulence profiles on a wall jet of a similar design but with a larger slot exit gap. The asymmetric velocity profile typical of the present wall jet design was observed in his case also. However the flow cross-sectional area was kept constant around the corner in his wall jet, which increases the possiblity of separation near the corner with reattachment of the flow downstream. More evidence of this behavior is given by the shape of the turbulence profile since it has a maximum near the wall but well above the bottom wall sublayer, as for a reattaching turbulent boundary layer. The details of Bowles'work are included in the Appendix A.

The disadvantage of the present wall jet design is that the frictional losses should be higher as compared to those for the jet design with a uniform velocity profile at the exit because of the steep flow curvature necessary for producing the asymmetric velocity profile. An attempt has been made to estimate the amount of frictional losses in the present design. An energy balance was made on the control volume surrounding the corner of the nozzle, using the velocity profile measurements at the slot and the static pressure measurements inside the nozzle.

The estimated frictional losses came to approximately 15% of the total energy input. Thus, there is a trade off between the increased frictional losses in producing an asymmetric velocity profile and the advantages of having an asymmetric velocity profile. Some more practical details have to be worked out before exploring the present jet design commercially. Analytical details of the estimation of frictional losses are given in Appendix B.

The thickness of the extruded end piece shown in Fig. 2.8 at its downstream lip was kept to a minimum value of 0.8 mm within the limits of the commercially available manufacturing capabilities. This thin lip feature prevents a large region of separation and base flow downstream of the lip, which is typical of wall jet flows with a thick lip.

Another one of the useful features of the extruded end piece shown in Fig. 2.8 is that the downstream portion of the top surface of this extrusion is slanting downwards. This gives rise to an increasing flow cross-sectional area as the distance between the jet body and the top wall of the tunnel increases as one goes downstream. In effect, the flow on this slanting surface experiences deceleration, resulting in a larger velocity gradient between the jet and the upstream boundary layer flow at the lip, resulting in better mixing. There is a possibility of flow separation around the crest of the extruded end piece because of the sharp edge there. This was checked by making flow visualization studies around the crest. No observable separation of the flow was found there.

2.2.3 (b) Two-Dimensionality of the Wall Jet Flow

The uniformity of the dynamic pressure along the wall jet exit was used as a check of the two-dimensional behavior. The exit dynamic pressure was measured with a square brass tube, the dimensions of which are shown in Fig. 2.12. The brass tube was kept with its cross section perpendicular to the flow and flush with the bottom wall of the tunnel. It is connected by a flexible tubing to an inclined tube manometer. Thus the measured dynamic pressure is the average dynamic pressure over the opening of the square brass tube.

The top wall of the wind tunnel was removed during the wall jet flow measurements, thereby ensuring that the static pressure at the exit is atmospheric. The wall jet flow measurements were made with no external stream. The dynamic pressure at the exit of the wall jet was measured at 25 mm intervals along the length of the jet starting from the center. The average exit velocity as measured by the square brass tube was set approximately at 42.7 m/sec. A second set of measurements was also taken at 36.6 m/sec. To start with, there was a 5% variation in the average exit velocity at various stations along the length of the wall jet. Particularly, there was a deficiency of flow at about 38 mm on each side from the center line of the tunnel indicated by the low value of the average velocity. To correct this, three

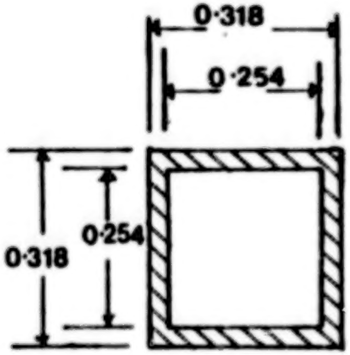
0·318
0·254
0·318
0·254

Fig. 2.12 Square Brass Tube for Measuring the Wall Jet Exit Dynamic Pressure
(All dimensions are in cm.)

holes (Fig. 2.9) of 4 mm diameter were drilled into the baffle plate at the entrance of the wall jet plenum. These holes allow more air to be supplied to the fluid deficient area, thus equalizing the average velocity at several locations. However, this step alone did not solve the problem completely. There was still a significant variation in the average dynamic head, although it was less than what it was without the above mentioned holes.

Another modification was made in the wall jet plenum to improve flow uniformity. A 0.1 mm thick steel sheet was rolled into a cylinder and inserted into the copper feed tube with a small portion of the steel sheet projecting out as shown in Fig. 2.9. The height of the projecting portion of the steel sheet was adjusted to produce the least variation in the average value of the dynamic head measured by the square brass tube. The steel sheet was then glued to the copper tube along its edges. The steel sheet acts as a baffle to divert the flow to the fluid deficient area. The projecting portion of the steel sheet on the left half (looking upstream) is approximately 1.6 mm and that on the right half (looking upstream) is approximately 0.8 mm.

With the above modifications, the wall jet maintained a uniform flow indicated by the average velocity. The average velocity as measured by the square brass tube varied within ±0.9% of its value at the center for the entire length of wall jet. There was a small region of high velocity at 89 mm from the center to the left (looking upstream) where the average velocity was higher than the central value by 1.45%.

2.2.3 (c) Calibration of the Wall Jet Flow

The static pressure inside the wall jet nozzle is related to the amount of the flow at the exit of the wall jet. Therefore the wall jet exit flow rate can be calibrated against the static pressure measurements inside the nozzle. A static pressure tap was made in the end plate on the left side (looking downstream) of the wall jet nozzle. The position of the static pressure tap is given in Fig. 2.5. The static pressure at this location was measured by an inclined tube manometer.

The wall jet was calibrated for different static pressure readings by measuring the velocity profile at the center of the wall jet. The velocity profile measurements were made with a rectangular mouth boundary layer total head probe shown in Fig. 3.1. The measurements were made after removing the top wall of the wind tunnel and without the external stream. The static pressure inside the wall jet was altered by adjusting the pressure regulator in the air input line. The nominal values of the maximum velocities in the velocity profile at the center of the jet were 30.5, 36.6, and 42.7 m/sec, corresponding to the three different static pressure settings for which the measurements were made. Thus for a given static pressure inside the wall jet, the flow rate can be calculated from the measured velocity profiles at the jet exit. By means of this method, the wall jet nozzle can also be used as a flow meter.

As a further check on the two-dimensional behavior of the wall jet, velocity profiles were also taken at 2.5 cm and 7.6 cm on each side of the center and for the above mentioned static pressure settings. The maximum variation in velocity at any given height from the floor of the tunnel and at any given static pressure setting was within 3%. In all the above mentioned velocity profile measurements the asymmetric nature of the jet exit velocity profile was observed.

CHAPTER III

INSTRUMENTATION

This chapter describes the different instruments that were used for measuring the mean and turbulent components of velocity, the Reynolds shear stress, and the skin friction. The instrumentation includes the pitot probes, Preston tubes, hot-wire probes, and the hot-wire signal processing equipment. A brief description of the calibrator is also included. The estimated uncertainties in the measurements using the above instrumentation are presented.

3.1 Pitot Probes and Preston Tubes

Pitot tube traverses were made only to check the two-dimensionality of the flow. The pitot tube used for this purpose is shown in Fig. 3.1. It is a total head rectangular-mouth boundary layer probe. The same pitot tube was also used

1. For measuring the jet exit velocity profile during the calibration of the wall jet, and

2. For the upstream boundary layer velocity profile measurements necessary for selection of the roughness element as described in Chapter 2.

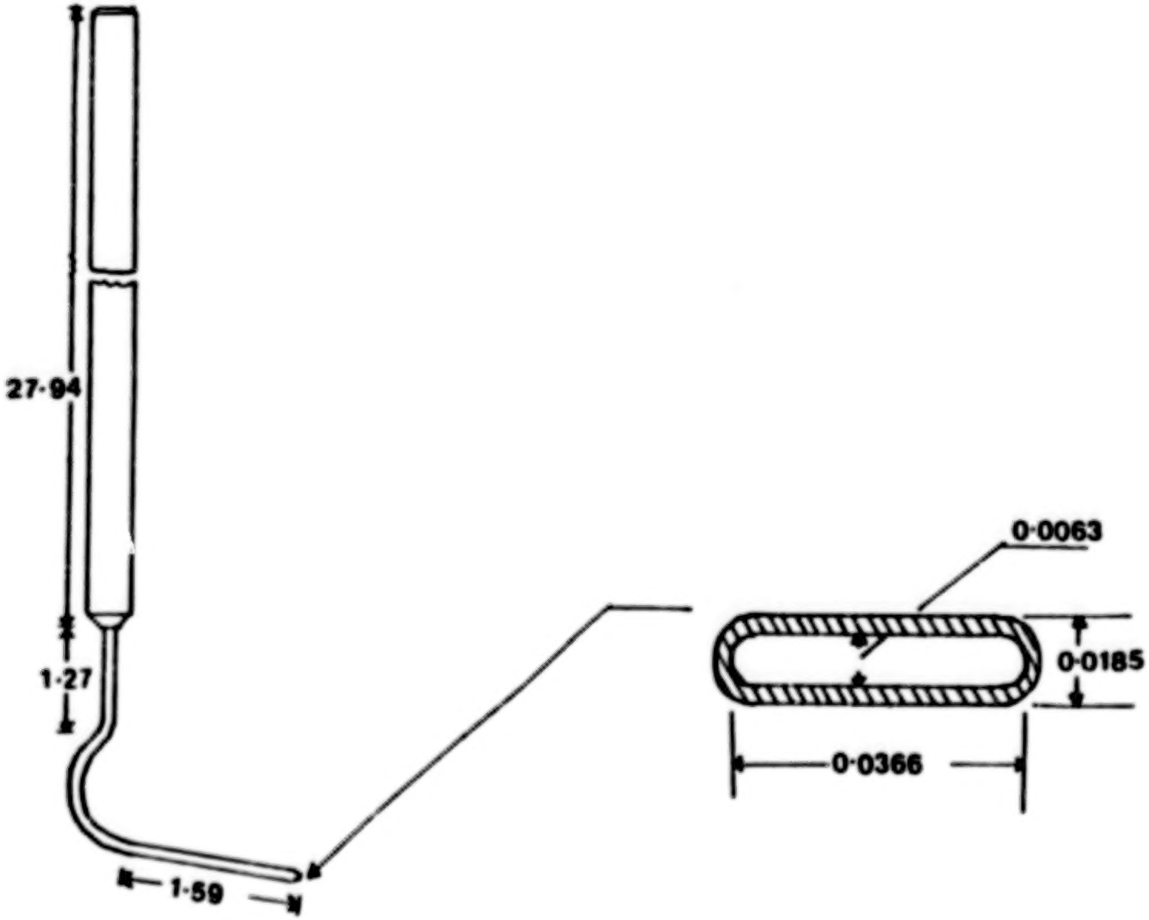
27·94
1·27
1·59
0·0063
0·0185
0·0366

Fig. 3.1 Rectangular Mouth Boundary Layer Pilot (total head) Tube
(All dimensions arc in cm.)

All other static and total pressure measurements were made with a United Sensor and Control Corporation model PAA-8-KL pitot tube. It had proper connections for measuring both the total head and the static head.

The skin friction was measured by means of a Preston tube using Patel's (1965) calibration curve. The Preston tube used in the zero pressure gradient studies has the mouth dimensions of 0.5 mm I.D. and 0.6 mm O.D. The Preston tube used in the adverse pressure gradient studies has the mouth dimensions of 0.78 mm I.D. and 0.88 mm O.D.

3.2 Hot-wire Probes

A TSI model 1274-10 normal hot-film probe was used to measure the mean velocity U and the turbulence intensity u_t/U_∞. A TSI model 1273-T 1.5 slant hot-wire was used to measure the Reynolds shear stress $-\overline{uv}$ and the turbulence intensities v_t/U_∞ and w_t/U_∞. The 45° slant wire probe is rotatable about its axis through a rotating mechanism described below. The shear stress and the normal stresses were deduced from the slant-wire measurements at seven angular positions about its axis. The choice of a single rotatable slant-wire over X wires was made for three reasons:

1. Any uncertainty about possible interaction between two wires and four prongs is eliminated.

2. The need for two anemometers and two linearizers together with a critical matching of the two hot-wire calibrations is avoided

3. w_t can also be measured with the rotatable single slant wire.

A TSI model 1210-20 rake hot wire probe was used to measure the velocity in the freestream at several locations which was required to adjust the pressure gradient in the case of zero pressure gradient flow.

3.2.1 Slant-wire Rotating Mechanism

Fig. 3.2 shows the slant-wire rotating mechanism with the probe mounted in it. The probe is free to rotate inside a cylindrical steel guide with its face turned smooth on a lathe to reduce the flow blockage. The steel guide is firmly attached to a rectangular rod which in turn is attached to another round rod in the traversing mechanism through a swivel joint. This swivel joint helps in rotating the slant wire probe about a horizontal axis through the joint. The probe can also be rotated about a vertical axis by turning the round rod in the traversing mechanism. These two movements are needed for the alignment of the probe with the free-streamlines. The probe stem itself passes through another slotted spindle with 12 slots cut on its rim at 30° intervals and can be attached to the probe stem by a set screw. The probe stem then passes through a rectangular steel block with

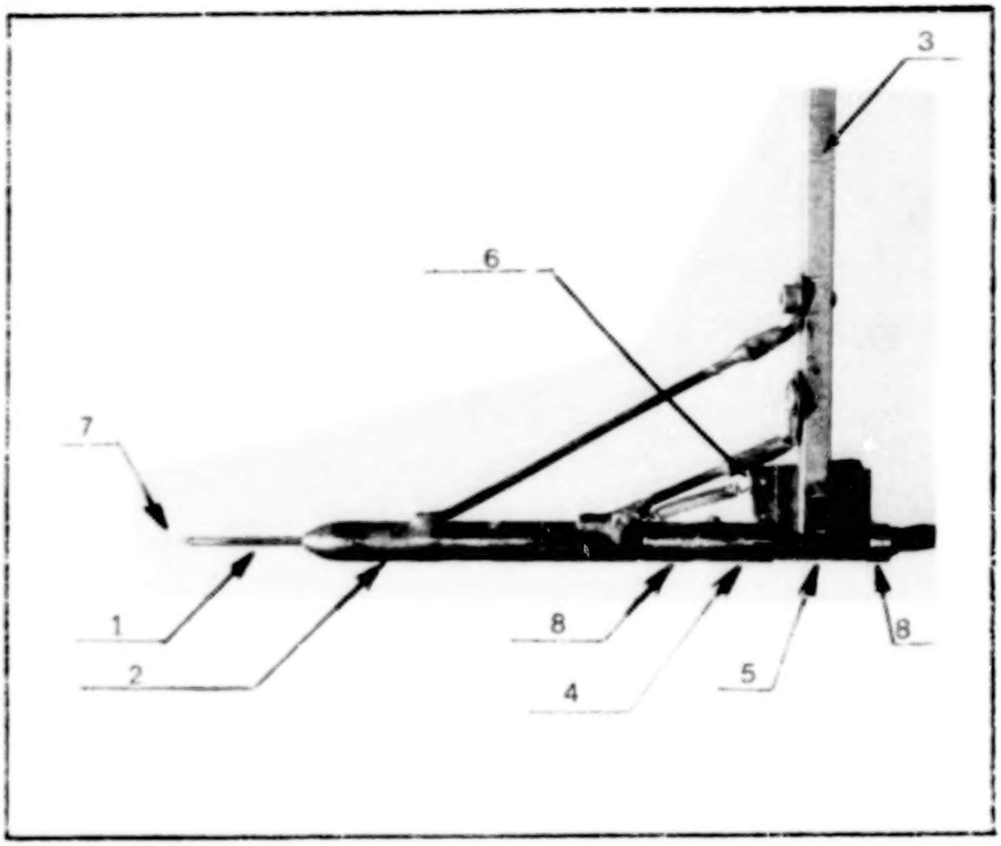

Fig. 3.2 Slant-Wire Rotating Mechanism with the Probe Mounted on It.

1. Probe Stem	5. Rectangular Steel Block
2. Cylindrical Steel Guide	6. Steel Strip
3. Rectangular Rod	7. Probe
4. Slotted Spindle	8. Steel Stops

a passage hole for the probe stem. This steel block is held in position by means of the rectangular rod mentioned above. A small steel strip that fits exactly into the slots of the slotted spindle is hinged to the steel block and can be raised or lowered into the slot by means of a fishing line attached to it and brought outside the tunnel through one of the probe holes. By raising the steel strip, the probe is free to rotate about its axis and by lowering the steel strip into a slot, the probe position can be locked at any one of the twelve orientations. Two small steel stops, one on each side of the steel block, prevent any horizontal movement of the probe. The first stop is attached to the rectangular rod by a spring and the second stop is attached to the probe stem by a set screw. The probe is rotated from the end of the tunnel by the cable carrying the hot-wire signal. With the above mechanism for rotating the slant wire, it was possible to rotate the probe with only an eccentricity of 0.25 mm between the probe stem axis and the axis of the mechanism.

3.2.2 Traversing Mechanism

The traversing mechanism used for the traversal of different probes consists of a brass screw having a movement of 0.635 mm per turn along with proper mountings. The probe can be set to an accuracy of .0254 mm by means of this traversing mechanism. The traversing mechanism is shown in Fig. 3.3.

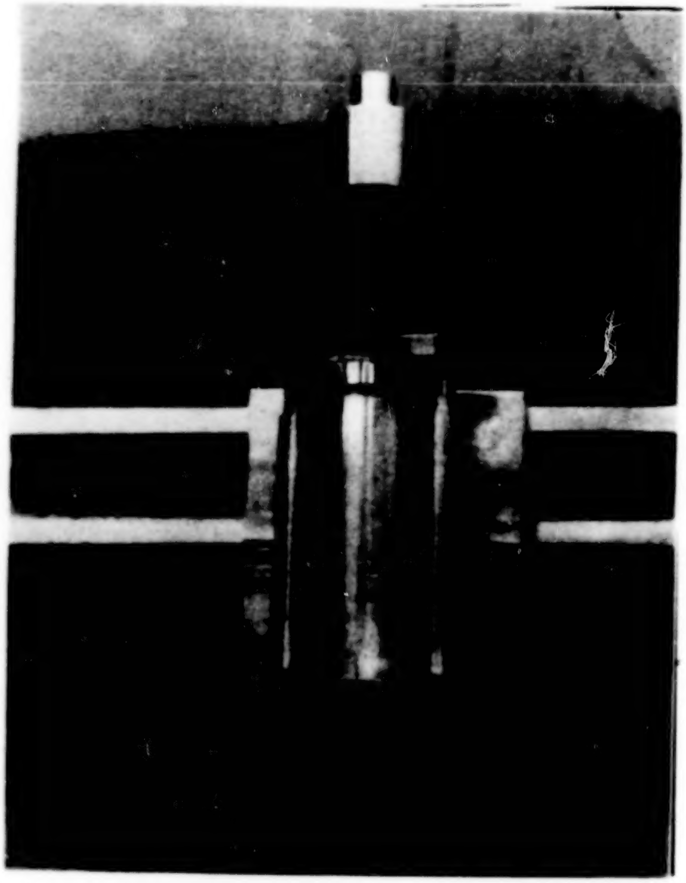

Fig. 3.3 Traversing Mechanism

3.3 Electronic Signal Processing

A TSI model constant temperature anemometer control unit and a TSI 1055 linearizer were used to produce the hot-wire signals. The root-mean-square voltages were measured using a HP model 400E voltmeter connected in series to a true integrating voltmeter, consisting of a Tektronix model DC503 counter. The signal was averaged over a 10 second interval. Two readings were taken for each data point and then an average was taken giving an effective averaging time interval of 20 seconds. The mean voltages were measured with a true integrating voltmeter, consisting of a Wavetek model 131 function generator with a voltage controlled frequency circuit, connected in series to an Anadex model CF600 counter. The mean voltages were also averaged over 10 second intervals. Two readings were taken for each data point and then an average was taken giving an effective averaging time interval of 20 seconds. The spectra were measured with a Princeton Applied Research Inc. model 4512 FFT real time spectrum analyzer. This spectrum analyzer was used over a frequency analysis range of 10Hz to 40KHz and a sensitivity range of 0.1 to 10 volts. The output of the spectrum analyzer was recorded on a Honeywell 320 XY recorder.

3.4 Calibrations

The calibration of different probes was done in a TSI model 1125 calibrator which can supply nearly turbulence free air at a given temperature. The calibrator is connected to a filtered compressed air supply available in the laboratory. The temperature of the air coming out of the calibrator can be electrically controlled by a heat exchanger in the flow path. The calibrator has different sets of nozzles that can be fitted in position for different velocity ranges and also it has two inner chambers for low velocity calibration of the probes.

The linearizer was adjusted to give a linear calibration within ±1% between the velocity and the output voltage of the linearizer. The linear calibration curve was obtained by a least square fit of the calibration points. During most of the experimental runs, the anemometer remained drift free. This was indicated by the calibrations done before and after each experimental run. The anemometer circuit had a flat frequency response in the range of frequencies (0 - 10 KHz) encountered in the present flows.

3.5 Uncertainties in the Measurements

The method of Kline and McClintock (1953) was used to estimate the uncertainties in the calculated data obtained from the primary measurements. The uncertainty of a particular variable R is denoted by ΔR. The uncertainty figures given in table 3.1 are the maximum possible values calculated for the cases of maximum possible error.

TABLE 3.1

UNCERTAINTIES IN THE DATA

Measurement	Uncertainty	Device Used
U	$\Delta U = \pm 0.4$ m/sec	Pitot tube
U	$\Delta U = \pm 0.15$m/sec	Normal hot-film and hot-wire
C_f	$\Delta C_f = \pm .00033$	Preston tube
$\overline{u^2}$	$\Delta(\overline{u^2})/\overline{u^2} = \pm 3\%$	Normal hot-film
$-\overline{uv}$	$\Delta(-\overline{uv})/-\overline{uv} = \pm 10\%$	Slant hot-wire
$\overline{v^2}$	$\Delta(\overline{v^2})/\overline{v^2} = \pm 12\%$	Slant hot-wire
$\overline{w^2}$	$\Delta(\overline{w^2})/\overline{w^2} = \pm 12\%$	Slant hot-wire

The uncertainties in the mean velocity measurements with pitot tube and the skin friction measurements with Preston tube are mainly due to the uncertainties in the pressure measurements. The uncertainty in the probe calibration is the main source of uncertainty in the measurements of U and $\overline{u^2}$ with the normal hot-film. The data of $-\overline{uv}$, $\overline{v^2}$, and $\overline{w^2}$ are mainly affected by the uncertainty in the probe calibration, uncertainty in the determination of the constant K_1 (Appendix C) and the uncertainty in the measurement of $\overline{u^2}$.

CHAPTER IV

EXPERIMENTAL RESULTS FOR THE ZERO PRESSURE GRADIENT FLOW

The experimental results for the zero pressure gradient flow are presented in this chapter. The objectives of the experiments are:

1. To obtain experimental data with thick upstream boundary layers and with low jet velocity ratios,
2. To obtain detailed turbulence data which would aid in the future developemnt of turbulence models and
3. To observe the effect of an asymmetric jet velocity profile on the flow development downstream of the slot.

The measured quantities presented here are the mean velocity, turbulence intensities, shear stress, skin friction and spectra. The derived quantities presented include the integral and profile parameters, eddy viscosity, mixing length, Prandtl-Kolmorgorov length scale, turbulent kinetic energy, correlation coefficients, production and dissipation rates of turbulent kinetic energy and bursting periods. A brief description of the flow conditions is given first followed by the presentation of the measured and derived experimental results.

4.1 Flow Conditions

The method of setting the zero pressure gradient flow, the two-dimensional nature of the flow and the qualities of the upstream boundary layer are described below in sequence.

The flow was set for a zero pressure gradient condition by measuring the free-stream velocity at several stations beginning from the slot by means of a rake hot-wire probe. The top wall of the tunnel was adjusted to give the same free-stream velocity at different stations along the tunnel. The initial adjustments of the pressure gradient were done by measuring the free-stream velocity with a pitot tube and the final setting was done with a rake hot-wire probe. The variation of the free-stream velocity measured with the hot-wire probe is shown in Table 4.1. The free-stream velocity was constant from the slot to the exit of the tunnel with an average variation of ±1%. The measured free-stream turbulence intensity u_t/U_∞ was found to be about 0.2%. The height of the top wall above the bottom wall at different locations is shown in Fig. 4.1. The wall jet was adjusted to have a maximum velocity in the slot velocity profile approximately equal to 37.8 m/sec for the measurements under zero pressure gradient. The flow rate through the jet slot was kept constant during the measurements by maintaining a constant static pressure difference between the inside of the jet nozzle and the free-stream above the jet exit.

TABLE 4.1

VARIATION OF THE FREE STREAM VELOCITY MEASURED WITH THE RAKE HOT-WIRE PROBE

x/y_c	$U_\infty/(U_\infty)_{16.5}$
16.51	1.000
35.05	1.001
53.74	0.998
74.48	0.997
92.29	0.996
108.36	0.996
146.18	1.001
182.83	1.000
220.65	1.000
260.80	0.998
289.72	0.993
337.33	0.984
360.40	0.985
399.54	0.982
440.42	0.992

$(U_\infty)_{16.5} = 25.97$ m/sec

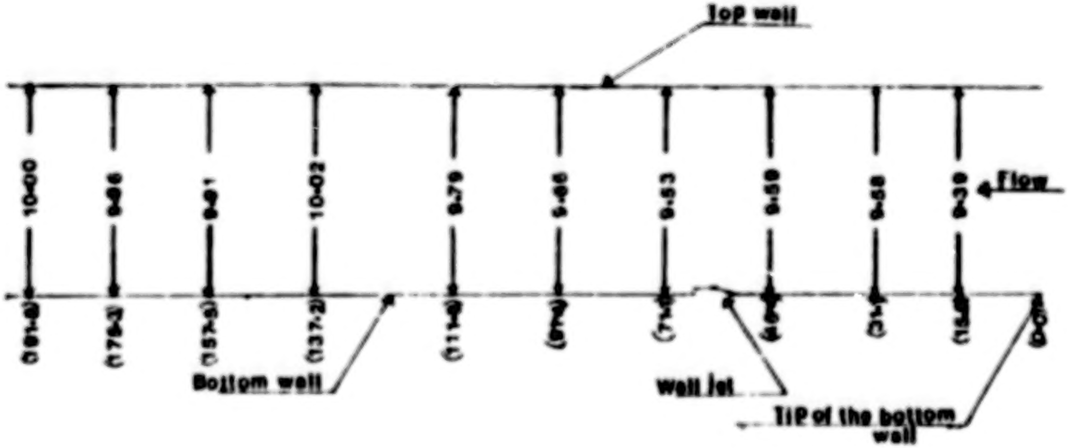

Top wall
10.00
9.86
9.81
10.02
9.79
9.66
9.53
9.59
9.58
9.39
Flow
(191.8)
(179.3)
(157.5)
(137.2)
(0.0)
Bottom wall
Wall jet
Tip of the bottom wall

Fig. 4.1 Position of the Top Wall for the Zero Pressure Gradient Flow

(All dimensions are in cm. The numbers in the brackets are the distances measured from the tip of the bottom wall near the end of the contraction.)

The important consideration which affects the quality of the flow in the present situation is the two-dimensional nature of the mean flow. The two-dimensional behavior of the flow was checked at several points:

1. Upstream of the slot at approximately 45 cm from the contraction exit

2. Downstream of the slot at approximately 5 cm from the slot exit, and

3. Downstream of the slot at approximately 61 cm from the slot exit.

These checks were made with the pitot tube traversals after setting the pressure gradient and the wall jet velocity to proper values. The velocity profiles were measured at the center of the tunnel and at 7.6 cm from the center on each side at each of the locations mentioned above. The velocity at any given y location on either side of the center was found to be within a maximum of ±4% and within an average of ±1.5% of the velocity at the center of the tunnel. A further check on the two-dimensional nature of the flow was made in section (4.2.3) by examining the two-dimensional integral momentum equation with the present measurements.

One of the objectives of the present measurements is to obtain data with a large upstream boundary layer at the slot. Therefore, the nature of the upstream boundary layer was studied by making velocity profile measurements with a normal hot-film at 21 cm upstream of the slot. Fig. 4.2 shows the velocity profile at 21 cm upstream of the

TABLE OF CONTENTS

LIST OF FIGURES . . . . vii 1/A12

LIST OF TABLES . . . . xiv 1/B5

NOMENCLATURE . . . . xv 1/B6

Chapter

I. INTRODUCTION 1 1/B12

- 1.1 Previous Work 2 1/B13
- 1.2 Asymmetric Jet Velocity Profile 9 1/C7
- 1.3 Objectives of the Thesis 11 1/C10
- 1.4 Outline of Thesis 12 1/C11

II. EXPERIMENTAL APPARATUS 15 1/C14

- 2.1 Description of the Wind Tunnel Components 15 1/C14
  - Heat exchanger
  - Blower system
  - Plenum chamber
  - Transition section
  - Test section
- 2.2 Description and Performance of the Wall Jet Flow System 27 1/D13
  - Air supply system
  - Wall jet assembly
  - Performance of the wall jet

III. INSTRUMENTATION 49 1/F12

- 3.1 Pitot Probes and Preston Tubes 49 1/F12
- 3.2 Hot-wire probes 51 1/G1
  - Slant-wire rotating mechanism
  - Traversing mechanism

3.3 Electronic Signal Processing 56 1/G6

3.4 Calibrations 56 1/G6

3.5 Uncertainties in the Measurements . . . 57 1/G7

IV. EXPERIMENTAL RESULTS FOR THE ZERO PRESSURE GRADIENT FLOW 59 1/G9

4.1 Flow Conditions 60 1/G10

4.2 Mean Flow Data 64 2/A5
- Skin friction C_f
- Mean velocity U
- Integral parameters
- Effect of the asymmetric jet velocity profile on the mean flow
- Profile parameters

4.3 Turbulence Data 89 2/C5
- Turbulence intensity u_t/U_∞
- Turbulence intensities v_t/U_∞, w_t/U_∞ and shear stress $-\overline{uv}$
- Effect of the asymmetric jet velocity profile on the turbulent quantities
- Turbulent kinetic energy k
- Correlation functions R_{uv} and a_1
- Eddy viscosity ν_{eff}
- Length scales L_{mix} and L_k
- Production of turbulent kinetic energy
- Spectra and dissipation measurements

V. EXPERIMENTAL RESULTS FOR THE ADVERSE PRESSURE GRADIENT FLOW 140 3/A8

5.1 Flow Conditions 141 3/A9

5.2 Mean Flow Data 147 3/B2
- Skin friction C_f
- Mean Velocity U
- Integral parameters
- Effect of the asymmetric jet velocity profile on the mean flow
- Profile parameters

- 5.3 Turbulence Data 167 3/C12
  - Turbulence intensity u_t/U_∞
  - Turbulence intensities v_t/U_∞, w_t/U_∞ and the shear stress $-\overline{uv}$
  - Turbulent kinetic energy k
  - Correlation functions R_{uv} and a_1
  - Eddy viscosity
  - Mixing length L_{mix} and Prandtl-Kolmogorov length scale L_k
  - Production of turbulent kinetic energy

VI. PREDICTION METHOD 192 3/F1

- 6.1 Selection of the Prediction Method 192 3/F1
- 6.2 Description of the Theoretical Method 194 3/F3
  - Turbulence model
  - Computational procedure
  - Starting procedure

VII. COMPUTED RESULTS 205 3/F14

- 7.1 Prediction of the Zero Pressure Gradient Flow 206 3/G1
  - Computations using the experimental initial velocity and turbulence profiles
  - Computations using the automatic starting procedure
- 7.2 Predictions of the Adverse Pressure Gradient Flow 216 3/G11
  - Computations using experimental initial profiles of velocity and turbulence
  - Computations using the automatic starting procedure
- 7.3 Comparison of the Performance of Linear and Uniform Jet Velocity Profiles 232 4/B3
  - Selection of the parameter a
  - Starting turbulence profiles
  - Prediction results

VIII. CONCLUSIONS 249 4/C8

APPENDIX A. MEASUREMENTS ON A WALL JET BY BOWLES (1977) 252 4/C11

APPENDIX B. ESTIMATION OF THE FRICTIONAL LOSSES IN THE WALL JET NOZZLE 255 4/C14

APPENDIX C. MEASUREMENT OF THE TURBULENCE INTENSITIES AND THE REYNOLDS SHEAR STRESS 259 4/D4

APPENDIX D. NORMAL HOT-FILM DATA FOR THE ZERO PRESSURE GRADIENT FLOW 272 4/E4

APPENDIX E. SLANT-WIRE DATA FOR ZERO PRESSURE GRADIENT FLOW 279 4/E14

APPENDIX F. NORMAL HOT-FILM DATA FOR ADVERSE PRESSURE GRADIENT FLOW 286 4/F13

APPENDIX G. SLANT-WIRE DATA FOR ADVERSE PRESSURE GRADIENT FLOW 291 4/G9

LIST OF REFERENCES 294 4/G14

slot plotted on the conventional semilogarithmic coordinates. The skin friction was determined from the Preston tube measurements. The velocity profile measurements are compared with the logarithmic law of the wall represented by the solid line in Fig. 4.2. The constants recommended by Patel (1965) were used in the logarithmic law of the wall given below:

$$\frac{U}{U_\tau} = 5.5 \ \mathrm{Log}_{10} \frac{U_\tau y}{\nu} + 5.45 \qquad (4.1)$$

The velocity profile data agree well with the logarithmic law of the wall at the upstream station mentioned above. The momentum thickness Reynolds number is equal to 3142 at this station. The strength of the wake component $\Delta(U/U_\tau)$ (Coles, 1962) is equal to 2.2. This value of $\Delta(U/U_\tau)$ agrees within 10% of its value given by Coles, for the same momentum thickness Reynolds number and for a "normal" turbulent boundary layer under a zero pressure gradient. Therefore, the boundary layer upstream of the slot is a developed turbulent boundary layer.

4.2 Mean Flow Data

The mean flow data presented here include the skin friction, the mean velocity profiles and the integral and profile parameters.

4.2.1 Skin Friction C_f

The variation of skin friction coefficient C_f obtained from the Preston tube measurements is shown in Fig. 4.3 (a). Fig. 4.3 (b) shows the variation of C_f with x/y_c on a logarithmic scale. It can be seen that

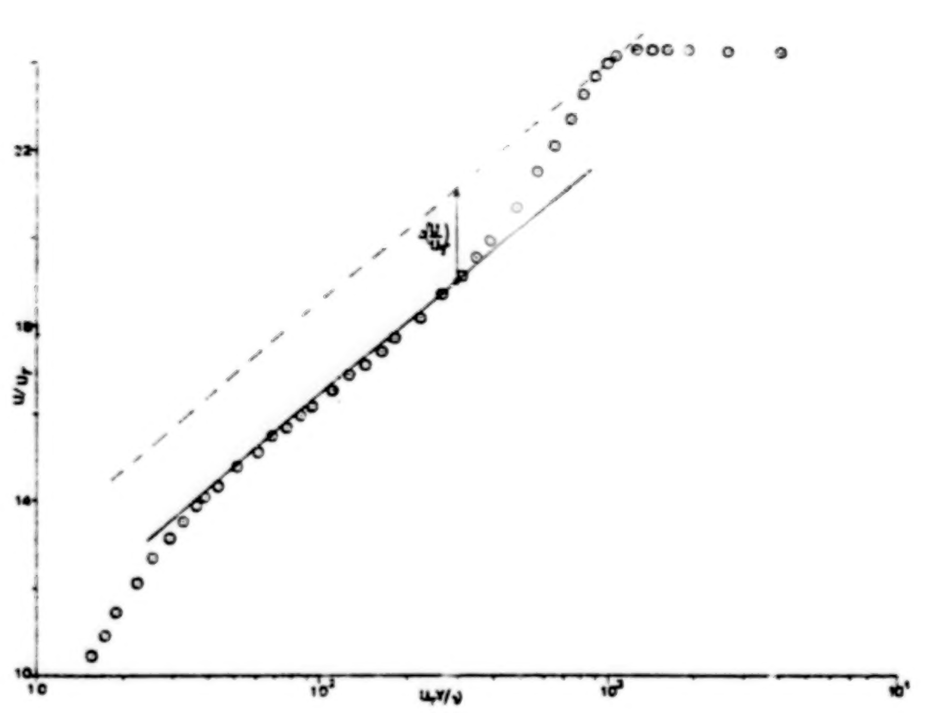

Fig. 4.2 Mean Velocity Profile in the Wall Coordinates at 21 cm Upstream of the Slot

—— Logarithmic law of the wall (Equation 4.1)

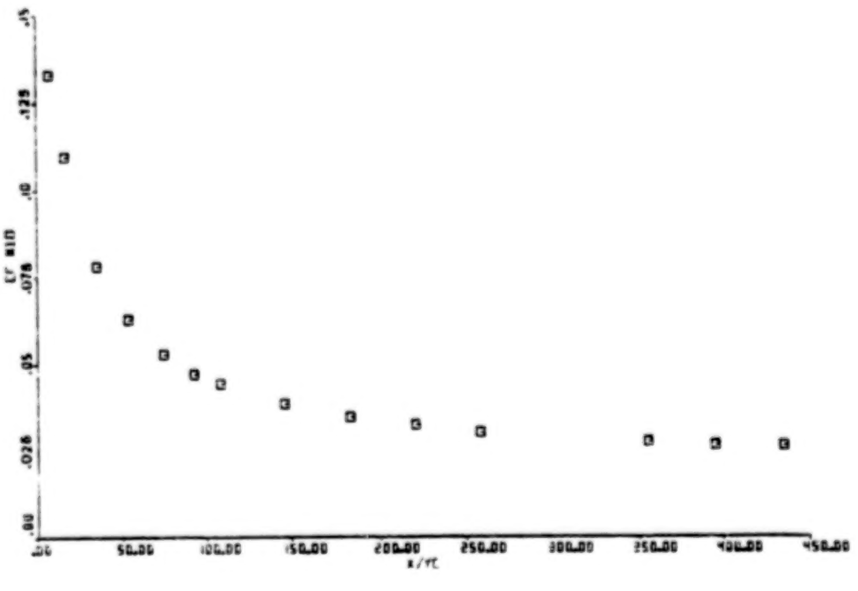

Fig. 4.3(a) Variation of Skin Friction

there is a power law variation between skin friction coefficient C_f and x/y_c.

It has been found in the literature that for self-preserving wall jet flows with and without pressure gradients, the skin friction varies according to the following relation:

$$\frac{\tau_w}{\frac{1}{2}\rho U_{max}^2} = A\left(\frac{U_{max}Y_{max}}{\nu}\right)^B \qquad (4.2)$$

where A and B are constants.

This relation holds only for self-preserving wall jet flows with only a velocity maximum and with a negligible upstream boundary layer. Irwin (1974) suggested on the basis of the recommendations made by Guitton (1970), Patel (1962), Bradshaw and Gee (1962), Kruka and Eskinazi (1964), and McGahan (1965) that $A = 0.026$ and $B = -0.18$ in the equation (4.2). Fig. 4.3 (c) shows the variation of $C_{fm} = \tau_w/(\frac{1}{2}\rho U_{max}^2)$ in the present case in comparison with the above equation for C_{fm}. The present data also show a power law variation of C_{fm}. However, the constants A and B are different than those suggested by Irwin. For the present data, $A = 0.102$ and $B = -0.33$. The difference in the constants A and B may be due to the non-self-preserving nature of the present flow.

4.2.2 Mean Velocity U

Figs. 4.4 (a-e) show the normal hot-film measurements of mean velocity profiles in the U/U_∞ vs y/δ coordinates. The negative sign on the x/y_c values in Fig. 4.4 (a)

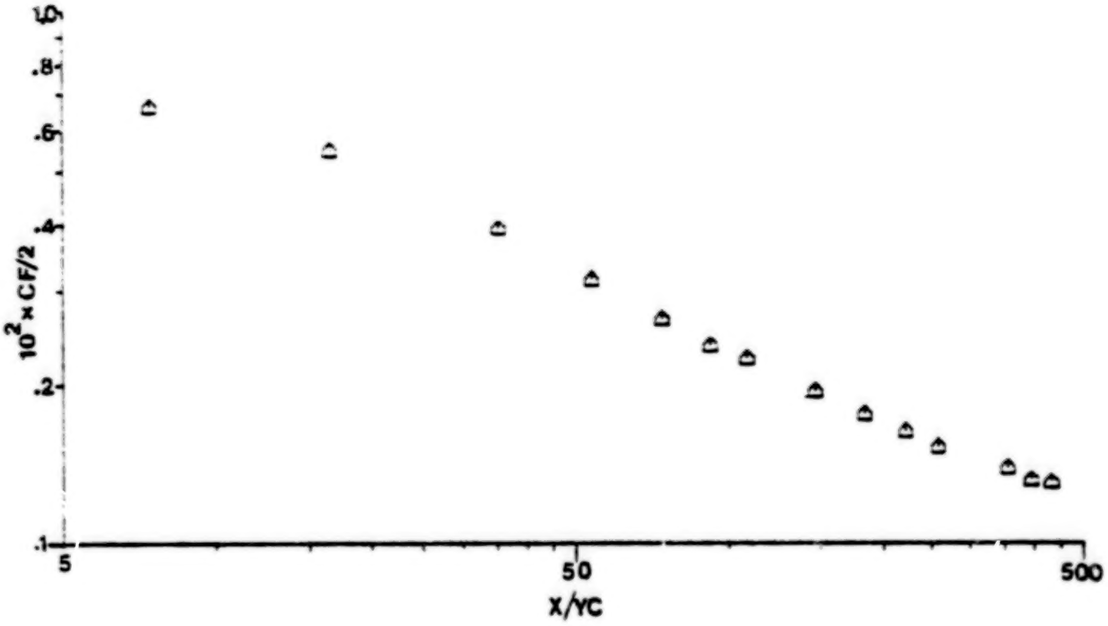

Fig. 4.3(b) Variation of Skin Friction in Logarithmic Coordinates

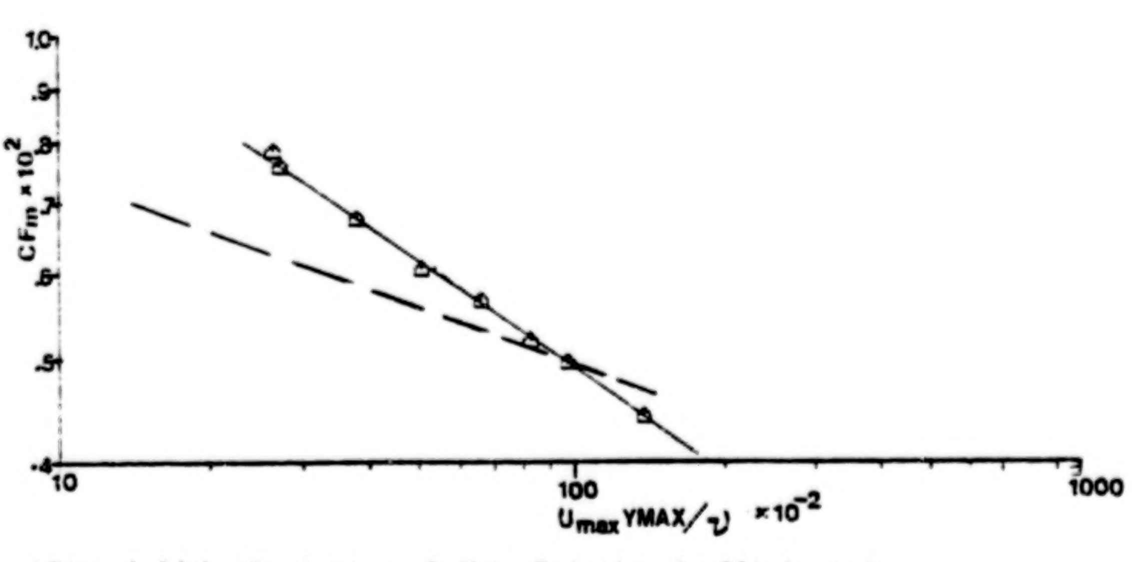

Fig. 4.3(c) Variation of Skin Friction Coefficient C_{fm}

---- Equation 4.2 with a = 0.026 and b = -0.18

—— Line fitting the experimental data

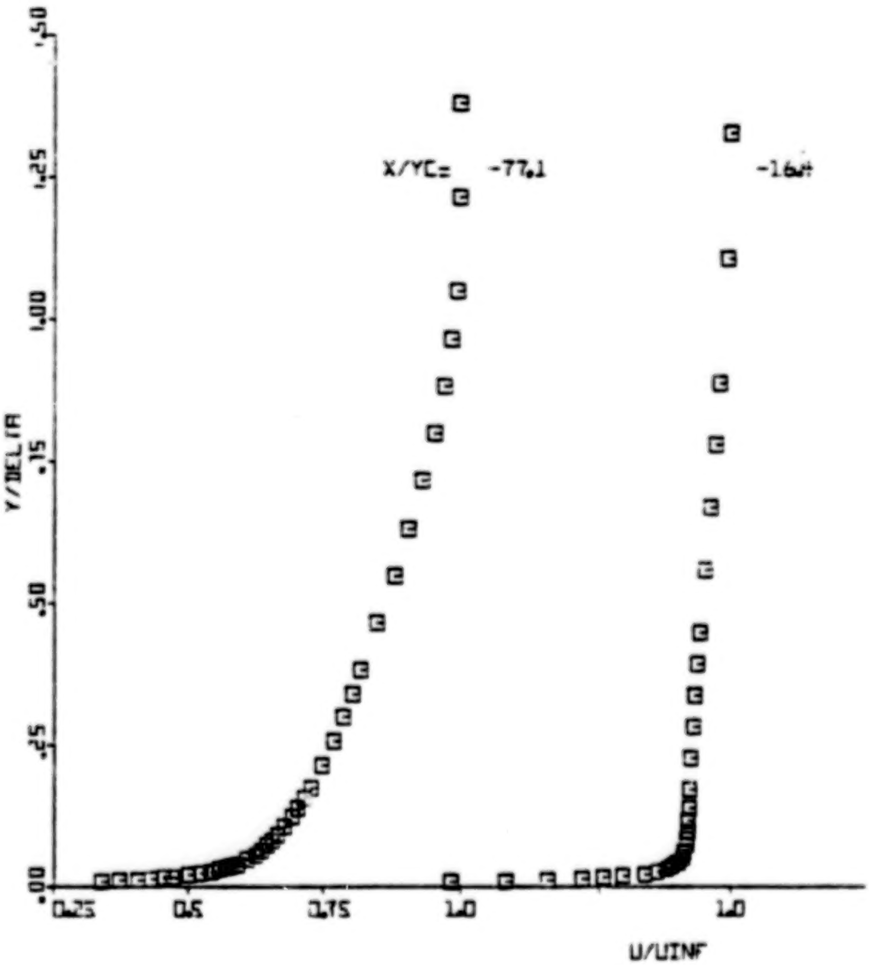

Fig. 4.4(a) Mean Velocity Profiles Upstream of the Slot (x/y_c = -77.1 and -16.4)

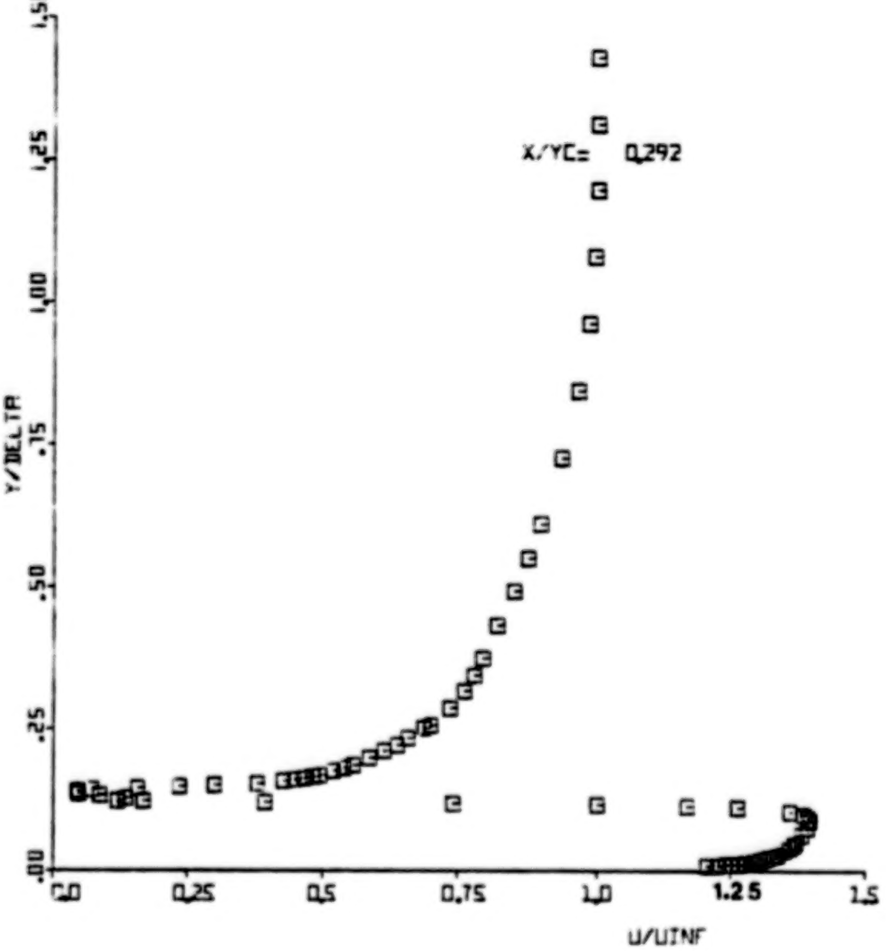

Fig. 4.4(b) Mean Velocity Profile at the Slot ($x/y_c = 0.292$)

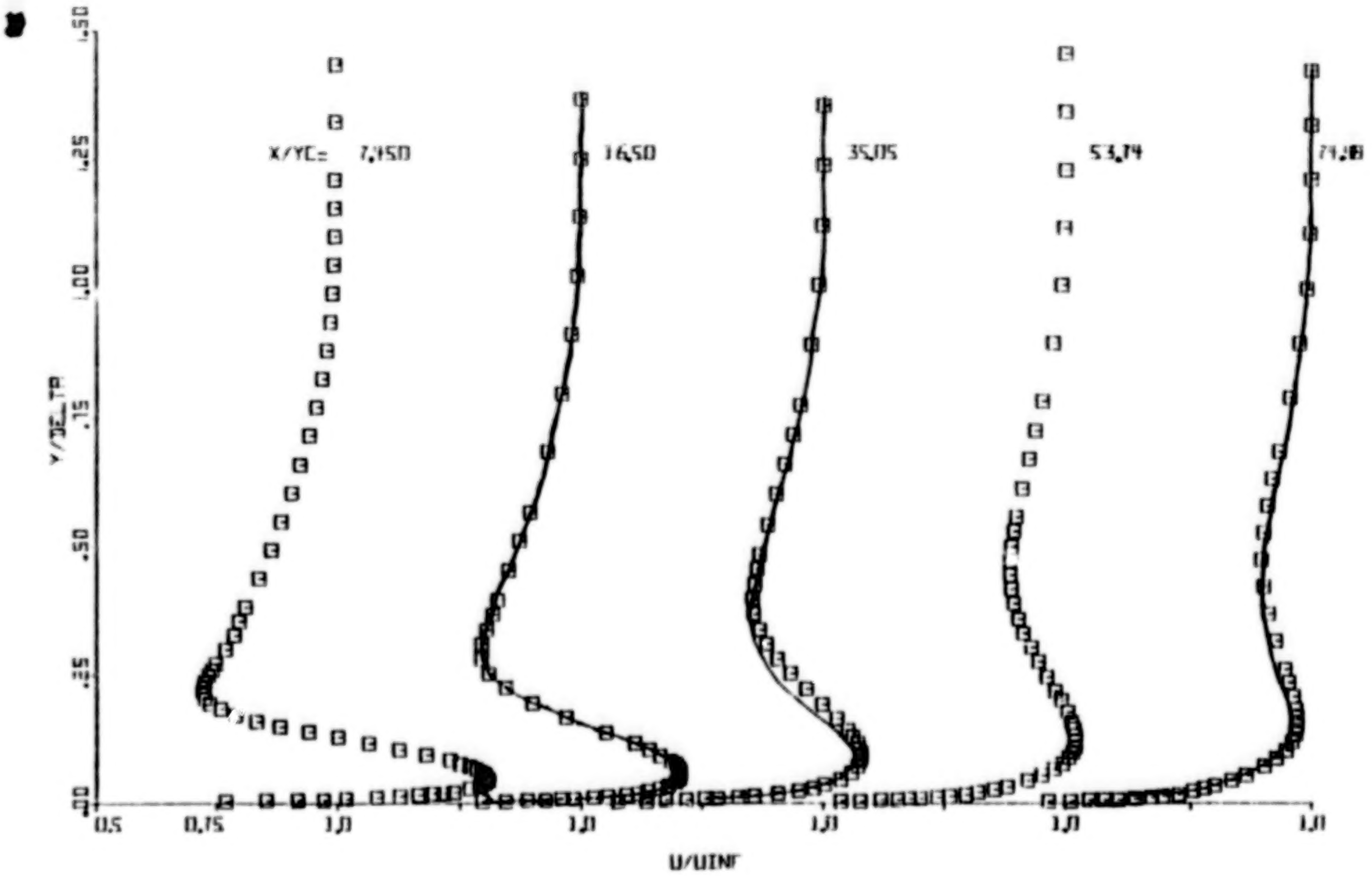

Fig. 4.4(c) Mean Velocity Profiles at x/y_c = 7.45 to 74.48

—— Predictions using experimental initial profiles

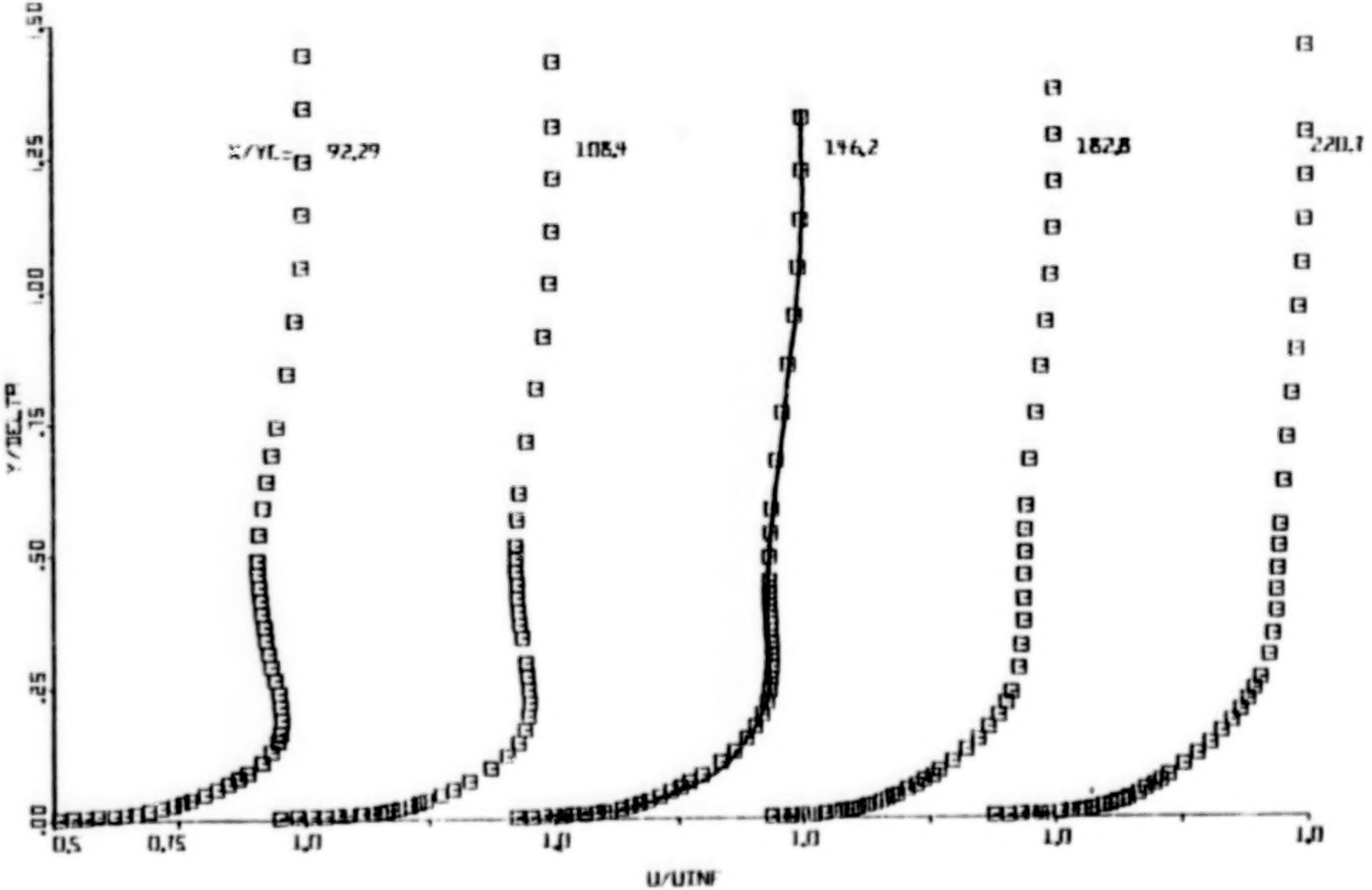

Fig. 4.4(d) Mean Velocity Profiles at x/y_c = 92.29 to 220.7

—— Predictions using experimental initial profiles

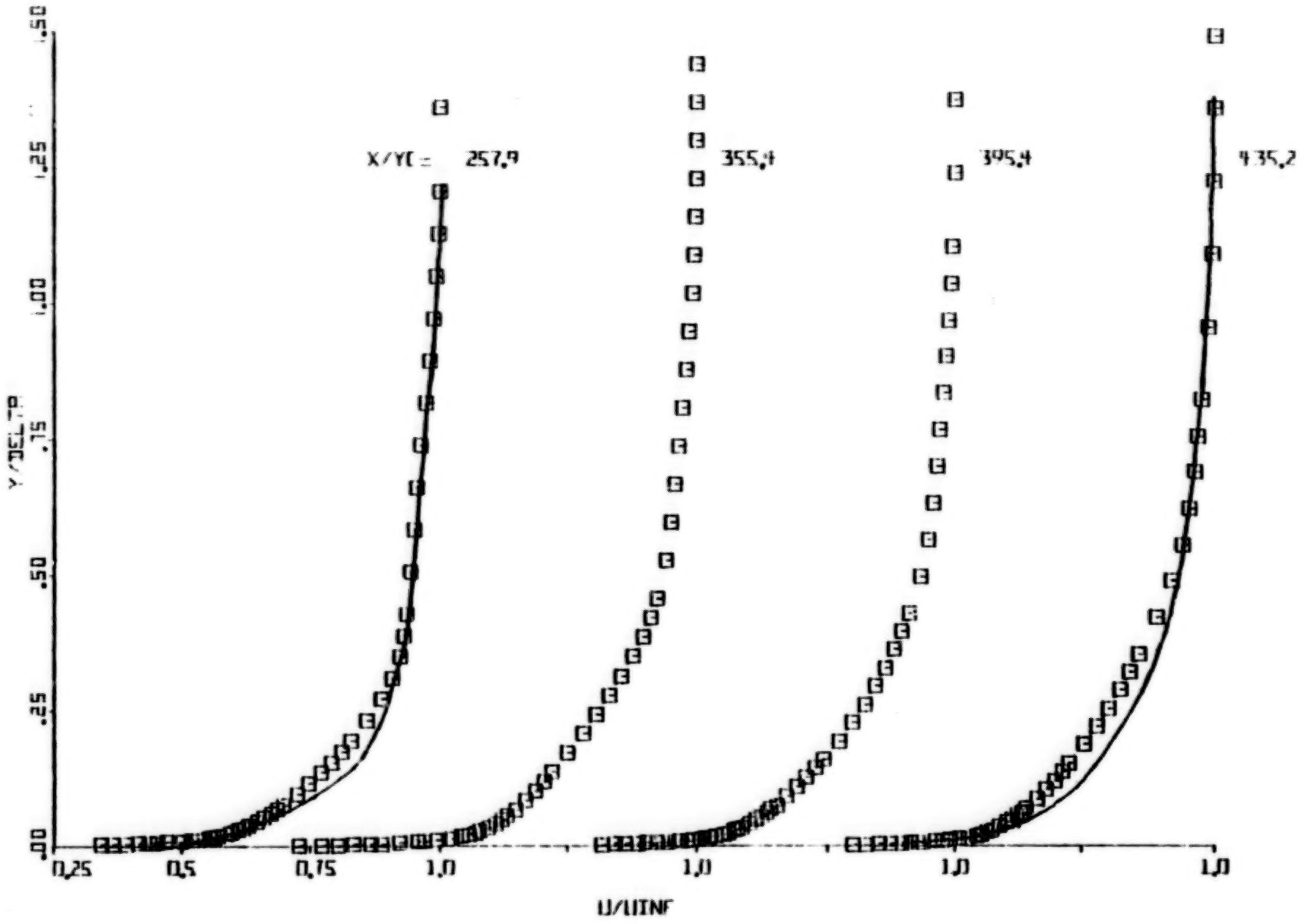

Fig. 4.4(e) Mean Velocity Profiles at x/y_c = 257.9 to 435.2

—— Predictions using experimental initial profiles

indicates that they are the distances measured upstream of the slot. The value x/y_c = -16.4 corresponds to the crest of the extruded aluminum end piece (section 2.2.2) and x/y_c = -77.1 corresponds to a position 21 cm upstream of the slot.

Fig. 4.4(b) shows the velocity profile at x/y_c = 0.292. Here it can be seen that the velocity profile in the jet is asymmetric with a relatively greater concentration of momentum in the upper half of the wall jet. This asymmetric velocity profile in the jet is typical of the present wall jet design as discussed in Chapter 2. By comparing the upstream boundary layer velocity profiles at x/y_c= -77.1 and x/y_c = 0.292, one can see that the wall jet body did not introduce any major changes in the mean velocity profile of the upstream boundary layer. The upstream boundary layer above the slot shown in Fig. 4.2(b) is very thick and it has a large deficit of momentum, satisfying one of the conditions under which the present measurements were intended to be made, as given in Chapter 1. Figs. 4.4 (c), (d) and (e) show the mean velocity profiles from x/y_c = 7.45 and onwards. The upstream boundary layer has been completely absorbed by the jet as the flow proceeds in the downstream direction. The velocity maxima and minima cannot be identified after x/y_c = 146.2. At x/y_c = 435.2, the velocity profile looks similar to a normal turbulent boundary layer.

Figs. 4.5(a) and (b) show the velocity profiles plotted on a conventional semilogarithmic plot with U/U_τ and $U_\tau y/\nu$ as the co-ordinates. The velocity profiles were shown for stations $x/y_c = 7.45$ and onwards. The frictional velocity U_τ was obtained from the Preston tube measurements. The velocity profile measurements were compared with the logarithmic law of the wall (Equation 4.1), with the constant recommended by Patel (1965). It can be seen from Figs. 4.5 (a) and (b) that the experimental data agree well with the logarithmic law of the wall for all the stations, except at $x/y_c = 7.45$ where a defined logarithmic region has not been formed yet because of its proximity to the slot.

The good agreement between the logarithmic law of the wall and the mean velocity data indicates that the skin friction measurements are accurate. This also indicates that the uncertainty in the skin friction measurements given in Chapter 3 may have been over estimated. The momentum thickness Reynolds number and the wake component $\Delta(U/U_\tau)$ (Coles, 1962) are equal to 6312 and 3.0, respectively, at $x/y_c = 435.2$. The wake component at $x/y_c = 435.2$ is 10% higher than its value given by Coles for a normal zero pressure gradient turbulent boundary layer at the same or higher momentum thickness Reynolds numbers. The mean velocity data are tabulated in Appendix D along with the data of u_t.

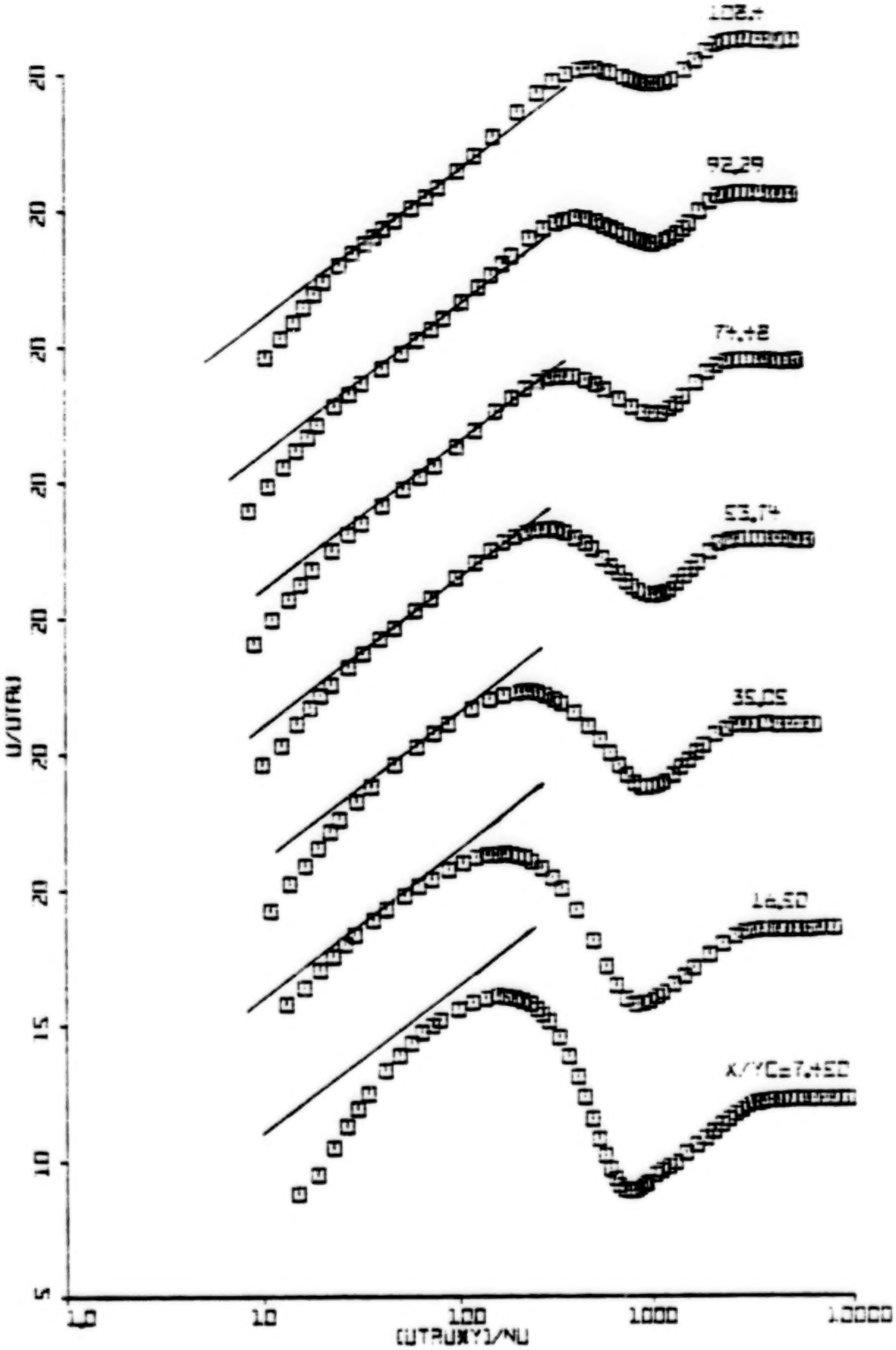

Fig. 4.5(a) Mean Velocity Profiles in the Wall Coordinates at x/y_c = 7.45 to 108.4

—— Logarithmic law of the wall (Equation 4.1)

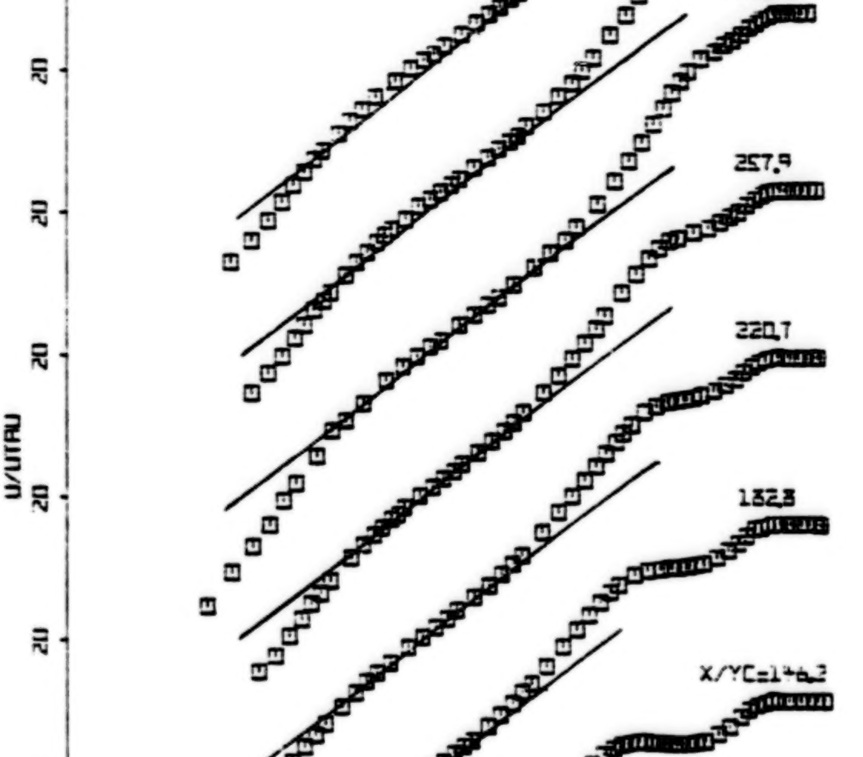

Fig. 4.5(b) Mean Velocity Profiles in the Wall Coordinates at x/y_c = 146.2 to 435.2

—— Logarithmic law of the wall (Equation 4.1)

Fig. 4.5 (c) shows the streamline pattern around the slot lip. It shows that there is no appreciable variation of the static pressure in the direction normal to the bottom wall of the tunnel as the streamlines are not steeply curved in the region of the slot lip.

4.2.3 Integral Parameters

The integral parameters evaluated are the boundary layer thickness (δ), displacement thickness (δ_1), momentum thickness (δ_2), shape factor (H), and the momentum thickness Reynolds number (Re_2). Figs. 4.6 (a-e) show the development of the integral parameters δ, δ_1, δ_2, H, and Re_2 respectively. The rates of increase of the momentum thickness, displacement thickness, and the boundary layer thickness seem to be very slow in the present experiments. The shape factor H tends to become a constant approximately equal to 1.35 at far downstream stations, which closely agrees with the value of $H = 1.4$ indicated by Schubauer and Klebanoff (1955, 1956) for a flat plate turbulent boundary layer.

The two-dimensional nature of the flow was examined by applying the two-dimensional integral momentum equation (4.3) to the present data.

$$\frac{dRe_2}{dRe_x} = \frac{C_f}{2} - \frac{d}{dx}\int_0^\infty \frac{\overline{u^2} - \overline{v^2}}{U_\infty^2}\,dy \qquad (4.3)$$

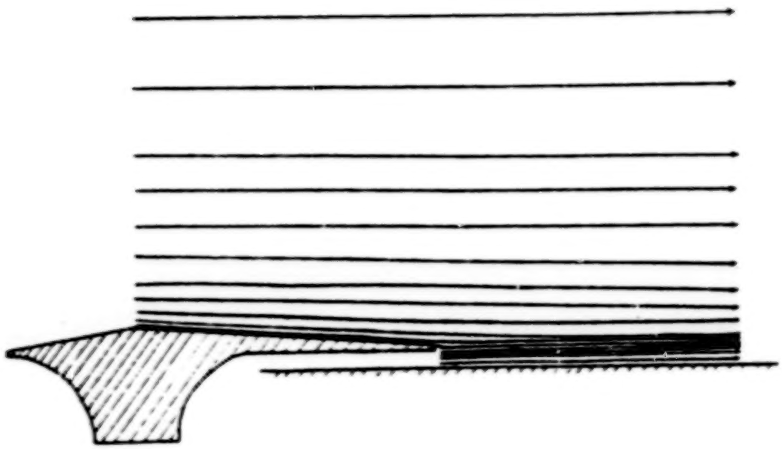

Fig. 4.5(c) Streamline Pattern Around the Slot Lip

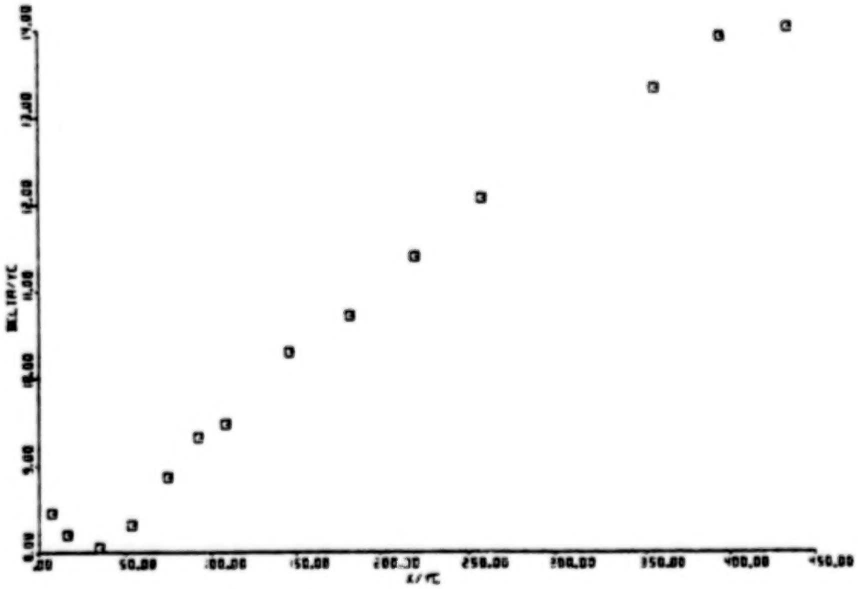

Fig. 4.6(a) Growth of the Boundary Layer Thickness

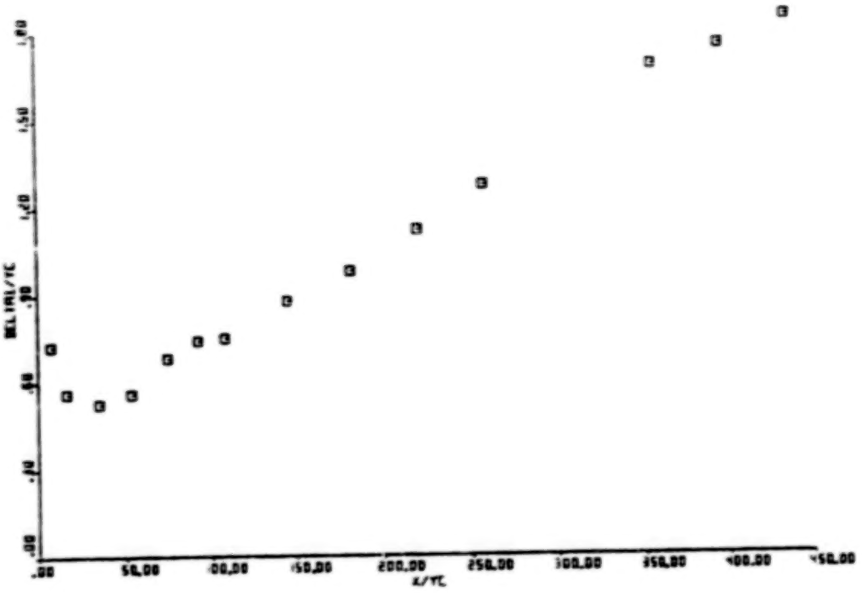

Fig. 4.6(b) Growth of the Displacement Thickness

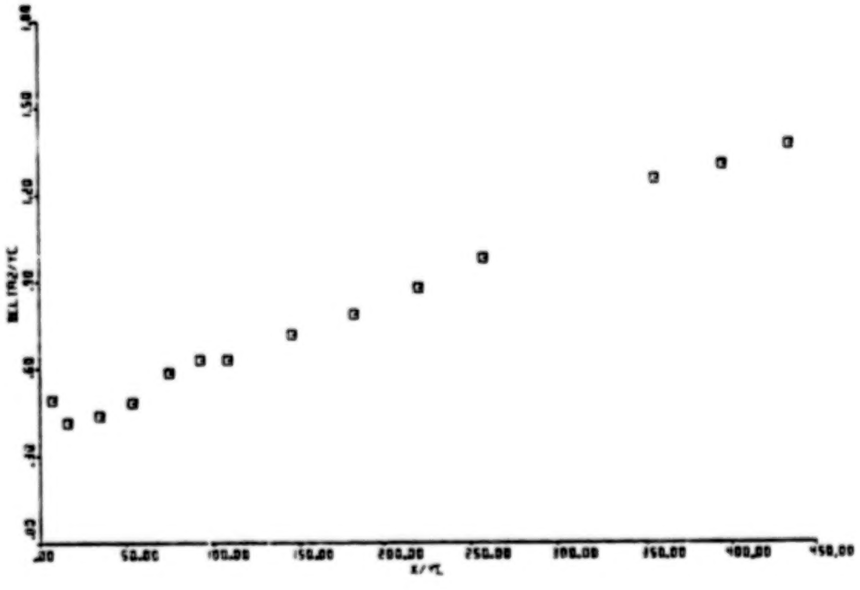

Fig. 4.6(c) Growth of the Momentum Thickness

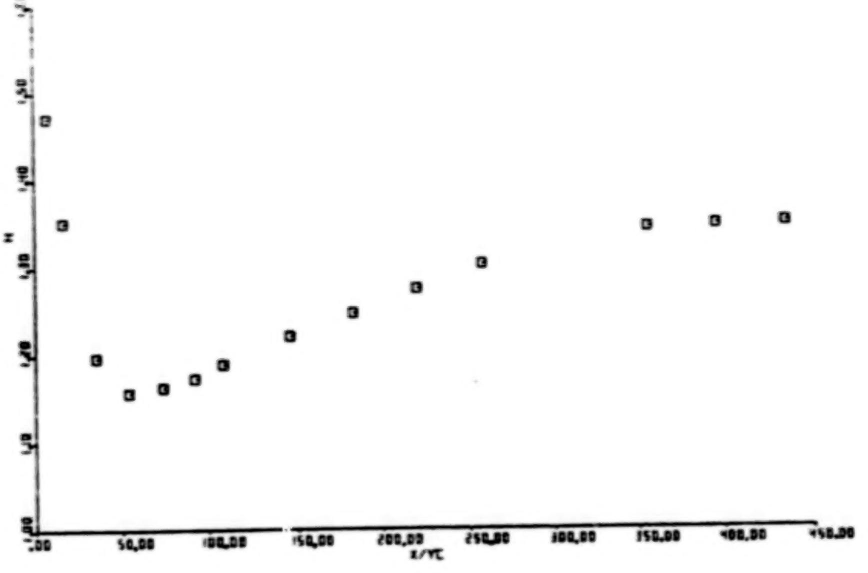

Fig. 4.6(d) Variation of the Shape Factor

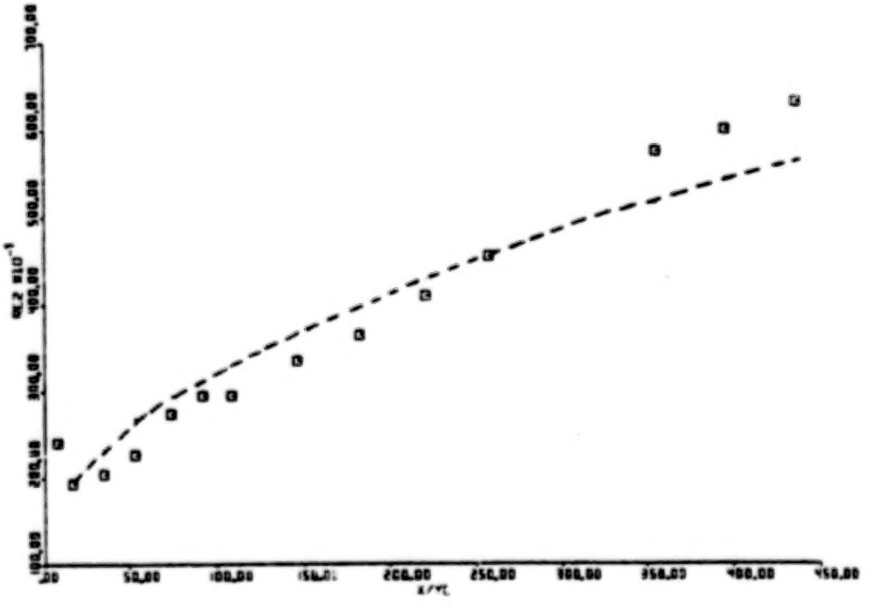

Fig. 4.6(e) Variation of the Momentum Thickness Reynolds Number Re_2

---- Re_2 obtained using the two-dimensional integral momentum equation (4.3) or,

$$Re_2 = \int_{x/y_c=16.5}^{x/y_c} \frac{C_f}{2}\, dRe_x + (Re_2)_{x/y_c=16.5} - \frac{U_\infty}{\nu}\left[\int_0^\infty \frac{\overline{u^2}-\overline{v^2}}{U_\infty^2}\, dy\right]_{x/y_c=16.5}^{x/y_c}$$

where

$$Re_2 = \frac{U_\infty \delta_2}{\nu} \quad \text{and} \quad Re_x = \frac{U_\infty x}{\nu}$$

The contribution of the normal stresses term $\int_0^\infty [(\overline{u^2} - \overline{v^2})/U_\infty^2]dy$ to the integral momentum equation was found to be smaller than 5% and hence it was neglected. The measured skin friction coefficients were used in the equation (4.3). Fig. 4.6(e) shows the values of Re_2 obtained from the two-dimensional integral momentum equation (4.3) along with the experimental values of Re_2. The experimental values of Re_2 agree with the values of Re_2 obtained from equation (4.3) within ±10% on the average, establishing the two-dimensionality of the flow.

4.2.4 Effect of the Asymmetric Jet Velocity Profile on the Mean Flow

The effect of the asymmetric jet velocity profile on the mean flow development is discussed below. A crude comparison of the development of the mean velocity profile for the present flow with that of similar flows in the literature (Kacker and Whitelaw, 1968) shows that the development of the jet requires a greater x/y_c distance in the present case. The flow takes a longer distance in the present case to achieve the state of a normal turbulent boundary layer. The effect of the jet momentum can be seen even as far as $x/y_c = 435.2$ due to the low value of Re_2 there. This can be attributed only to the asymmetric nature of the jet velocity profile. The asymmetric velocity profile spreads the jet momentum more uniformly in the layer by supplying more momentum to the momentum deficient upstream boundary layer than wasting the same jet momentum in the form of friction at the wall. In comparison, the uniform jet velocity profile has a relatively large concentration of momentum near the wall which results in greater frictional losses. Thus the momentum of the jet is carried away to a much longer distance in the case of an asymmetric jet velocity profile.

The rates of increase of momentum thickness, displacement thickness and boundary layer thickness seem to be very slow for the present case where a highly momentum deficient upstream boundary layer is meeting a wall jet of moderate momentum. In a case like this, one would expect the integral thicknesses to increase rapidly, indicating deficiency of momentum if it was a uniform profile in the jet. The uniform jet velocity profile cannot meet the momentum requirements of the upstream boundary layer as efficiently as an asymmetric jet velocity profile. This results in the development of momentum deficient regions in the case of a uniform jet velocity profile. Hence the integral thicknesses can be expected to increase rapidly in the case of uniform jet velocity profile. Therefore, the present slow growth rate of the integral thicknesses can only be attribututed to the asymmetric nature of the jet velocity profile.

4.2.5 Profile Parameters

The profile parameters are the quantities related to the mean velocity profile. The profile parameters presented here include Y_{max}, Y_{min}, Y_{half}, U_{max} and U_{min}. With reference to Fig. 1.1 (b), Y_{max} is the position of the maximum velocity U_{max}, Y_{min} is the position of minimum velocity U_{min}, and Y_{half} is the position where $U = (U_{max} + U_{min})/2$. The velocity maximum and the velocity minimum could not be identified after $x/y_c = 146.2$. Hence, all the profile parameters were plotted only up to $x/y_c = 146.2$.

4.2.5 (a) Development of Y_{max}, Y_{half}, and Y_{min}

Fig. 4.7 (a) shows the development of Y_{max} and Y_{half}. Fig. 4.7 (b) shows the development of Y_{min}. The developments of Y_{max} and Y_{half} are of particular interest here. It has been found in previous research that Y_{max} can be expressed as a universal linear function of the distance x/y_c for self-preserving wall jet flows under zero and adverse pressure gradients. The survey of the existing data on self-preserving wall jets by Narayan

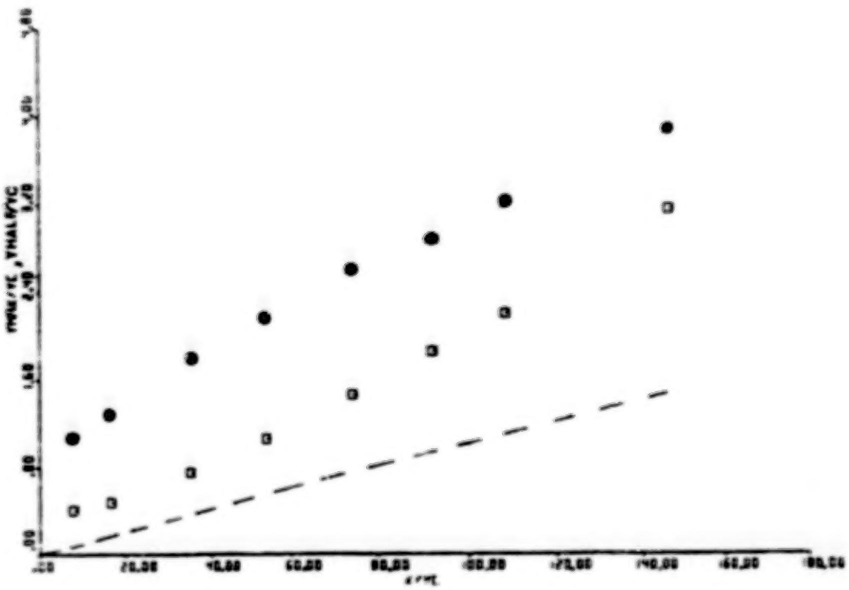

Fig. 4.7(a) Development of Y_{max} and Y_{half}

▫ , ● Experimental data of Y_{max} and Y_{half} respectively

---- Universal distribution of Y_{max}

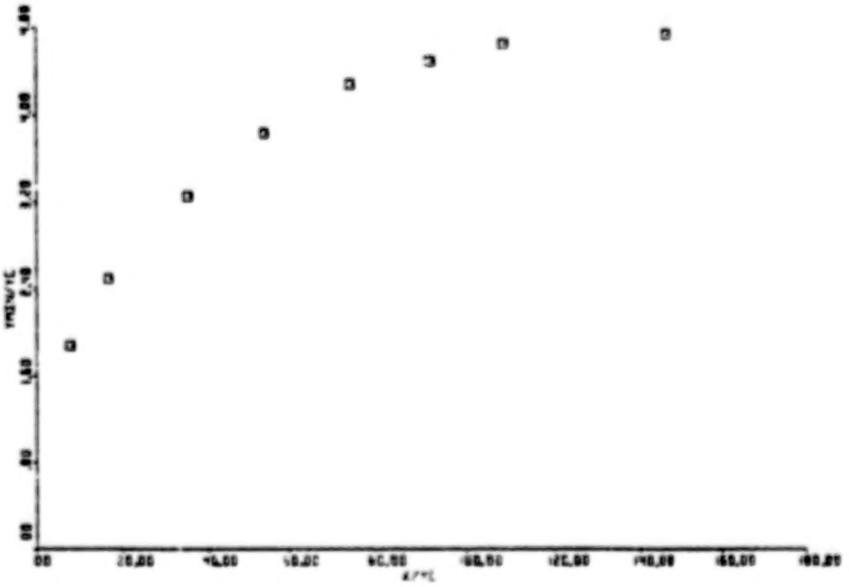

Fig. 4.7(b) Development of Y_{min}

and Narasimha (1973) confirms the universal behavior of the Y_{max} distribution. The data of Irwin (1973) also reveal the universal behavior of the Y_{max} distribution. The universal Y_{max} distribution for the self-preserving wall jet flows is shown in Fig. 4.7 (a). However, it is not clear whether the non-self-preserving wall jets exhibit similar universal behavior for the Y_{max} development. The data of Ramaprian (1973) show that even for non-self-preserving wall jets under adverse pressure gradients, the Y_{max} development is universal. The data of Irwin (Newman and Irwin, 1975) do not indicate a universal behavior for the Y_{max} development in the case of non-self-preserving adverse pressure gradient flows.

The present flow is a non-self-preserving flow. The Y_{max} distribution for the present flow does not seem to follow the universal distribution as revealed by the Fig. 4.7 (a). The growth rate of Y_{max} in the present case is higher than that of the universal Y_{max} distribution. This can be partly attributed to the asymmetric jet velocity profile as explained below. The experimental asymmetric jet velocity profile has its maximum velocity located nearer to the slot lip to start with. Hence, the asymmetric velocity profile has relatively more momentum near the slot lip. The inner layer corresponding to the region of maximum velocity spreads out more rapidly in an effort to meet the momentum requirements of the upstream boundary layer. Therefore, the position of maximum velocity (Y_{max}) moves more rapidly into the outer layer. In comparison, a wall jet with uniform jet velocity profile has its momentum distributed evenly across the slot. Hence, the growth rate of Y_{max} is relatively slow for a uniform jet velocity profile. Also, a wall jet with uniform jet velocity profile retains a considerable part of injected momentum nearer to the wall, thereby losing a relatively larger amount of momentum as surface frictional losses.

The data of Irwin (1973), Irwin (Newman and Irwin, 1975), Ramaprian (1973), Gartshore and Newman (1969), and the data of various authors presented in Narayan's (1973) work indicated that the growth rate of Y_{half} is always higher than that of Y_{max} for wall jets with uniform injection at the slot. The above data also indicate that the development of Y_{half} is not universal and it depends strongly on the conditions upstream of the slot and the ratio of the jet velocity to the free-stream velocity. However, the growth rate of Y_{half} in the present experiments is almost the same as that of Y_{max} shown in Fig. 4.7 (a). The slower growth rate of Y_{half} in the present experiments can be attributed to the asymmetric jet velocity profile. The experimental asymmetric profile has relatively higher concentration of momentum in the upper half of the jet and nearer to the momentum deficient region in the outer layer. Therefore, the outer layer tries to extract more momentum from the inner layer rather than extracting momentum from the free-stream. This results in slower growth of the outer layer and hence the slower growth rate of Y_{half}.

4.2.5 (b) Variation of U_{max} and U_{min}

Fig. 4.8 (a) shows the variation of U_{max}/U_{Jave} and U_{min}/U_{Jave} with x/y_c. Fig. 4.8 (b) shows the variation of $(U_{max} - U_{min})/U_{Jave}$ with x/y_c. U_{Jave} is the uniform jet velocity for an equivalent jet with uniform profile and having the same momentum as the experimental asymmetric jet. Wall jet data in the literature show that the variation of U_{max} and U_{min} depends on several parameters like the ratio of jet velocity to the free-stream velocity, the pressure gradient and the conditions upstream of the slot. Hence an attempt has not been made to compare the present variation of U_{max} and U_{min} with the data in the literature. It can be seen from Fig. 4.8 (a) that the rate of decay of U_{max} is greater than the growth rate of U_{min}. Ramaprian's (1973) data for different non-self-preserving wall jets under adverse pressure gradients show that for a given ratio of jet velocity to free-stream velocity, the decay of maximum velocity is the same as that for plane self-preserving wall jets under zero pressure gradient. However, this is not true in general.

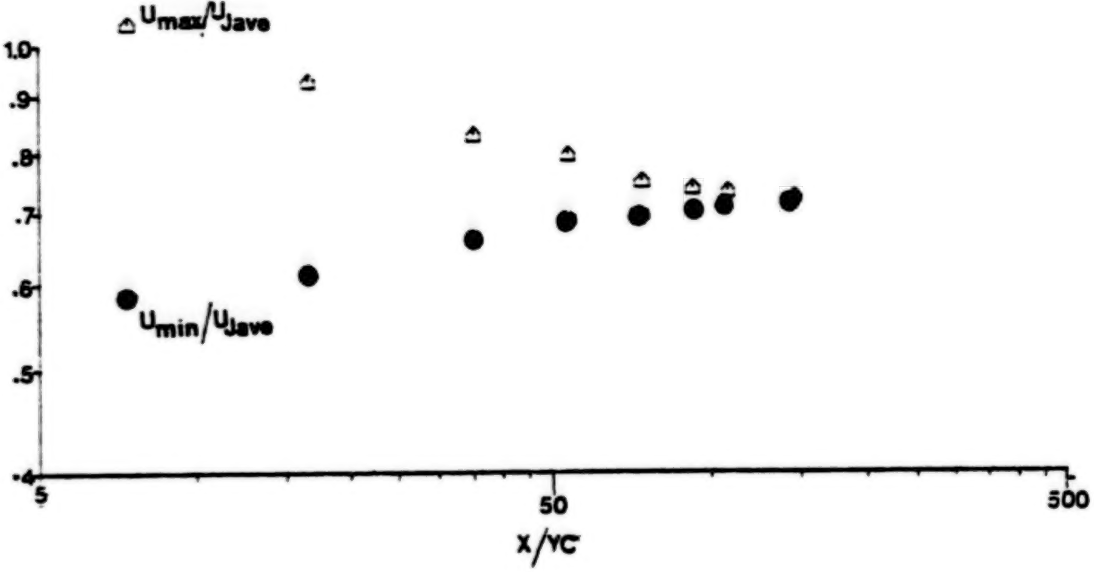

Fig. 4.8(a) Variation of U_{max} and U_{min}

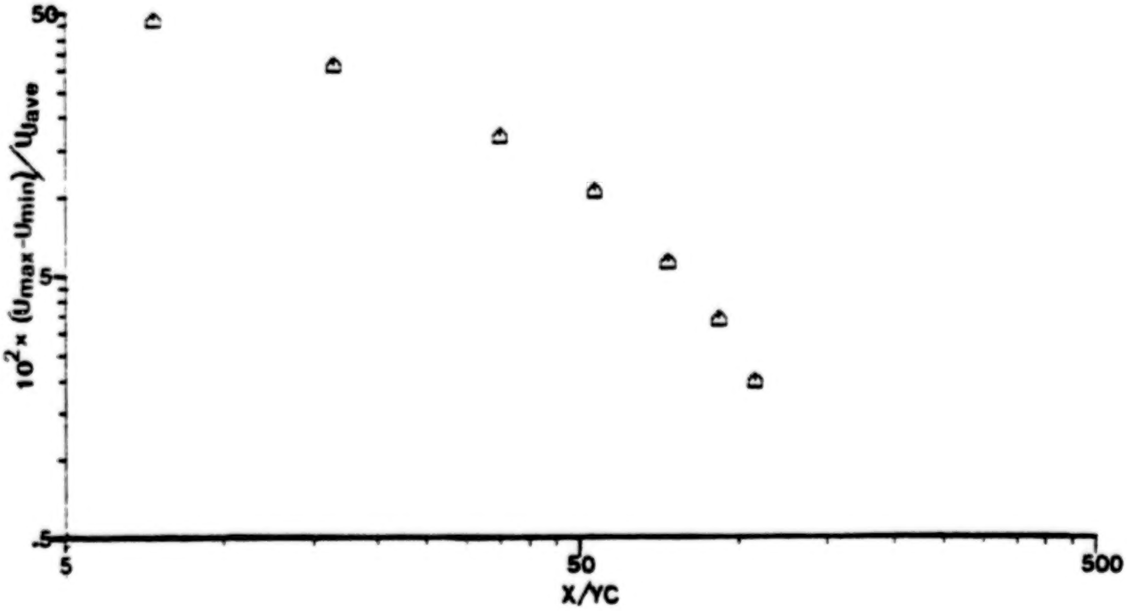

Fig. 4.8(b) Variation of (U_{max} - U_{min})

4.3 Turbulence Data

The measured turbulence data include the results of the measured turbulence intensities (u_t/U_∞, v_t/U_∞ and w_t/U_∞), the measured turbulent shear stress $-\overline{uv}$ and the measured spectra of $\overline{u^2}$. The quantities derived from the measured turbulence data include the eddy viscosity, mixing length, Prandtl-Kolmogorov length scale, turbulent kinetic energy, correlation coefficients, production and dissipation rates of turbulent kinetic energy and bursting periods. The results of the measured and derived turbulent quantities are given below in detail.

4.3.1 Turbulence Intensity u_t/U_∞

The u_t data were obtained from normal hot-film traversals at several stations starting from $x/y_c = 0.292$. Figs. 4.9 (a-c) show the variation of u_t/U_∞ vs $y/_\delta$ for different x locations. The negative sign on the value of x/y_c indicates that those stations are located upstream of the slot. The positions of the stations $x/y_c = -16.4$ and $x/y_c = -77.1$ are as given in section 4.2.2. The profile of u_t/U_∞ at $x/y_c = 0.292$ shows that the flow inside the jet is not an inviscid one, instead it is a fully turbulent flow, because of the high turbulence intensities existing there. The level of turbulence intensity gradually decreases as one proceeds downstream starting from the jet.

Fig. 4.10 (a) and (b) show the variation of u_t in wall coordinates. Most of the data are limited to

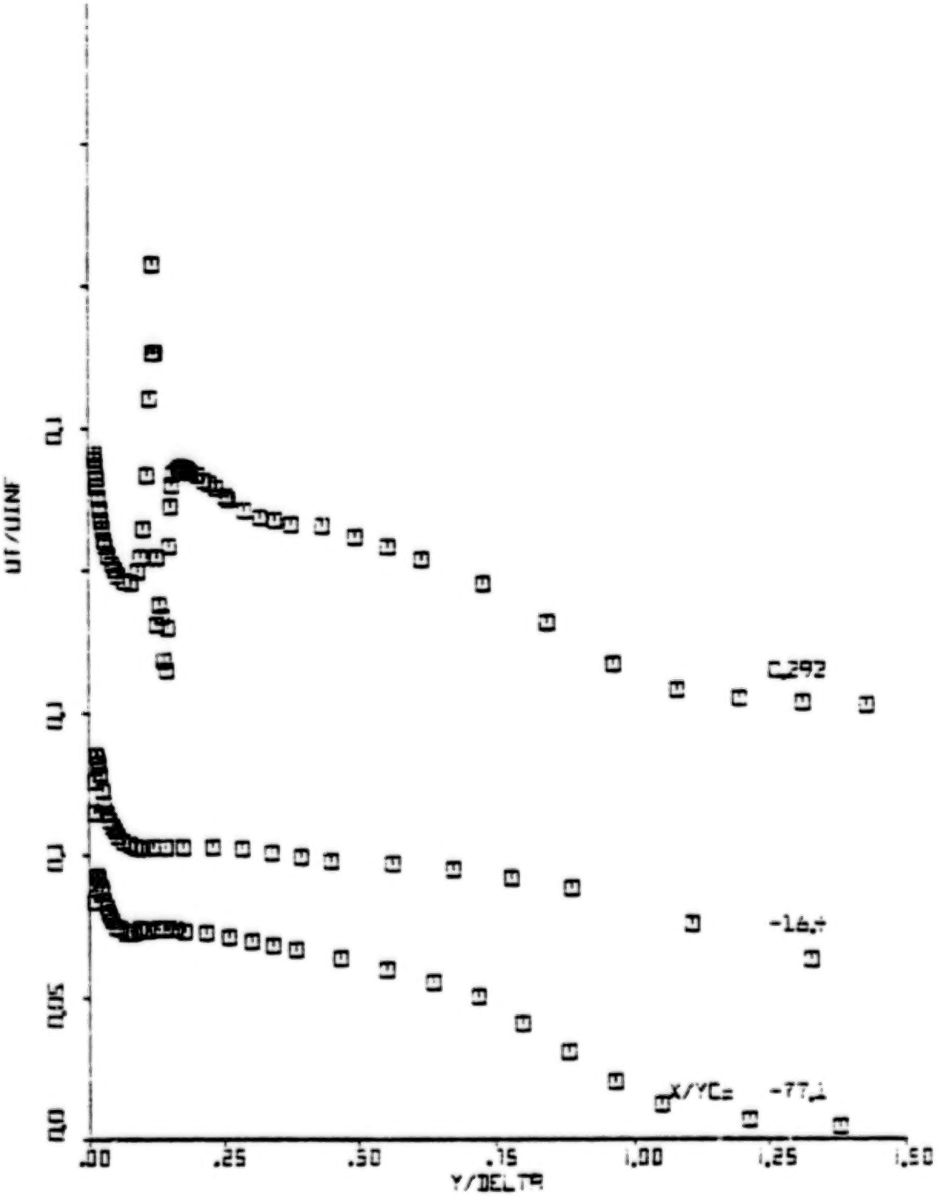

Fig. 4.9(a) Distribution of the Turbulence Intensity u_t/U_∞ at x/y_c = -77.1, -16.4 and 0.292

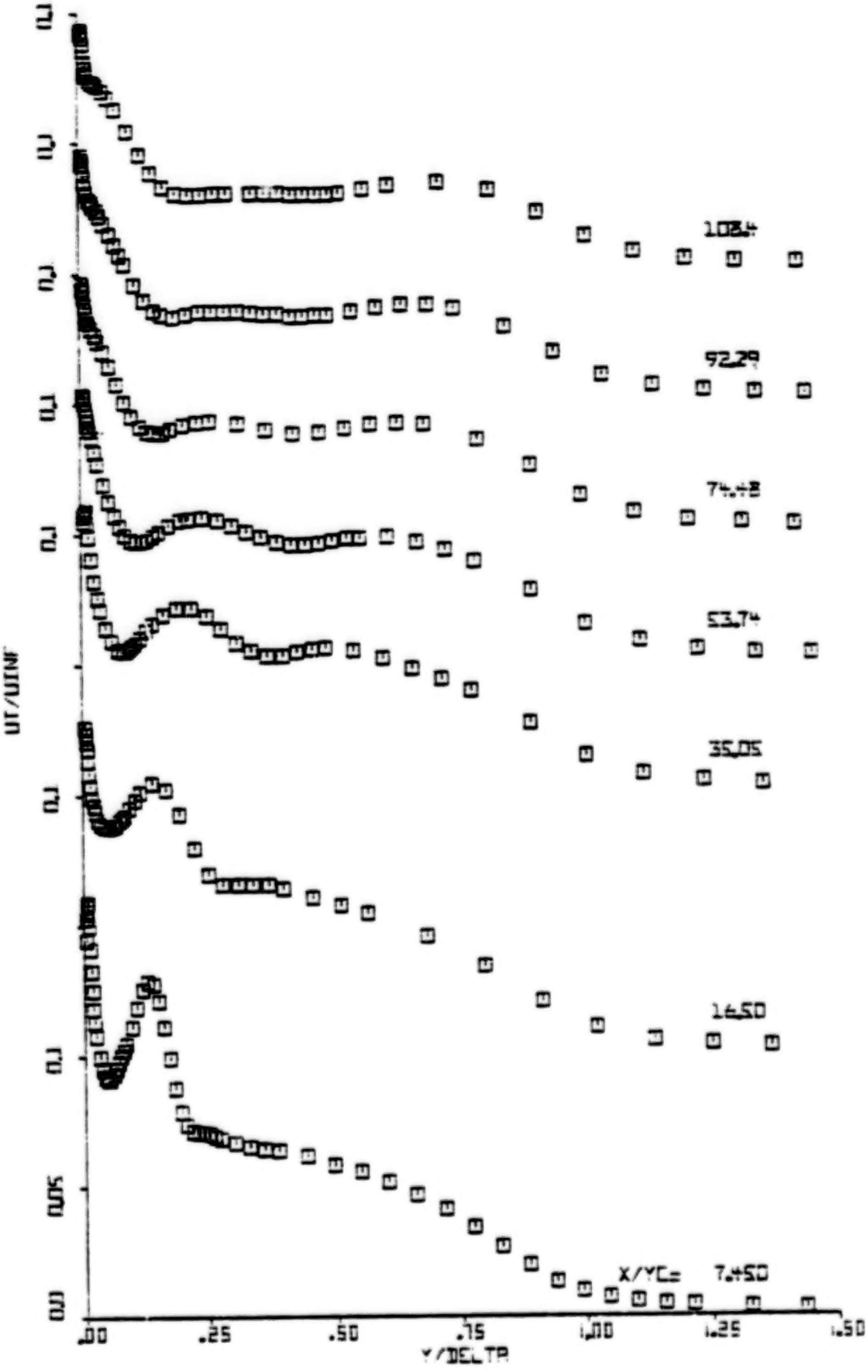

Fig. 4.9(b) Distribution of the Turbulence Intensity u_t/U_∞ at x/y_c = 7.45 to 108.4

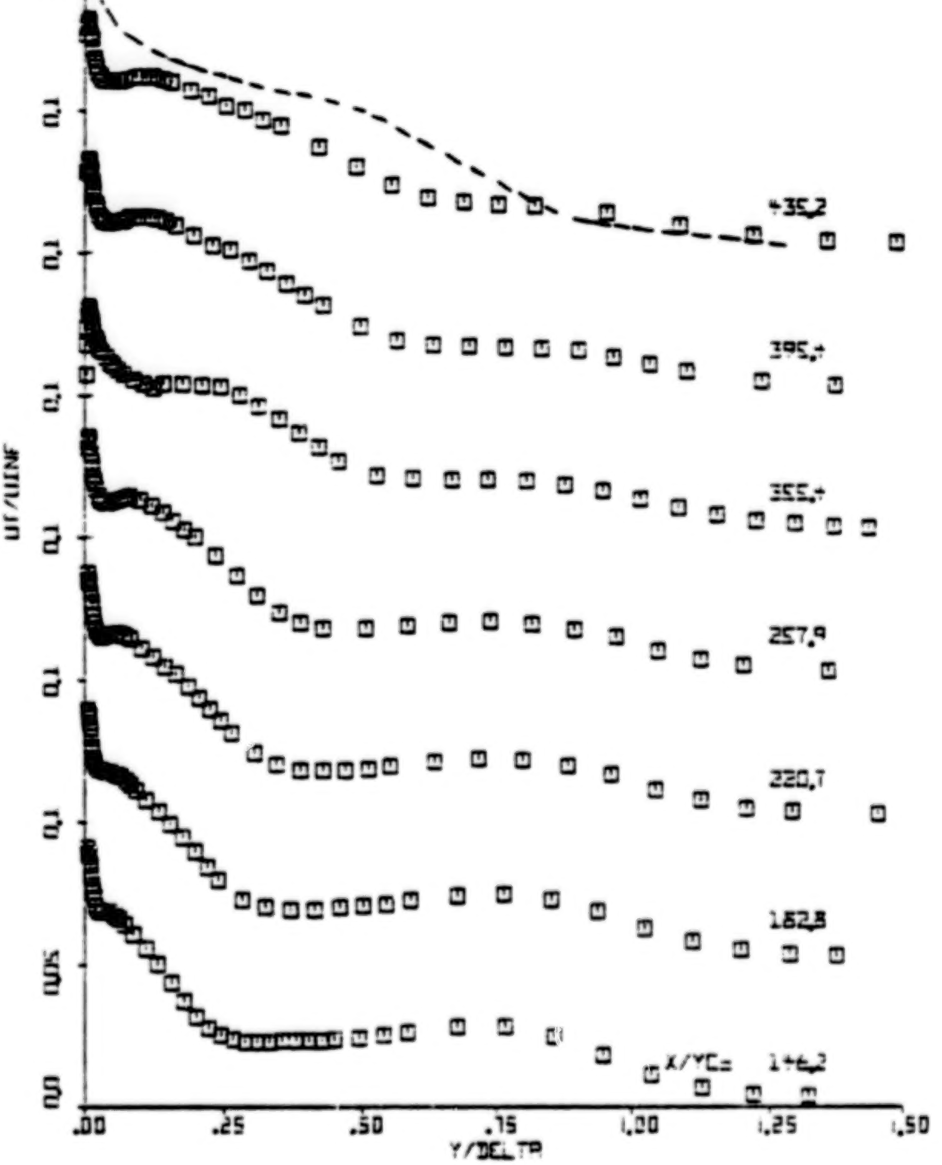

Fig. 4.9(c) Distribution of the Turbulence Intensity u_t/U_∞ at x/y_c = 146.2 to 435.2

---- u_t/U_∞ data by Klebanoff (1955) for a turbulent boundary layer on a flat plate (reproduced from Rotta (1962))

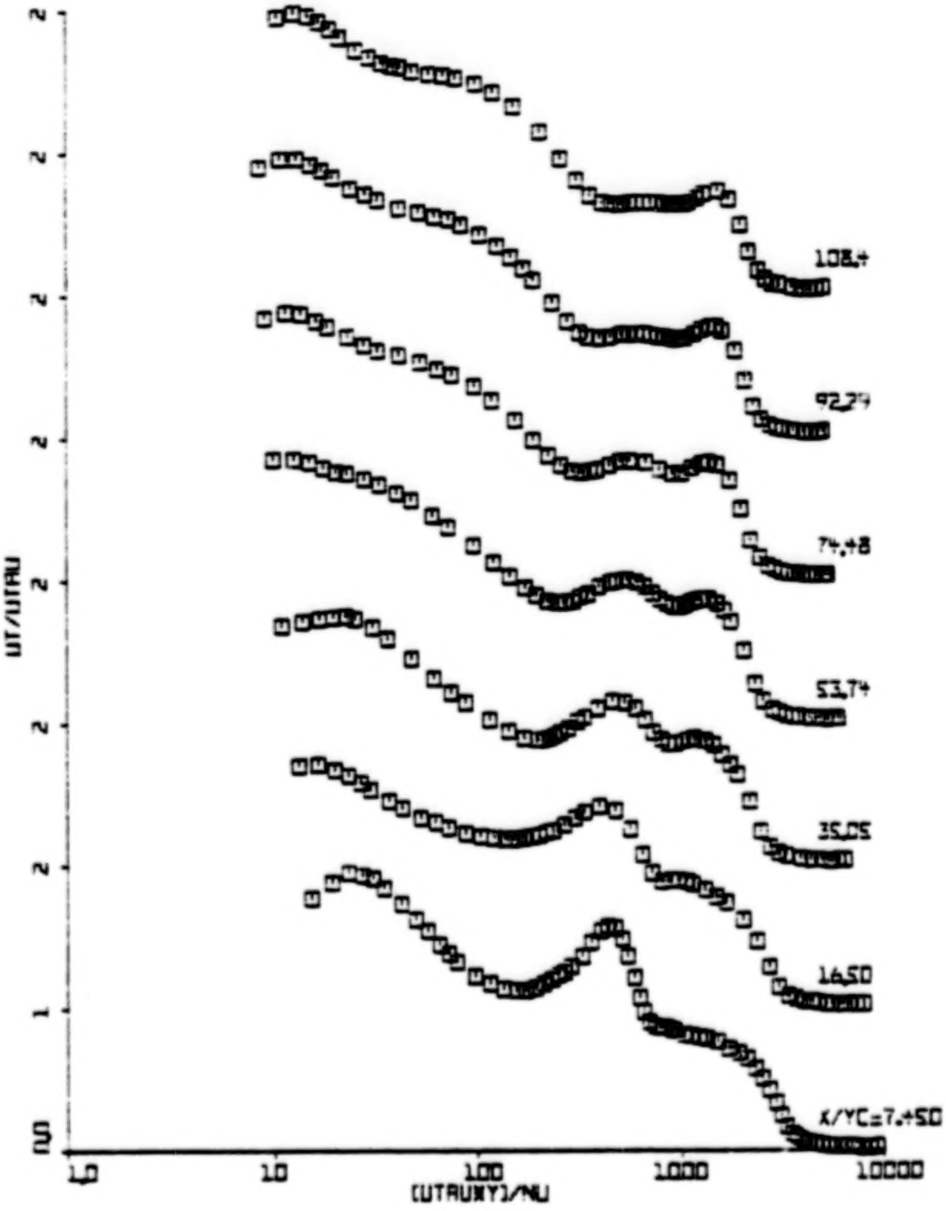

Fig. 4.10(a) Distribution of u_t in the Wall Coordinates at x/y_c = 7.45 to 108.4

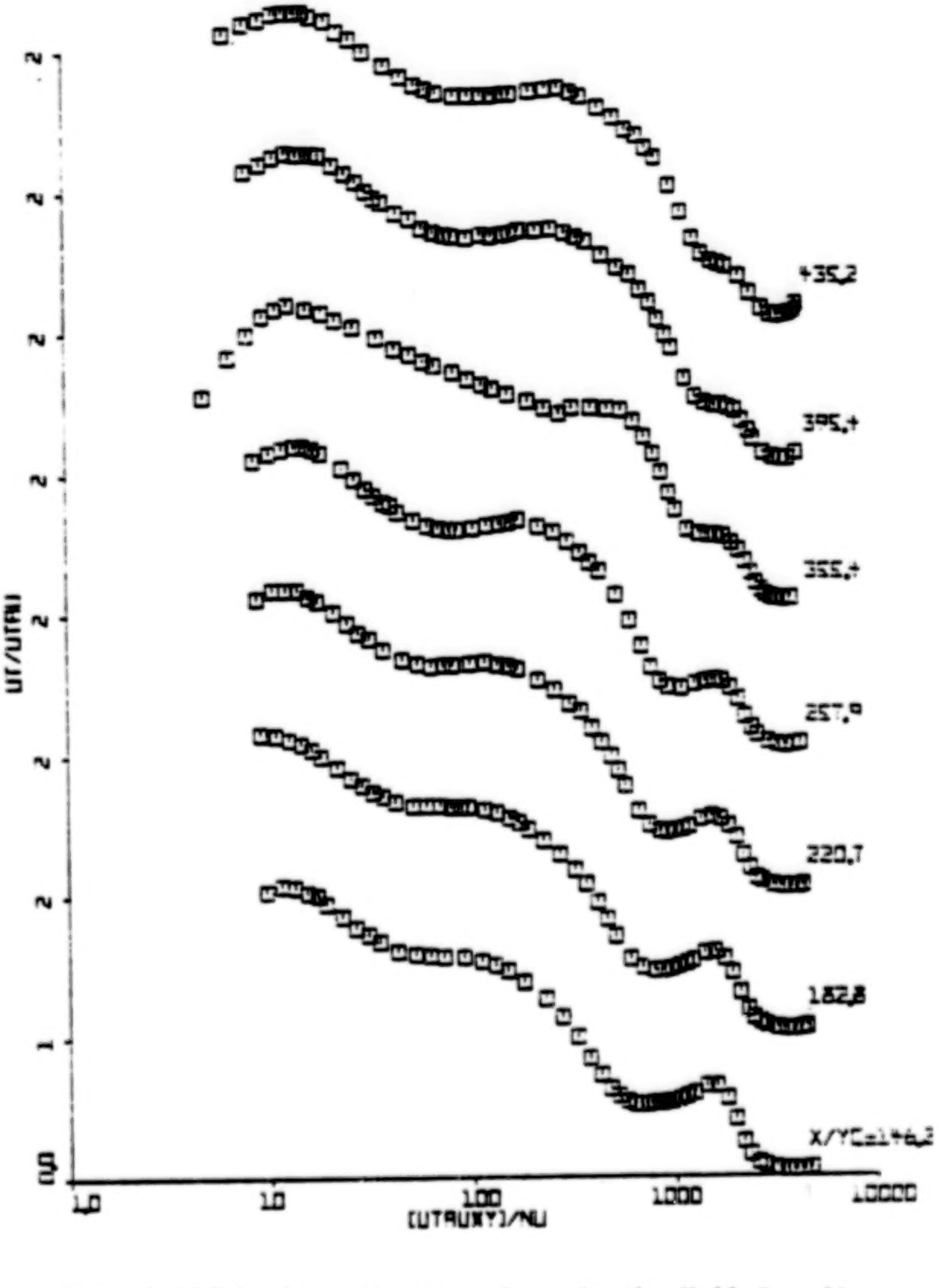

Fig. 4.10(b) Distribution of u_t in the Wall Coordinates at x/y_c = 146.2 to 435.2

the outer edge of the viscous sublayer with few stations as exception. The point of first maximum in u_t was always found to be near the wall and at the edge of the viscous sublayer. The point of minimum u_t in the inner layer generally corresponded with the region of maximum velocity even though the exact position was generally nearer to the wall than the point of maximum velocity. Sufficient slant-wire data were not available in the inner layer to describe the location of minimum u_t with respect to the point of zero shear stress. The point of second maximum in u_t was found to be in between the points of velocity maximum and the velocity minimum and nearer to the maximum velocity gradient. The u_t was found to be either minimum or constant around the point of velocity minimum. The steep drop in u_t far away in the outer layer was found to begin from the point of maximum velocity gradient between the velocity minima and the freestream. The data for u_t are given in Appendix D.

4.3.2 Turbulence Intensities v_t/U_∞, w_t/U_∞ And Shear Stress $-\overline{uv}$

A rotatable slant-wire (Chapter 3) was used to obtain v_t, w_t, and the shear stress $-\overline{uv}$. The $\overline{u^2}$ data obtained from the normal hot-film were used in the solution of the simultaneous equations for $-\overline{uv}$, $\overline{v^2}$ and $\overline{w^2}$. The details of obtaining v_t, w_t, and $-\overline{uv}$ from the slant wire data including the relevant mathematical details are given in Appendix C. The data of v_t, w_t, and $-\overline{uv}$ for all the slant-wire data stations are tabulated in Appendix E. Appendix E also shows the interpolated data of u_t and $\partial(U/U_\infty)/\partial(y/\delta)$ obtained from the normal hot-film data. Because of the size limitations set by the slant-wire probe supports, the slant-wire data at almost all the stations were taken only above the point of velocity maxima with a few exceptions. The results of the turbulence intensities v_t/U_∞, w_t/U_∞, and the shear stress $-\overline{uv}$ are described below in detail.

4.3.2 (a) Turbulence Intensities v_t/U_∞ and w_t/U_∞

Figs. 4.11 (a), (b) and 4.12 (a), (b) show the variation of v_t/U_∞ and w_t/U_∞ respectively at several stations, starting from $x/y_c = 16.5$. The slant wire data at $x/y_c = 0.292$ and $x/y_c = -16.4$ were not shown on the plots.

The point of maximum in v_t and w_t between the points of velocity maximum and velocity minimum has been found to be in the region of maximum velocity gradient. The level of magnitude of v_t and w_t dropped very rapidly between $x/y_c = 16.5$ and $x/y_c = 74.5$ and then the level of magnitude remains the same further downstream. For stations up to $x/y_c = 108.4$, the magnitudes of both v_t and w_t remained nearly equal at a given station. However, for stations beyond $x/y_c = 108.4$, w_t was found to be higher than v_t indicating the tendency to become a normal boundary layer (Klebanoff, 1955).

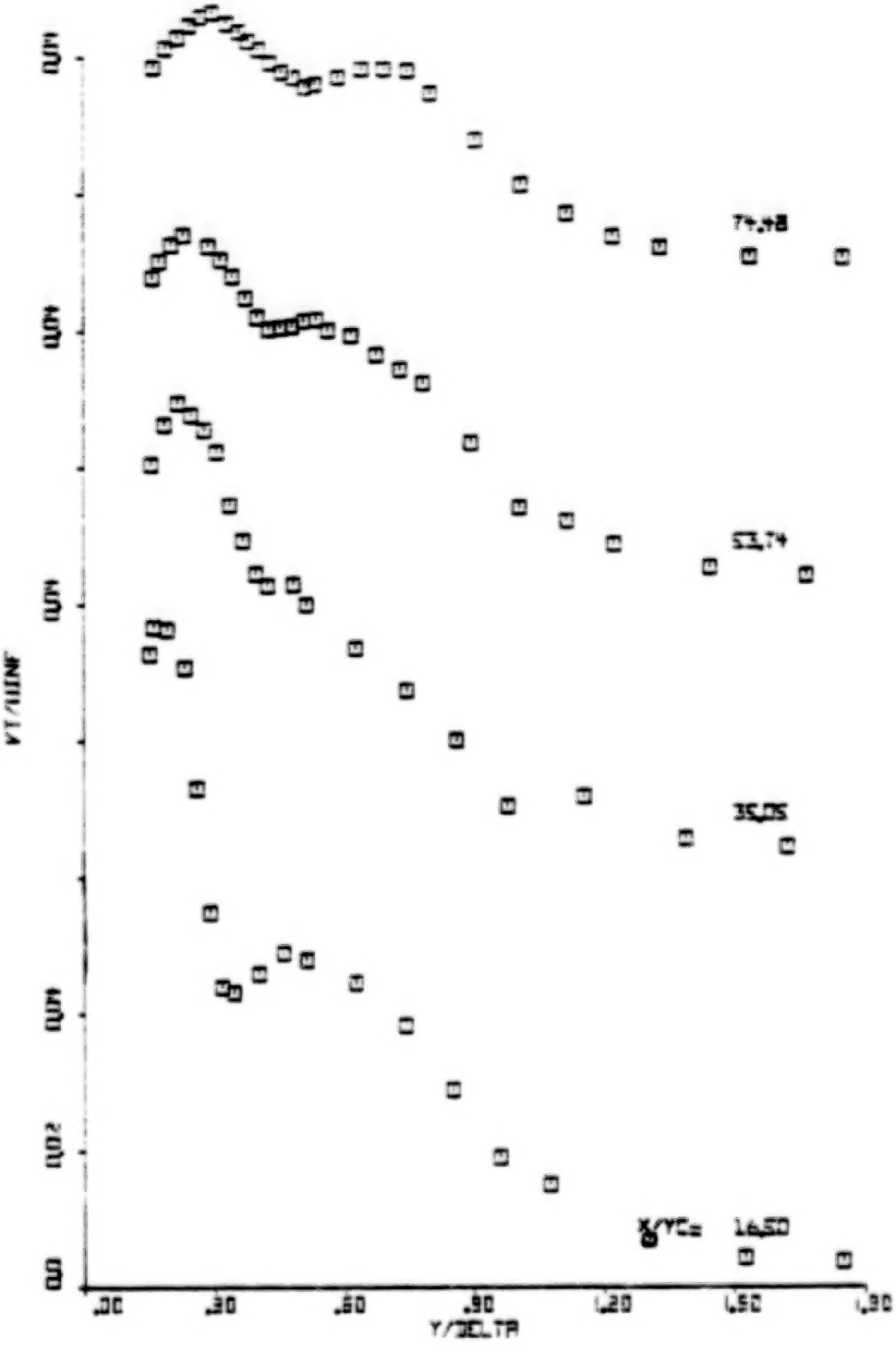

Fig. 4.11(a) Distribution of the Turbulence Intensity v_t/U_∞ at x/y_c = 16.5 to 74.48

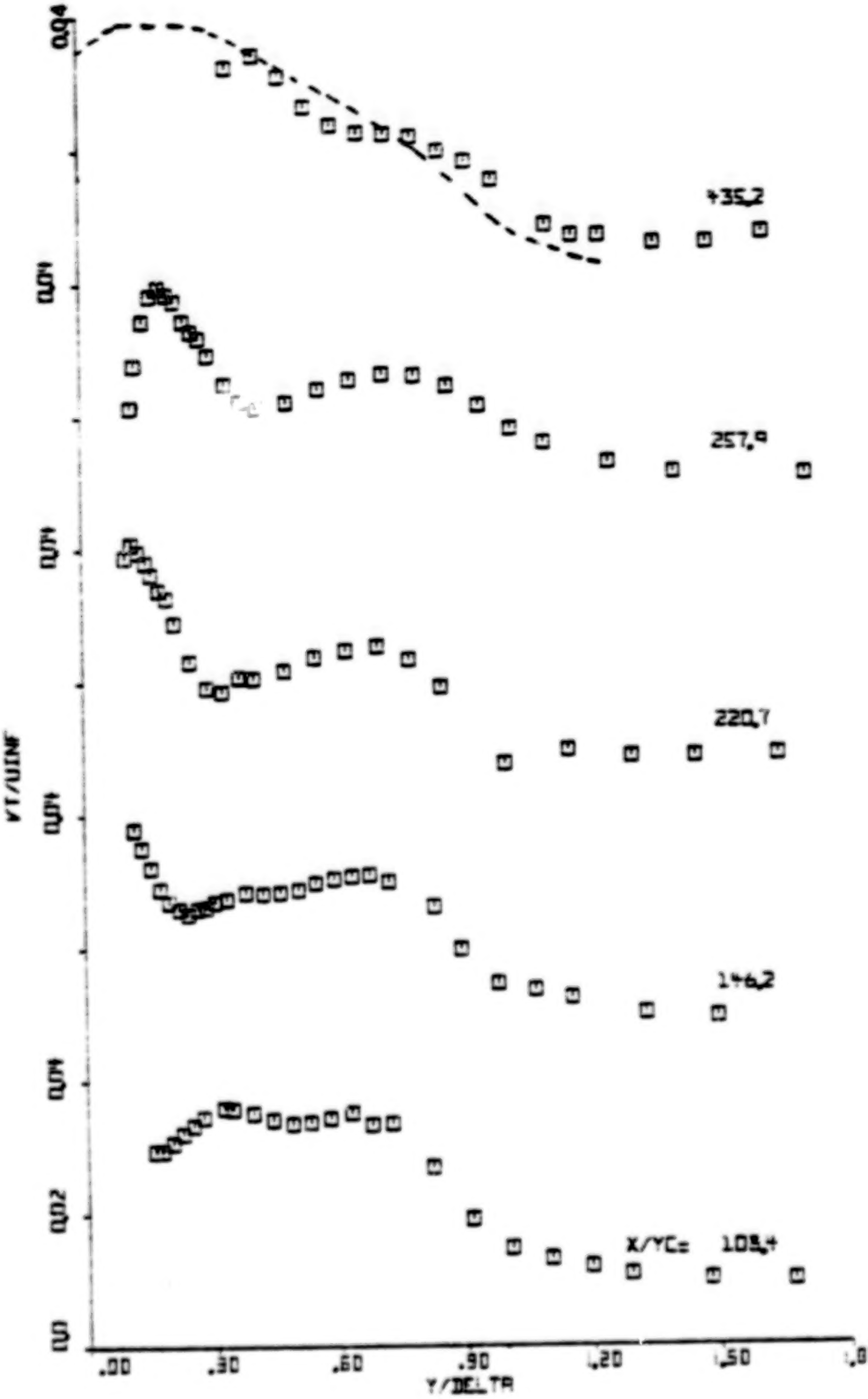

Fig. 4.11(b) Distribution of the Turbulence Intensity v_t/U_∞ at x/y_c = 108.4 to 435.2

---- v_t/U_∞ data by Klebanoff (1955) for a turbulent boundary layer on a flat plate (reproduced from Rotta (1962))

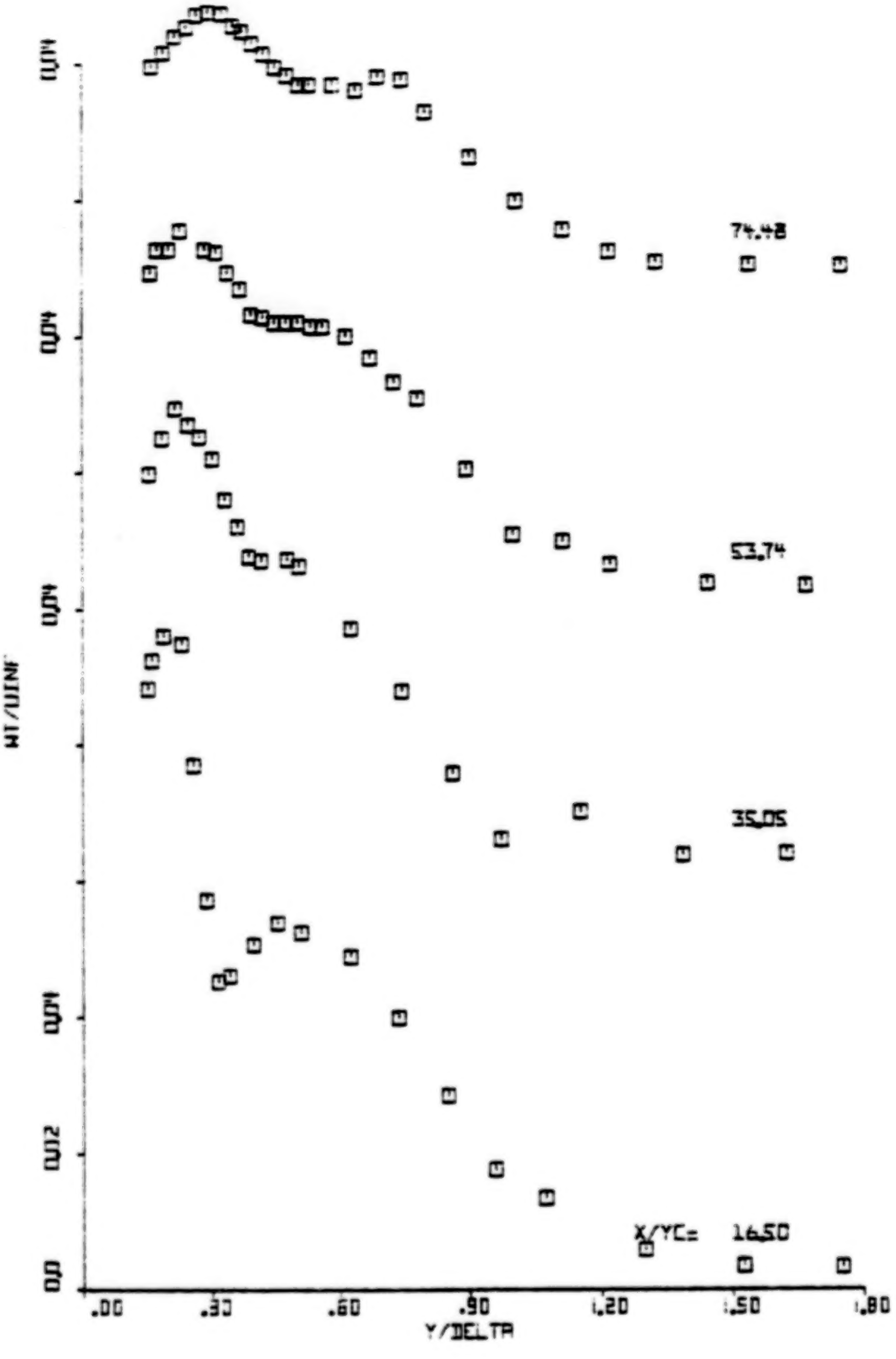

Fig. 4.12(a) Distribution of the Turbulence Intensity w_t/U_∞ at x/y_c = 16.5 to 74.48

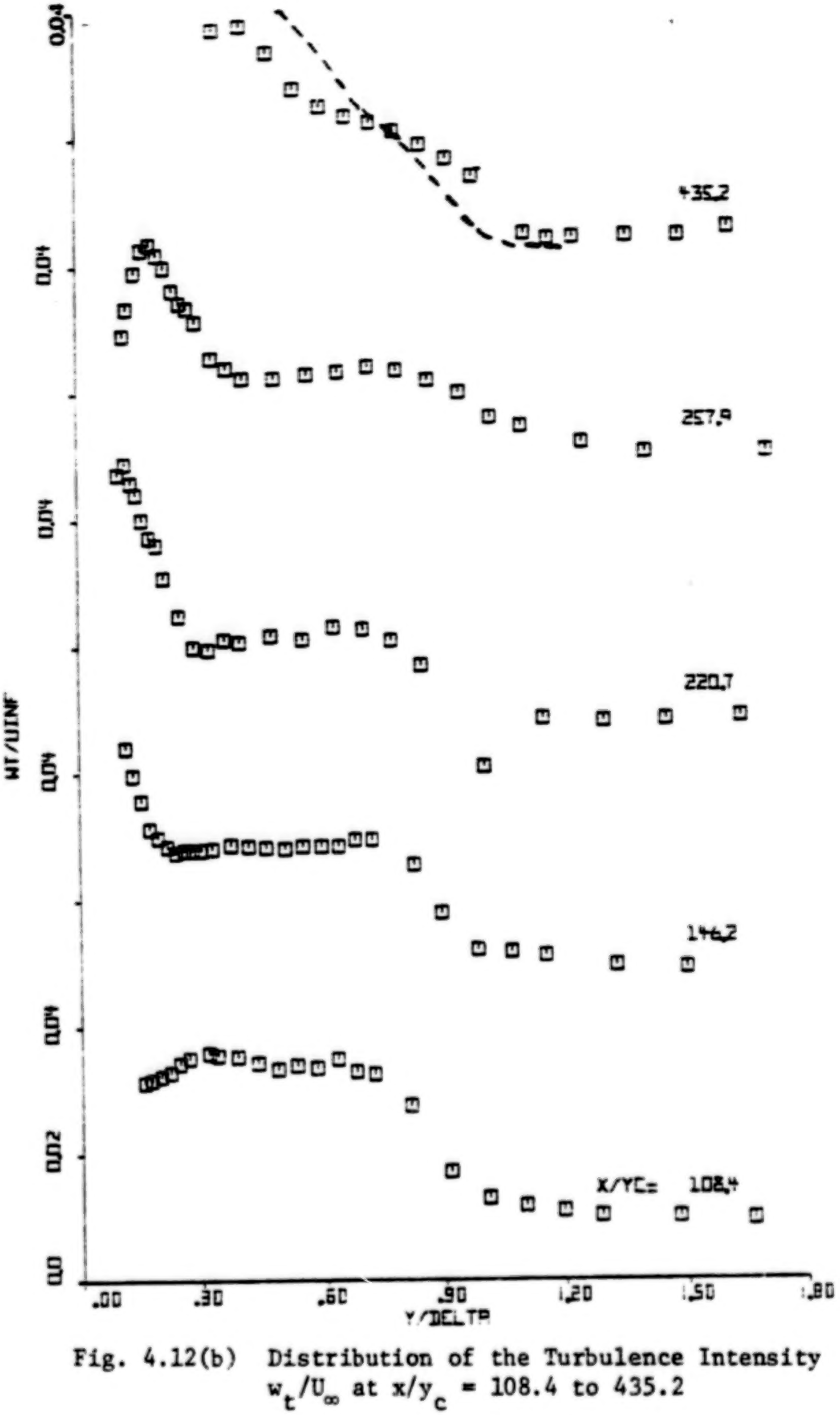

Fig. 4.12(b) Distribution of the Turbulence Intensity w_t/U_∞ at x/y_c = 108.4 to 435.2

---- w_t/U_∞ data by Klebanoff (1955) for a turbulent boundary layer on a flat plate (reproduced from Rotta (1962))

4.3.2 (b) Shear Stress $-\overline{uv}$

Figs. 4.13 (a) and (b) show the distribution of $-\overline{uv}/U_\infty^2$ at different stations. The slant-wire data at $x/y_c = 0.292$ and $x/y_c = -16.4$ were not shown on the plots. The points of zero shear can be seen distinctly in the $-\overline{uv}$ distributions shown in Figs. 4.13 (a) and (b). At a given station, there should be two points of zero shear corresponding to the two points of zero velocity gradients. The two points of zero velocity gradients refer to the points of maximum and minimum velocities in the velocity profile. The first point of zero shear encountered as one goes away from the bottom wall is called the inner point of zero shear and the second zero shear point is called the outer point of zero shear.

In the present $-\overline{uv}$ data, both the inner and outer points of zero shear can be observed only at stations $x/y_c = 108.4$ and $x/y_c = 146.2$. Only the outer point of zero shear can be observed for the stations upstream of $x/y_c = 108.4$, since it was not possible to make slant wire measurements closer to the wall at those stations. This was because of the size limitations set by the slant wire probe supports. The points of zero shear do not coincide with the points of zero velocity gradients. Both the inner and outer points of zero shear were found to be closer to the bottom wall than the corresponding points of zero velocity gradient. This result is in agreement

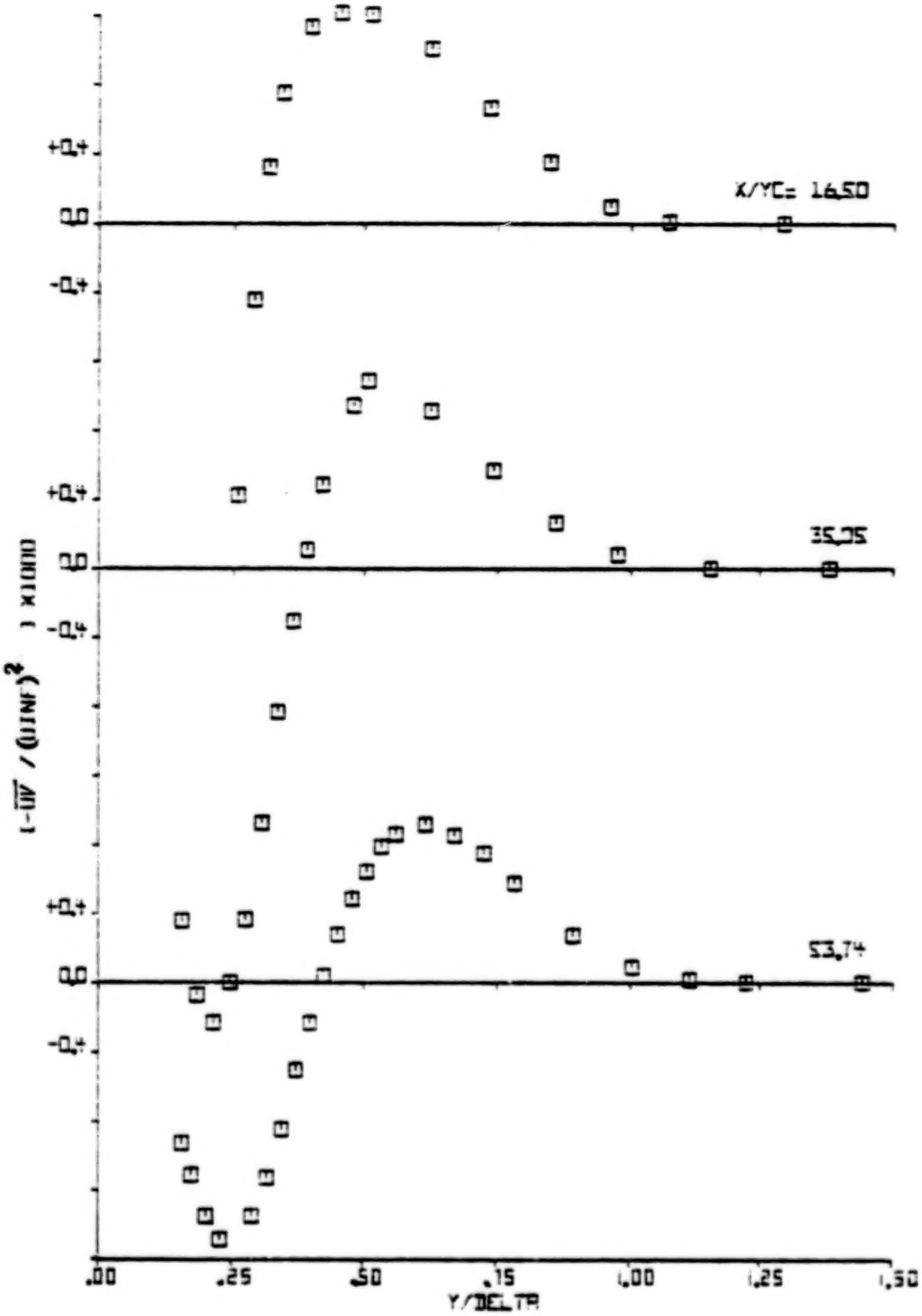

Fig. 4.13(a) Distribution of the Shear Stress at x/y_c = 16.5 to 53.74

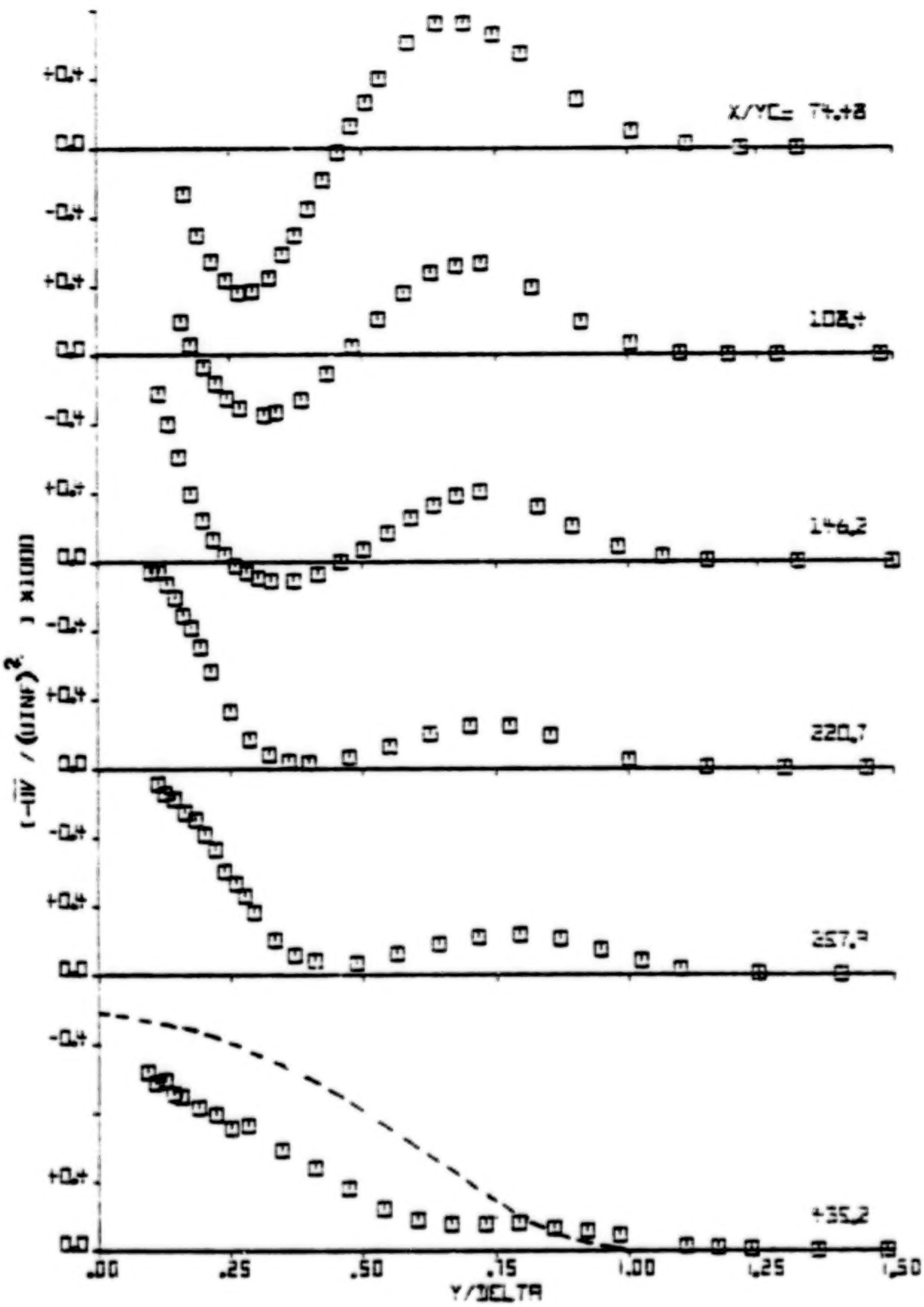

Fig. 4.13(b) Distribution of the Shear Stress at x/y_c = 74.48 to 435.2

---- Shear stress data by Klebanoff (1955) for a turbulent boundary layer on a flat plate (reproduced from Rotta (1962)) with a similar fact reported in the literature on wall jet data.

The velocity maxima and minima cannot be identified beyond $x/y_c = 146.2$. Therefore, the $-\overline{uv}$ profiles beyond $x/y_c = 146.2$ do not show points of zero shear. The points of maximum shear stress between the inner point of zero shear and the freestream were found to be in the region of maximum velocity gradients.

4.3.3 Effect of the Asymmetric Jet Velocity Profile on The Turbulent Quantities

The profiles of u_t, v_t, w_t, and $-\overline{uv}$, at $x/y_c = 435.2$ are compared with those of a turbulent boundary layer on a flat plate by Klebanoff (1955) in Figs. 4.9 (c), 4.11 (b), 4.12 (b), and 4.13 (b) respectively. The present profile of u_t at $x/y_c = 435.2$ is significantly different from that of a flat plate boundary layer. A region of constant u_t can be found in the present data at $x/y_c = 435.2$. The profiles of v_t and w_t at $x/y_c = 435.2$ also differ considerably from those for a flat plate boundary layer. The influence of the jet seems to persist as far as $x/y_c = 435.2$. This was indicated by the departure of the turbulence profiles from that of a flat plate boundary layer. Kacker and Whitelaw's (1968, 1971) experiments show that the distribution of the turbulence intensities approach normal flat plate boundary layer patterns in a much shorter distance for flows similar to the present flow and with a uniform jet velocity profile. This supports the fact that an asymmetric profile carries the influence of the jet to a much longer distance than a uniform jet.

The shape of the $-\overline{uv}$ distribution at $x/y_c = 435.2$ shown in Fig. 4.13 (b) is not comparable to that of the flat plate boundary layer by Klebanoff. The $-\overline{uv}$ drops to a very small value even at $y/\delta = 0.5$, indicating that there are no appreciable velocity gradients beyond $y/\delta = 0.5$. It means that the momentum of the jet is distributed evenly across the layer thereby reducing the momentum deficient region and the large velocity gradients associated with it. This is caused by the asymmetric velocity profile in the jet which mainly distributes the momentum evenly across the layer instead of concentrating it in the region very near the wall as in the case of a uniform jet velocity profile.

Kacker and Whitelaw's (1968, 1971) experiments on flows similar to the present flow show that the $-\overline{uv}$ distribution approaches the present distribution for $x/y_c = 435.2$ at a much shorter distance. This indicates that the flow with a uniform jet velocity profile has a tendency to return to a normal boundary layer pattern at a much shorter distance than an asymmetric profile. Hence, the asymmetric profile carries the jet momentum to a much longer distance than a uniform profile, since one can see the effect of the jet as far as $x/y_c = 435.2$ in the case of asymmetric profile.

4.3.4 Turbulent Kinetic Energy k

Figs. 4.14 (a) and (b) show the distribution of turbulent kinetic energy. The point of maximum kinetic energy coincides with the region of maximum u_t, v_t, and w_t and also the region of maximum velocity gradients. A region of constant turbulent kinetic energy can be seen in the profiles starting from $x/y_c = 53.74$. The turbulent kinetic energy decreases rapidly up to $x/y_c = 53.74$; later on the decrease is more gradual.

4.3.5 Correlation Functions R_{uv} and a_1

The correlation function R_{uv} is defined as $R_{uv} = -\overline{uv}/(u_t\ v_t)$. The correlation function a_1, also called the Bradshaw's turbulence intensity parameter, is defined as $a_1 = -\overline{uv}/(u_t^2 + v_t^2 + w_t^2)$. These two coefficients show the correlation between the different fluctuating components of velocity at the same point. The above correlation functions are very useful in understanding the structure of turbulence. The distributions of R_{uv} and a_1 for the present flow are given below.

4.3.5 (a) Correlation Function R_{uv}

Figs. 4.15 (a) and (b) show the distribution of the correlation function R_{uv} at different stations. This function is either negative or positive depending on the sign of $-\overline{uv}$ and it is zero at the point of zero shear stress. The value of R_{uv} reaches a maximum value lying between

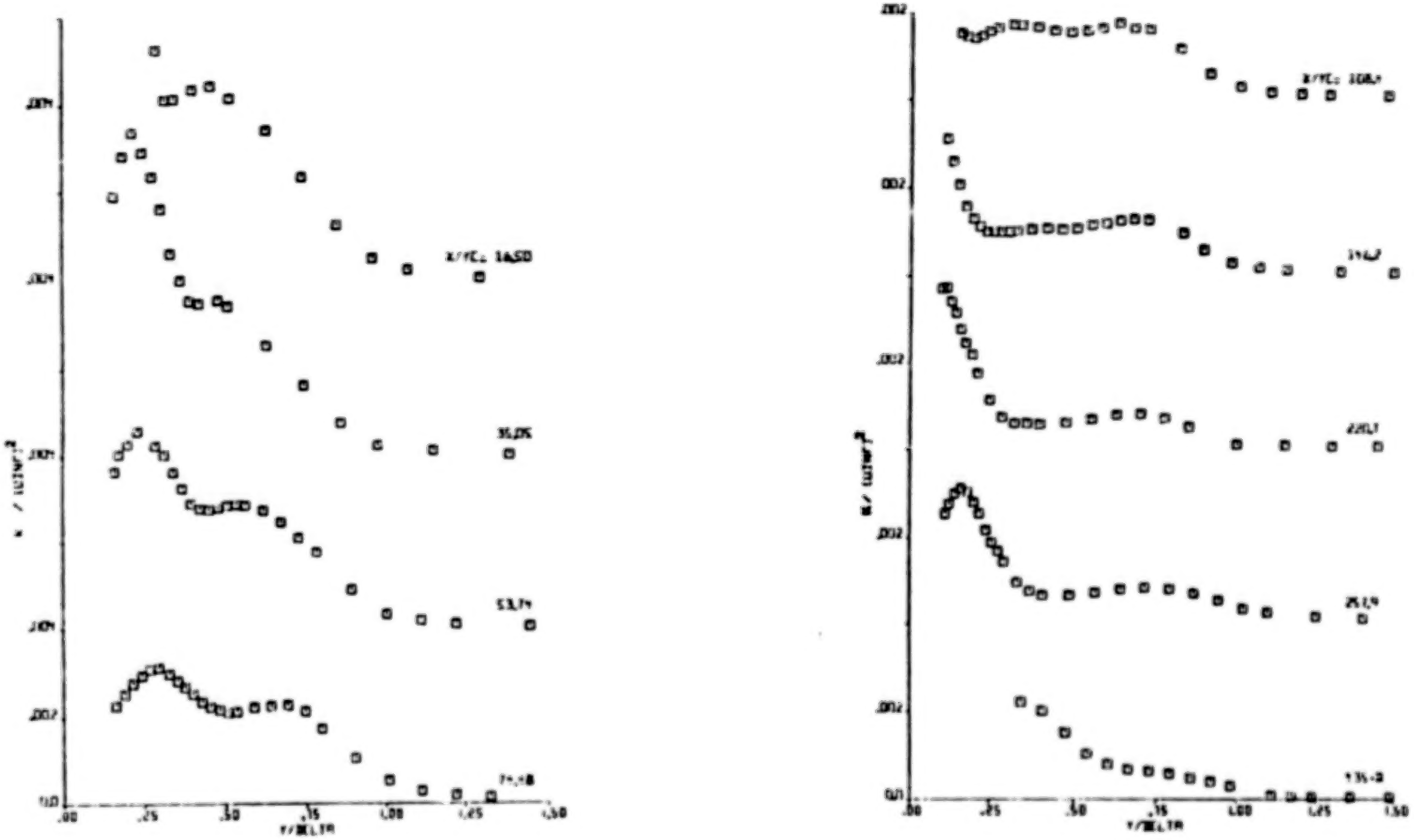

(a)

(b)

Fig. 4.14 Distributions of the Turbulent-Kinetic Energy k

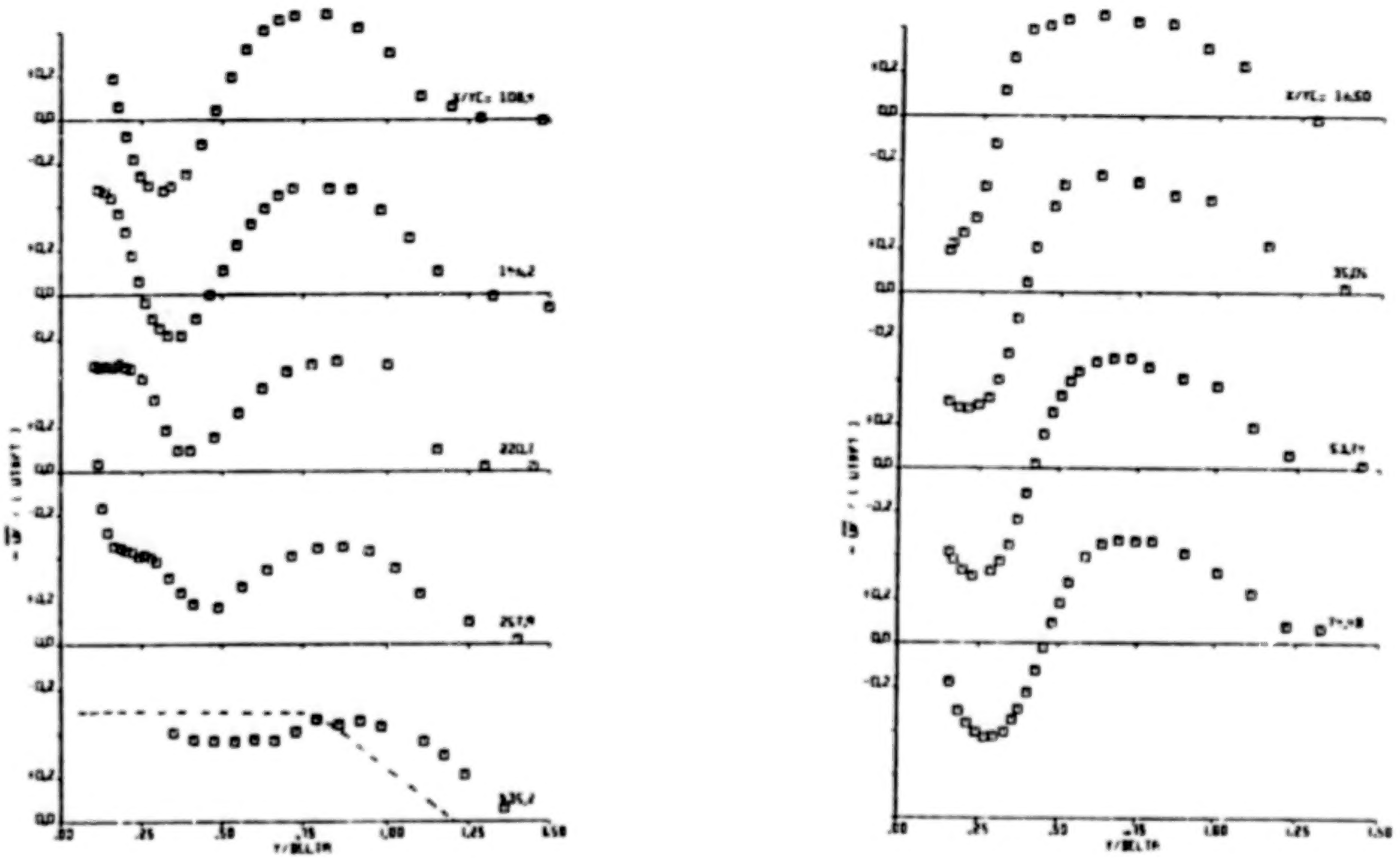

(b)

(a)

Fig. 4.15 Distributions of the Correlation Function R_{uv}

---- R_{uv} data by Klebanoff (1955) for a turbulent boundary layer on a flat plate (reproduced from Rotta (1962))

+0.4 and +0.5 for points beyond the outer point of zero shear. The minimum value of R_{uv} between the inner and outer points of zero shear is around -0.5 to start with, gradually decreasing in absolute value as the value of x/y_c increases. R_{uv} is always positive at $x/y_c = 220.7$ and beyond. At $x/y_c = 435.2$, R_{uv} is nearly a constant varying between +.35 and +.45 up to $y/\delta = 1.0$ and then gradually decreasing to zero in the freestream.

The distribution of R_{uv} at $x/y_c = 435.2$ is compared in Fig. 4.15 (b) with the distribution of R_{uv} for a turbulent boundary layer on a flat plate (Klebanoff, 1955). The distribution of R_{uv} at $x/y_c = 435.2$ is similar in pattern to the turbulent boundary layer on a flat plate. The magnitudes of R_{uv} at $x/y_c = 435.2$ also compare well with those of a flat plate boundary layer.

4.3.5 (b) Correlation Function a_1

Figs. 4.16 (a) and (b) show the distribution of the correlation function a_1. The distribution of a_1 exhibits similar features as in the case of R_{uv}. The value of a_1 becomes zero when the shear stress is zero. The value of a_1 reaches a maximum value ranging between +.15 and +.18 for points beyond the outer point of zero shear. The minimum value of a_1 between the inner and outer points of zero shear is around -0.2 to start with, gradually decreasing in absolute value as x/y_c increases. At $x/y_c = 435.2$,

BLANK PAGE

BLANK PAGE

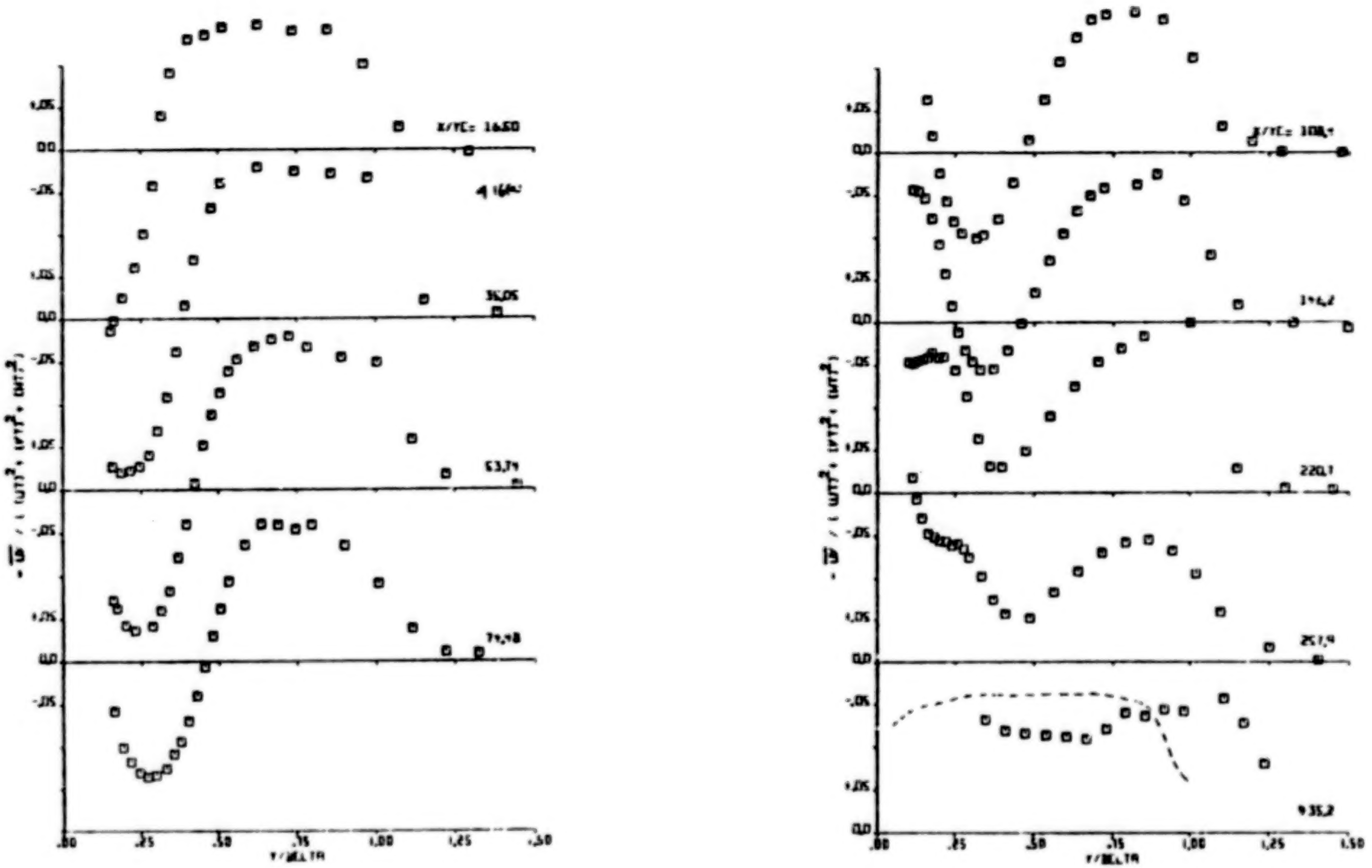

(a) (b)

Fig. 4.16 Distributions of the Correlation Function a_1

---- Distribution of a_1 for a turbulent boundary layer on a flat plate obtained by Hinze (1959) from the data by Klebanoff (1954)

a_1 is nearly a constant, varying between +.11 and +.15 up to $y/\delta = 1.0$ and then gradually decreasing to zero in the freestream. The distribution of a_1 at $x/y_c = 435.2$ is compared in Fig. 4.16 (b) with the distribution of a_1 for a turbulent boundary layer on a flat plate obtained by Hinze (1959) from the data of Klebanoff (1954). The distribution of a_1 at $x/y_c = 435.2$ is similar in pattern to the turbulent boundary layer on a flat plate. The magnitudes of a_1 at $x/y_c = 435.2$ also compare well with those of a flat plate boundary layer.

4.3.6 Eddy Viscosity ν_{eff}

The study of the eddy viscosity distributions is very useful in the development of turbulence models and prediction procedures. Fig. 4.17 (a-c) shows the distributions of eddy viscosity $\nu_{eff} = -\overline{uv}/(\partial U/\partial y)$ non-dimensionalized with $(U_\infty \delta_1)$. The trends of the experimental results are indicated by the dashed lines. It can be easily seen that there is a region of singularity exhibited at each station up to $x/y_c = 146.2$. The eddy viscosity becomes either negative or undefined in these singular regions because of the following reasons.

As mentioned earlier (section 4.3.2 (b)), the points of zero shear do not coincide with the points of maximum or minimum velocity. Therefore, the value of $-\overline{uv}$ is different from zero and $\partial U/\partial y$ is equal to zero at the point of maximum or minimum velocity. Hence the eddy

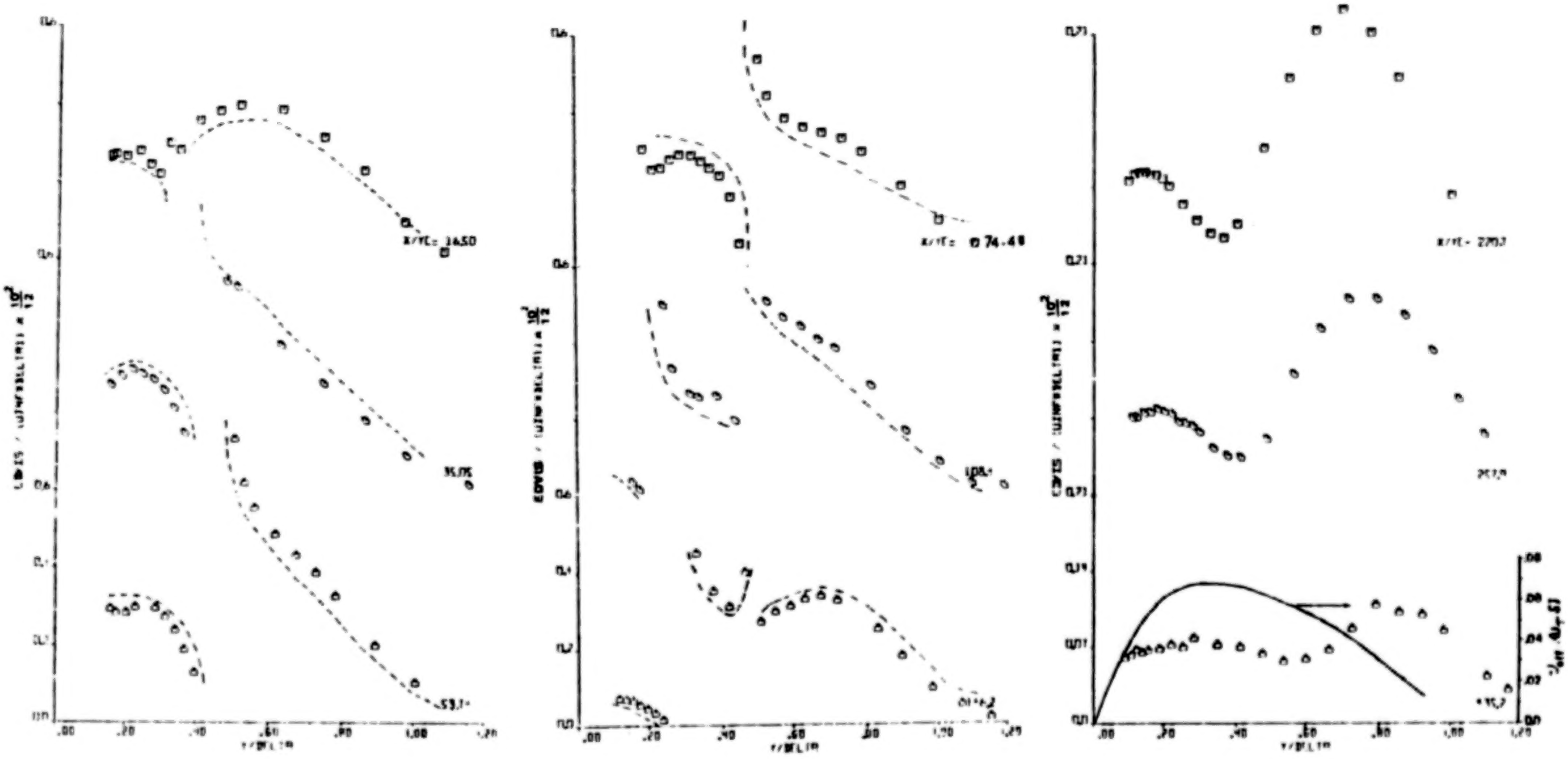

(a) (b) (c)

Fig. 4.17 Distributions of the Eddy Viscosity

---- Trends exhibited by the experimental data

—— Eddy viscosity distribution for a turbulent boundary layer on a flat plate obtained by Hinze (1959) from the data by Klebanoff (1954) viscosity becomes undefined at the point of maximum or minimum velocity. Also, $-\overline{uv}$ and $\partial U/\partial y$ are of different sign in the region between the point of zero shear and the point of velocity maximum or minimum. Hence the eddy viscosity becomes negative there.

The eddy viscosity finally drops to zero in the freestream. The eddy viscosity distributions at $x/y_c = 108.4$ and $x/y_c = 146.2$ exhibit two regions of singularity, as they are the only stations where the slant wire measurements cover both the points of maximum and minimum velocity. The above mentioned features of the eddy viscosity distributions were also observed by Kacker and Whitelaw (1968) in their wall jet experiments.

At $x/y_c = 435.2$, the eddy viscosity is nearly constant over most of the layer up to $y/\delta = 0.6$. The eddy viscosity starts increasing after $y/\delta = 0.6$ and it attains a maximum value near $y/\delta = 0.8$. Afterwards, it gradually goes to zero in the freestream. The eddy viscosity distribution at $x/y_c = 435.2$ is compared in Fig. 4.17(c) with the eddy viscosity distribution for a flat plate turbulent boundary layer obtained by Hinze (1959) from the data of Klebanoff (1954). The residual effect of the jet may be responsible for the different patterns of the eddy viscosity distributions for the flat plate boundary layer and for the present wall jet at $x/y_c = 435.2$. On the whole, there does not seem to be any similarity behavior in the present viscosity distributions.

4.3.7 Length Scales L_{mix} and L_k

Two length scales were calculated from the present measurements. They are the Prandtl mixing Length L_{mix}, defined as $L_{mix} = [\nu_{eff}/(|\frac{\partial U}{\partial y}|)]^{\frac{1}{2}}$ and the Prandtl-Kolmogorov turbulent length scale L_k defined as $L_k = \nu_{eff}/(C_\mu\sqrt{k})$. C_μ is a constant and k is the turbulent kinetic energy equal to $\frac{1}{2}(u_t^2 + v_t^2 + w_t^2)$. Both these length scales are very useful in the prediction methods.

4.3.7 (a) Prandtl Mixing Length L_{mix}

Figs. 4.18 (a-c) show the distribution of the Prandtl mixing length non-dimensionalized with δ. Here also, the singularity can be observed around the points of zero shear as in the case of the eddy viscosity. The trends of the experimental results are indicated by the dashed lines.

At $x/y_c = 16.5$, the mixing length is essentially constant in the outer layer beyond the outer point of zero shear which is due to the effect of upstream boundary layer. Two distinct regions, i.e., the outer and inner regions, can be found in the distributions of L_{mix}. The length scale in the outer region is in general approximately twice that of in the inner region, and this ratio is much higher for $x/y_c = 146.2$ and beyond. At $x/y_c = 435.2$, the value of L_{mix}/δ in the inner region is nearly a constant equal to around 0.04 and in the outer region it is

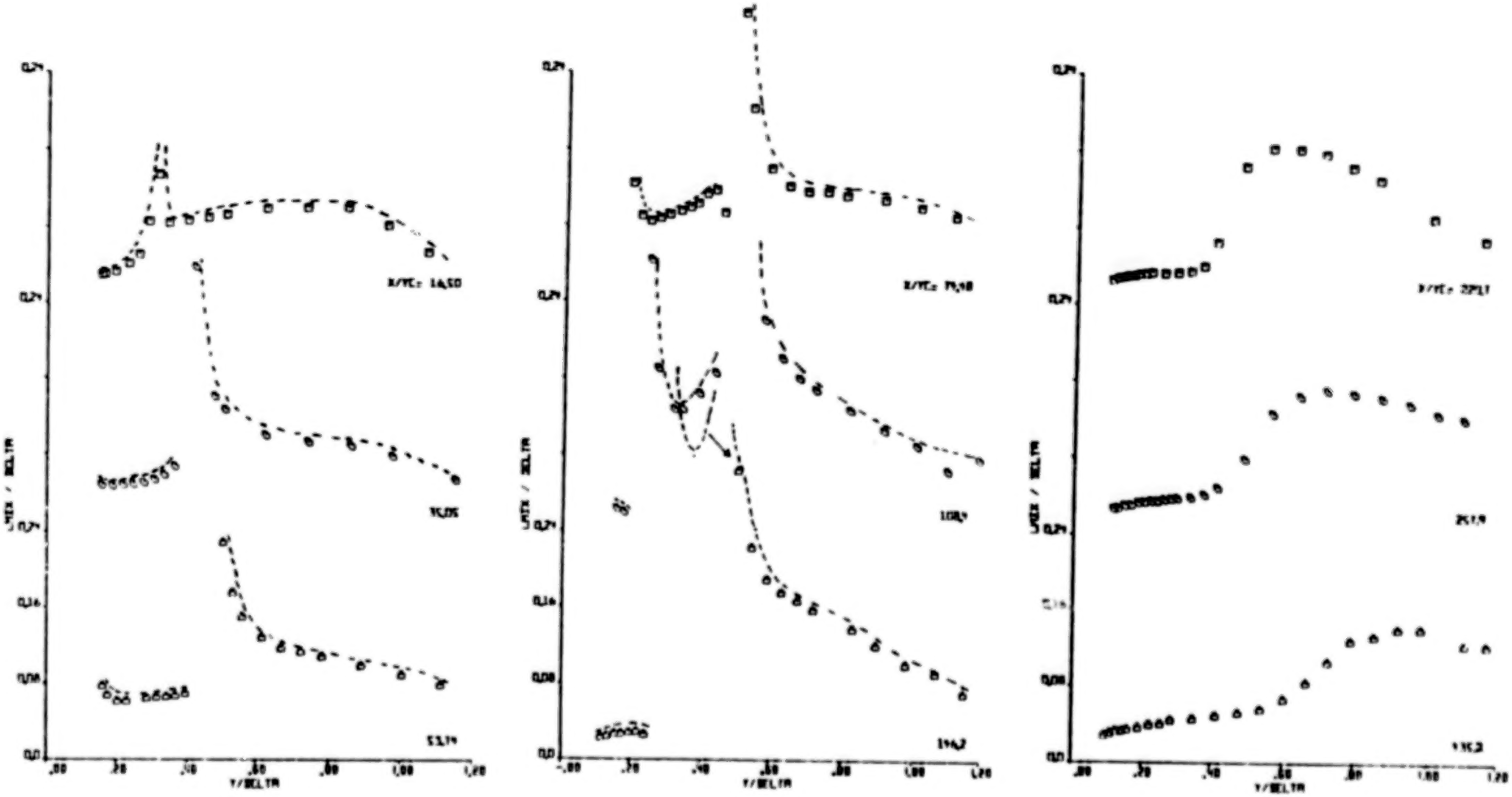

(a) (b) (c)

Fig. 4.18 Distributions of the Prandtl Mixing Length L_{mix}

---- Trends exhibited by the experimental data

around 0.14 with a smooth transition between them. In general the tendency of L_{mix}/δ in the outer region is to approach a uniform value of around 0.08 at higher values of y/δ. However, the value of L_{mix}/δ approaches a uniform value of around 0.12 at $x/y_c = 257.9$ and 435.2 for large values of y/δ. The mixing length distributions do not show any similarity behavior among themselves. Kacker and Whitelaw (1968, 1971) observed similar mixing length distributions in their experiments on wall jets and the order of magnitudes of L_{mix}/δ were found to be the same as the present data.

4.3.7 (b) Prandtl-Kolmogorov Length Scale L_k

Figs. 4.19 (a-c) show the distribution of Prandtl-Kolmogorov length scale L_k, non-dimensionalized with δ. A value of $C_\mu = 0.2$ (Kacker and Whitelaw, 1968, 1971) was used in the evaluation of L_k. The length scale L_k exhibits similar features as the mixing length, except that that magnitude of L_k is different. At $x/y_c = 146.2$ and beyond, the magnitude of L_k in the outer region is about four times that of the inner region. At $x/y_c = 435.2$, the value of L_k/δ is around 0.13 in the inner region and around 0.35 in the outer region with a smooth transition in between them. The Prandtl-Kolmogorov length scale distributions do not show any similarity behavior among themselves. Kacker and Whitelaw (1968, 1971) observed

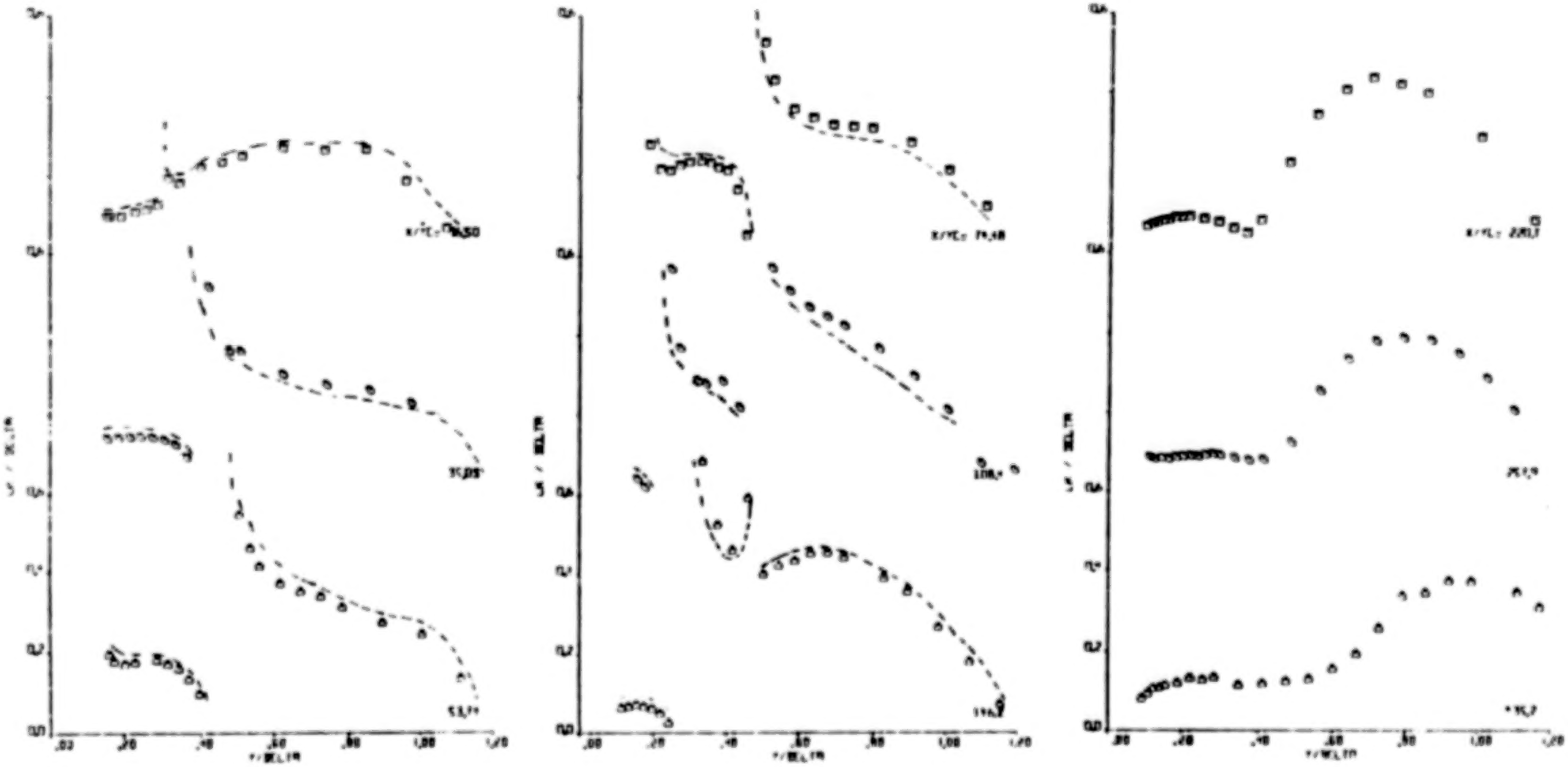

(a) (b) (c)

Fig. 4.19 Distributions of the Prandtl-Kolmogorov Length Scale L_k

---- Trends exhibited by the experimental data

similar Prandtl-Kolmogorov length scale distributions in their experiments on wall jets, and the order of magnitudes of L_k/δ were found to be the same as the present data.

Both the Prandtl mixing length model and the Prandtl-Kolmogorov model fail near the point of zero shear. The length scales L_{mix} and L_k as defined above, become either negative or imaginary around the point of zero shear. This is because ν_{eff} becomes negative around the point of zero shear due to the different signs of the velocity gradient and the shear stress.

Therefore, there is a necessity for a turbulence model that is suitable for wall jets where the point of zero shear and the point of velocity maxima or minima do not coincide. Launder (1969) has proposed an expression for the effective viscosity based on the Prandtl-Kolmogorov model which includes the second order terms like $\partial^2U/\partial y^2$ to take care of the region around the point of zero shear. However, no attempt has been made here to test the applicability of the Launder's expression for the effective viscosity to the present flow.

4.3.8 Production of Turbulent Kinetic Energy

The equation for the conservation of turbulent kinetic energy (Rotta, 1962) involves the advection, production, diffusion and the dissipation terms. A full scale energy balance has not been attempted here. However, an attempt has been made to evaluate the production and dissipation terms in the equation for the turbulent kinetic energy from the present measurements. The dissipation rate is evaluated from spectral measurements and the dissipation results are presented in the next section. The production of turbulent kinetic energy can be divided into normal stress production and the shear stress production. The shear stress production is given by $-\overline{uv}\,\frac{\partial U}{\partial y}$ and the normal stress production is given by $(\overline{u^2} - \overline{v^2})\,\frac{\partial U}{\partial x}$. Both the shear stress and the normal stress production terms were evaluated from the present measurements and the results are shown below.

Figs. 4.20 (a-c) show the distribution of the shear stress production of turbulent kinetic energy given by $-\overline{uv}\,\frac{\partial U}{\partial y}\,(\delta/U_\infty^3)$ on a semi-logarithmic scale. It can be seen here that there are two distinct levels of turbulent energy production corresponding to the inner and outer regions. These two production levels differ by an order of magnitude to start with and they gradually become equal. At $x/y_c = 108.4$, the production level in the region between the two points of zero shear is of the same order of magnitude as in the region beyond the outer point of zero shear. As mentioned earlier (section 4.3.6), there is a small region around the points of zero shear where $-\overline{uv}$ and $\frac{\partial U}{\partial y}$ are of different sign. In this region, the shear stress production becomes negative and these

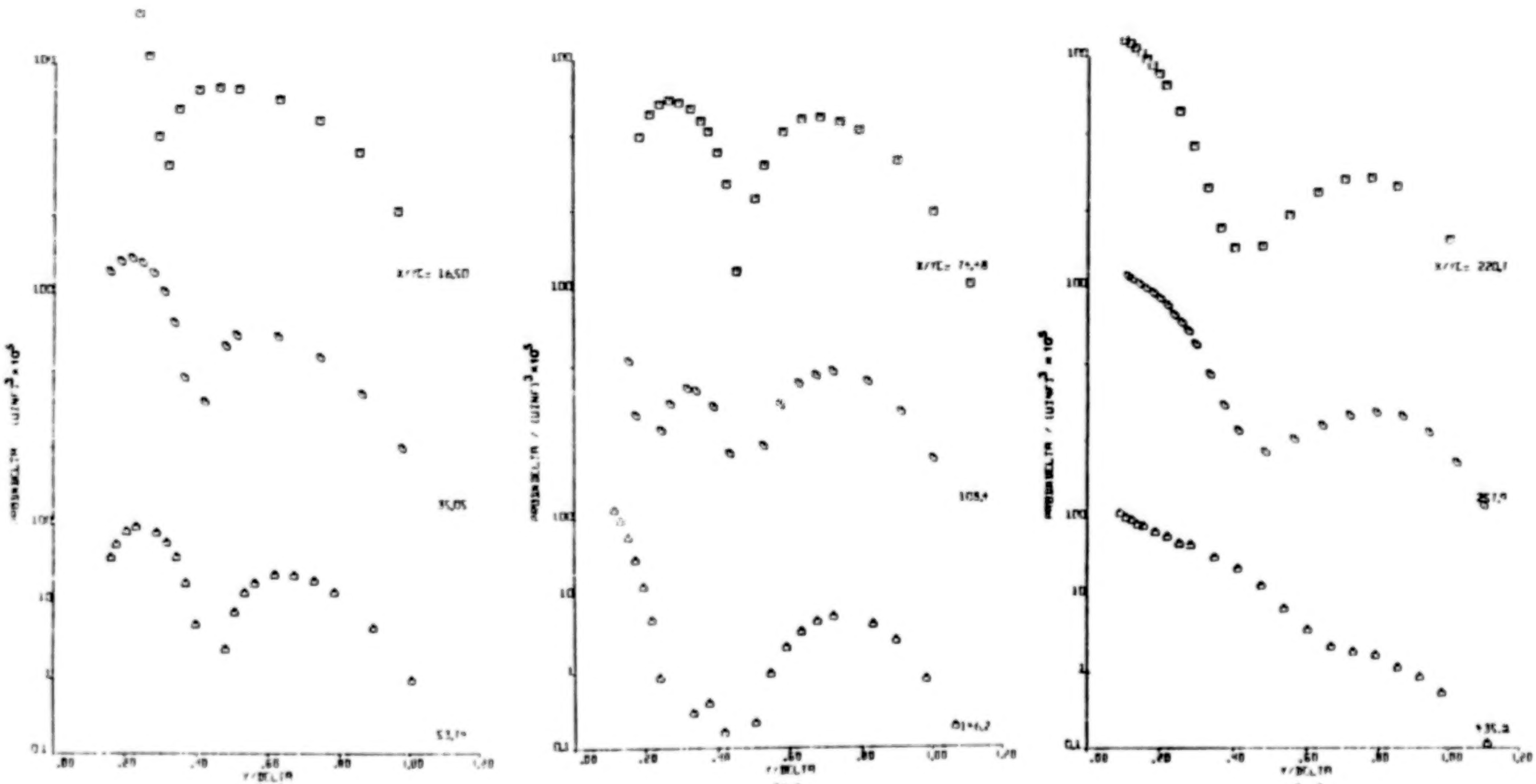

(a) (b) (c)

Fig. 4.20 Distributions of the Shear Stress Production of Turbulent Kinetic Energy

negative production points are not shown in the plots. The negative production terms were found to be in the order of $-\overline{uv}\,\frac{\partial U}{\partial y}\,(\delta/U_\infty^3) = 0.3\text{X}10^{-5}$. At $x/y_c = 146.2$ and thereafter, the slant-wire measurements extend into the layer near the wall and the production is maximum near the wall at those stations. Also, there is a minimum production region representing small velocity gradients for stations $x/y_c = 146.2$, 220.7 and 257.9. For these stations, the production attains a maximum also in the outer region. At $x/y_c = 435.2$, the distribution of shear stress production is almost linear in the semi-logarithmic co-ordinates with a maximum near the wall and the shear stress production gradually decreases to zero in the freestream.

The normal stress production term obtained from the present measurements was generally found to be two orders of magnitude lower than the shear stress production term. The normal stress terms were found to be relatively higher for stations very close to the slot.

4.3.9 Spectra and Dissipation Measurements

The results of the spectral measurements are presented in this section along with the results of the dissipation rate of turbulent kinetic energy and the bursting frequencies.

4.3.9 (a) Spectra Measurements

The spectrum function F(n) of $\overline{u^2}$ is defined as

$$\overline{u^2}\int_0^\infty F(n)\,dn = \overline{u^2}$$

where n is the frequency in Hz. The spectrum function F(n) was obtained at several points across the layer at each streamwise location.

Figs. 4.21, 4.22, and 4.23 show various spectra of $\overline{u^2}$ representing the present flow at various stations. The spectra shown are smooth lines drawn through the experimental curves. Only representative spectra are presented here. F(n) is presented here in the non-dimensional form of N_0 F(n). N_0 is a constant of the spectrum analyser equal to 20 Hz for the 10 KHz range. The magnitudes of N_0 F(n) are not given on the N_0 F(n) axis. The position of each spectrum with respect to the N_0 F(n) ordinate can be fixed with the aid of Table (4.2), showing the magnitude of N_0 F(n) at 1 KHz for each spectrum that is presented in Figs. 4.21, 4.22 and 4.23.

The $\overline{u^2}$ spectra were taken in the present case with two points in view:

1. To find out the range of frequencies where n F(n) is constant, (i.e., $F(n) \propto n^{-1}$) which correspond to the most energetic frequencies and

2. To locate the range of frequencies where $F(n) \propto n^{-5/3}$.

The two points given above lead to the determination of the dissipation rate ε as discussed later in this section.

Figs. 4.21 (a) and (b) show the spectra at x/y_c = 0.292 for different values of y/y_c. It can be seen from

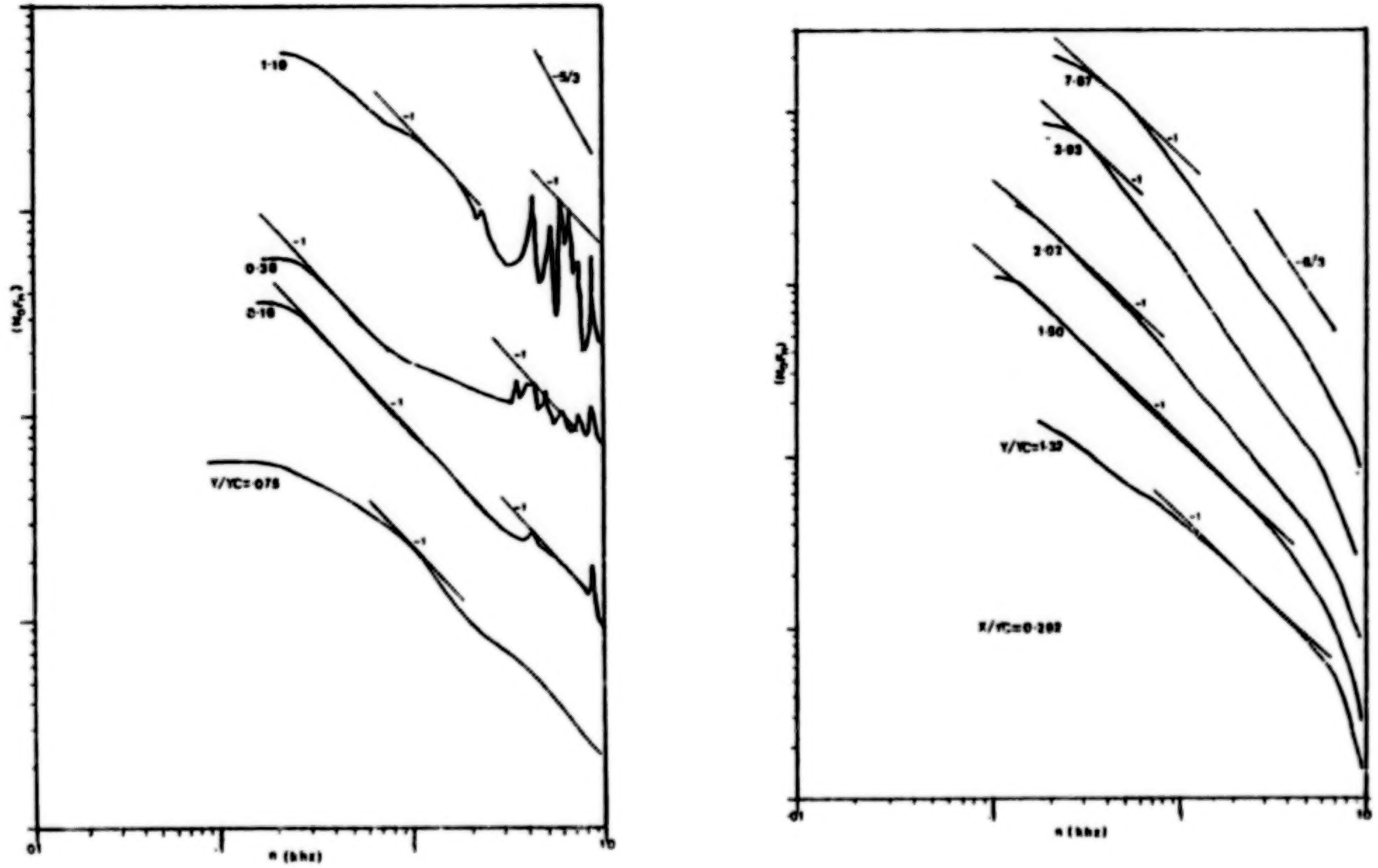

(a)

(b)

Fig. 4.21 Spectra of $\overline{u^2}$ at x/y_c = 0.292 and at Different y/y_c Locations

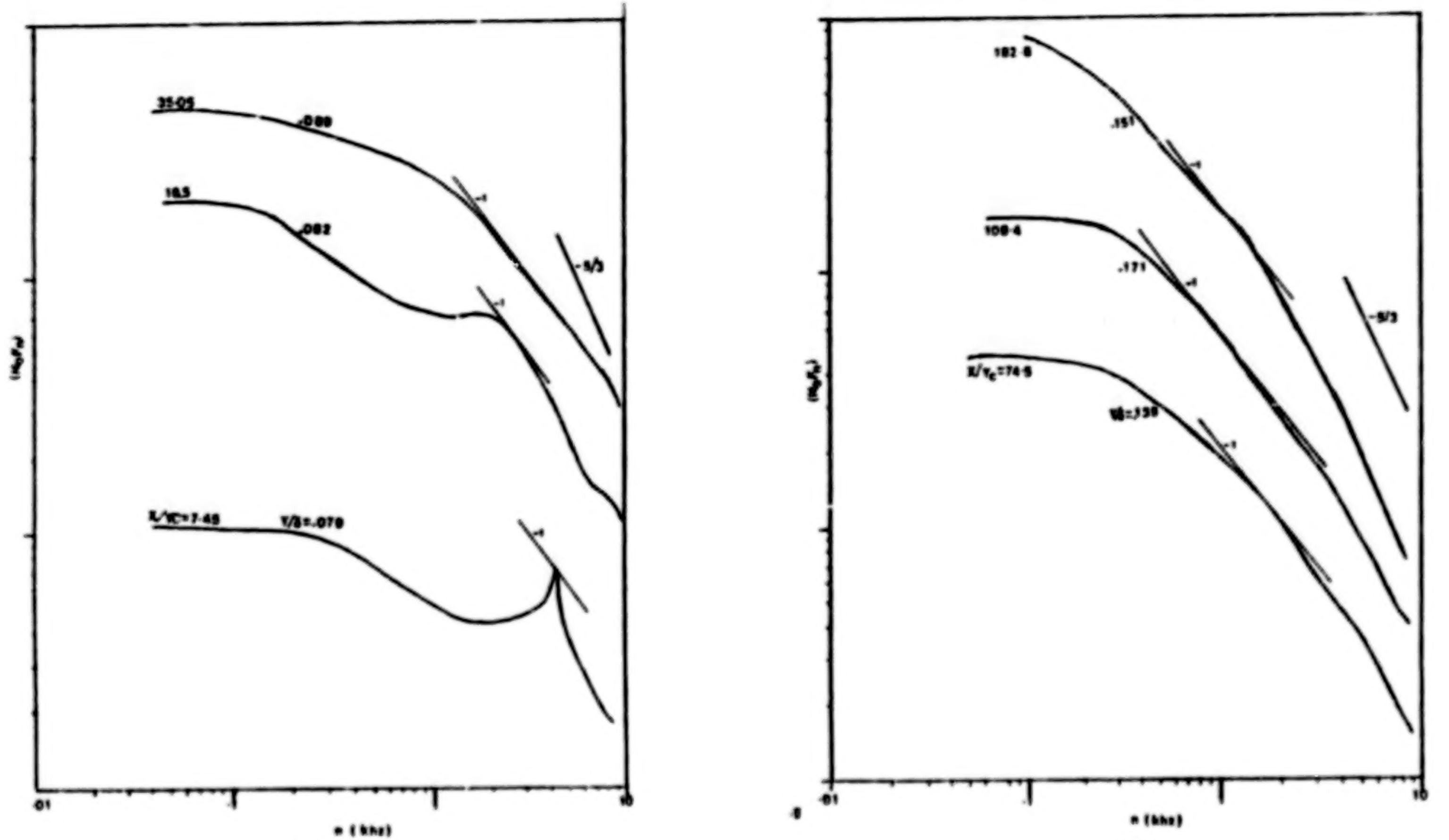

(a) (b)

Fig. 4.22 Spectra of $\overline{u^2}$ Representing the Inner Layer at Different Stations

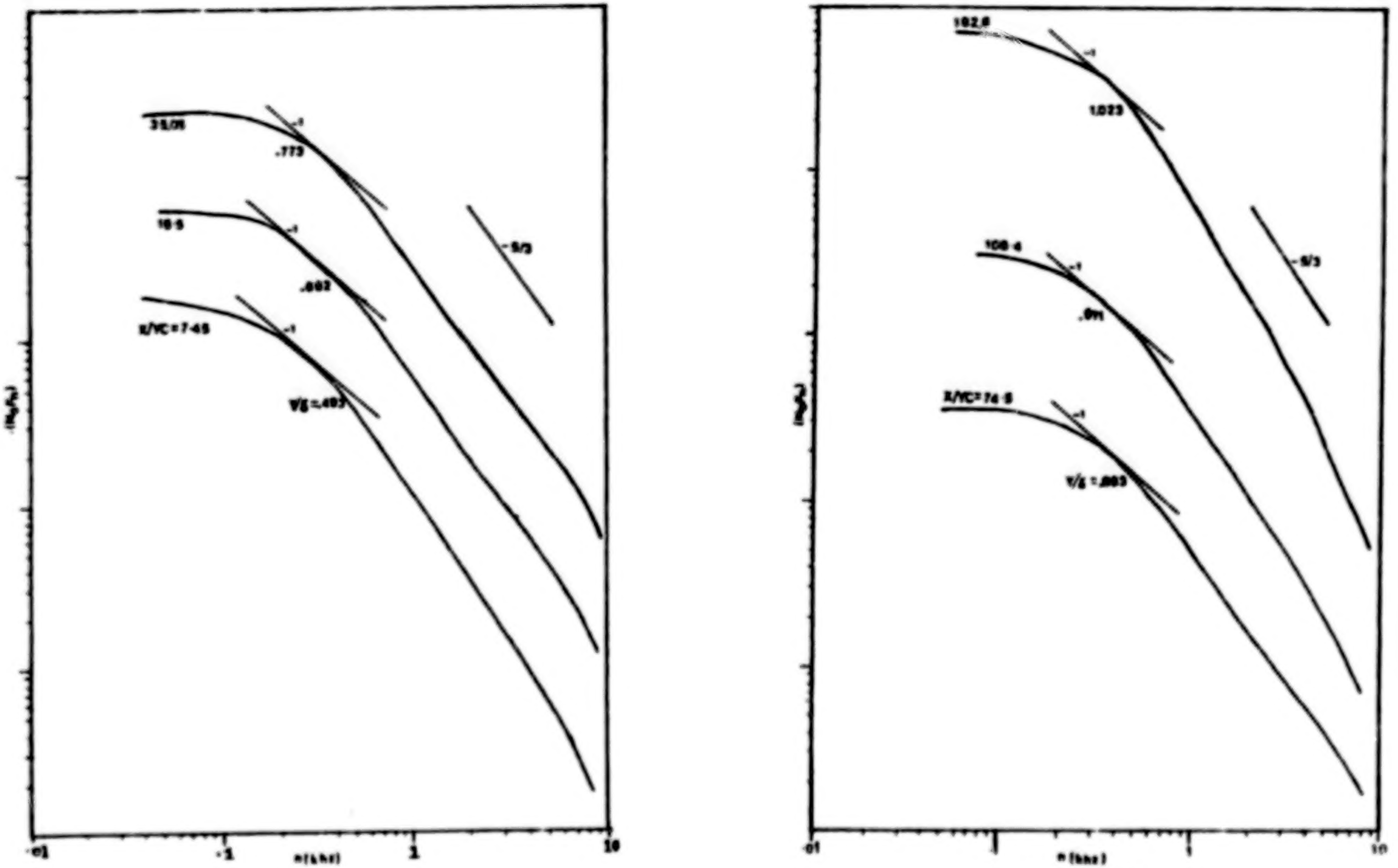

(a)

(b)

Fig. 4.23 Spectra of $\overline{u^2}$ Representing the Outer Layer at Different Stations

125

TABLE 4.2

MAGNITUDES OF N_0 F(n) at 1 KHz FOR THE SPECTRA PRESENTED IN FIGS. 4.21, 4.22, 4.23

Spectra at $x/y_c = 0.292$ (Fig. 4.21)		Spectra Representing the Inner Layer (Fig. 4.22)			Spectra Representing the Outer Layer (Fig. 4.23)		
y/y_c	N_0 F(n) at 1 KHz X 10^3	x/y_c	y/δ	N_0 F(n) at 1 KHz X 10^3	x/y_c	y/δ	N_0 F(n) at 1 KHz X 10^3
0.075	10.56	7.45	0.079	4.56	7.45	0.493	7.04
0.16	7.62	16.5	0.082	7.73	16.5	0.682	7.92
0.38	6.19	35.05	0.089	10.54	35.05	0.773	8.24
1.19	12.73	74.5	0.135	12.64	74.48	0.683	7.20
1.32	9.43	108.4	0.171	10.78	108.4	0.911	11.17
1.50	7.7	182.8	0.151	10.08	182.8	1.023	12.33
2.02	7.55						
3.93	8.12						
7.67	14.65						

Fig. 4.21 (a) that inside the jet a considerable amount of energy was contained in the high frequency range beyond 3 KHz. A series of high frequency peaks were observed very near to the slot lip in the range of 3 to 10 KHz. These peaks diminished away from the lip. One of the spectra taken near the lip has a peak at 756 Hz. This spectrum was not presented here. However, the energy contained in that peak was relatively small compared to the total energy under the spectral curve. As shown in Fig. 4.21 (a), the spectra inside the jet exhibit two ranges of n^{-1} slope. The first range corresponds to the low frequencies below 3 KHz and the second range corresponds to the high frequencies beyond 3 KHz. Beyond the lip, the spectra at $x/y_c = 0.292$ (Fig. 4.21 (b)) are similar to that of a normal turbulent boundary layer representing the upstream boundary layer. The region of n^{-1} slope was in the high frequency range for spectra immediately above the lip corresponding to the wall region of the upstream boundary layer. The energy content of the higher frequencies decreased away from the lip. The -5/3 slope was observed over a greater region of the spectrum for spectra far away in the outer layer.

Fig. 4.22 (a) and (b) show the spectra representing the inner layer at various stations starting from $x/y_c =$ 7.45. A peak was observed at 4.3 KHz for $x/y_c = 7.45$

and at the y/δ indicated. The range of -1 slope slowly shifts from high to low frequencies as one goes downstream in the inner layer. It should be noted that this shift is only relative and from an absolute viewpoint, the range of -1 slope at $x/y_c = 182.8$ in the inner layer still lies on the high frequency side around 1 KHz. The -5/3 slope was found over a greater region in the inner layer spectra at stations farther from the jet than at stations nearer to the jet.

Fig. 4.23 (a) and (b) show the spectra representing the outer layer at various stations starting from $x/y_c = 7.45$. It can be clearly seen that at all stations a considerable region of -5/3 slope exists. The region of -1 slope can be found only in the low frequency range between 200 to 700 Hz.

It has been found in general that more energy is contained in the higher frequencies for the spectra near to the wall. As the value of y increased towards the freestream, the energy content of the higher frequencies decreased. This result is in accord with findings of Klebanoff (1954), for the developed zero pressure gradient turbulent boundary layer. The spectra also indicated that the -5/3 slope is found over a greater region of the spectrum for points away from the wall than close to the wall. This result is also in accord with the findings of

Klebanoff (1954) for the developed zero pressure gradient turbulent boundary layer flow.

4.3.9 (b) Dissipation Rate ε

The dissipation rate of turbulent kinetic energy was estimated from two different methods, the -5/3 spectral law and the Tchen's high mean velocity spectral model (Hinze, 1975). The -5/3 law of the inertial subrange states that

$$\overline{u^2}\, F(n) = K\, \varepsilon^{2/3} \left(\frac{2\pi}{U}\right)^{-2/3} n^{-5/3} \qquad (4.4)$$

where K is a constant equal to 0.49 (Corrsin, 1964; Bradshaw, 1967a) and U is the local mean velocity. The -5/3 law was used to obtain the dissipation rate in places where a clear -5/3 region was found. The same method was used even when clear -5/3 region was not found, by drawing a tangent of appropriate slope to the spectrum. However, the region of -5/3 slope did not exist at all for some spectra near the jet and in the inner layer. No attempt has been made to evaluate ε using -5/3 law in those cases. Bradshaw (1967b) suggested that the turbulence Reynolds number $Re_\lambda = (\overline{u^2})^{1/2} \lambda/\nu$ where $\lambda = (15\nu\overline{u^2}/\varepsilon)^{1/2}$ must be greater than 100 for an inertial subrange to exist. In the present case, $25 < Re_\lambda < 98$ for most spectra where -5/3 region has been found.

Tchen's high mean vorticity model (Hinze, 1975) relates F(n) to the turbulent dissipation ε by

$$\frac{\varepsilon\nu}{U_\infty^4} = \frac{3}{2}\alpha\ [n\ F(n)]\ \frac{\overline{u^2}}{U_\infty^2}\ \frac{\partial f}{\partial \eta} \qquad (4.5)$$

where $f = U/U_\infty$ and $\eta = \frac{U_\infty y}{\nu}$ and α is a constant.

In the present results $\alpha = 0.8$ was used, which is in accord with the value of α for Klebanoff's (1955) flat plate boundary layer. Here the value of nF(n) to be used in the equation (4.5) is the value corresponding to -1 slope.

The dissipation rate ε was also evaluated using the equilibrium relationship

$$\varepsilon = -\overline{uv}\ \frac{\partial U}{\partial y} \qquad (4.6)$$

which naturally holds good only in the logarithmic velocity profile region where turbulence dissipation equals production (Rotta, 1962). The $-\overline{uv}$ measured from slant-wire data was used in this method of evaluating ε.

Figs. 4.24 (a), (b) and (c) show the distribution of $\varepsilon\nu/U_\infty^4$ at various stations starting from $x/y_c = 0.292$. The three different values of ε obtained from the three different methods mentioned above were plotted in these figures. It should be noted that $\varepsilon\nu/U_\infty^4$ is plotted on a full logarithmic scale against y/δ. At points where two ranges of n^{-1} slope have been found, the values of ε obtained from Tchen's theory for the second range corresponding to high frequencies were shown as solid symbols. In general ε has a maximum value near the wall and then

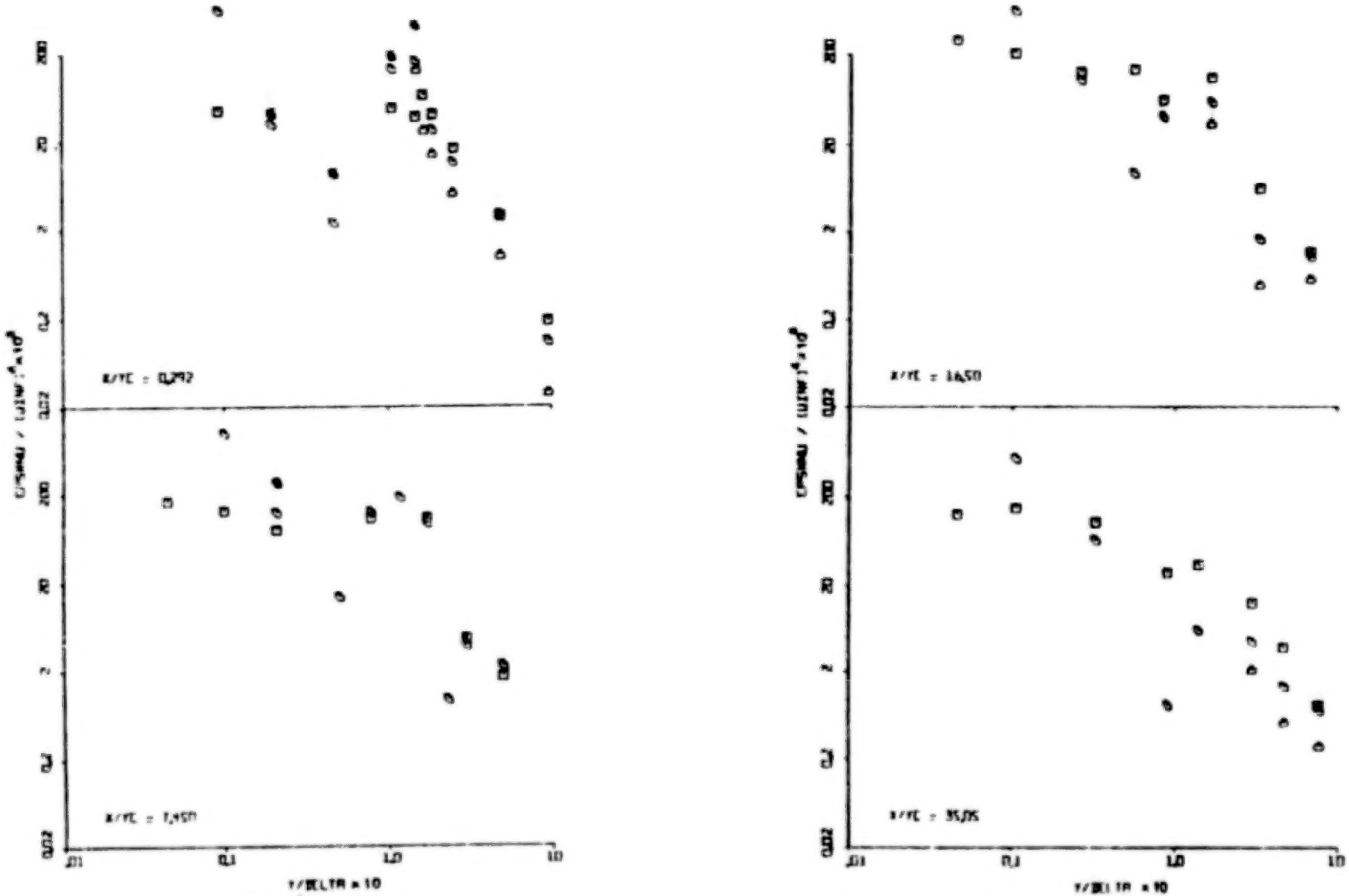

Fig. 4.24(a) Distribution of the Dissipation Rate at x/y_c = 0.292 to 35.05

□ Using -5/3 law
⊘ Using Tchen's Theory
○ Using equilibrium relationship, the solid symbols correspond to the second n^{-1} range (high frequency) in the case of Tchen's Theory

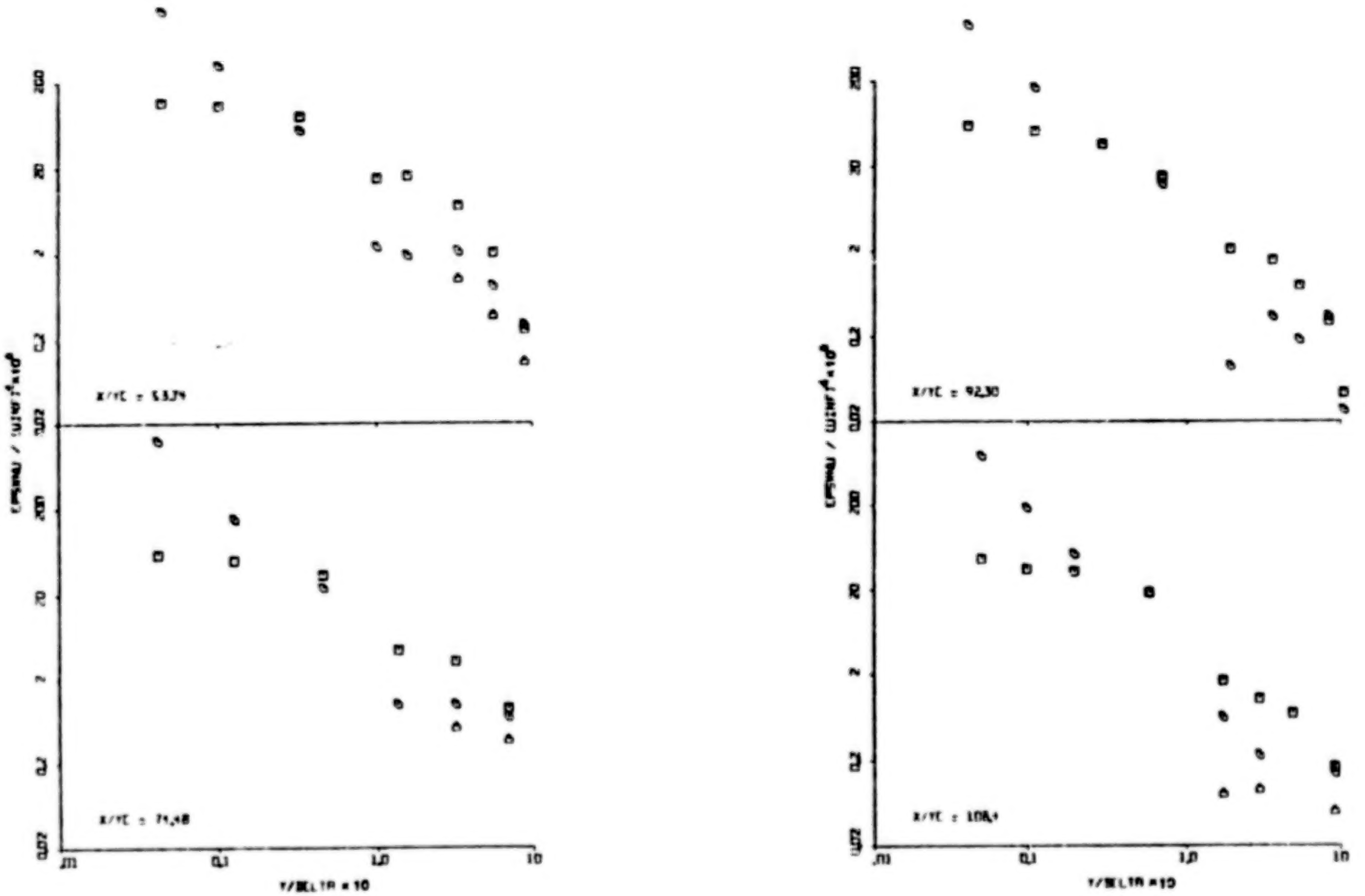

Fig. 4.24(b) Distributions of the Dissipation Rate at x/y_c = 53.74 to 108.4

- □ Using -5/3 law
- ⊘ Using Tchen's Theory
- ○ Using equilibrium relationship

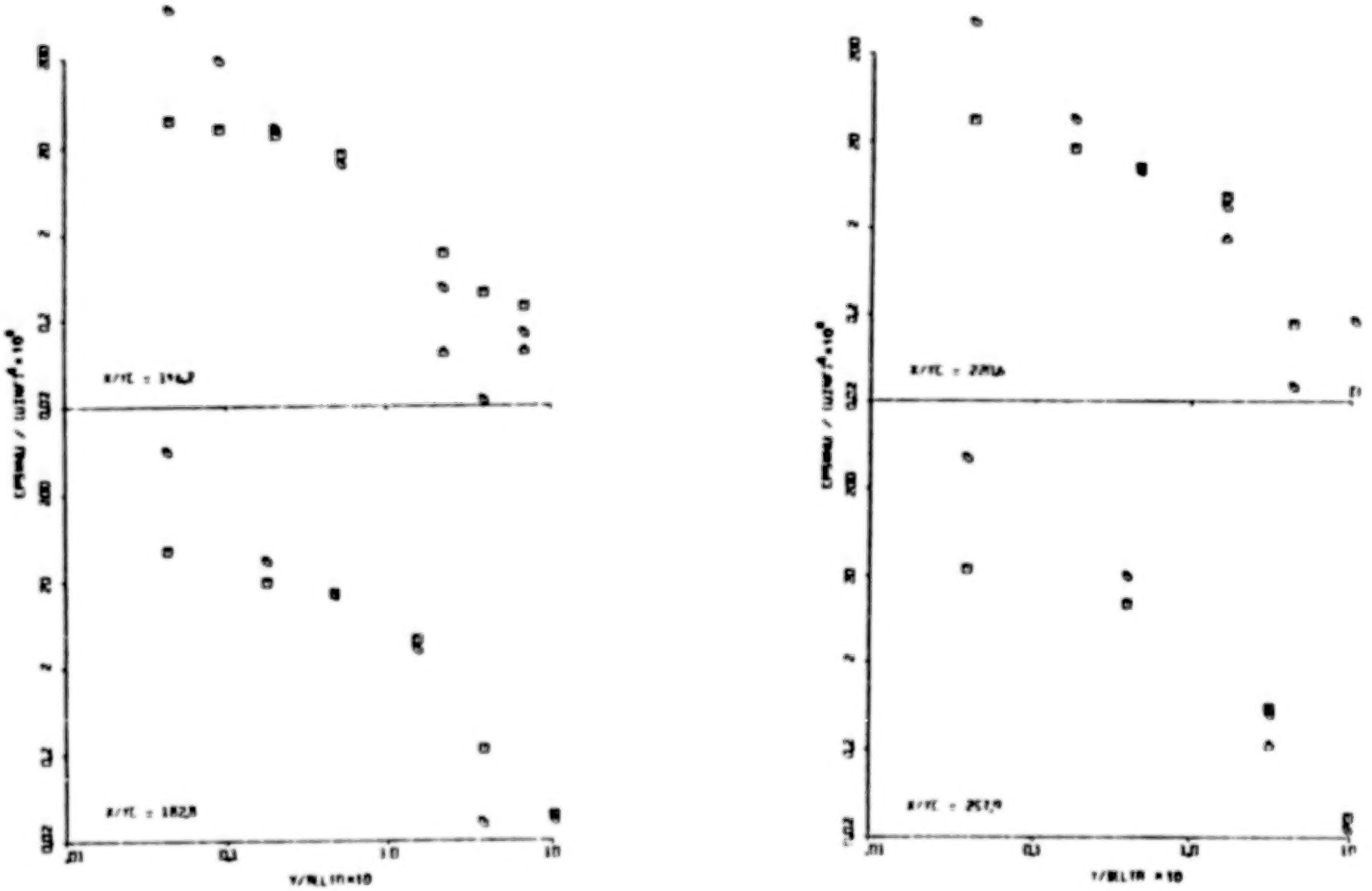

Fig. 4.24(c) Distribution of the Dissipation Rate at x/y_c = 146.2 to 257.9

- ☐ Using -5/3 law
- ⊘ Using Tchen's Theory
- △ Using equilibrium relationship

it decreases rapidly by about three orders of magnitude as one goes towards the freestream. Tchen's theory gives higher values of ε as compared to the -5/3 law at points very near to the wall. Beyond $y/\delta = 0.01$, Tchen's theory agrees very well with the -5/3 law although there is some scatter in the far region of the outer layer. This region where Tchen's theory agrees with the -5/3 law generally corresponded with the logarithmic region in the velocity profile.

The equilibrium assumption between production and dissipation was generally found to give lower value of ε than either Tchen's theory or the -5/3 law. However, most of the slant wire data used in the evaluation of ε using equilibrium assumption were taken beyond $y/\delta = 0.1$ where no logarithmic velocity profile exists and the validity of the equilibrium assumption there is doubtful.

The dissipation length scale $L_\varepsilon = k^{3/2}/\varepsilon$ was calculated using the value of ε obtained from the -5/3 law. Here k is the turbulent kinetic energy. No definite pattern has been observed in the distribution of L_ε. However, it starts with a low value in the inner region and gradually increases as one goes towards the freestream.

4.3.9 (c) Bursting Frequency

Strickland and Simpson (1973, 1975) have shown that there is a one to one correspondence between the bursting frequency of wall shear stress spectra in the turbulent boundary layer and the peak of the nF(n) spectral distribution. This principle is used in the present case to obtain the bursting frequencies across the layer. However, most of the spectra taken here have shown a range of frequencies where -1 slope is valid instead of a defined peak. Therefore, it is difficult to select a precise single frequency at which nF(n) is a maximum for a given spectral distribution. Hence the bursting frequency was chosen as the frequency corresponding to the center of the range of frequencies over which -1 slope is valid.

The bursting frequency was normalized with U_∞ and δ giving rise to a non-dimensional bursting period $U_\infty/n_b\delta$, where n_b is the bursting frequency. Figs. 4.25 (a), (b) and (c) show the distributions of the bursting period in semi-logarithmic co-ordinates. For spectra where two ranges of -1 slope have been observed, the bursting periods for the second range corresponding to the high frequencies were shown as solid symbols. It can be seen that the bursting period starts with a value lying between 0.5 and 2.0 for points very close to the wall ($y/\delta < .01$) and then decreases rapidly to about half of its starting value at a point somewhere in between $y/\delta = 0.01$ and $y/\delta = 0.1$. After $y/\delta = 0.1$, the bursting period increases rapidly to values up to 4.0. This means that in the inner layer most of the energy is contained in the high frequency range. In comparison, the outer layer

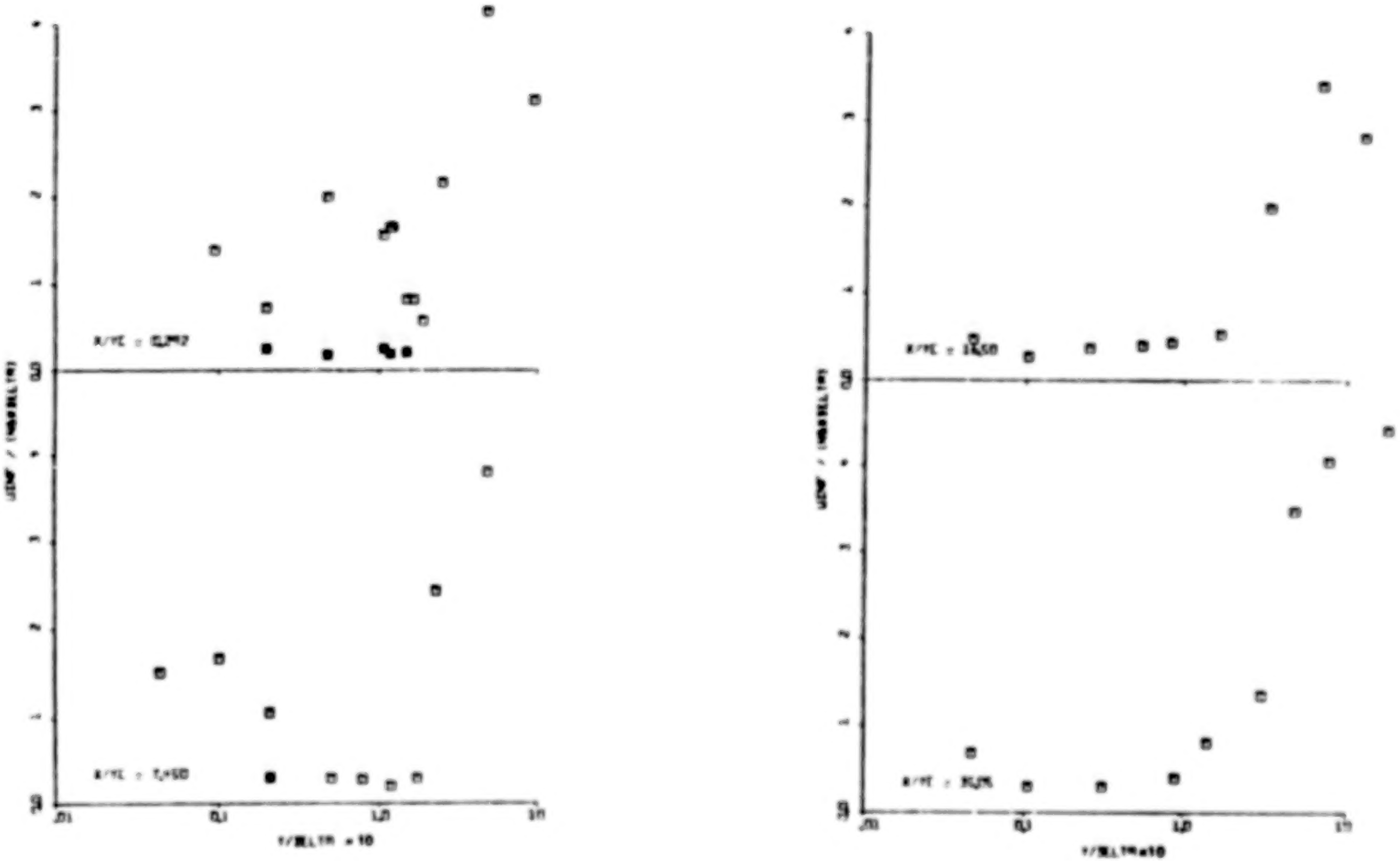

Fig. 4.25(a) Distribution of the Bursting Period at x/y_c = 0.292 to 35.05

The solid symbols correspond to the second n^{-1} range (high frequency)

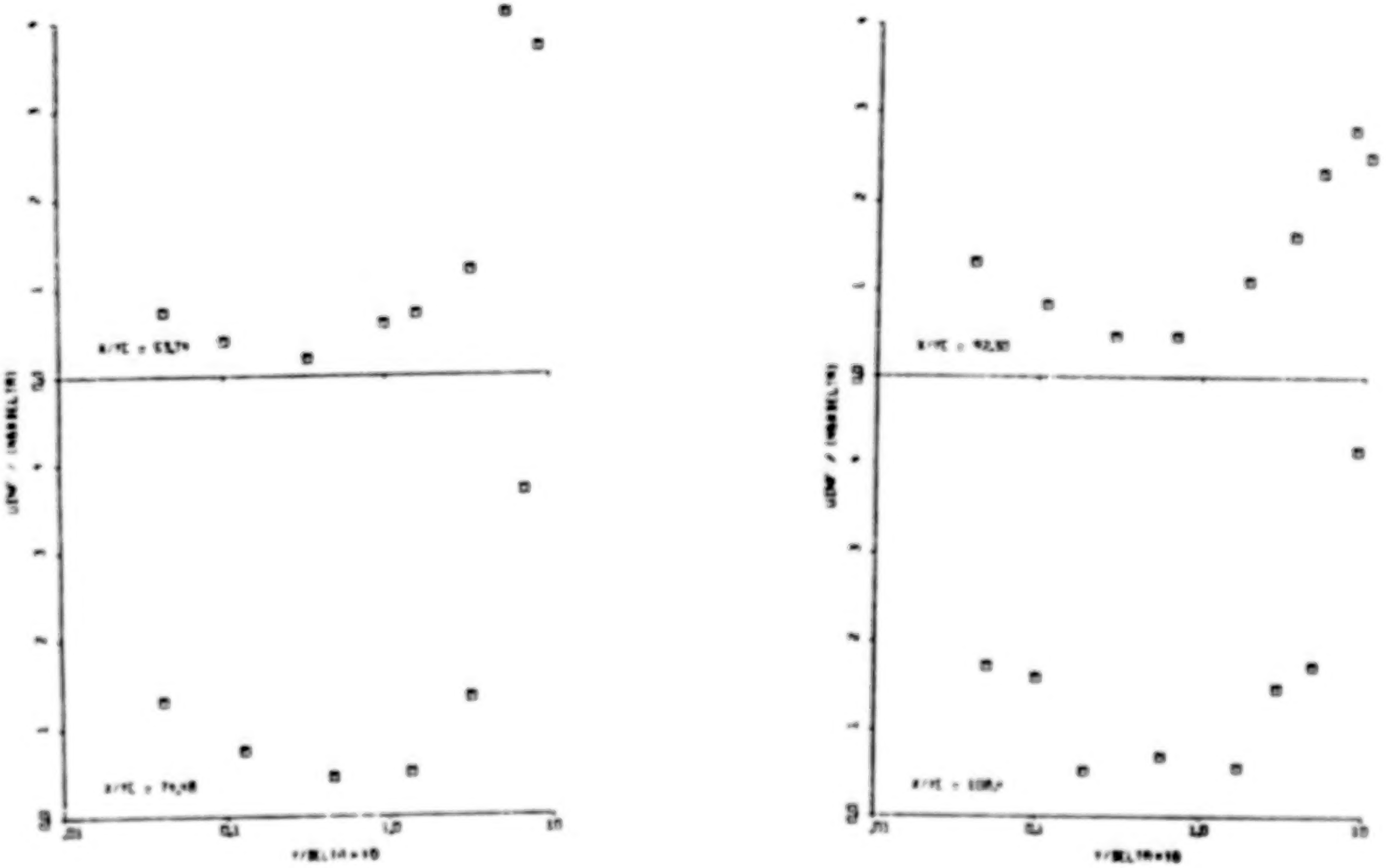

Fig. 4.25(b) Distribution of the Bursting Period at x/y_c = 53.74 to 108.4

TABLE OF CONTENTS

LIST OF FIGURES . . . . vii 1/A12

LIST OF TABLES . . . . xiv 1/B5

NOMENCLATURE . . . . xv 1/B6

Chapter

I. INTRODUCTION 1 1/B12

1.1 Previous Work 2 1/B13

1.2 Asymmetric Jet Velocity Profile 9 1/C7

1.3 Objectives of the Thesis 11 1/C10

1.4 Outline of Thesis 12 1/C11

II. EXPERIMENTAL APPARATUS 15 1/C14

2.1 Description of the Wind Tunnel Components 15 1/C14

Heat exchanger
Blower system
Plenum chamber
Transition section
Test section

2.2 Description and Performance of the Wall Jet Flow System 27 1/D13

Air supply system
Wall jet assembly
Performance of the wall jet

III. INSTRUMENTATION 49 1/F12

3.1 Pitot Probes and Preston Tubes 49 1/F12

3.2 Hot-wire probes 51 1/G1

Slant-wire rotating mechanism
Traversing mechanism

3.3 Electronic Signal Processing 56 1/G6

3.4 Calibrations 56 1/G6

3.5 Uncertainties in the Measurements . . . 57 1/G7

IV. EXPERIMENTAL RESULTS FOR THE ZERO PRESSURE GRADIENT FLOW 59 1/G9

4.1 Flow Conditions 60 1/G10

4.2 Mean Flow Data 64 2/A5
- Skin friction C_f
- Mean velocity U
- Integral parameters
- Effect of the asymmetric jet velocity profile on the mean flow
- Profile parameters

4.3 Turbulence Data 89 2/C5
- Turbulence intensity u_t/U_∞
- Turbulence intensities v_t/U_∞, w_t/U_∞ and shear stress $-\overline{uv}$
- Effect of the asymmetric jet velocity profile on the turbulent quantities
- Turbulent kinetic energy k
- Correlation functions R_{uv} and a_1
- Eddy viscosity ν_{eff}
- Length scales L_{mix} and L_k
- Production of turbulent kinetic energy
- Spectra and dissipation measurements

V. EXPERIMENTAL RESULTS FOR THE ADVERSE PRESSURE GRADIENT FLOW 140 3/A8

5.1 Flow Conditions 141 3/A9

5.2 Mean Flow Data 147 3/B2
- Skin friction C_f
- Mean Velocity U
- Integral parameters
- Effect of the asymmetric jet velocity profile on the mean flow
- Profile parameters

5.3 Turbulence Data 167 3/C12
Turbulence intensity u_t/U_∞
Turbulence intensities v_t/U_∞, w_t/U_∞ and the shear stress $-\overline{uv}$
Turbulent kinetic energy k
Correlation functions R_{uv} and a_1
Eddy viscosity
Mixing length L_{mix} and Prandtl-Kolmogorov length scale L_k
Production of turbulent kinetic energy

VI. PREDICTION METHOD 192 3/F1

6.1 Selection of the Prediction Method 192 3/F1

6.2 Description of the Theoretical Method 194 3/F3
Turbulence model
Computational procedure
Starting procedure

VII. COMPUTED RESULTS 205 3/F14

7.1 Prediction of the Zero Pressure Gradient Flow 206 3/G1
Computations using the experimental initial velocity and turbulence profiles
Computations using the automatic starting procedure

7.2 Predictions of the Adverse Pressure Gradient Flow 216 3/G11
Computations using experimental initial profiles of velocity and turbulence
Computations using the automatic starting procedure

7.3 Comparison of the Performance of Linear and Uniform Jet Velocity Profiles 232 4/B3
Selection of the parameter a
Starting turbulence profiles
Prediction results

VIII. CONCLUSIONS 249 4/C8

APPENDIX A. MEASUREMENTS ON A WALL JET BY BOWLES (1977) 252 4/C11

APPENDIX B. ESTIMATION OF THE FRICTIONAL LOSSES IN THE WALL JET NOZZLE 255 4/C14

APPENDIX C. MEASUREMENT OF THE TURBULENCE INTENSITIES AND THE REYNOLDS SHEAR STRESS 259 4/D4

APPENDIX D. NORMAL HOT-FILM DATA FOR THE ZERO PRESSURE GRADIENT FLOW 272 4/E4

APPENDIX E. SLANT-WIRE DATA FOR ZERO PRESSURE GRADIENT FLOW 279 4/E14

APPENDIX F. NORMAL HOT-FILM DATA FOR ADVERSE PRESSURE GRADIENT FLOW 286 4/F13

APPENDIX G. SLANT-WIRE DATA FOR ADVERSE PRESSURE GRADIENT FLOW 291 4/G9

LIST OF REFERENCES 294 4/G14

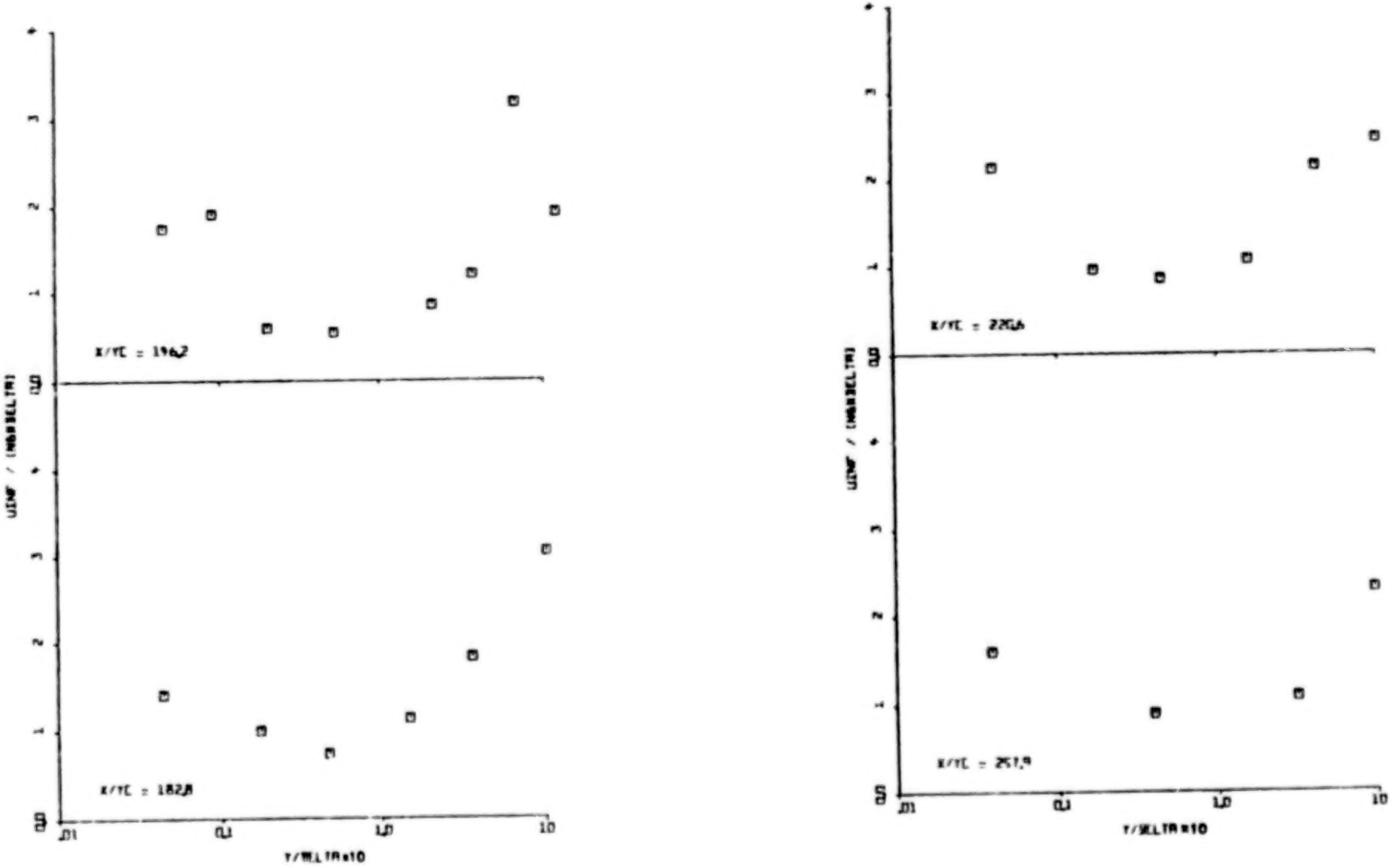

Fig. 4.25(c) Distribution of the Bursting Period at x/y_c = 146.2 to 257.9

has the most energetic frequencies in the low frequency range. However, within the inner layer two ranges of bursting frequencies can be found, one being for points very close to the wall ($y/\delta < .01$) and the other for points lying between $0.01 < y/\delta < 0.1$.

It was mentioned above that the bursting period in the region $.01 < y/\delta < 0.1$ was found to be half of its value for points very close to the wall ($y/\delta < .01$). The region $0.01 < y/\delta < 0.1$ corresponds to approximately $20 < y^+ < 300$ where $y^+ = \frac{U_\tau y}{\nu}$. The first spectral data point for most of the stations corresponds with a y+ value approximately equal to 9 and was taken at the closest possible distance from the wall. Therefore, the bursting period for points lying between $20 < y^+ < 300$ is half of that at $y^+ \approx 9$. This is in agreement with a similar result for plane turbulent boundary layer by Ueda and Hinze (1975).

At $x/y_c = -77.1$, the bursting periods for $y^+ \approx 10.0$ and $y^+ \approx 95.0$ were found to have values around 4.8 and 2.3 respectively. These bursting periods for the upstream boundary layer at $x/y_c = -77.1$ also agree with those reported by Ueda and Hinze (1975) for a plane turbulent boundary layer.

CHAPTER V

EXPERIMENTAL RESULTS FOR THE ADVERSE PRESSURE GRADIENT FLOW

The experimental results for the adverse pressure gradient flow are presented in this chapter. The objectives of the experiments are:

1. To obtain experimental data on a wall jet under an adverse pressure gradient with a thick upstream boundary layer and with a low jet velocity ratio;

2. To obtain turbulence data on such a wall jet flow for future use in the development of turbulence models; and

3. To further observe the effect of an asymmetric jet velocity profile on the flow development downstream of the slot under an adverse pressure gradient.

The measured quantities presented here are the mean velocity, Reynolds stresses, and skin friction. The derived quantities presented include the integral and profile parameters, eddy viscosity, mixing length, Prandtl-Kolmogorov length Scale, turbulent kinetic energy, correlation coefficients and the rate of production of turbulent kinetic energy. A brief description of the flow conditions is first given, followed by the presentation of the measured and derived experimental results.

5.1 Flow Conditions

The selection of the required adverse pressure gradient and the method of setting the pressure gradient are described below in detail.

One of the important considerations in selecting the proper pressure gradient or the external velocity distribution was that it should represent a typical free-stream velocity distribution that occurs in practice such as on aerofoils and jet flaps. An external velocity distribution which has a steep decrease in velocity initially followed by a more gradual decrease is generally typical of the external velocity distributions on aerofoils and jet flaps (Irwin, 1974). The external velocity falls between 0.6 and 0.3 of its value at the slot in normal external velocity distributions on jet flaps (Irwin, 1974). The other considerations in selecting the proper pressure gradient were:

1. To keep the ratio of the jet velocity to the free-stream velocity around 1.5 because it falls in the practical working range, especially for high speed flows;

2. To have the most severe pressure gradient that the flow can withstand without flow reversal at the above mentioned ratio of the jet velocity to the free-stream velocity.

The strength of the pressure gradient can be increased by increasing the level of the static pressure inside the tunnel. One can easily see that the higher the static pressure level inside the tunnel, the greater is the amount of flow through the perforations in the top wall and hence the stronger is the perssure gradient. However, the capacity of the blower limits the static pressure level that can be maintained inside the tunnel without drastically reducing the free-stream velocity at the slot.

In order to satisfy the above requirements, a trial and error method had to be adopted to set up the proper pressure gradient. The flow through the perforated top wall was tailored by adding or removing duct tape of proper width uniformly across the upper wall of the tunnel at several streamwise locations. The perforated top wall was completely covered with the duct tape from the contraction exit to the slot. Also, the last 51 cm of the top wall was completely covered with duct tape. The height of the top wall (Fig. 5.1) above the bottom wall was approximately the same as that for the zero pressure gradient case except that it slightly increases with distance in the downstream direction. This gradual increase in the height of the top wall continues the process of reducing the free-stream velocity even after the flow bleeding stops in the last 51 cm of the tunnel

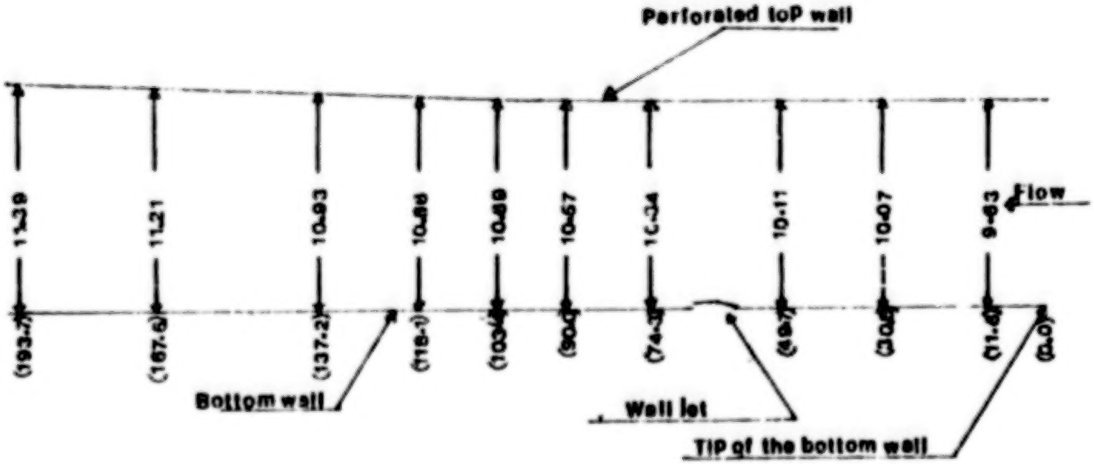

Perforated top wall
11.39
11.21
10.93
10.86
10.80
10.67
10.34
10.11
10.07
9.83
Flow
(193.7)
(167.6)
(137.2)
(118.1)
(0.0)
Bottom wall
Wall jet
Tip of the bottom wall

Fig. 5.1 Position of the Top Wall for the Adverse Pressure Gradient Flow

(All dimensions are in cm. The numbers in the brackets are the distances measured from the tip of the bottom wall near the end of the contraction.)

length. The static pressure level inside the tunnel was tailored by blocking the perforations in the end plate with a duct tape.

Flow visualization studies were first performed using dried tea leaves and tufts to observe flow reversal for a given distribution of the duct tape on the top wall and the end plate. These studies have shown that the sidewall boundary layers were separating and prevention of it became the main concern. The side wall boundary layers were then sucked off by using false plexiglas side walls with a sharp leading edge. These false side walls are 4.8 mm in thickness and are attached to the aluminum angle that reinforces the top wall. The bottom edges of the false side walls were sealed against the bottom wall with foam weather strip. The distance between the false side walls was 19.4 cm compared to the distance of 24 cm between the glass side walls. The false side walls start at 21 cm from the slot and extend all the way to the end of the tunnel. The flow between the false side walls and the actual glass side walls was bled from the top wall through 13 cm long openings located at 95 cm from the slot and on either side of the center of the tunnel. The remaining portions of the top wall between the false and actual side walls was completely covered with duct tape. Upstream of the false side wall, the duct tape strips extended across the tunnel from one glass side wall to the other.

At this stage, several trials were made with the distribution of the duct tape on that portion of the top wall where the main flow was being bled and on the end plate. These trials were made in view of the three important considerations mentioned at the beginning of the chapter. Flow visualization studies were simultaneously made with tufts to observe any flow reversal. Figs. 2.2 and 2.4 show the final positions of the duct tape on the top wall and the end plate respectively. After fixing all the different parameters involved, the wall jet velocity was increased slightly to prevent any flow separation due to the flow blackage by the measuring probes.

The final free-stream velocity at the slot was approximately 18.3 m/sec and the maximum velocity in the wall jet velocity profile was 30.4 m/sec. The wall jet velocity was kept constant during the experiments by keeping a constant static pressure difference between the inside of the jet nozzle and the freestream at the slot. The free-stream velocity at different x locations was calculated from the static pressure measurements in the freestream, assuming that the total pressure was constant along a streamline in the freestream. The final free-stream velocity distribution along the tunnel is given in Fig. 5.2 There is a steep decrease in the external velocity initially followed by a more gradual decrease. The external velocity fell to 0.4 times its

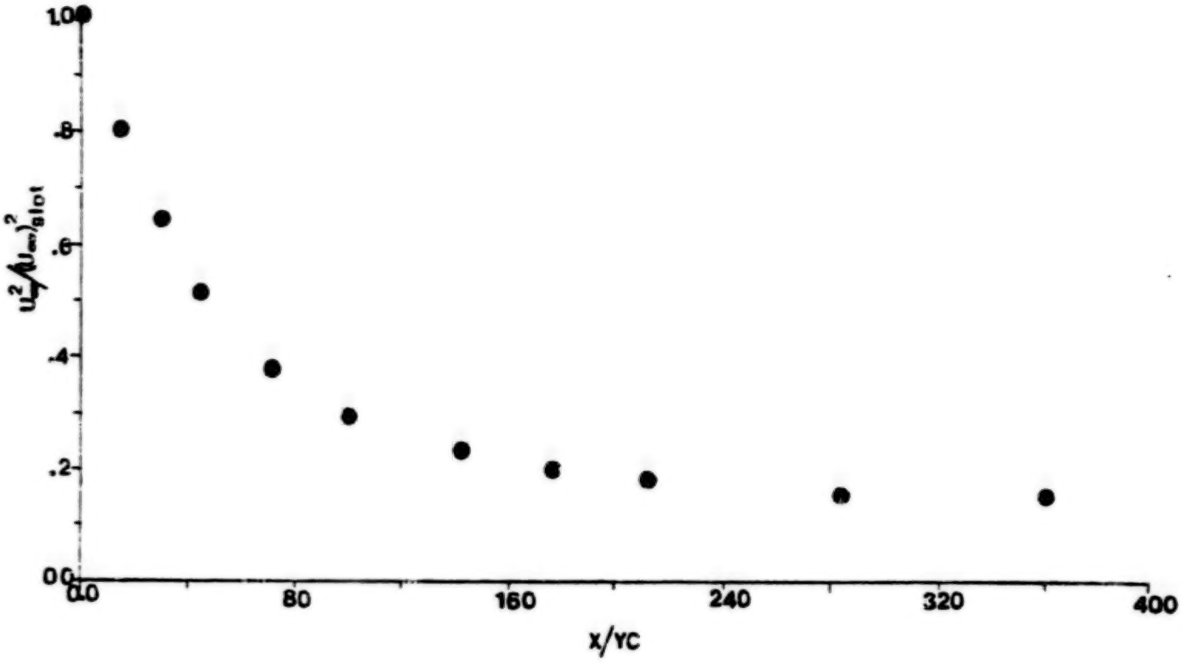

Fig. 5.2 Free-Stream Velocity Distribution

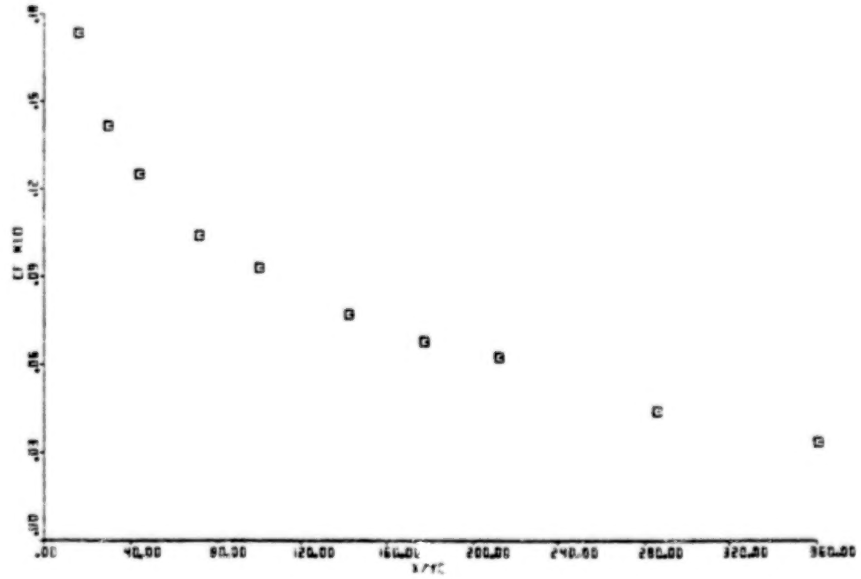

Fig. 5.3(a) Variation of Skin Friction

value at the slot in about 360 slot heights. The flow upstream of the slot was maintained under zero pressure gradient. It should be mentioned here that the flow was separating from the bottom wall at a point very close to the slot when no fluid was introduced through the jet and the entire downstream flow on the lower wall was separated.

5.2 Mean Flow Data

The mean flow data presented here include the skin friction, mean velocity profiles and the integral and profile parameters.

5.2.1 Skin Friction C_f

The variation of skin friction coefficient C_f obtained from the Preston tube measurements is shown in Fig. 5.3 (a). Fig. 5.3 (b) shows the variation of C_f with x/y_c on a logarithmic scale. It can be seen that there is a power law variation between C_f and x/y_c up to x/y_c = 143.0.

It has been found in the literature (section 4.2.1) that for self-preserving wall jets under pressure gradients, the skin friction $C_{fm} = \tau_w/(\frac{1}{2}\rho U_{max}^2)$ varies according to the equation (4.2). Fig. 5.3 (c) shows the variation of C_{fm} with $U_{max}Y_{max}/\nu$ for the present case. No definite pattern is found in the distribution of C_{fm} except that it follows a power law in the initial region. The failure of C_{fm} to follow a power law all the way unlike the case

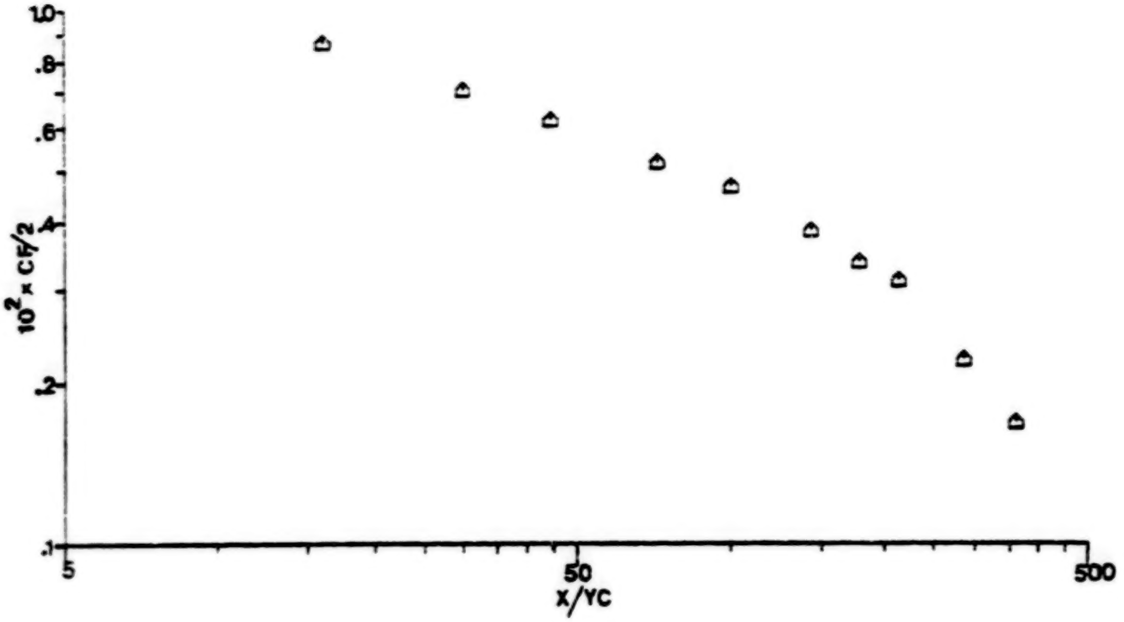

Fig. 5.3(b) Variation of Skin Friction in Logarithmic Coordinates

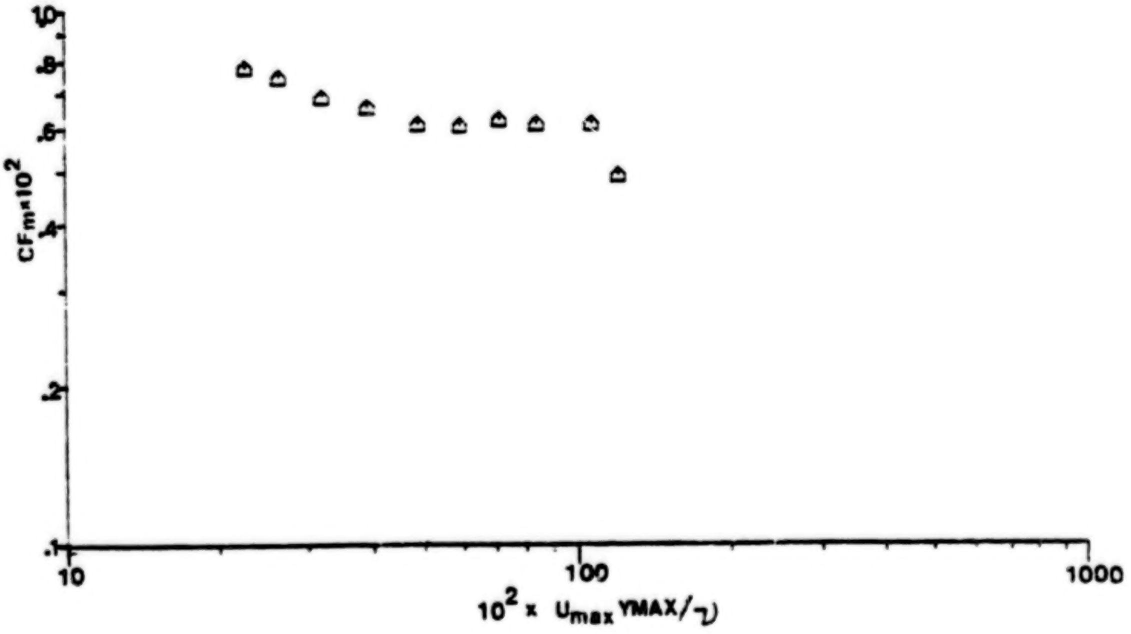

Fig. 5.3(c) Variation of Skin Friction Coefficient C_{fm}

of zero pressure gradient flow can be explained in the following way. Because of the severity of the adverse pressure gradient, the value of Y_{max} increases very rapidly at far downstream stations. Therefore, at farther downstream stations, the Y_{max} point cannot be considered as part of the inner layer and hence a defined correlation between C_{fm} and $U_{max}Y_{max}/\nu$ cannot be found.

5.2.2 Mean Velocity U

Figs. 5.4 (a-c) show the normal hot-film measurements of mean velocity profiles in the U/U_∞ vs y (cm) co-ordinates. The negative sign on the x/y_c value in Fig. 5.4 (a) indicates that it is the distance measured upstream of the slot. The value $x/y_c = -16.4$ corresponds to the crest of the extruded aluminum end piece (section 2.2.2).

Fig. 5.4 (a) also shows the velocity profile at $x/y_c = 0.292$. Here it can be seen again that the velocity profile in the jet is asymmetric with a relatively greater concentration of momentum in the upper half of the wall jet. We will see in the later sections of this chapter how this asymmetric jet velocity profile helps in better control of separation compared to a uniform velocity profile in the jet. The upstream boundary layer at the jet (Fig. 5.4 (a)) is very thick and has a large deficit of momentum satisfying one of the proposed conditions under which the present measurements were intended to be made as given in Chapter 1.

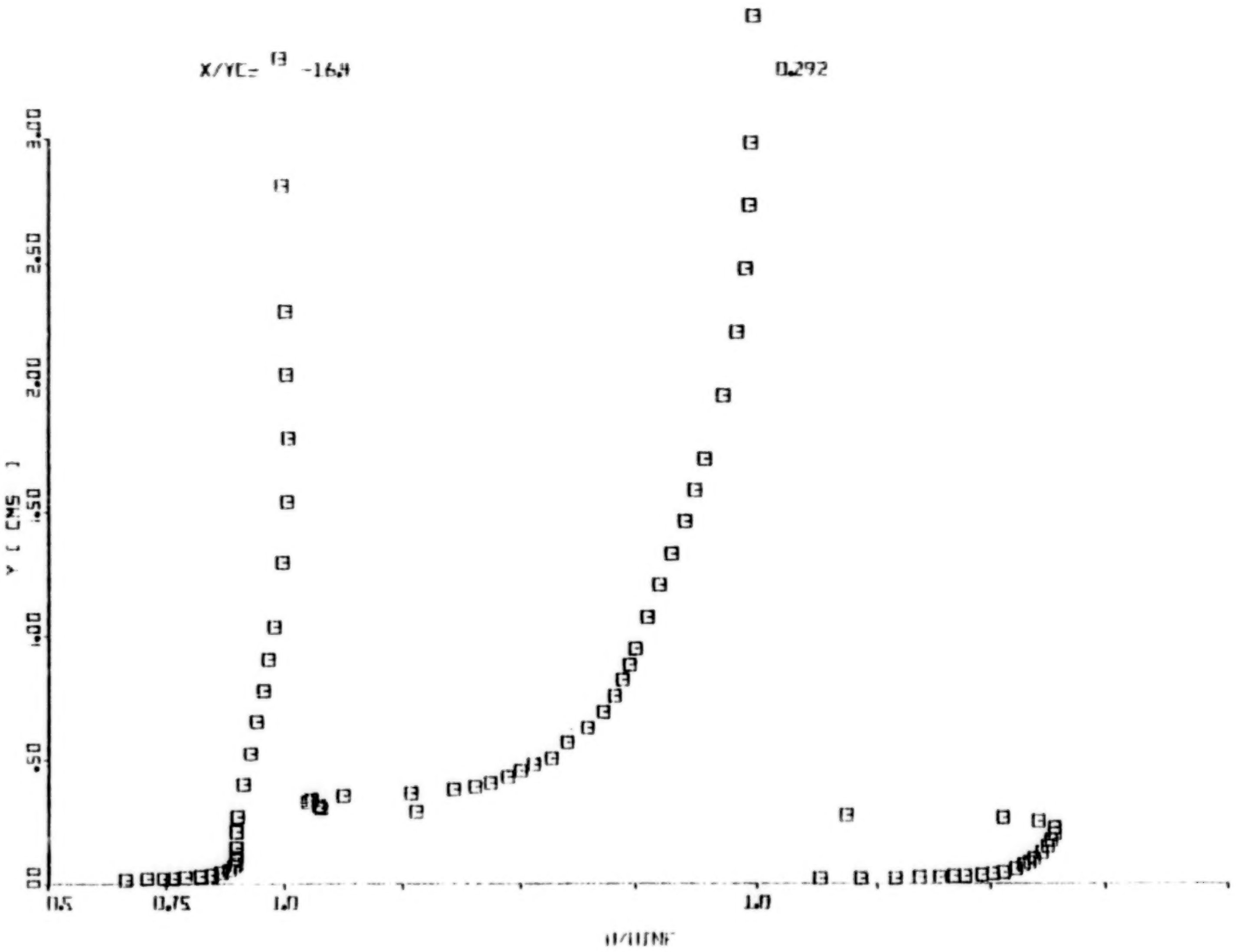

Fig. 5.4(a) Mean Velocity Profiles Upstream of the Slot ($x/y_c = -16.4$) and at the Slot ($x/y_c = 0.292$)

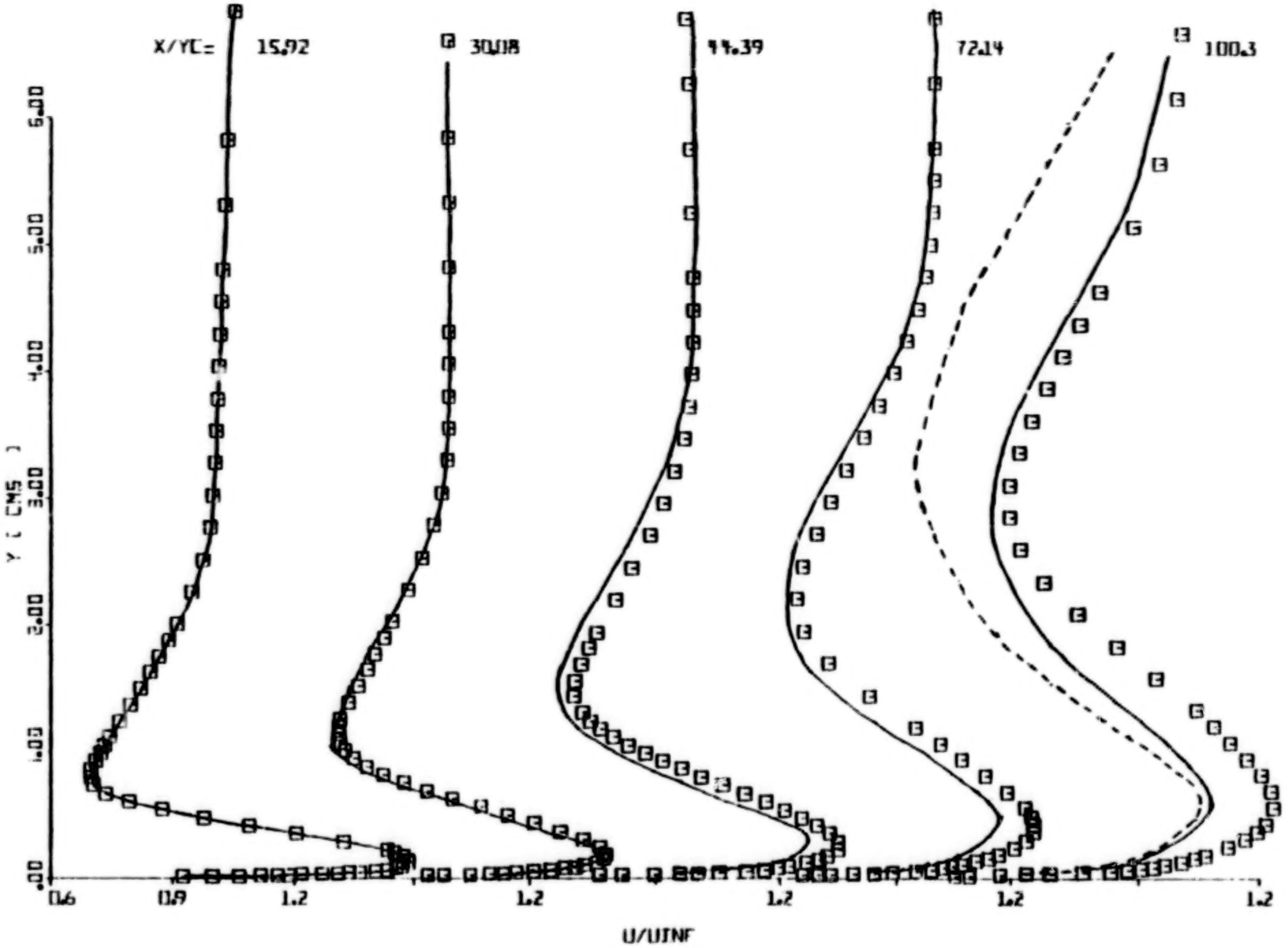

Fig. 5.4(b) Mean Velocity Profiles at x/y_c = 15.92 to 100.3

—— Predictions using experimental initial profiles

---- Predictions using automatic starting procedure

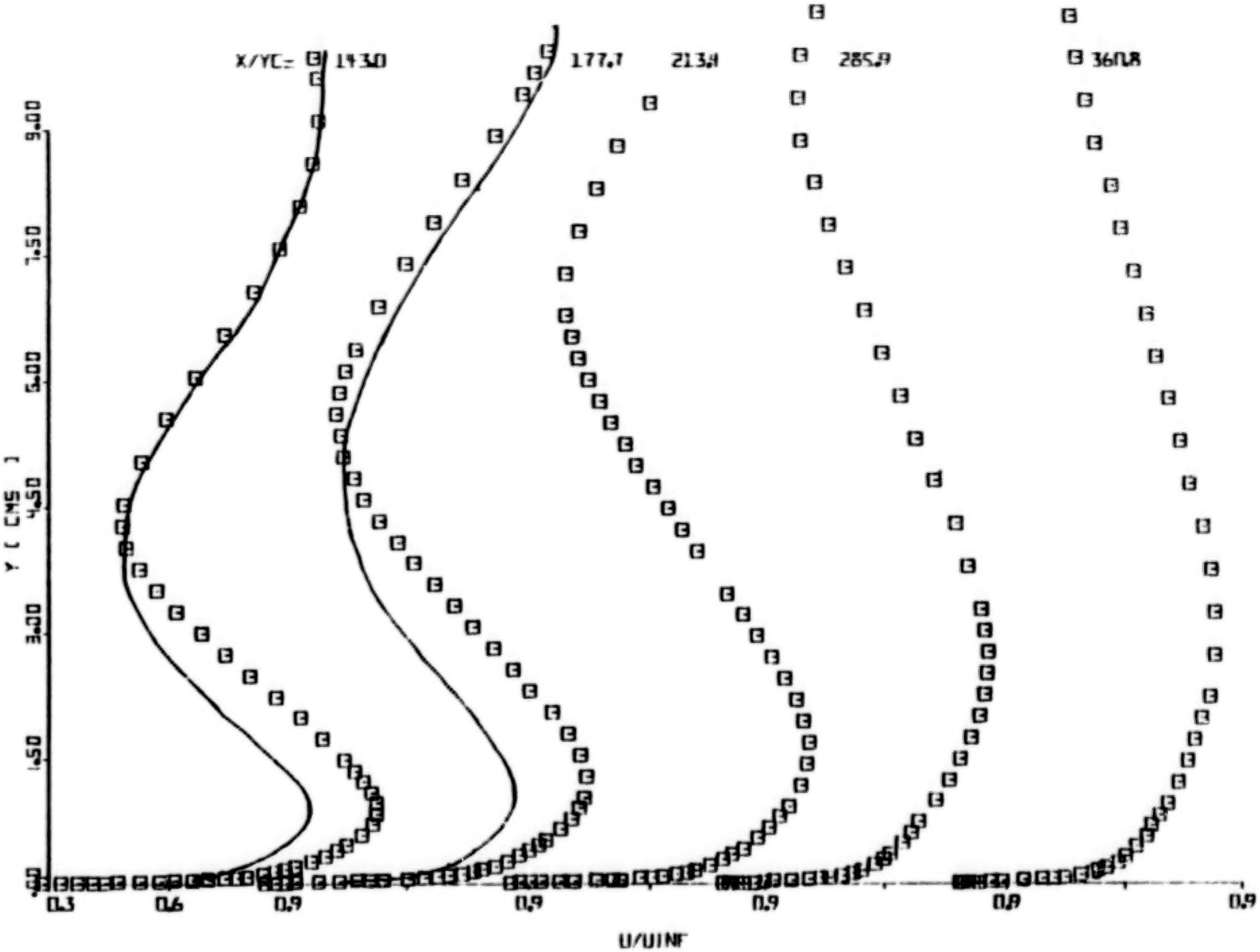

Fig. 5.4(c) Mean Velocity Profiles at x/y_c = 143.0 to 360.8

—— Predictions using experimental initial profiles

Figs. 5.4 (b) and (c) show the mean velocity profiles from $x/y_c = 15.92$ and onwards. It should be mentioned here that the entire height of the tunnel was almost completely filled with the shear layer at $x/y_c = 177.7$ and onwards. Therefore, the experimental data at $x/y_c = 177.7$ and beyond have to be treated with caution from every point of view. The data beyond $x/y_c = 177.7$ are especially useful in finding out the effectiveness of an asymmetric jet velocity profile in the control of separation. The boundary layer thickness δ could not be determined beyond $x/y_c = 143.0$ since no freestream was observed. Hence, the velocity profiles were plotted against y in cm. The free-stream velocity used in the data reduction at stations beyond $x/y_c = 143.0$ was only an imaginary one that would produce the measured static pressure in an irrotational freestream.

As mentioned in section 5.1, the present pressure gradient was the most severe one that the flow could withstand with a ratio of jet velocity to free-stream velocity at the slot around 1.5. In other words, any stronger pressure gradient beyond the present case, keeping the jet velocity to free-stream velocity ratio constant, would lead to flow separation downstream. Because of the severe pressure gradient imposed on the flow, the shear layer rapidly became thicker and eventually filled the whole tunnel as shown in Figs. 5.4 (b) and (c). The upstream boundary layer was not absorbed completely by the jet, unlike in the case of the zero pressure gradient flow. The velocity maxima was observed throughout the flow and the velocity minima could be observed until x/y_c = 285.9.

Fig. 5.5 (a) and (b) show the velocity profiles plotted on a conventional semi-logarithmic plot with U/U_τ and $U_\tau y/\nu$ as the co-ordinates. The velocity profiles are shown for stations x/y_c = 15.92 and onwards. The shear velocity U_τ was obtained from the Preston tube measurements. The velocity profile measurements were compared with the logarithmic law of the wall,

$$\frac{U}{U_\tau} = 5.5 \operatorname{Log}_{10} \frac{U_\tau y}{\nu} + 5.45 \qquad (5.1)$$

with the constants recommended by Patel (1965). It can be seen from Figs. 5.5 (a) and (b) that the experimental data agree well with the logarithmic law of the wall up to x/y_c = 143.0. The exception is at station x/y_c = 15.92, where a defined logarithmic region is not present because of its proximity to the slot. A defined logarithmic region can be observed even beyond x/y_c = 143.0. However, the constant in the logarithmic law of the wall has to be different from 5.45 to fit the data. At far downstream stations, the data extended considerably into the viscous sublayer. The mean velocity data are tabulated in Appendix F along with the data of u_t.

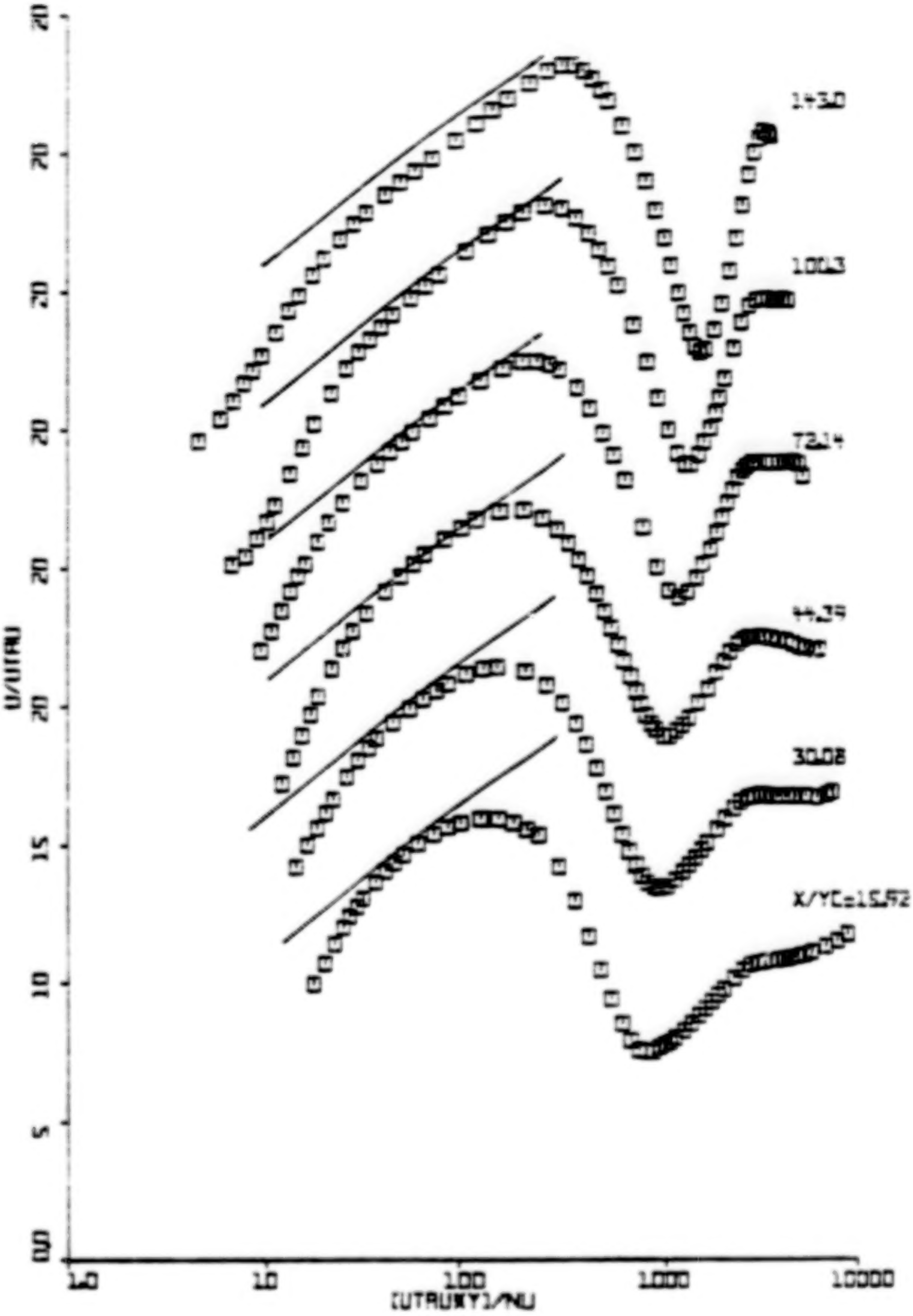

Fig. 5.5(a) Mean Velocity Profiles in the Wall Coordinates at x/y_c = 15.92 to 143.0

—— Logarithmic law of the wall (Equation 5.1)

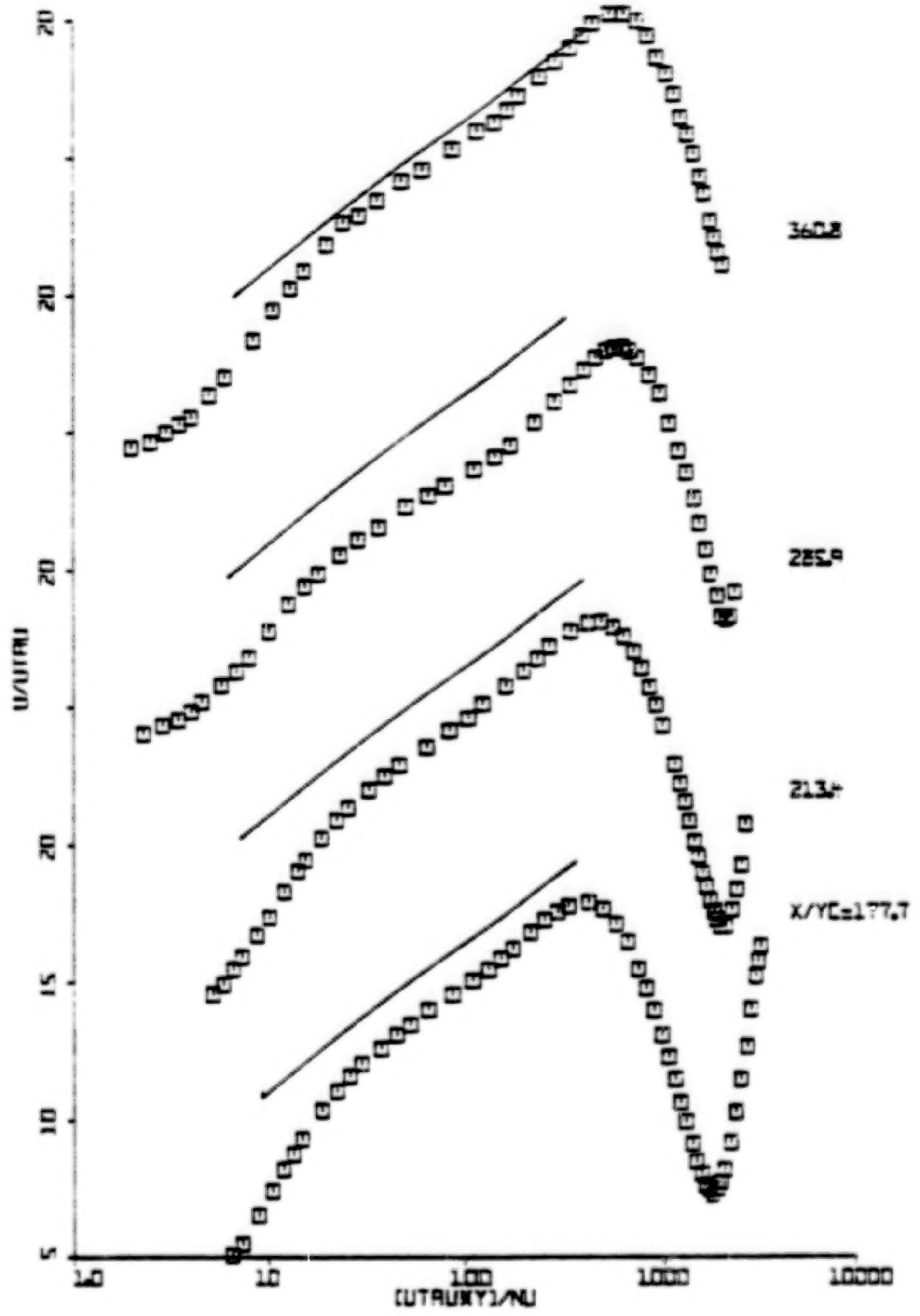

Fig. 5.5(b) Mean Velocity Profiles in the Wall Coordinates at x/y_c = 177.7 to 360.8

—— Logarithmic law of the Wall (Equation 5.1)

5.2.3 Integral Parameters

The integral parameters evaluated are the boundary layer thickness (δ), displacement thickness (δ_1), momentum thickness (δ_2), shape factor (H) and the momentum thickness Reynolds number (Re_2).

Figs. 5.6 (a-e) show the development of the integral parameters δ/y_c, δ_1/y_c, δ_2/y_c, H and Re_2 respectively. The value of δ beyond $x/y_c = 143.0$ was taken equal to the value of y at the last data point. Because of the severe adverse pressure gradient imposed on the flow, δ_1 and δ_2 increased very rapidly in the initial region up to $x/y_c = 177.7$. The displacement thickness increased more rapidly than the momentum thickness up to $x/y_c = 177.7$. The growth of δ_1 and δ_2 decreased beyond $x/y_c = 177.7$. This was partly due to the fact that the outer edge of the outer layer was already touching the top wall of the tunnel at $x/y_c = 177.7$ and hence the full velocity profile was not accounted for in the evaluation of δ_1 and δ_2 at $x/y_c = 177.7$ and beyond. The reduction in the growth rates of δ_1 and δ_2 at far downstream stations was also partly due to dU_∞/dx being small there compared to the region near the jet.

The two-dimensional nature of the flow was examined by applying the two-dimensional integral momentum equation (5.2) to the present data.

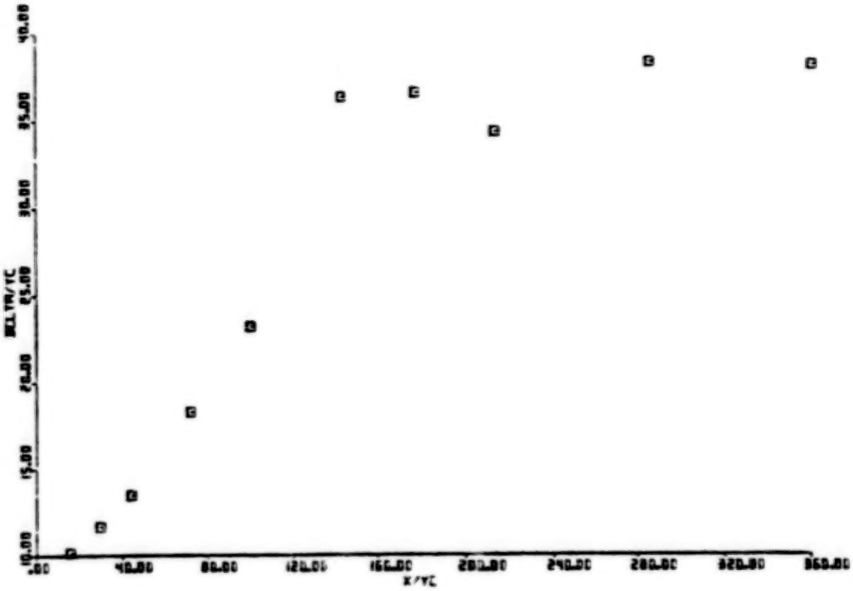

Fig. 5.6(a) Growth of the Boundary Layer Thickness

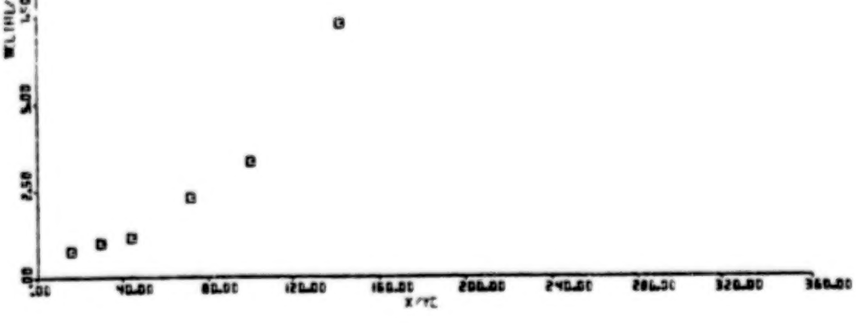

Fig. 5.6(b) Growth of the Displacement Thickness

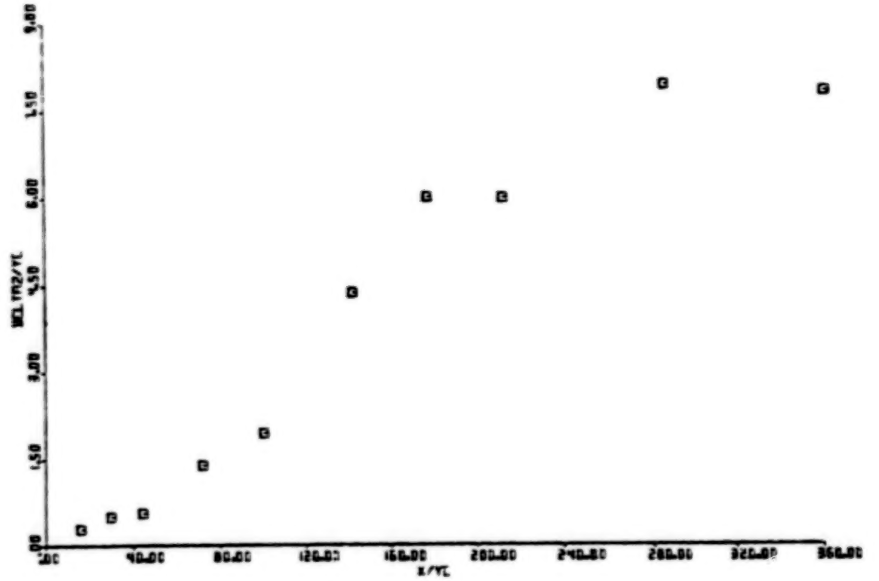

Fig. 5.6(c) Growth of the Momentum Thickness

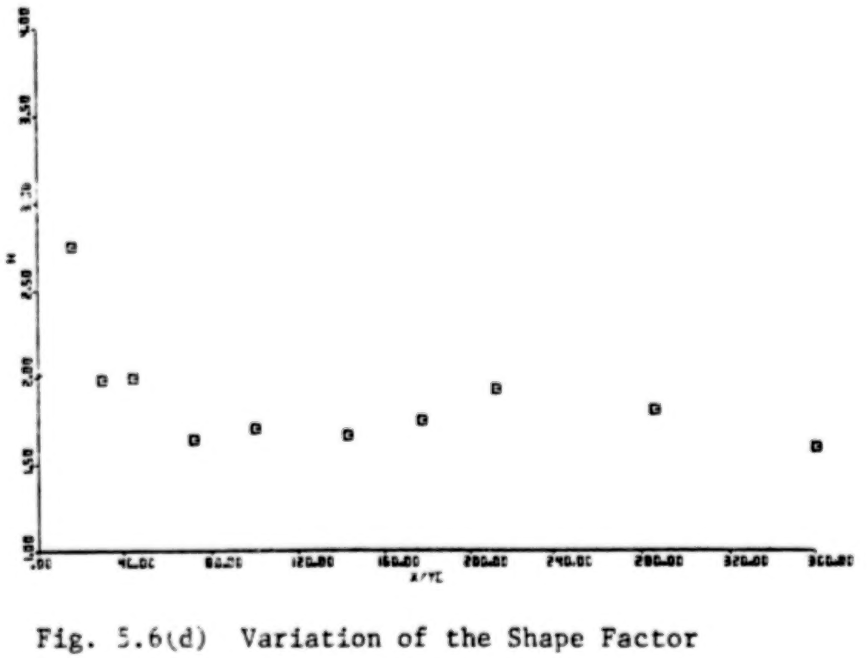

Fig. 5.6(d) Variation of the Shape Factor

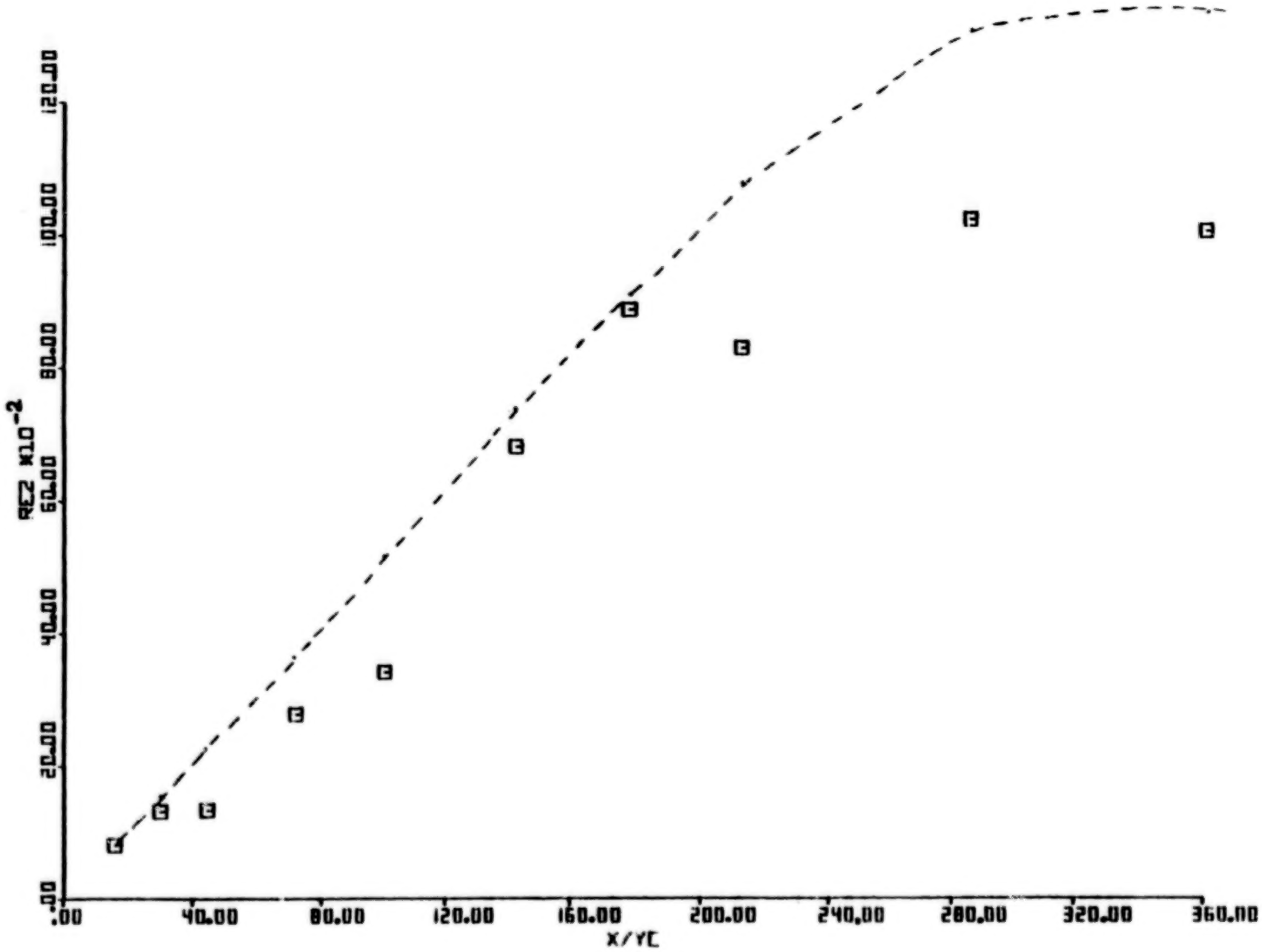

Fig. 5.6(e) Variation of the Momentum Thickness Reynolds Number Re_2

---- Re_2 obtained using two-dimensional integral momentum equation (5.2)

$$\frac{d\delta_2}{dx} + \frac{\delta_2\ (2 + H)}{U_\infty}\frac{dU_\infty}{dx} = \frac{C_f}{2} - \frac{1}{U_\infty^2}\frac{d}{dx}\int_0^\infty (\overline{u^2} - \overline{v^2})\,dy \qquad (5.2)$$

or,

$$(U_\infty^2\delta_2) = (U_\infty^2\delta_2)_{x/y_c=15.92} + \int_{x/y_c=15.92}^{x/y_c} U_\infty^2\,\frac{C_f}{2}\,dx - \int_{x/y_c=15.92}^{x/y_c} \delta_1 U_\infty\left[\frac{dU_\infty}{dx}\right]dx$$

$$- \left[U_\infty^2\int_0^\infty \frac{\overline{u^2}-\overline{v^2}}{U_\infty^2}\,dy\right]_{x/y_c=15.92}^{x/y_c}$$

The contribution of the normal stress terms $\int_0^\infty [(\overline{u^2}-\overline{v^2})/U_\infty^2]\,dy$ to the integral momentum equation was found to be smaller than 5% and hence it was neglected. The measured distributions of the skin friction coefficient, external velocity and displacement thickness were used in the equation 5.2. Fig. 5.6 (e) shows the values of $Re_2 = U_\infty\delta_2/\nu$ obtained from the two-dimensional integral momentum equation (5.2) along with the experimental values of Re_2. The values of Re_2 obtained from the equation (5.2) agree with the experimental values of Re_2 within 15% on the average up to $x/y_c = 177.7$. The failure of the experimental data of Re_2 to agree with the values of Re_2 obtained from the integral momentum equation beyond $x/y_c = 177.7$ was mainly due to the fact that the entire tunnel height was filled by the shear layer beyond $x/y_c = 177.7$. Because the shear layer was spread over the entire tunnel height, the full velocity profile was not accounted for in the evaluation of Re_2 from the experimental data.

5.2.4 Effect of the Assymetric Jet Velocity Profile on the Mean Flow

The effect of the asymmetric jet velocity profile on the mean flow development is discussed below. A preliminary comparison of the present flow with similar flows in the literature (Irwin, 1974; Goradia and Colwell, 1971; and Ramaprian, 1973, 1975) has shown that the present flow was able to withstand much more severe adverse pressure gradient without separation even with a modest jet momentum. Even though a direct comparison cannot be made, there was an indication from the references mentioned above that with the present pressure gradient and the injection velocities, the flow will separate downstream if a uniform velocity profile was used in the jet.

The asymmetric jet velocity profile used in the present case was mainly responsible for the prevention of separation even under the severe adverse pressure gradient employed and the low injection velocities used. As mentioned earlier (section 4.2.4), the asymmetric jet velocity profile helps in distributing the jet momentum evenly across the layer by supplying more momentum to the momentum deficient upstream boundary layer than a uniform profile. The asymmetric profile also reduces the momentum losses due to friction at the wall by keeping a higher concentration of jet momentum in the upper half of the jet than the lower half. In comparison, the uniform jet velocity profile tries to retain more momentum near the wall instead of supplying sufficient momentum to the momentum deficient upstream boundary layer. This might result in the development of a large momentum deficient region downstream near the point of minimum velocity and eventual flow reversal there. The relatively large concentration of momentum near the wall results in greater frictional losses at the wall in the case of a uniform profile. The above conditions might lead to eventual flow separation at the bottom wall in the case of the uniform jet velocity profile. An additional proof of the advantages of the asymmetric jet velocity profile over the uniform jet velocity profile was obtained from the theoretical prediction of the present flows using uniform and asymmetric jet velocity profiles (Chapter 7).

The development of δ_1 and δ_2 for the present flow was compared with that of a similar flow by Irwin (1974). Irwin's flow has a ratio of jet velocity to free-stream velocity of the same order and a relatively less severe pressure gradient. An exact comparison cannot be made because the exact flow conditions are different in each case. The increase in δ_1 and δ_2 for a given x/y_c distance was found to be lower for the present flow. The asymmetric jet velocity profile is mainly responsible for the slow growth of δ_1 and δ_2 in the present flow.

The asymmetric profile distributes the momentum more evenly than a uniform jet and prevents build-up of a large momentum deficient region downstream near the minimum velocity point, thereby resulting in slow growth of δ_1 and δ_2. In comparison, the uniform jet velocity profile might result in a large momentum deficient region downstream near the minimum velocity point as mentioned above. This will lead to large values of δ_1 and δ_2 in the case of a uniform jet velocity profile, which is an unwanted effect in the efforts to prevent separation.

5.2.5 Profile Parameters

The mean velocity profile parameters presented here include Y_{max}, Y_{half}, Y_{min}, U_{max} and U_{min}. The significance of these parameters was given in section 4.2.5. No minima in velocity was found at $x/y_c = 360.84$. Therefore, the last data point near the top wall was taken as the point of minimum velocity.

5.2.5 (a) Development of Y_{max}, Y_{half} and Y_{min}

Fig. 5.7 (a) shows the development of Y_{max} and Y_{half}. Fig. 5.7 (b) shows the development of Y_{min}. Fig. 5.7 (a) also shows the development of Y_{max} for the zero pressure gradient flow. It can be seen that the rate of growth of Y_{max} is almost the same for both zero and adverse pressure gradients and the pressure gradient does not seem to influence the Y_{max} development. The universal Y_{max} development found in the literature (section 4.2.5 (a))

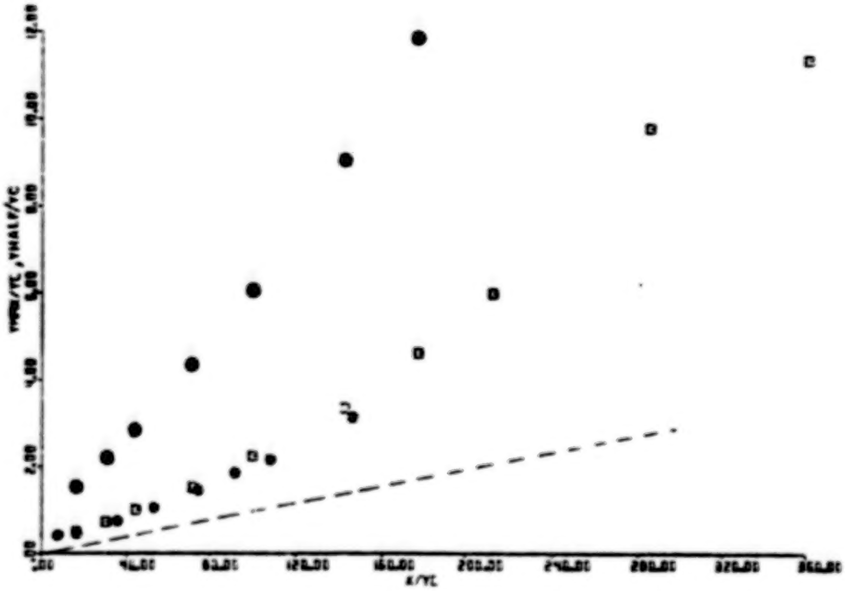

Fig. 5.7(a) Development of Y_{max} and Y_{half}

□, ● Experimental data of Y_{max} and Y_{half} respectively for $dP/dx > 0$

● Experimental data of Y_{max} for $dP/dx = 0$

---- Universal distribution of Y_{max}

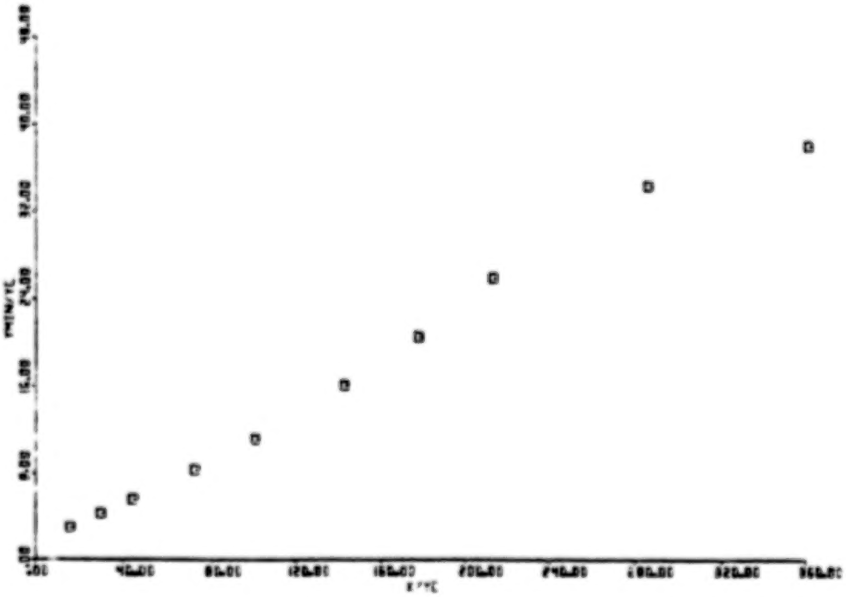

Fig. 5.7(b) Development of Y_{min}

for self-preserving flows with and without pressure gradients was also shown in Fig. 5.7 (a). As mentioned in section 4.2.5 (a), it is not clear whether the non-self-preserving wall jets exhibit universal behavior for the Y_{max} development. However, the increased Y_{max} growth rate in the present case as compared to the universal line for self-preserving flows can be partly attributed to the asymmetric jet velocity profile. The physical explanation for the increased Y_{max} growth rate for an asymmetric jet velocity profile was given in detail in Chapter 4 under the section 4.2.5 (a). The development of Y_{half} is affected considerably by the pressure gradient. The growth rate of Y_{half} is higher than that for the zero pressure gradient case and also it is higher than the growth rate of Y_{max} for the adverse pressure gradient case.

A comparison of the ratio of the growth rates of Y_{max} and Y_{half} for the adverse pressure gradient flow with that of similar flows in the literature (Irwin, 1974; Ramaprian, 1973; Gartshore and Newman, 1969) shows that the present growth rate of Y_{half} is not very large compared to the Y_{max} growth rate. The relatively slow growth rate of Y_{half} can be attributed to the asymmetric jet velocity profile. The physical explanation for the relatively slow growth rate of Y_{half} for an asymmetric profile was given in detail in Chapter 4 under the section 4.2.5 (a).

5.2.5 (b) Variation of U_{max} and U_{min}

Figs. 5.8 (a-c) show the variation of U_{max}/U_{Jave}, U_{min}/U_{Jave}, and $(U_{max}-U_{min})/U_{Jave}$ respectively with x/y_c. U_{Jave} is the uniform jet velocity for an equivalent jet with an uniform profile and having the same momentum as the experimental asymmetric jet. Wall jet data in the literature show that the variation of U_{max} and U_{min} depends on several parameters, such as the ratio of the jet velocity to the free-stream velocity, the pressure gradient, and the conditions upstream of the slot. Hence an attempt has not been made to compare the present variation of U_{max} and U_{min} with the data in the literature. However, the U_{max} decay seems to follow a power law variation (Equation 5.3) as shown in Fig. 5.8 (a).

$$\frac{U_{max}}{U_{Jave}} = 3.513\ (x/y_c)^{-.474} \qquad (5.3)$$

5.3 Turbulence Data

The measured turbulence data include the turbulence intensities (u_t/U_∞, v_t/U_∞, and w_t/U_∞) and the turbulent shear stress $-\overline{uv}$. The quantities derived from the measured turbulence data include, the eddy viscosity, mixing length, Prandtl-Kolmogorov length scale, turbulent kinetic energy, correlation coefficients and the rate of production of turbulent kinetic energy. The results of the measured and derived turbulent quantities are given below in detail.

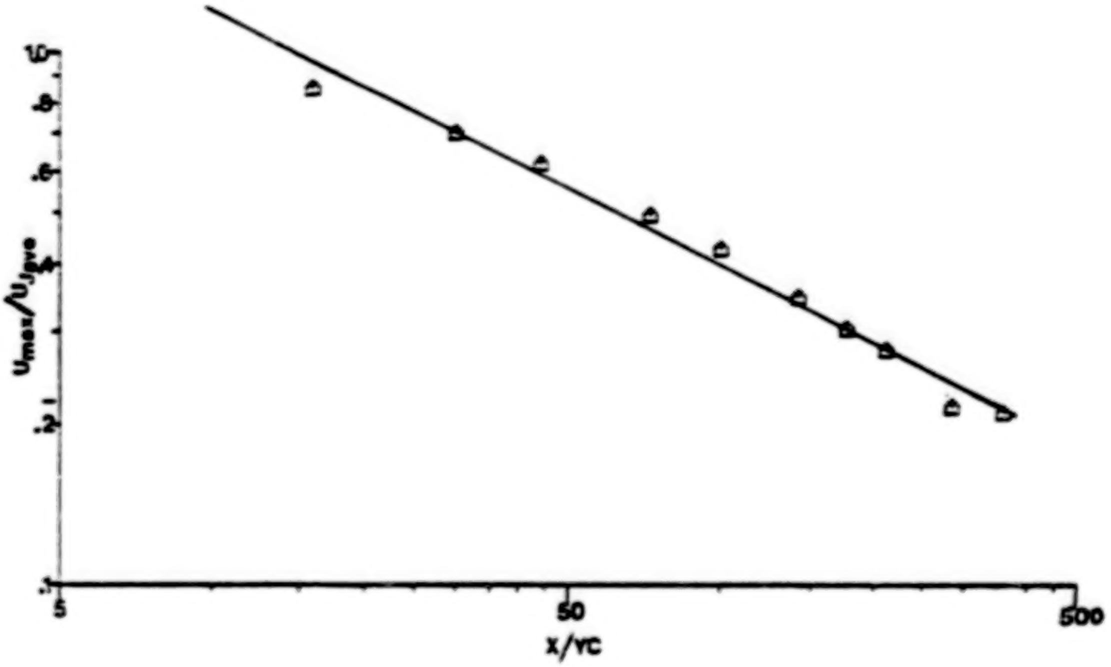

Fig. 5.8(a) Variation of U_{max}

—— Line fitting the experimental data (Equation 5.3)

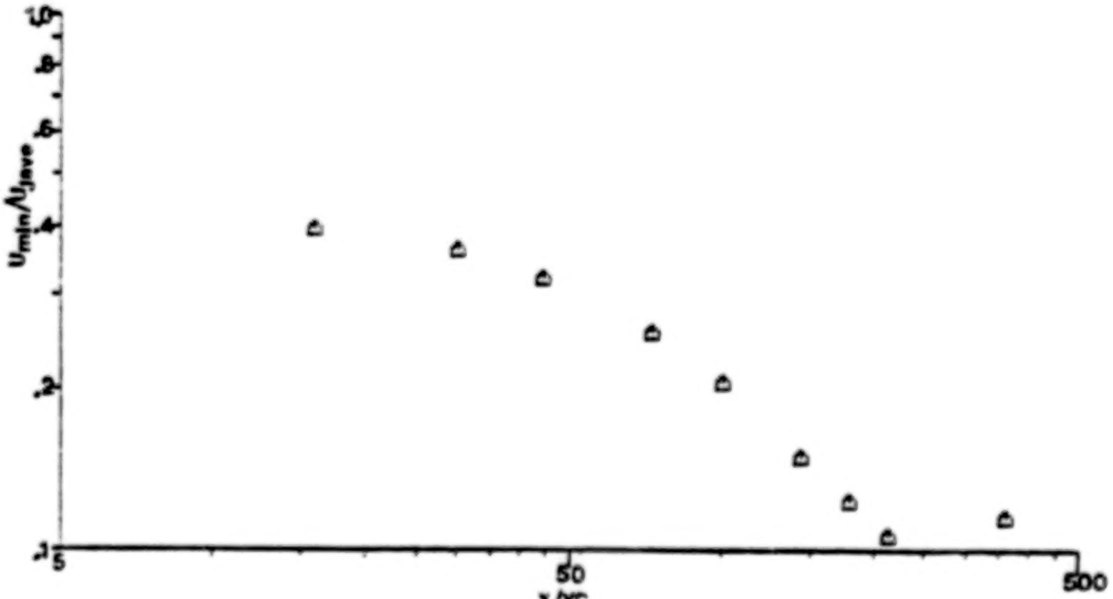

Fig. 5.8(b) Variation of U_{min}

BLANK PAGE

BLANK PAGE

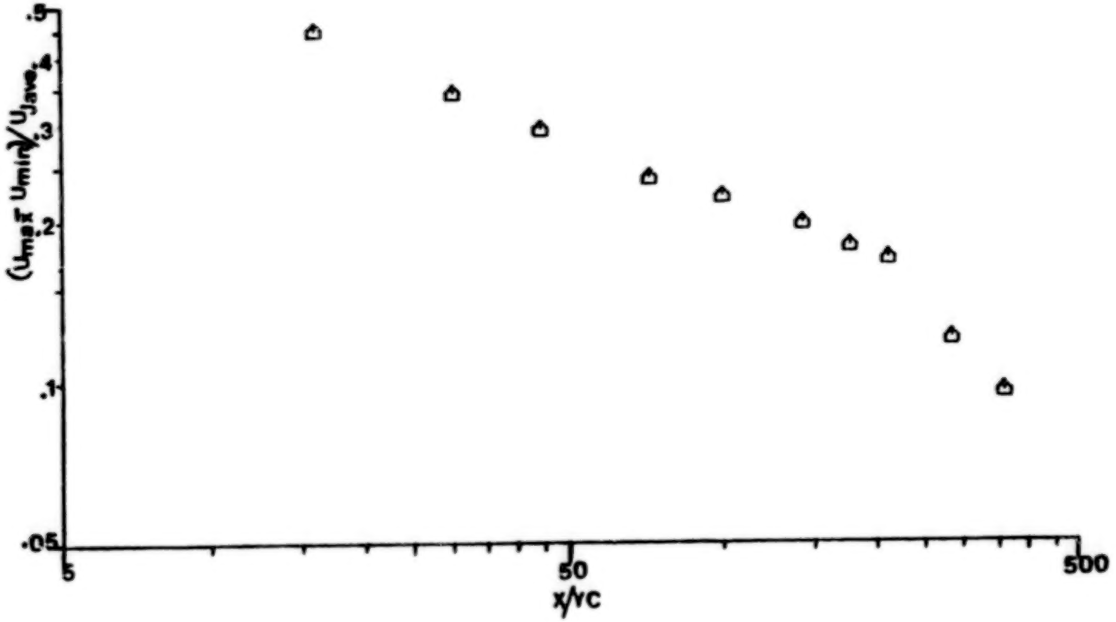

Fig. 5.8(c) Variation of $(U_{max} - U_{min})$

5.3.1 Turbulence Intensity u_t/U_∞

The u_t data were obtained from the normal hot-film traversals at several stations starting from $x/y_c = 0.292$. Figs. 5.9 (a-c) show the variation of u_t/U_∞ vs. y(cms). The negative sign on the value of x/y_c indicates that those stations are located upstream of the slot. The position of $x/y_c = -16.4$ is the same as given in section 5.2.2.

Figs. 5.10 (a) and (b) show the variation of u_t in wall coordinates. For the stations near the slot, all of the data were out of the viscous sublayer, whereas for far downstream stations the data extend considerably into the sublayer. The point of first maximum in u_t is always near the wall and at the outer edge of the sublayer. The point of minimum u_t in the inner layer generally corresponds with the region of maximum velocity even though the exact position was generally nearer to the wall than the point of maximum velocity. The point of second maximum in u_t was found to be between the points of velocity maximum and the velocity minimum and nearer to the point of maximum velocity gradient. The point of minimum u_t in the outer layer was found to be around the point of minimum velocity. The steep drop in u_t far away in the outer layer was found to begin from the point of maximum velocity gradient between the velocity minima and the freestream. Some of the above features are not applicable

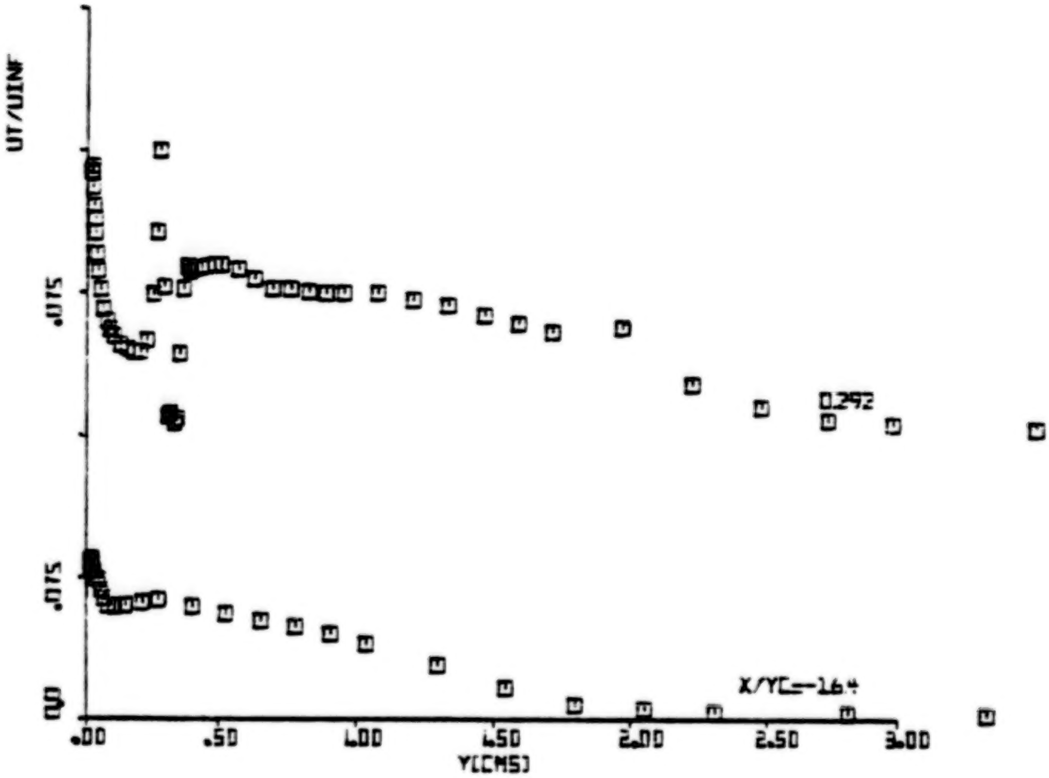

Fig. 5.9(a) Distribution of the Turbulence Intensity u_t/U_∞ at x/y_c = -16.4 and 0.292

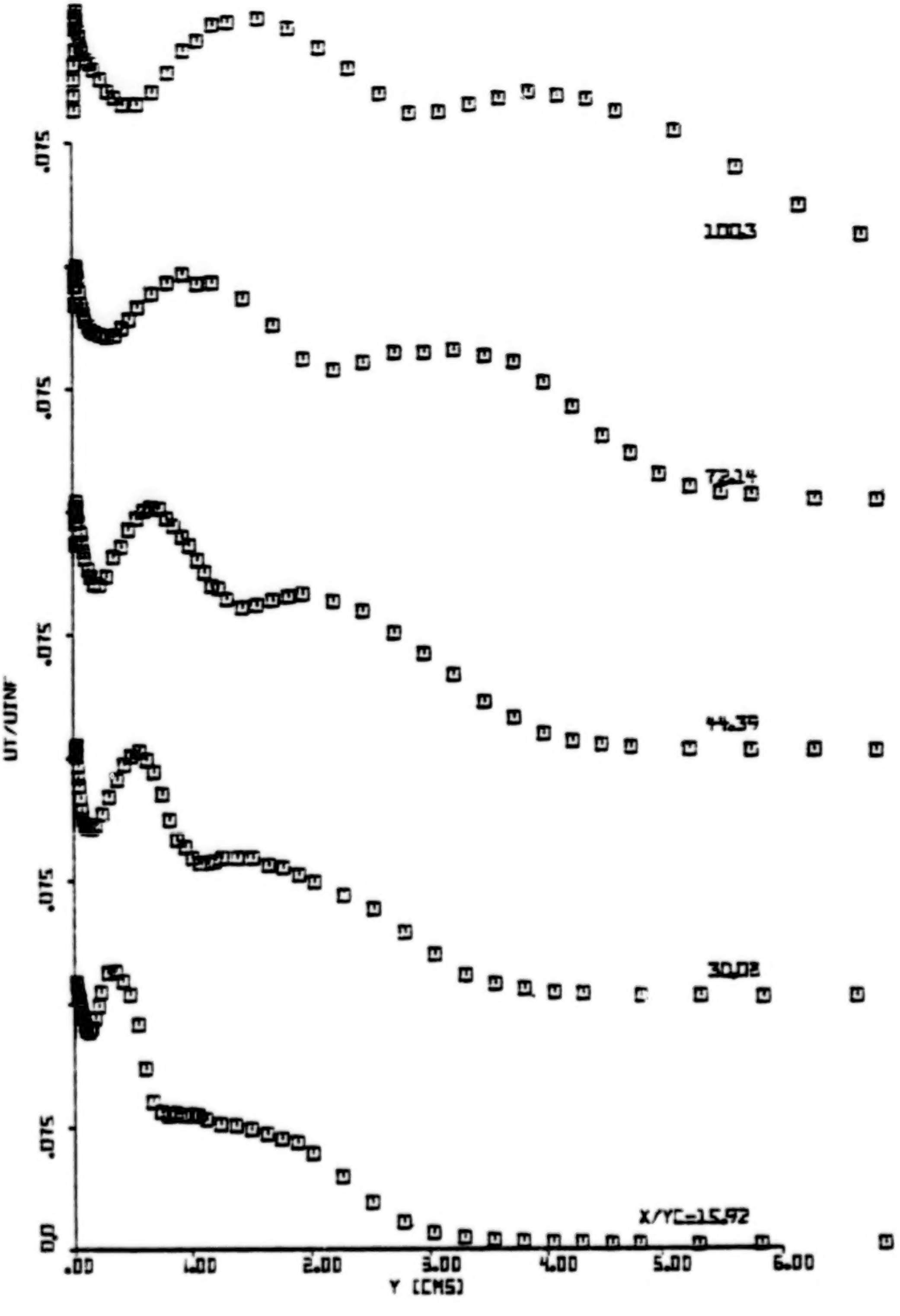

Fig. 5.9(b) Distribution of the Turbulence Intensity u_t/U_∞ at x/y_c = 15.92 to 100.3

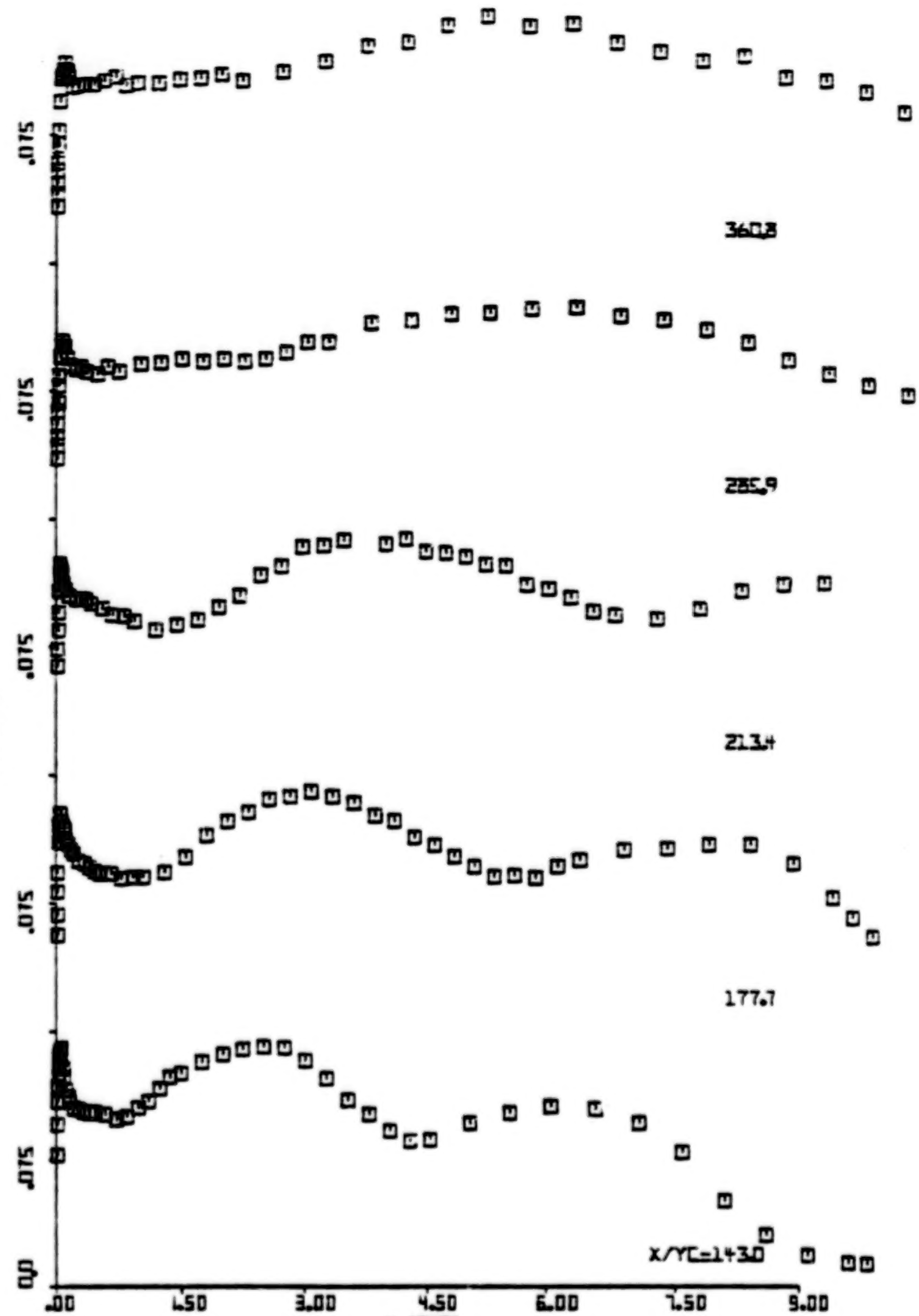

Fig. 5.9(c) Distribution of the Turbulence Intensity u_t/U_∞ at x/y_c = 143.0 to 360.8

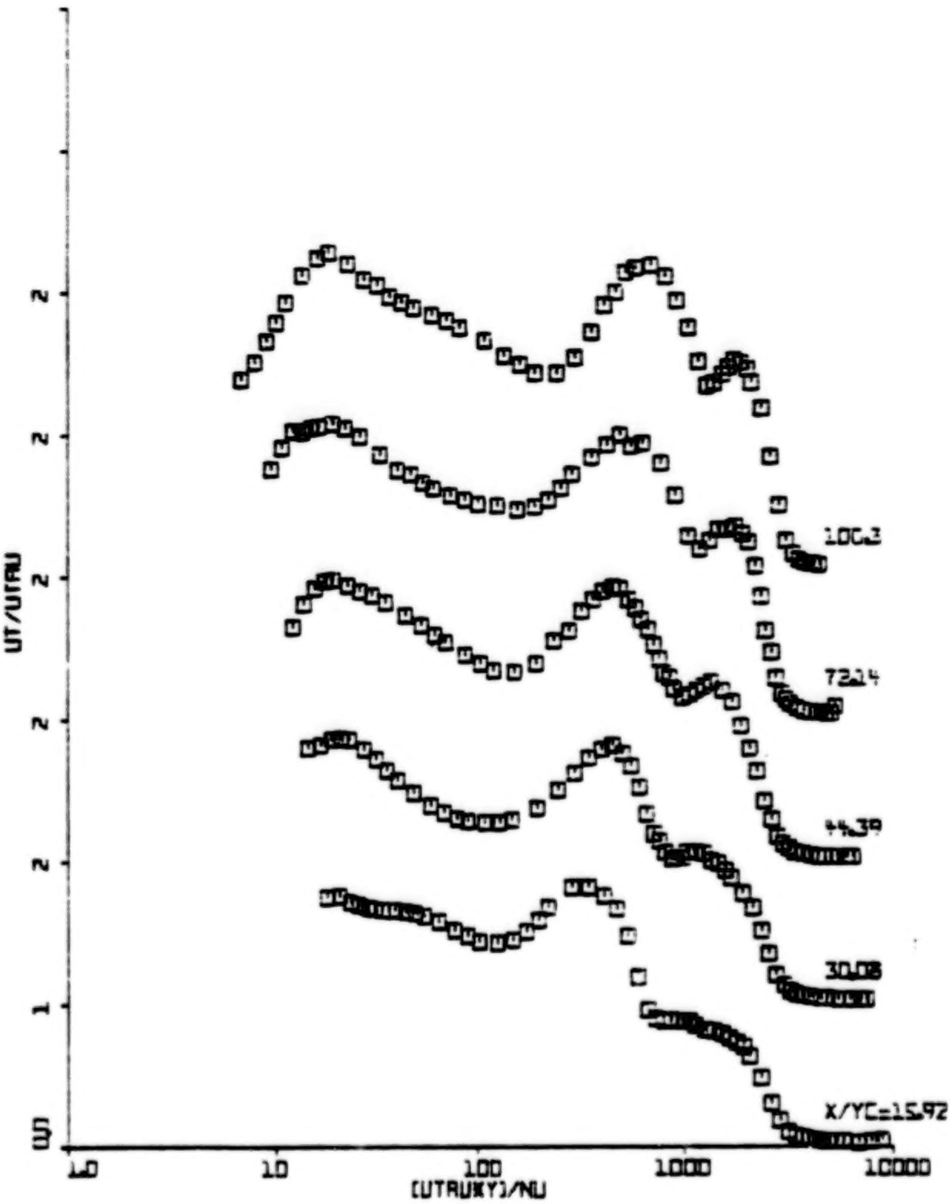

Fig. 5.10(a) Distribution of u_t in Wall Coordinates at x/y_c = 15.92 to 100.3

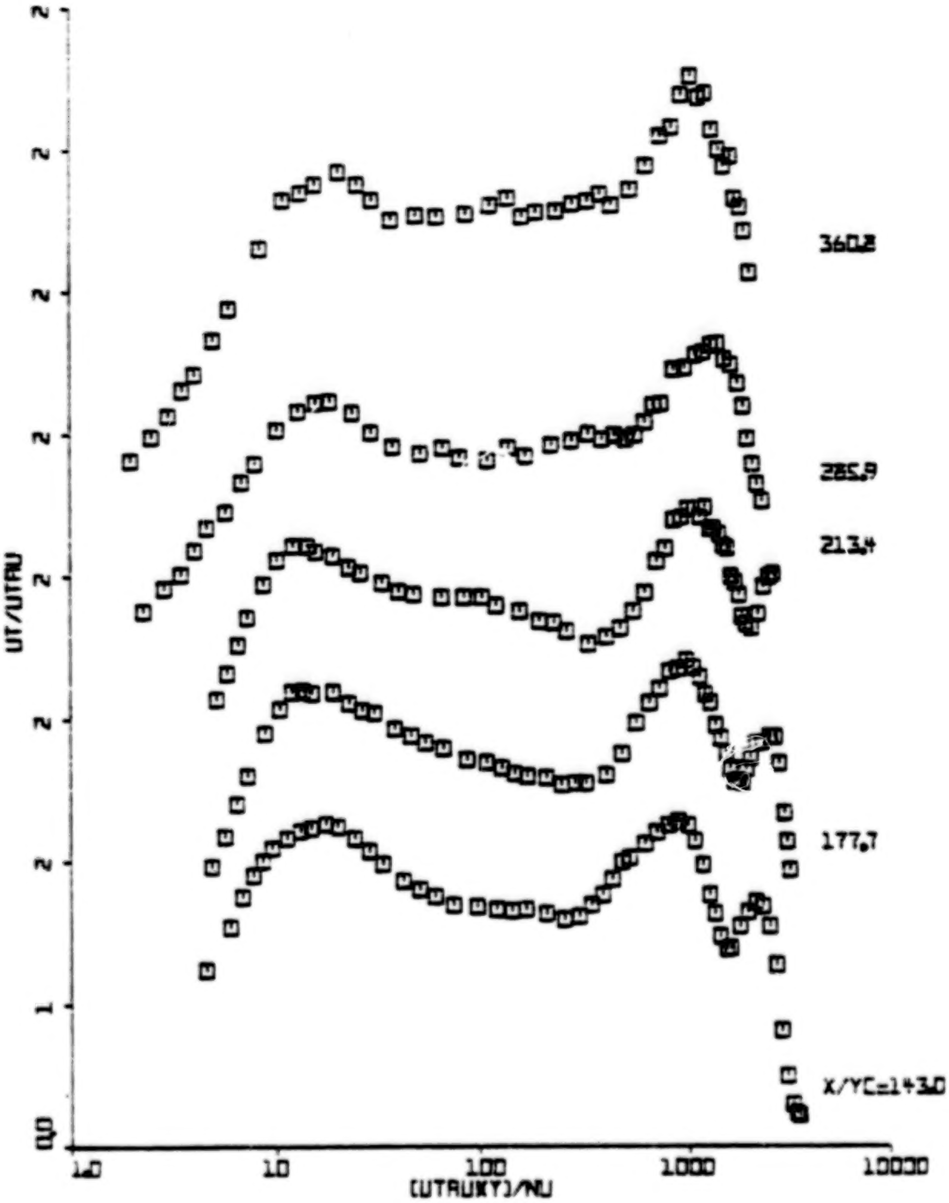

Fig. 5.10(b) Distribution of u_t in Wall Coordinates at x/y_c = 143.0 to 360.8

to u_t profiles beyond $x/y_c = 177.7$, since the outer edge of outer layer was already touching the top wall at $x/y_c = 177.7$. Most of the above mentioned features of the u_t profiles have been observed in the case of zero pressure gradient flow also. The u_t data are given in Appendix F.

5.3.2 Turbulence Intensities v_t/U_∞, w_t/U_∞ And the Shear Stress $-\overline{uv}$

A rotatable slant-wire was used to obtain v_t, w_t and the shear stress $-\overline{uv}$, as in the case of zero pressure gradient flow (section 4.3.2). The details of obtaining the turbulence intensities and the shear stress from the slant wire data are given in Appendix C. The data of v_t, w_t, and $-\overline{uv}$ are tabulated in Appendix G. Appendix G also shows the interpolated data of u_t and $\partial(U/U_\infty)/\partial(y/\delta)$ obtained from the normal hot-film data. Because of the size limitations set by the slant wire probe supports, the slant wire data at some of the stations were taken only above the point of the velocity maximum. Slant-wire data were obtained only at four stations, compared to a greater number of slant-wire data stations for the case of zero pressure gradient flow. As mentioned in the Appendix C, the angle between the flow vector and the axis of the probe in the vertical plane was higher in the case of the adverse pressure gradient flow than for the zero pressure gradient flow. Details on the accuracy of the slant-wire data with respect to the flow inclination are given in the Appendix C. The results of the turbulence intensities v_t/U_∞, w_t/U_∞, and the shear stress $-\overline{uv}$ are described below.

5.3.2 (a) Turbulence Intensities v_t/U_∞ and w_t/U_∞

Figs. 5.11 and 5.12 show the variation of v_t/U_∞ and w_t/U_∞ at different stations. Generally, the positions of the maxima and minima in v_t and w_t were not well defined with respect to other variables. The maxima in v_t and w_t were found to be nearer to the region of maximum velocity gradients for the stations $x/y_c = 15.92$ and 44.39.

5.3.2 (b) Shear Stress $-\overline{uv}$

Figs. 5.13 (a) and (b) show the distribution of $-\overline{uv}$ at different stations. The significance of the inner and the outer points of zero shear was explained in Chapter 4 under section 4.3.2 (b). In the present $-\overline{uv}$ data, the inner point of zero shear was observed only at x/y_c = 100.3 and 177.7. It was not possible to make slant wire measurements up to the inner point of zero shear for stations $x/y_c = 15.92$ and 44.39. This was mainly because of size limitations set by the slant-wire probe supports. The outer point of zero shear is shown in Figs. 5.13 (a) and (b) only for stations $x/y_c = 15.92$, 44.39, and 100.3. The outer point of zero shear for $x/y_c = 177.7$ can be observed nearer to the last data point in the tabulated data (Appendix G) and it was not shown in the plots. The inner point of zero shear was observed to be closer to the bottom wall than the point of zero velocity

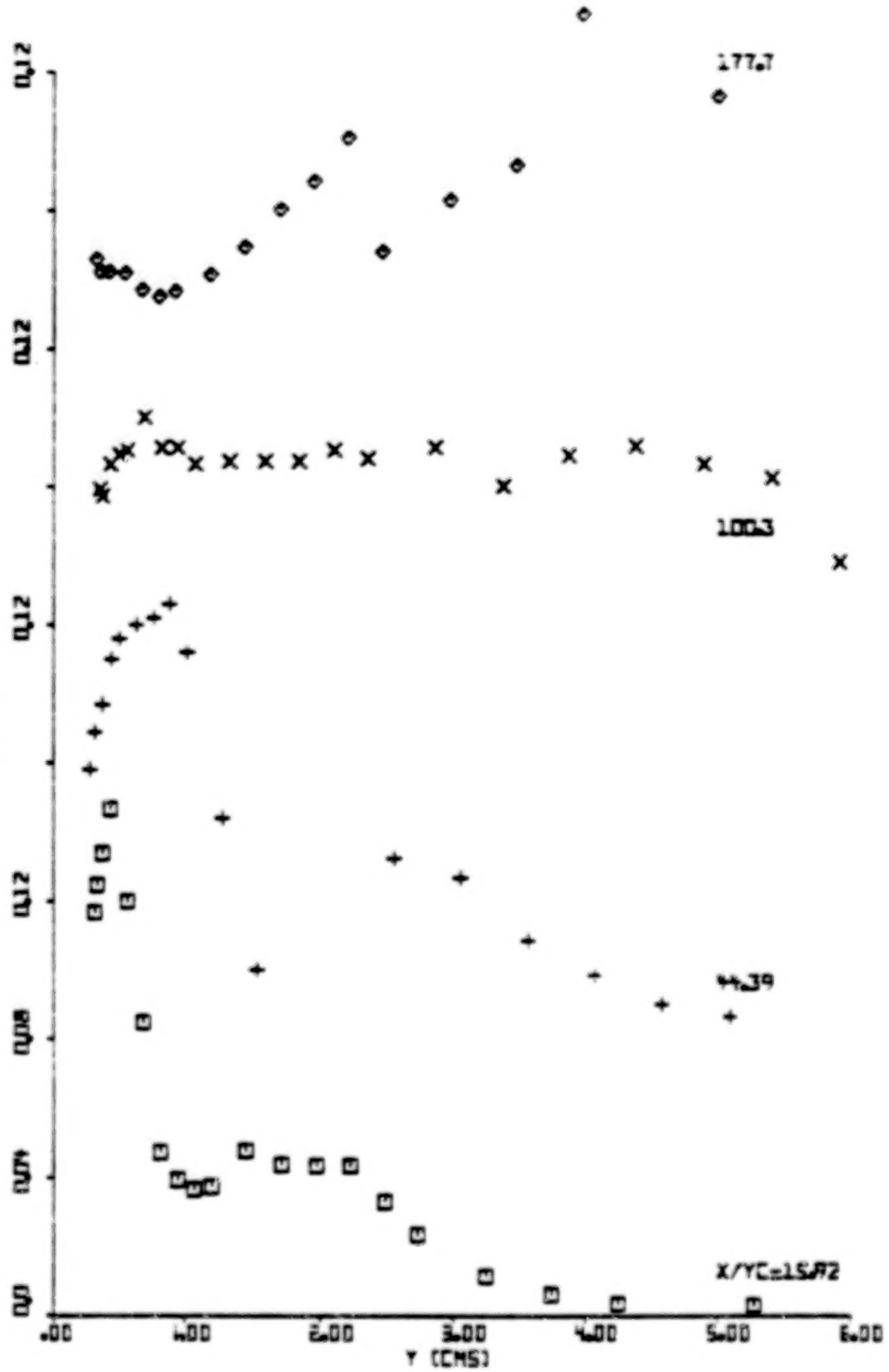

Fig. 5.11 Distributions of the Turbulence Intensity v_t/U_∞

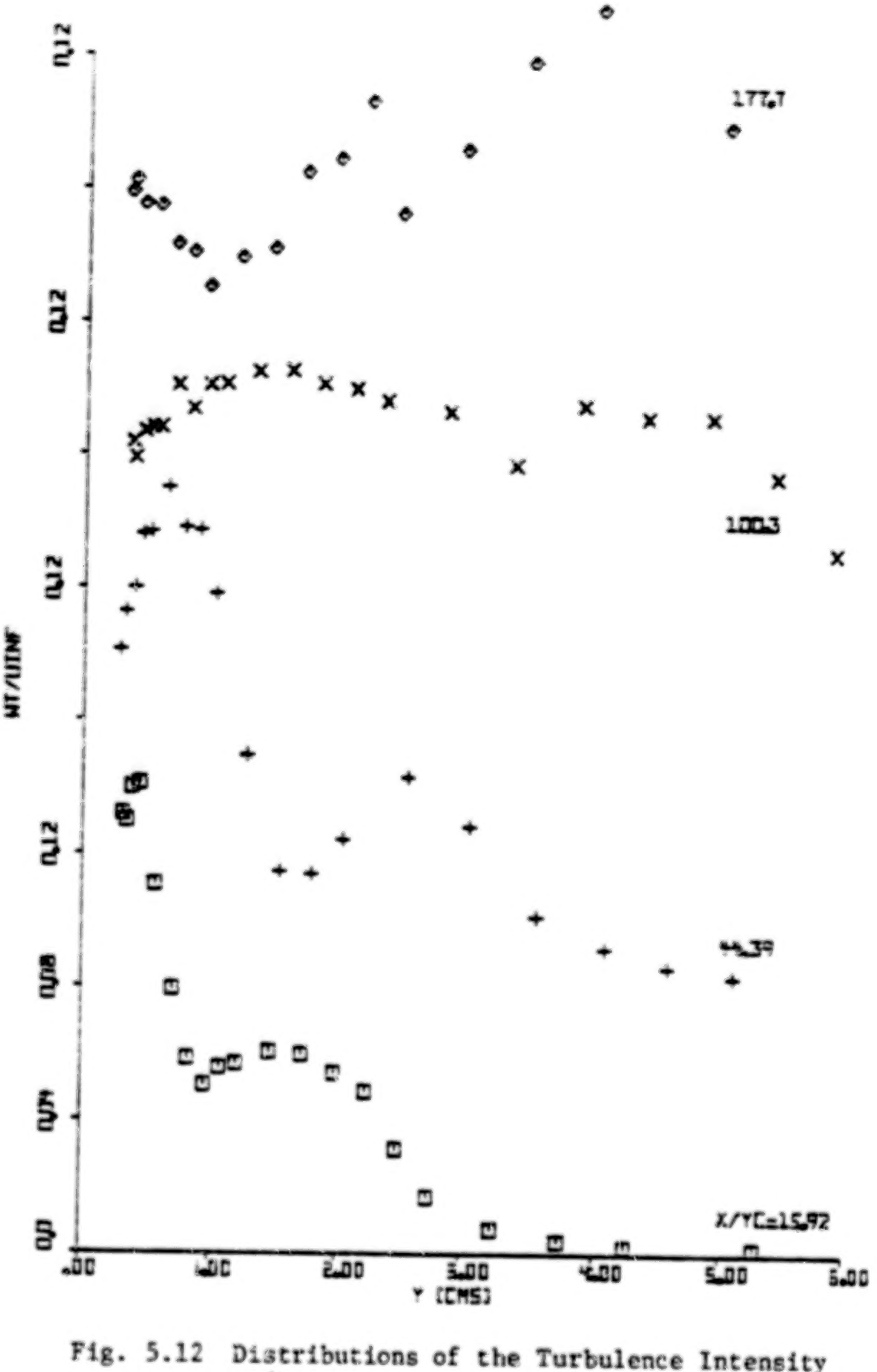

Fig. 5.12 Distributions of the Turbulence Intensity w_t/U_∞

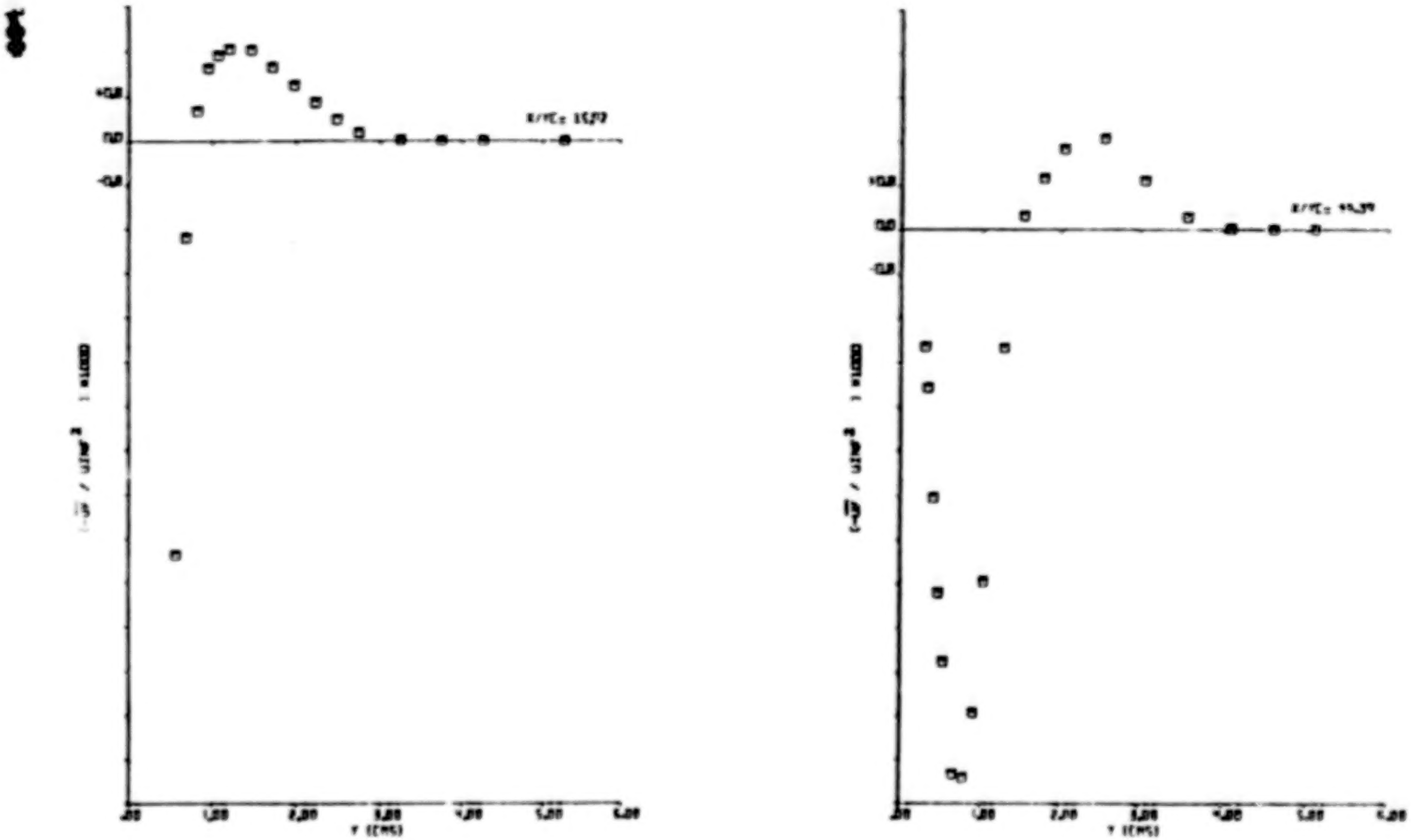

Fig. 5.13(a) Distribution of the Shear Stress at x/y_c = 15.92 and 44.39

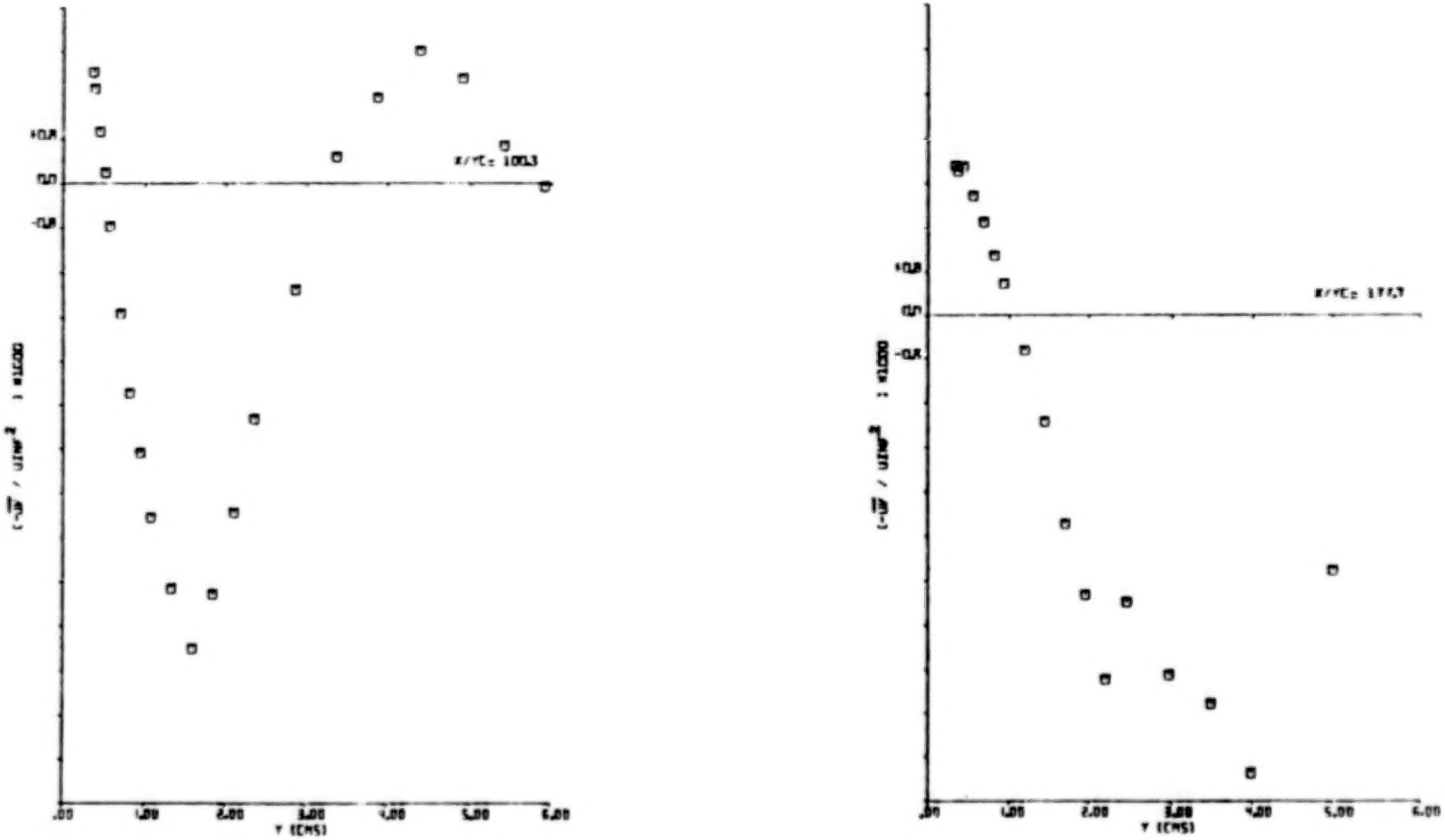

Fig. 5.13(b) Distribution of the Shear Stress at x/y_c = 100.3 and 177.7

gradient corresponding to the velocity maximum. The outer point of zero shear was also found to be closer to the bottom wall than the point of zero velocity gradient corresponding to the velocity minimum for stations x/y_c = 15.92 and 44.39. The above results concerning the position of the points of zero shear are in agreement with similar results reported in the literature on the wall jet data. However, the outer point of zero shear at x/y_c = 100.3 and 177.7 was found to be farther from the bottom wall than the point of zero velocity gradient corresponding to the minimum velocity. The slant-wire data were not corrected for the flow inclination (Appendix C). The flow inclination angle near the outer point of zero shear was found to be higher at x/y_c = 100.3 and 177.7. Therefore, the increased flow inclination angle may be responsible for the observed discrepancy in the position of the outer point of zero shear at x/y_c = 100.3 and 177.7. The points of maximum shear stress were found to be in the region of maximum velocity gradients between inner and outer points of zero shear and also between the outer point of zero shear and the freestream.

5.3.3 Turbulent Kinetic Energy k

Fig. 5.14 shows the distribution of turbulent kinetic energy. Generally, the positions of the maxima and minima in the turbulent kinetic energy were not well defined with respect to other variables. The point of

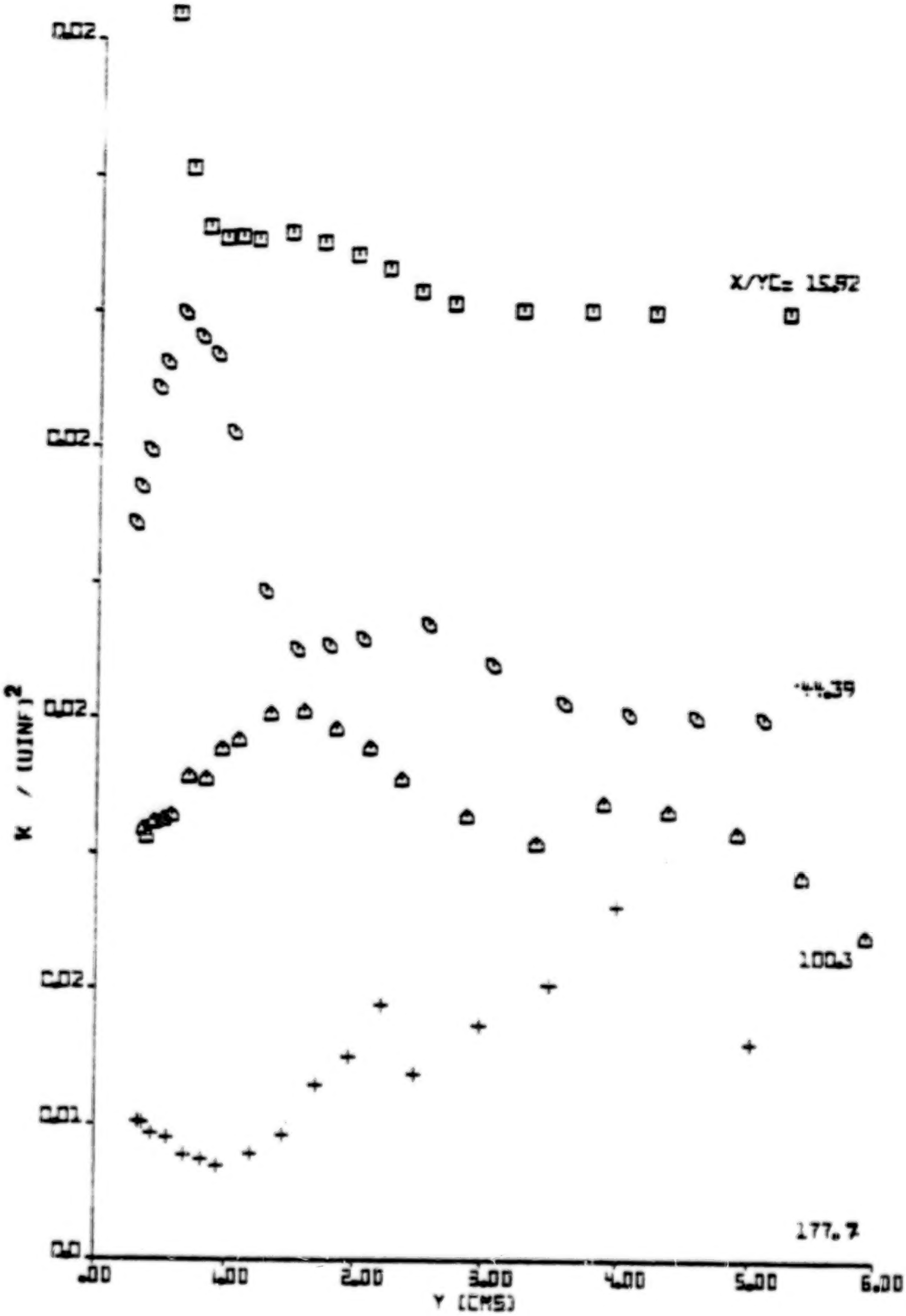

Fig. 5.14 Variation of the Turbulent Kinetic Energy k

maximum kinetic energy falls in the range of maximum velocity gradients and the maximum shear stress.

5.3.4 Correlation Functions R_{uv} and a_1

The significance and the definition of the correlation functions R_{uv} and a_1 are given in Chapter 4 under section 4.3.5. Figs. 5.15 and 5.16 show the distributions of the correlation functions R_{uv} and a_1 respectively. Both the functions become zero at the points of zero shear and they change sign according to the sign of $-\overline{uv}$. The maximum value of R_{uv} between the outer point of zero shear and the freestream is around +0.57 to start with, gradually decreasing to about +0.27 at $x/y_c = 100.3$. At $x/y_c = 177.7$, no positive values of R_{uv} can be observed since the slant-wire data did not extend far beyond the outer point of zero shear. The minimum value of R_{uv} between the inner and outer points of zero shear lies between -0.7 and -0.55.

Similarly, the maximum value of a_1 between the outer point of zero shear and the freestream is around ±0.15 to start with, gradually decreasing to about +0.09 at $x/y_c = 100.3$. The minimum value of a_1 between the inner and outer points of zero shear lies between -0.23 and -0.17. Both R_{uv} and a_1 tend to become zero in the freestream.

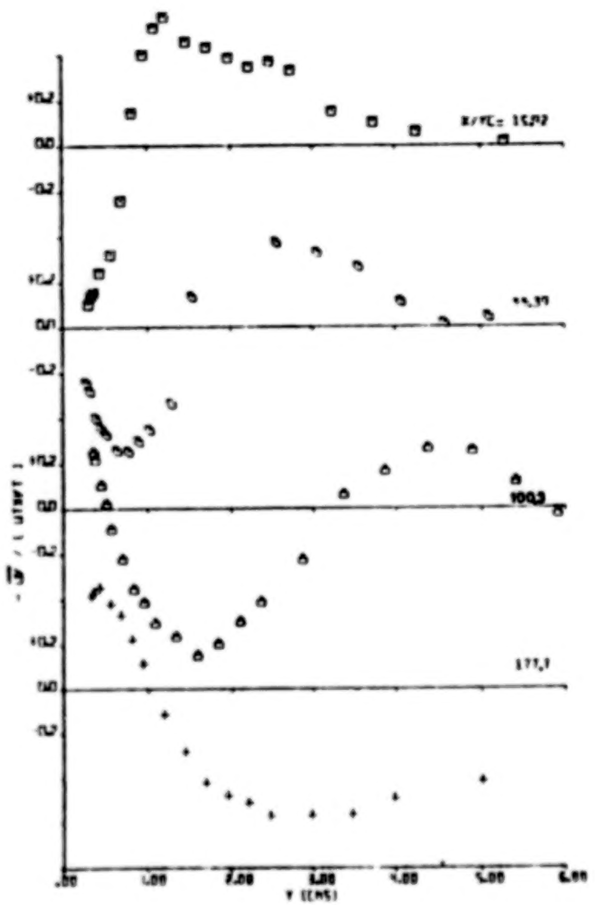

Fig. 5.15 Variation of the Correlation Function R_{uv}

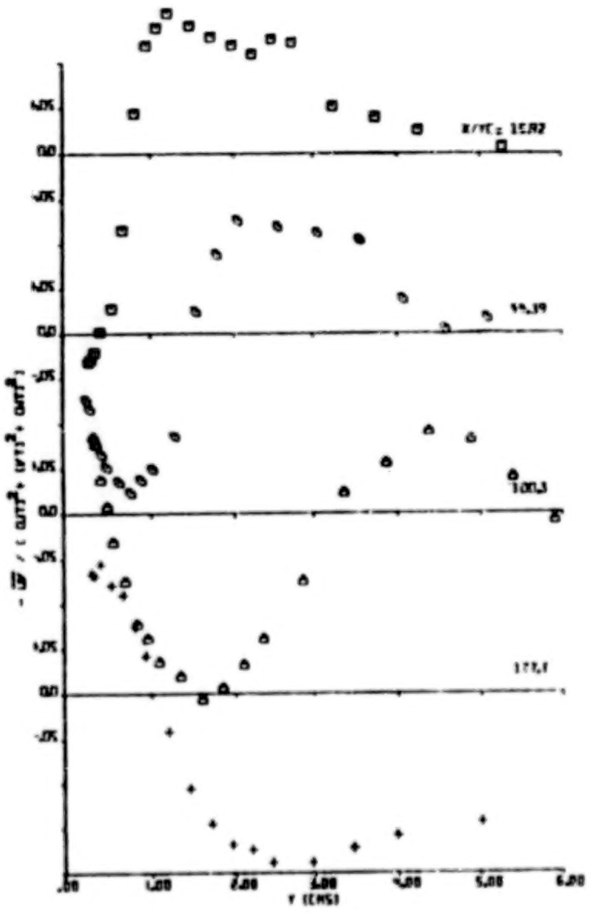

Fig. 5.16 Variation of the Correlation Function a_1

5.3.5 Eddy Viscosity

Fig. 5.17 shows the distributions of eddy viscosity $\nu_{eff} = -\overline{uv}\ (\partial U/\partial y)$. The trends of the experimental results are indicated by the dashed lines. It can be easily seen that there is a region of singularity exhibited at each station. As discussed earlier (section 4.3.6), the eddy viscosity becomes either negative or undefined in these singular regions. The eddy viscosity distribution at $x/y_c = 100.3$ exhibits two regions of singularity corresponding to the points of maximum and minimum velocity. The eddy viscosity finally drops to zero in the freestream. The present eddy viscosity distributions do not show any similarity behavior.

5.3.6 Mixing Length L_{mix} and Prandtl-Kolmogorov Length Scale L_k

The significance and the definitions of the Prandtl mixing length L_{mix} and the Prandtl-Kolmogorov length scale L_k were given in Chapter 4 under section 4.3.7. A value of $C_\mu = 0.2$ (Kacker and Whitelaw, 1968, 1971) was used in the evaluation of L_k. Fig. 5.18 and 5.19 show the distributions of L_{mix} and L_k respectively. The trends of the experimental data are shown in dashed lines. As in the case of eddy viscosity, both the length scale distributions show regions of singularity. The length scales become either negative or imaginary in these singular regions. The length scale distributions at $x/y_c = 100.3$

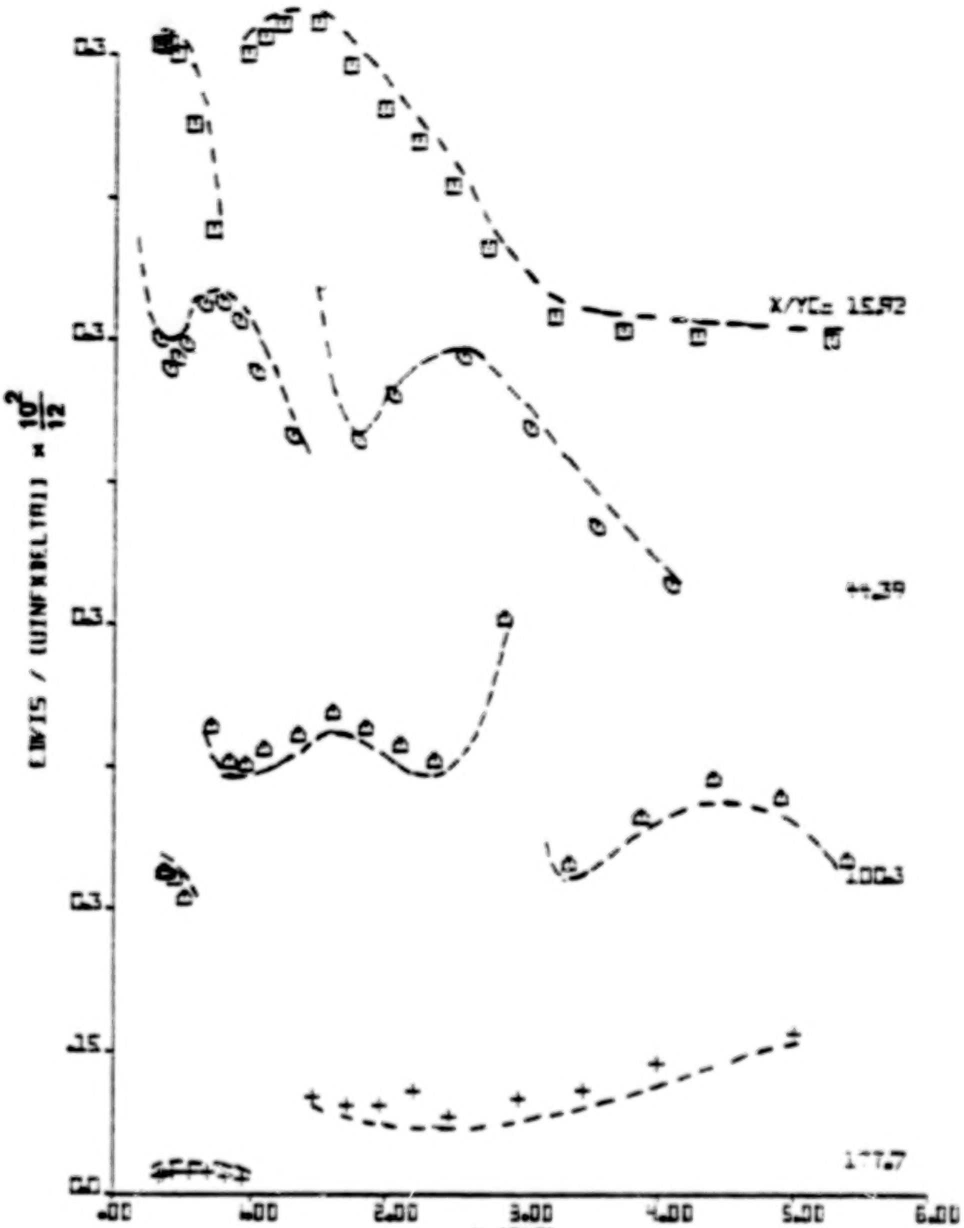

Fig. 5.17 Distributions of the Eddy Viscosity

---- Trends exhibited by the experimental data

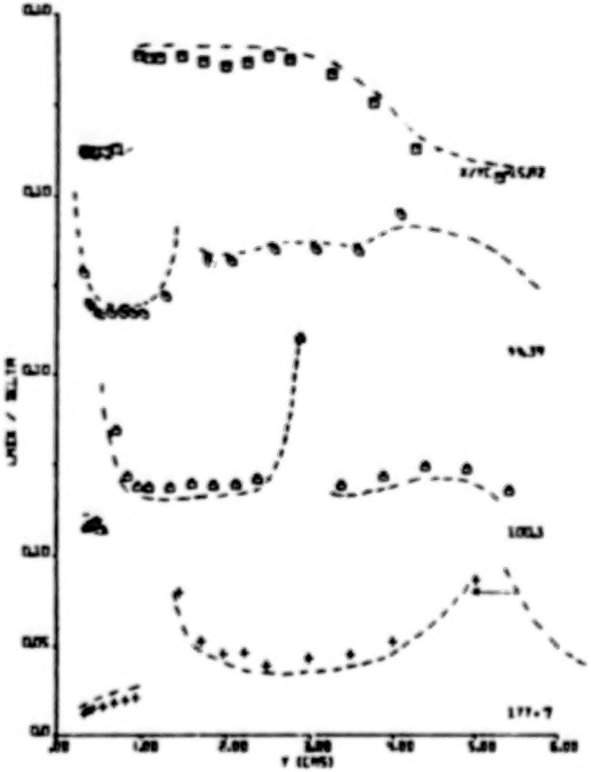

Fig. 5.18 Distributions of the Prandtl Mixing Length L_{mix}

---- Trends exhibited by the experimental data

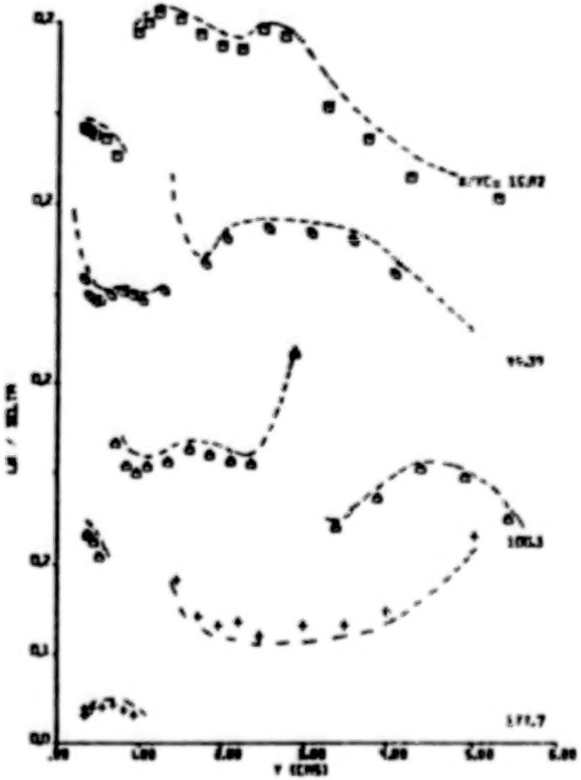

Fig. 5.19 Distributions of the Prandtl-Kolmogorov Length Scale L_k

---- Trends exhibited by the experimental data

exhibit two regions of singularity corresponding to the points of maximum and minimum velocity. The length scales (L_{mix} and L_k) beyond the outer point of zero shear were about three times higher than the length scales in between the inner and outer points of zero shear at $x/y_c = 15.92$. These length scales gradually become nearly equal at $x/y_c = 100.3$. Similarly, the length scales (L_{mix} and L_k) in between the inner and outer points of zero shear were about three times higher than the length scales below the inner point of zero shear at $x/y_c = 100.3$ and 177.7. The present length scale distributions do not show any similarity behavior.

5.3.7 Production of Turbulent Kinetic Energy

The significance of the shear stress production term $-\overline{uv}\ \frac{\partial U}{\partial y}$ was given in Chapter 4 under section 4.3.8. The shear stress production term was evaluated using the present measurements.

Fig. 5.20 shows the distribution of the shear stress production of turbulent kinetic energy given by $-\overline{uv}\ \frac{\partial U}{\partial y}\ (\delta/U_\infty^3)$ on a logarithmic scale. A small region was observed around the points of zero shear where the production became negative. This is because of the fact that the points of zero shear do not coincide with the points of zero velocity gradients due to which $\frac{\partial U}{\partial y}$ and $-\overline{uv}$ assume different signs in the region around the points of zero shear. The negative production terms were found

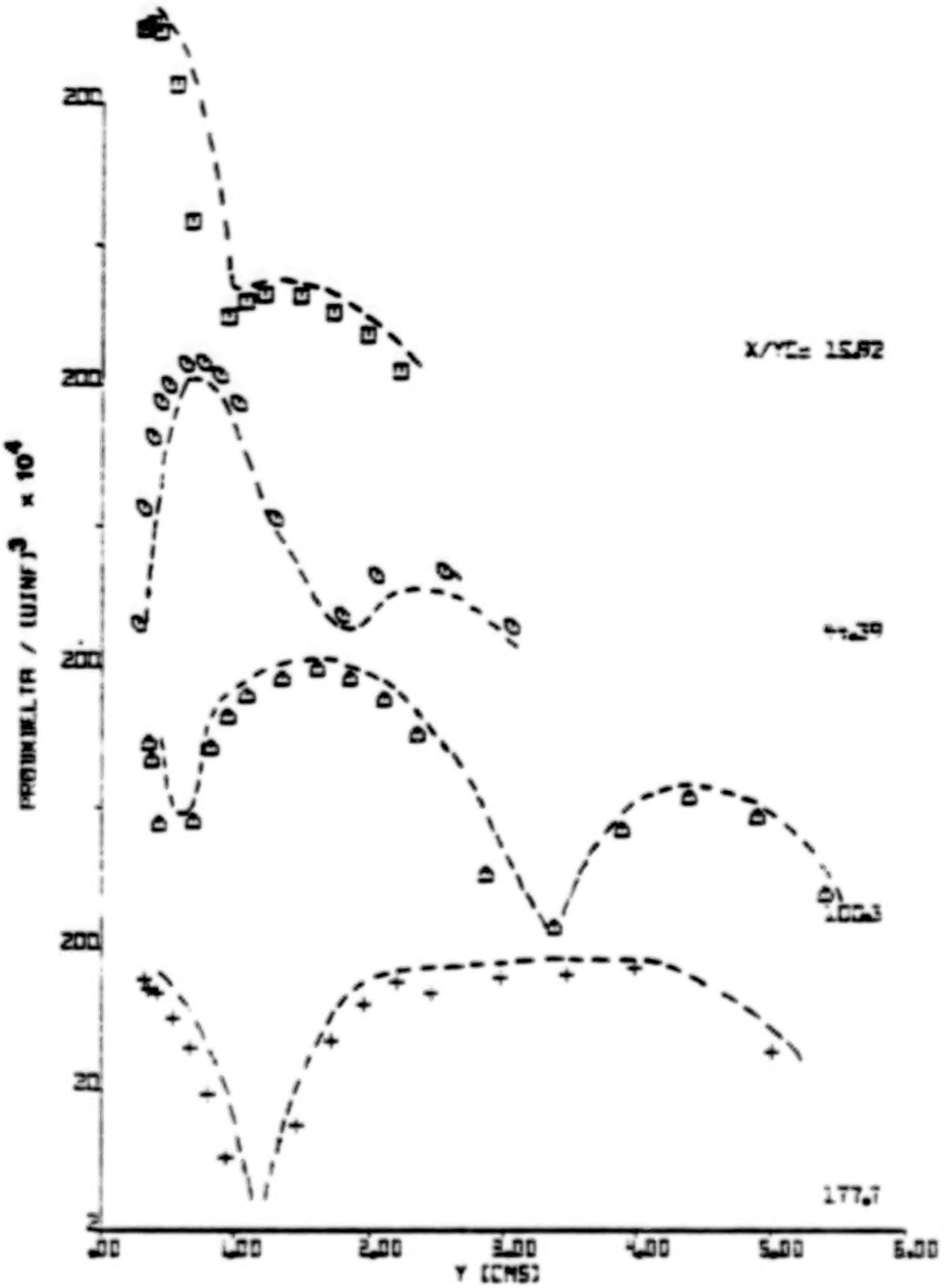

Fig. 5.20 Distributions of the Shear Stress Production of Turbulent Kinetic Energy

---- Trends exhibited by the experimental data

to be in the order of $-\overline{uv}\frac{\partial U}{\partial y}(\delta/U_\infty^3) = 1.5\text{X}10^{-4}$. The negative production points were not shown on the plots. It can be seen that the production level in the layer between the points of zero shear is about two orders of magnitude higher than that of in the layer beyond the outer point of zero shear to start with. Gradually, this difference in the production levels decreases as one goes downstream.

CHAPTER VI

PREDICTION METHOD

The objectives of the theoretical prediction of the present flows are as follows:

1. To investigate the applicability of an existing prediction method to the present flows

2. To investigate the ability of the theoretical prediction method to show the difference in the flow development between a uniform jet velocity profile and an asymmetric jet velocity profile

3. To establish that the asymmetric jet velocity profile has distinct advantages over uniform jet velocity profile.

6.1 Selection of the Prediction Method

A preliminary survey was made of the existing prediction methods for blown boundary layers in view of the above mentioned objectives. The integral methods, for example Kind (1971), tend to be disqualified in view of the second and third objectives mentioned above. The asymmetric jet velocity profile is a detail connected with the initial velocity profile, and integral methods are insensitive to such details of the profiles, since they perform integration over a region. In comparison, differential methods can incorporate the details of the initial velocity profiles like the asymmetric profile into the computational scheme.

Among the available differential methods, the method of Irwin (1974) was found to be the best suited for the present case of blown boundary layers. In contrast to other methods such as those of Launder and Spalding (1972), Ng and Spalding (1965), Hanjalic and Launder (1972), and Rodi (1972), Irwin's method is particularly suited for wall jets and blown boundary layers and it involves relatively less empiricism. For most of the other differential methods, different empirical constants are required in going from plane flows to axisymmetric flows, from "strong" shear flows to "weak" shear flows, and from plane flows to flows with streamline curvature. In comparison, the empirical constants in Irwin's method were found to be independent of the above restrictions.

Irwin has tested his prediction method for a variety of flows. They include wall jets in still air, blown boundary layers with pressure gradients, conventional boundary layers with and without pressure gradients and curved wall jets. Irwin's method gave accurate predictions of blown boundary layers with pressure gradients. The position of zero shear stress was predicted to be nearer to the wall than that of the velocity maximum in accord with the experimental data. Most of the other differential methods fail to predict this result since the turbulence models used in them imply that $-\overline{uv} = 0$ at $\frac{\partial U}{\partial y} = 0$. Irwin's prediction method also gave good results in the case of conventional boundary layers, curved wall jets, and wall jets in still air. Therefore, Irwin's method has been chosen as the best available method for the prediction of the present flows.

6.2 Description of the Theoretical Method

The prediction method developed by Irwin essentially uses the finite difference computing method developed by Spalding and Patankar (1967, 1969) and the turbulence model of Launder, Reece, and Rodi (1973). The turbulence model of Launder, Reece, and Rodi was modified to take account of the effect of the wall on turbulence and the effect of streamline curvature.

The starting point of Irwin's method is the Reynolds-averaged Navier-Stokes equations for incompressible fluids without body forces. For steady two-dimensional flows, the application of boundary layer approximations and the assumption of local isotropy along with the relevant mathematical manipulations will lead to the following set of equations for the mean momentum and the Reynolds stresses.

$$\frac{DU}{Dt} = -\frac{1}{\rho}\frac{dP}{dx} - \frac{\partial}{\partial y}(\overline{uv}) \qquad (6.1)$$

$$\frac{D}{Dt}(\tfrac{1}{2}\overline{u^2}) = -\overline{u^2}\frac{\partial U}{\partial x} - \overline{uv}\frac{\partial U}{\partial y} + \overline{p\frac{\partial u}{\partial x}} - \frac{\partial}{\partial y}(\tfrac{1}{2}\overline{vu^2}) - \frac{1}{3}\varepsilon \qquad (6.2)$$

$$\frac{D}{Dt}(\tfrac{1}{2}\overline{v^2}) = \overline{v^2}\frac{\partial U}{\partial x} - \overline{\frac{p}{\rho}\frac{\partial v}{\partial y}} - \frac{\partial}{\partial y}(\frac{\overline{pv}}{\rho}) - \frac{\partial}{\partial y}(\tfrac{1}{2}\overline{v^3}) - \frac{1}{3}\varepsilon \qquad (6.3)$$

$$\frac{D}{Dt}(\tfrac{1}{2}\overline{w^2}) = \overline{\frac{p}{\rho}\frac{\partial w}{\partial z}} - \frac{\partial}{\partial y}(\tfrac{1}{2}\overline{vw^2}) - \frac{1}{3}\varepsilon \qquad (6.4)$$

$$\frac{D}{Dt}(\overline{uv}) = -\overline{v^2}\frac{\partial U}{\partial y} + \overline{\frac{p}{\rho}(\frac{\partial u}{\partial y} + \frac{\partial v}{\partial x})} - \frac{\partial}{\partial y}(\frac{\overline{pu}}{\rho}) - \frac{\partial}{\partial y}(\overline{uv^2}) \qquad (6.5)$$

where

$$\frac{D}{Dt} = U\frac{\partial}{\partial x} + V\frac{\partial}{\partial y}$$

P and p are the mean and fluctuating components of pressure, ε is the dissipation rate, and ρ is the density.

The viscous term and the normal stresses term have been neglected in the mean momentum equation 6.1 because of the following reasons. For points away from the wall, the viscous terms were experimentally found to be negligible in fully-turbulent flows. Viscous terms are important only at points very close to the wall and the law of the wall velocity profile is generally applied in that region. The normal stresses term $\frac{\partial}{\partial x}(\overline{u^2} - \overline{v^2})$ is generally found to be small in comparison with the other terms in the mean momentum equation. As mentioned in Chapter 4 (section 4.2.3) and Chapter 5 (section 5.2.3), the contribution of the normal stresses term to the mean integral momentum equation was found to be small even in the present experiments.

6.2.1 Turbulence Model

The solution of the equation 6.1 to 6.5 requires that they should form a closed set. Equations 6.1 to 6.5 do not form a closed set unless the third order correlations in the equations 6.2 to 6.5 are expressed in terms of Reynolds stresses and the mean velocity. Also, the closure of the problem requires an equation for the dissipation rate ε.

The turbulence model of Launder, Reece, and Rodi (1973) was used in the closure of the equations 6.1 to 6.5. The original turbulence model of Launder et al. (1973) is basically applicable to free turbulent flows. Irwin (1974) modified the original model to account for the wall turbulence. This modification affects mainly the pressure-velocity-gradient correlations in the equations 6.2 to 6.5.

It should be mentioned here that the later work of Launder, Reece, and Rodi (1975) does take account of the wall turbulence.

The important features of the turbulence model of Launder, Reece, and Rodi (1973) are given below. This model is essentially a modified version of an earlier model by Hanjalic and Launder (1972). The major limitation of the model is that it is applicable only to those flow regions where the turbulence Reynolds number is high. The turbulence Reynolds number $R_{e\lambda}$ is given by $R_{e\lambda} = (\overline{u^2})^{\frac{1}{2}}\lambda/\nu$, where $\lambda = (15\nu\overline{u^2}/\varepsilon)^{\frac{1}{2}}$. The requirement of high turbulence Reynolds number enables the viscous diffusion term in the equations for the Reynolds stresses to be neglected. Also, under the condition of high turbulence Reynolds number, the very small eddies of turbulence responsible for the viscous dissipation are isotropic. This local isotropy condition implies that the viscous dissipation terms in each of the three equations for Reynolds normal stresses are equal to each other, taking the value $1/3\varepsilon$. The above assumptions are already incorporated in the equations 6.2 to 6.4.

The pressure diffusion terms $\frac{\partial}{\partial y}(\frac{\overline{pv}}{\rho})$ and $\frac{\partial}{\partial y}(\frac{\overline{pu}}{\rho})$ in equations 6.3 and 6.5 were neglected since they were found to be small from experimental data. The triple velocity correlations (equations 6.2 to 6.5) were modelled by simplifying the exact transport equation using the gradient diffusion principle. The quadruple velocity correlations appearing in the exact transport equation for the triple correlations were expressed in terms of the second order correlations, by assuming that the triple correlations are small and their distribution is Gaussian For the dissipation rate ε, a simplified transport equation obtained from the exact transport equation for ε was used. A number of approximations were made in obtaining the simplified transport equation for ε.

Using the condition of approximately homogeneous turbulence, and Rotta's (1951, 1962) considerations, the pressure-velocity-gradient correlations were expressed in terms of the mean velocity, Reynolds stresses and ε. However, Irwin (1974) introduced additional modifications in the pressure-velocity-gradient correlations to account for the wall turbulence.

Thus all the terms on the right-hand side of equation 6.2 to 6.5 have been expressed in terms of the Reynolds stresses and the mean velocity, resulting in a closed set of equations 6.1 to 6.5.

6.2.2 Computational Procedure

Irwin (1974) has predicted a variety of flows including the blown boundary layers using the method described above. The finite difference scheme of Spalding and Patankar (1967, 1969) was adopted to solve the set of equations 6.1 to 6.5. The "source" term is a terminology typical of the Spalding-Patankar scheme, which includes all the terms except the advection and diffusion for a given equation among the equations 6.1 to 6.5. This "source" term has been treated accordingly by Irwin for the Reynolds stress equations. However, Irwin uses an alternative procedure for the entrainment rate which worked well for the kind of flows he predicted. Details regarding the treatment of source terms, diffusion terms, entrainment and the boundary conditions as applicable to Spalding-Patankar's scheme, can be found in Irwin's (1974) work.

The step size was taken as a fraction of the total flow width. Irwin suggested this fraction to be 0.05 for blown boundary layers. He also suggested the number of grid points to be between 50 and 60.

6.2.3 Starting Procedure

The solution of the equations 6.1 to 6.5 using the computer scheme mentioned above requires the specification of the initial starting profiles. The profiles of mean velocity, Reynolds stresses and the dissipation rate are to be specified at the starting station as a part of the starting procedure.

Irwin has used two types of starting procedures:

1. Available experimental velocity and turbulence profile data as the starting profiles, and

2. An "automatic starting" procedure.

Both of these starting procedures were used in the present case in order to examine their effects on the computed results. The first method is straightforward. However, the second method involves certain assumptions and needs to be studied in greater detail. Therefore, the "automatic starting" procedure is described in detail in the following paragraphs.

The term "automatic starting" stems from the fact that it develops the initial profiles automatically using the given integral parameters at the jet slot as input. In blown boundary layers, the region near the slot really requires the solution of an elliptic set of equations rather than the parabolic set used in the present calculations. However, the "automatic starting" procedure assumes that the region over which the governing equations are elliptic does not extend very far downstream and that further downstream the flow is mainly affected by the initial momentum of the jet, the momentum thickness of the boundary layer on the slot lip, the value of its form parameter, and the logitudinal pressure gradient. The elliptic nature of the flow near the slot was thus ignored and the parabolic equations were used right from the slot exit plane. A problem arises, however, because at the slot there is a region of zero velocity on the downstream face of the slot lip and the parabolic method cannot handle such a region. This was overcome by replacing the real starting profile by an equivalent one which was acceptable to the parabolic method.

The "automatic starting" procedure of Irwin generates the starting velocity profile in two following steps:

1. The real velocity profile at the slot was first replaced with a top-hat profile in the jet and a power law profile in the boundary layer on the slot lip as shown in Fig. 6.1 (a). The velocity U_J in the jet is such that the momentum of the jet is the same as the momentum in the real jet. The value of δ_{BL} and the exponent 1/n of the boundary layer region were such as to give the same value of δ_{2BL} and H_{BL} as the real profile.

2. The equivalent profile shown in Fig. 6.1 (a) was replaced by another profile which has the same momentum and mass flux as the first one but contains a mixing layer joining the jet and the boundary layer regions. The new velocity profile is shown in Fig. 6.1 (b). A cosine velocity profile was adopted for the mixing layer. By making a mass and momentum balance between the profiles shown in Figs. 6.1 (a) and 6.1 (b), the entire velocity profile shown in Fig. 6.1 (b) can be generated. The profile shown in Fig. 6.1 (b) is the actual starting velocity profile used in the computations with automatic starting conditions.

This procedure needs $\frac{\delta_{2J}}{y_c}$, $\frac{\delta_{2J}}{\delta_{2BL}}$, H_{BL} and "a" as the input. Here, "a" is the fraction of the slot height over which the velocity profile is assumed to be uniform

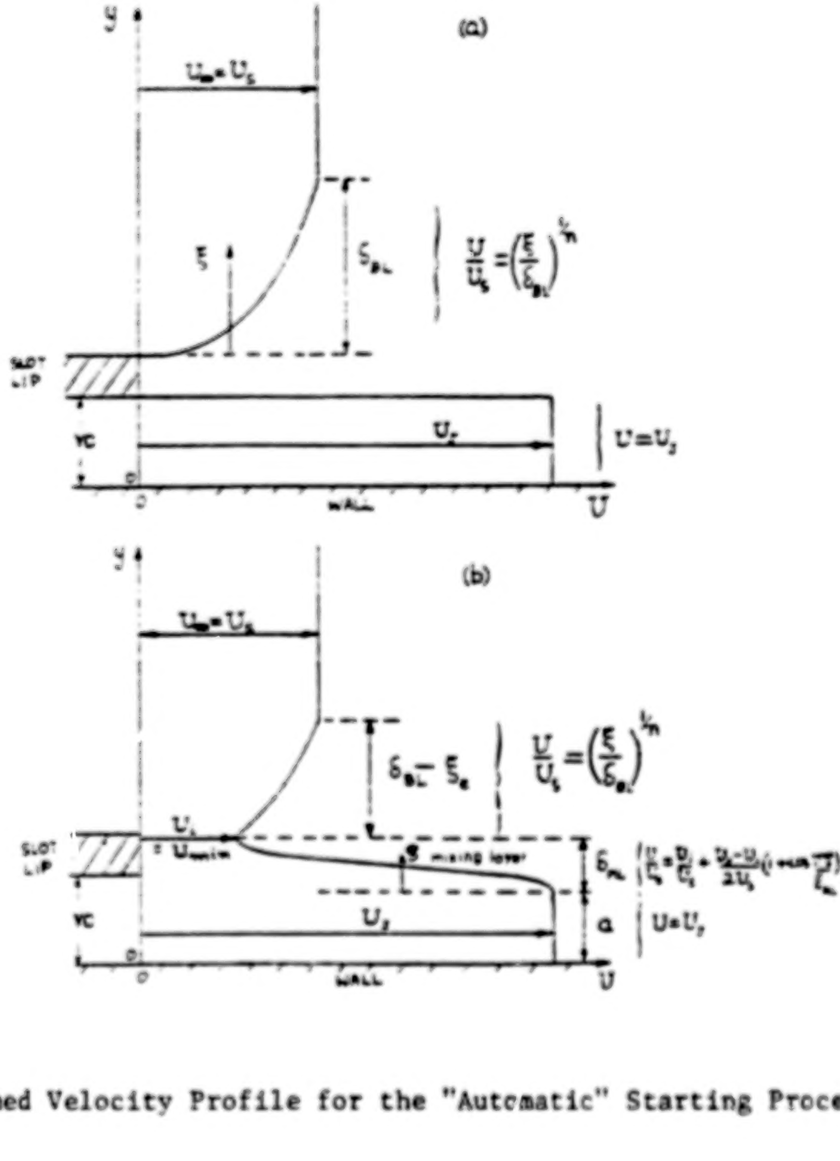
(a)
y
$U_\infty = U_s$
ξ
δ_{BL}
$\frac{U}{U_s} = \left(\frac{\xi}{\delta_{BL}}\right)^{1/n}$
SLOT LIP
YC
U_J
$U = U_J$
0
WALL
U
(b)
y
$U_\infty = U_s$
$\delta_{BL} - \xi_e$
$\frac{U}{U_s} = \left(\frac{\xi}{\delta_{BL}}\right)^{1/n}$
SLOT LIP
$U_s = U_{min}$
ξ mixing layer
δ_m
$\frac{U}{U_s} = \frac{U_J}{U_s} + \frac{U_s - U_J}{2U_s}\left(1 + \sin \frac{\pi \xi}{\delta_m}\right)$
YC
U_J
a
$U = U_J$
0
WALL
U

Fig. 6.1 Assumed Velocity Profile for the "Automatic" Starting Procedure

as shown in Fig. 6.1 (b), δ_{2BL} is the momentum thickness of the boundary layer above the slot lip, H_{BL} is the form parameter of the boundary layer above the slot lip and $\frac{\delta_{2J}}{y_c} = \frac{U_J}{U_\infty} (1 - \frac{U_J}{U_\infty})$. Irwin recommends a value of $a = 0.6$.

6.2.3 (a) Starting Turbulence Profiles

The starting distributions of the Reynolds stresses for the automatic procedure were obtained as follows. The starting profiles for the mixing layer and the boundary layer are given first followed by the profiles for the jet portion.

The $-\overline{uv}$ profile was calculated from $-\overline{uv} = \nu_{eff}(\partial U/\partial y)$ with empirical expressions for the eddy viscosity in the mixing layer and the boundary layer. The three normal stresses ($\overline{u^2}$, $\overline{v^2}$, and $\overline{w^2}$) were set equal to each other and equal to $|-\overline{uv}|/0.45$, with their minimum values not allowed to go below the free-stream turbulence level. The dissipation rate was set equal to the rate of production of turbulent kinetic energy, i.e., $\varepsilon = -\overline{uv}\ (\partial U/\partial y)$.

For the jet region, $-\overline{uv}$ is equal to zero. The three normal stresses ($\overline{u^2}$, $\overline{v^2}$, and $\overline{w^2}$) were set equal to each other and equal to $(0.03\ U_J)^2$. The dissipation was set equal to $\frac{4k^{3/2}}{y}$ where k is the turbulent kinetic energy.

Here it should be noted that the starting turbulence profiles used in the automatic starting procedure do not represent the actual conditions and involve certain arbitrary assumptions. However, as Irwin (1974) has indicated, the wall jet flows were observed to be fairly insensitive to the starting turbulence conditions at the slot.

6.3 Comments on the Automatic Starting Procedure

Even though the automatic starting procedure was primarily developed for blown boundary layers, Irwin (1974) used it satisfactorily for several other types of flows also, such as wall jets in still air, self-preserving wall jets, curved wall jets, and boundary layers. Hence, the automatic starting procedure was used with confidence in the present case backed by Irwin's satisfactory predictions using the automatic starting procedure. It may be noted here that for any details regarding the theoretical method and the computational procedure, the work of Irwin (1974) should be referred to.

CHAPTER VII

COMPUTED RESULTS

The purpose of this chapter is to present the results of the computations using the prediction method described in Chapter 6 and to theoretically establish the effectiveness of an asymmetric jet velocity profile over the uniform jet velocity profile.

One of the major assumptions made in the present predictions was that the "automatic starting" velocity profile described in Chapter 6 and shown in Fig. 6.1 (b) represents the case of a uniform jet velocity profile. In other words, a uniform jet velocity is assumed to result in a velocity profile shown in Fig. 6.1 (b) at a few slot heights downstream of the slot. The good quality of the predictions made by Irwin (1974) in a number of wall jet cases using the automatic starting procedure for a uniform jet velocity profile confirms that the above assumption is a valid one.

The present computed results are classified into three categories:

1. Predictions of the zero pressure gradient flow were made using the experimental initial velocity and turbulence profiles and were compared with the experimental

data. The results were then compared with the computations using the automatic starting procedure for a uniform jet velocity profile with the same jet momentum as the experimental asymmetric profile at the slot.

2. Predictions of the adverse pressure gradient flow were made using the experimental initial velocity and turbulence profiles and were compared with the experimental data. The results were then compared with the predictions using the automatic starting procedure for a uniform jet velocity profile with the same jet momentum as the experimental asymmetric profile at the slot.

3. Comparison of the computations for the adverse pressure gradient flow using the automatic starting procedure with two different types of jet velocity profiles; uniform jet velocity profile and a hypothetical linear jet velocity profile described later in this chapter to represent the ideal case of an asymmetric jet velocity profile.

7.1 Prediction of the Zero Pressure Gradient Flow

7.1.1 Computations Using the Experimental Initial Velocity and Turbulence Profiles

The computations were done using the prediction method described in Chapter 6. The experimental velocity and turbulence profiles at $x/y_c = 16.5$ were given as the starting profiles. The station $x/y_c = 16.5$ was chosen as the starting station because it was the first station

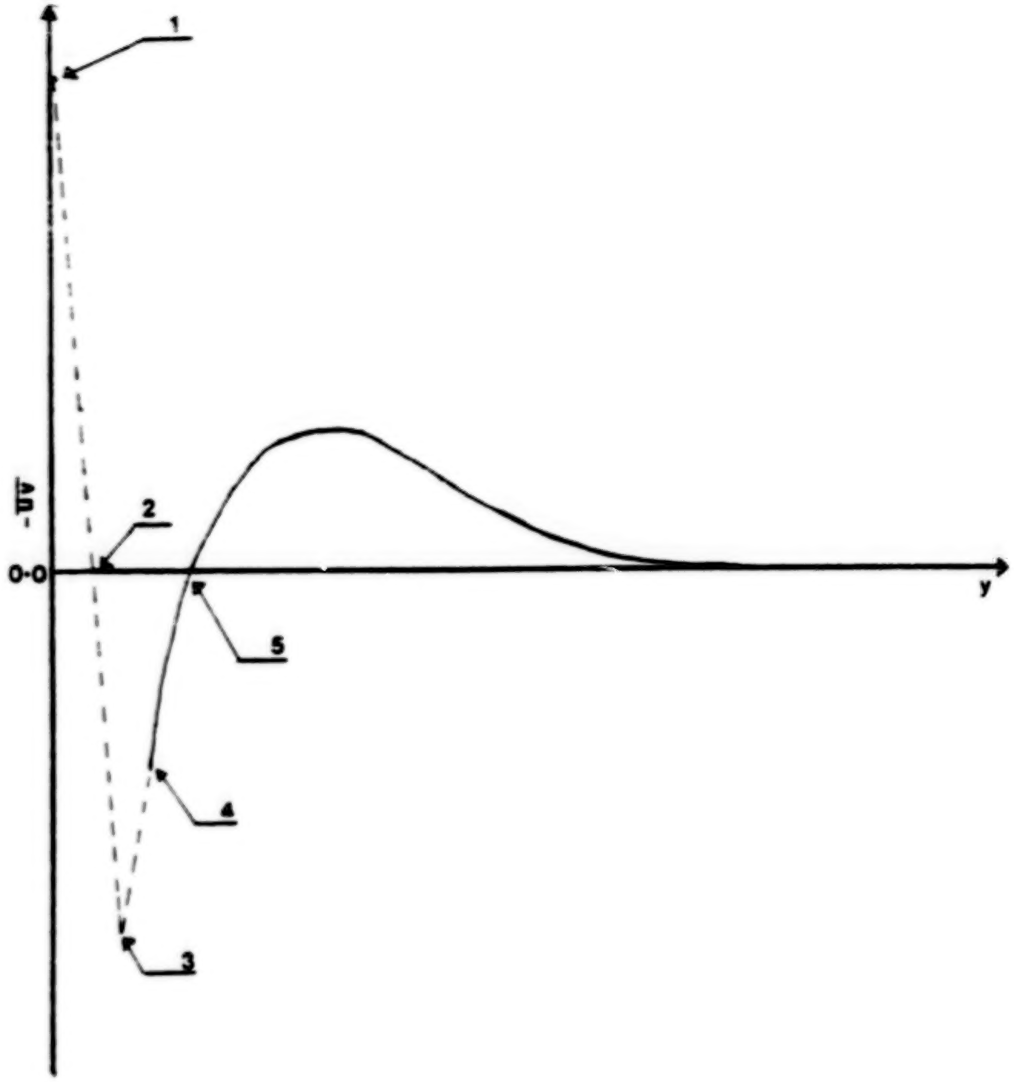

Fig. 7.1(a) Initial Profile of $-\overline{uv}$ for the Computations Using Experimental Initial Profiles in the case of Zero Pressure Gradient Flow

—— experimental distribution; ---- assumed distribution

1. First normal hot-film data point where

$$\frac{-\overline{uv}}{U_\infty^2} = \frac{C_f}{2}$$

2. Point of maximum velocity where $-\overline{uv} = 0$
3. Point of maximum $|-\overline{uv}|$
4. First slant-wire data point
5. Point of minimum velocity

downstream of the slot and away from the slot where slant-wire turbulence measurements were available.

7.1.1 (a) Initial Mean Velocity and $\overline{u^2}$ Profiles

The measured normal hot-film data of the mean velocity and $\overline{u^2}$ at $x/y_c = 16.5$ were used as the initial profiles. The grid points coincided with the data points in number and position.

7.1.1 (b) Initial Profiles of $\overline{v^2}$, $\overline{w^2}$, $-\overline{uv}$, and ε

The slant-wire data of $\overline{v^2}$, $\overline{w^2}$, and $-\overline{uv}$ were interpolated to obtain their values corresponding to the position of the normal hot-film. However, the slant-wire data did not extend as close to the wall as the normal hot-film data. Therefore, the following assumptions were made for the profiles of $\overline{v^2}$, $\overline{w^2}$ and $-\overline{uv}$ between the first normal hot-film data point and the first slant-wire data point. $\overline{v^2}$ and $\overline{w^2}$ were set equal to $\overline{u^2}$. A linear variation of $-\overline{uv}$ was assumed with $-\overline{uv} = 0$ at the point of maximum velocity. Fig. 7.1 (a) shows the assumed $-\overline{uv}$ distribution. The dissipation rate $\varepsilon = 0.3k(\partial U/\partial y)$ was assumed as suggested by Irwin (1974), where k is the turbulent kinetic energy. The step size was taken as .03 times the flow width.

7.1.1 (c) Results

The computed velocity profiles are compared with the experimental data in Figs. 4.4 (c-e). The computed profiles were shown only at selected representative stations to prevent overcrowding. The predictions compare well with the data. Figs. 7.1 (b-d) show the predictions of δ_1, δ_2, and C_f compared with the data. The agreement between the experimental data and the predictions is generally good. However, the predicted values of δ_1 and δ_2 are lower than the data at far downstream stations and the predicted C_f values are lower than the data by about a maximum of 10%.

Fig. 7.1 (e) shows the predicted development of profile length scales, Y_{max}, Y_{half}, and Y_{min}. Fig. 7.1 (f) shows the predicted variation of U_{max} and U_{min} compared with experiments. Here also the agreement is good.

7.1.2 Computations Using the Automatic Starting Procedure

The predicted results using the automatic starting procedure for zero pressure gradient flow are shown in Figs. 7.1 (b-f) along with the experimental data and the computations using experimental starting profiles. A value of a = 0.6 was used as suggested by Irwin. The fraction of the slot height over which the velocity is assumed to be uniform is "a," as shown in Fig. 6.1 (b). The number of grid points used was 60. The step size was chosen as .015 times the flow width up to $x/y_c = 15.0$ and .03 times the flow width after $x/y_c = 15.0$.

The computations using the automatic starting procedure did not show any major difference as compared to the computations using the experimental initial profiles. On the basis of the arguments given in Chapter 4, it was expected that the growth rate of Y_{max} would be lower, while the growth rates of Y_{half}, Y_{min}, δ_1 and δ_2 would be higher

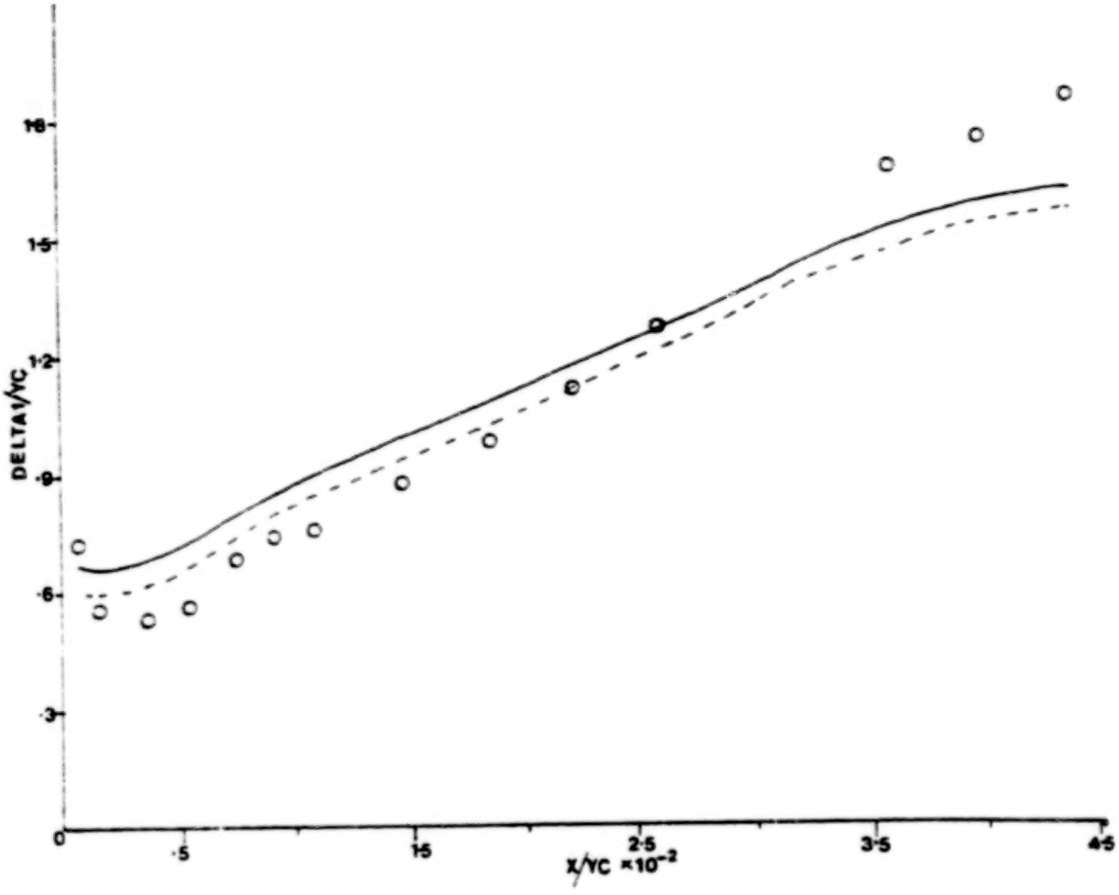

Fig. 7.1(b) Predicted Development of the Displacement Thickness for the Zero Pressure Gradient Flow

○ Experimental Data

---- Predictions using the experimental initial profiles

—— Predictions using the automatic starting procedure

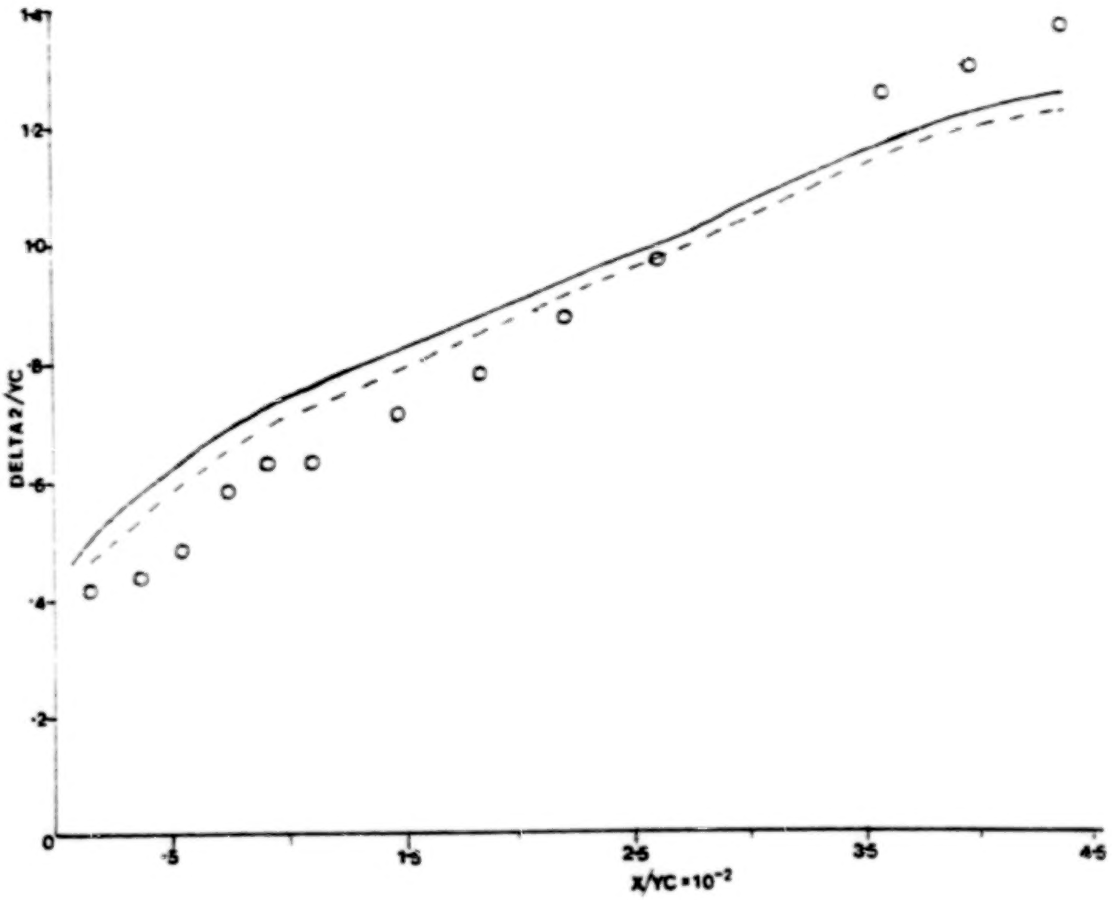

Fig. 7.1(c) Predicted Development of the Momentum Thickness for the Zero Pressure Gradient Flow

○ Experimental Data

---- Predictions using the experimental initial profiles

____ Predictions using the automatic starting procedure

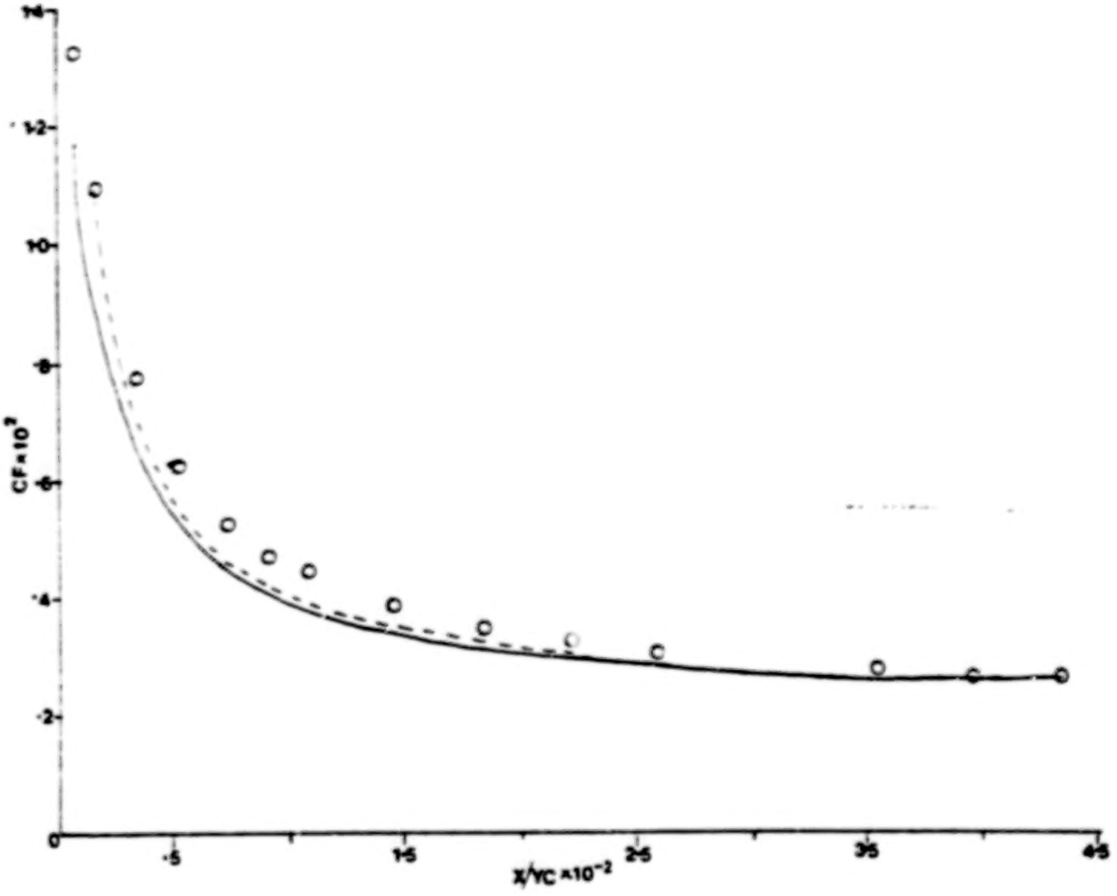

Fig. 7.1(d) Predicted Variation of the Skin Friction for the Zero Pressure Gradient Flow

○ Experimental Data

---- Predictions using the experimental initial profiles

—— Predictions using the automatic starting procedure

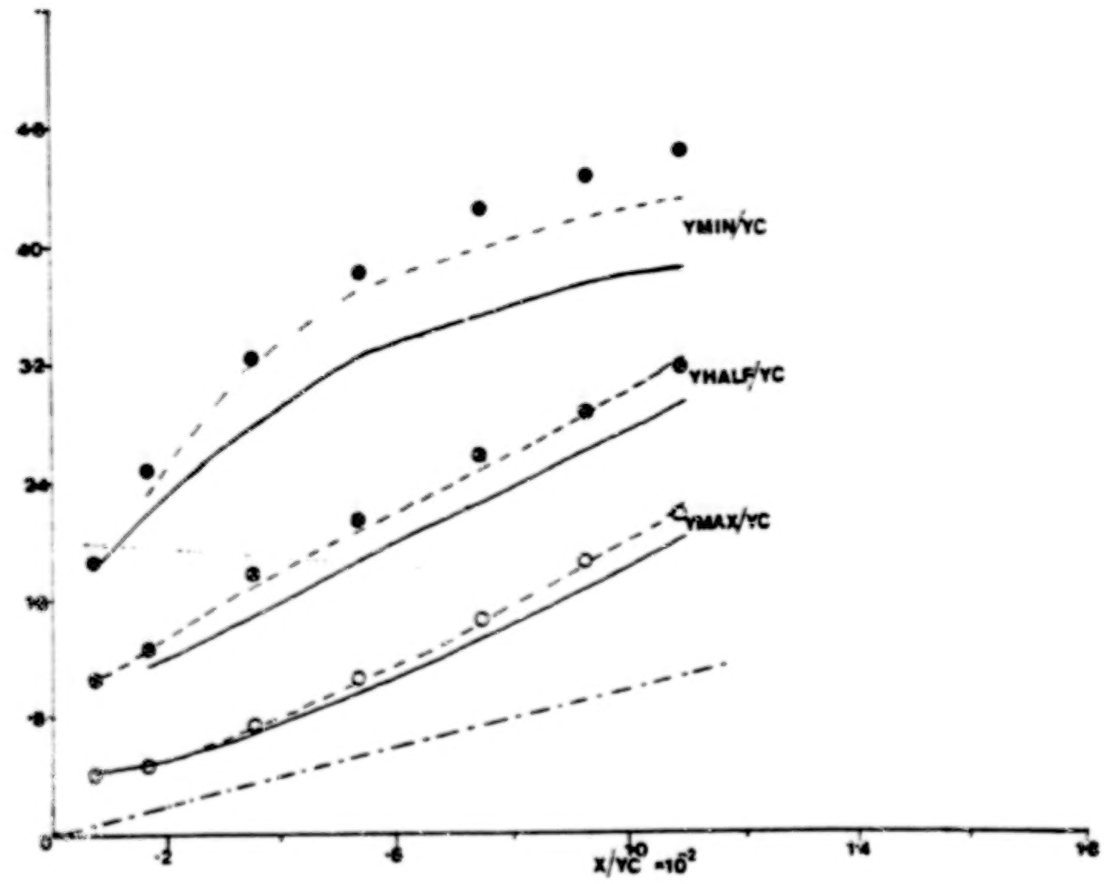

Fig.7.1(e) Predicted Variation of the Profile Length Scales for the Zero Pressure Gradient Flow

○, ◉, ● Experimental Data

---- Predictions using experimental initial profiles

—— Predictions using the automatic starting procedure

— -- — — — Universal Y_{max} distribution

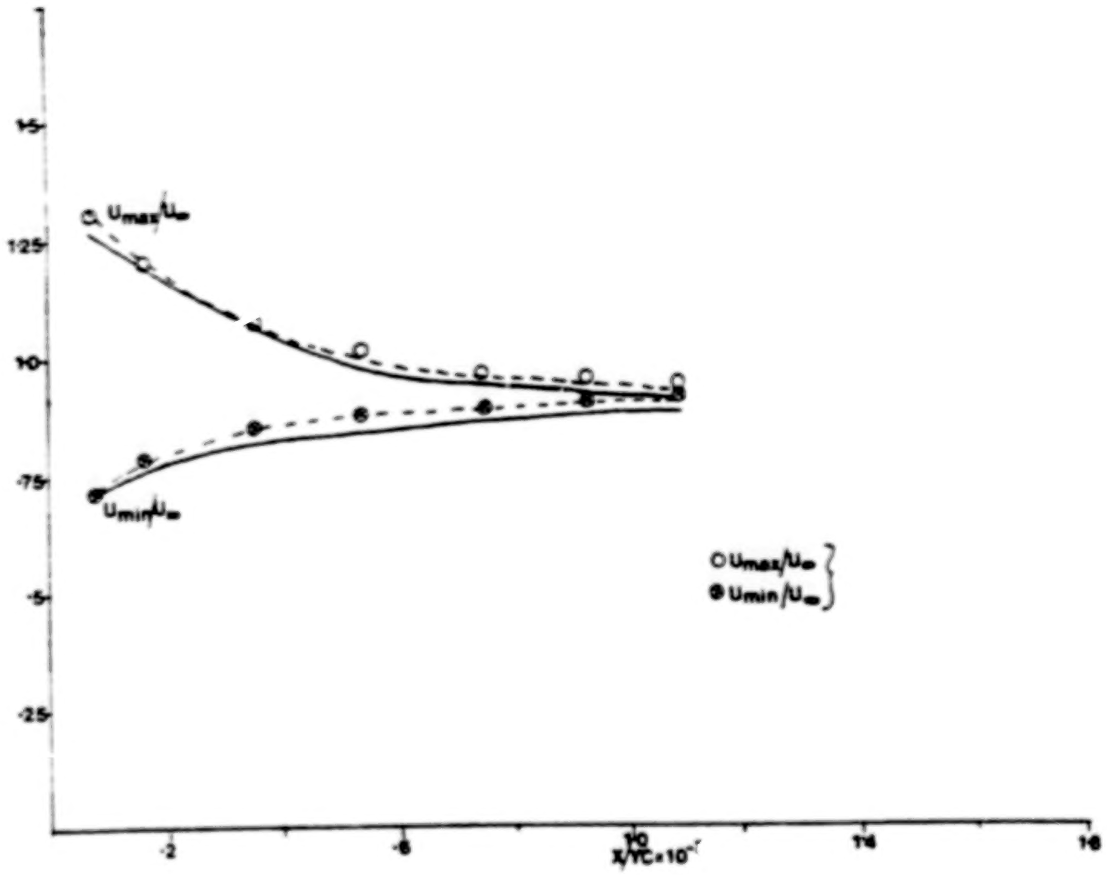

Fig. 7.1(f) Predicted Variation of U_{max} and U_{min} for the Zero Pressure Gradient Flow

○, ● Experimental Data

---- Predictions using the experimental initial profiles

—— Predictions using automatic starting procedure in the case of automatic starting procedure. This is due to the unique behavior of an experimental asymmetric jet velocity profile as compared with a uniform jet velocity profile used in the automatic starting procedure. The predictions showed that the growth rate of Y_{max} distribution was tending towards the universal Y_{max} distribution discussed earlier in Chapter 4. However, the predicted growth rates of Y_{half} and Y_{min} were lower instead of being higher. The predicted growth rates of δ_1 and δ_2 were almost the same as those predicted using experimental initial conditions.

The present discrepancies between the predictions using experimental asymmetric jet velocity profile and the predictions using uniform jet velocity profile (automatic starting procedure) might be due in part to the inability of the prediction method to show the difference in uniform and asymmetric profiles when no pressure gradient was imposed on the flow. This is further confirmed by the predictions in the case of adverse pressure gradient flow.

The superiority of an asymmetric profile can be justified on the following physical grounds even though it has not been revealed by the predictions. The asymmetric profile has lower velocity gradients at the wall than a uniform velocity profile and this feature results in reduced momentum losses due to friction at the wall. The asymmetric profile has a higher concentration of momentum in the upper portion of the slot. This feature provides greater momentum to the momentum deficient area of the upstream boundary layer and results in the even distribution of momentum. As mentioned later in section (7.3.3), the mass flow rate in the case of an asymmetric profile is less than that of a uniform profile for the same total jet momentum. This feature results in savings in mass flow rate in the case of an asymmetric profile.

7.1.2 (a) Universal Y_{max} Distribution

According to Narayan (1973), the value of the quantity $\delta_{2s} = \delta_{2BL}U_\infty^2/(U_{Jave}^2\ y_c)$ should be low to observe the universal Y_{max} distribution mentioned in Chapter 4. Accordingly, a few prediction runs were made using the automatic starting procedure with U_{Jave} and y_c values higher than in the experiments, thereby reducing the value of δ_{2s}. The results show that the Y_{max} distribution does not follow the universal Y_{max} distribution when the momentum deficit of the upstream boundary layer is relatively higher. The value of δ_{2s} was of the order of 0.48 in the present experiments.

7.2 Predictions of the Adverse Pressure Gradient Flow

7.2.1 Computations Using Experimental Initial Profiles of Velocity and Turbulence

Predictions of the adverse pressure gradient flow were made using the velocity and turbulence profiles at $x/y_c = 15.92$ as the starting profiles.

7.2.1 (a) Initial Mean Velocity and $\overline{u^2}$ Profiles

The measured normal hot-film data of the mean velocity and $\overline{u^2}$ at $x/y_c = 15.92$ were used as the initial profiles. The grid points coincided with the data points in number and position.

7.2.1 (b) Initial Profiles of $\overline{v^2}$, $\overline{w^2}$, $-\overline{uv}$ and ε

The initial profiles of $\overline{v^2}$, $\overline{w^2}$, $-\overline{uv}$ and ε were obtained in the same way as given in section 7.1.1 (b). Fig. 7.2 (a) shows the assumed $-\overline{uv}$ distribution. The step size was taken as 0.03 times the flow width.

7.2.1 (c) Results

The predicted velocity profiles were compared with the experimental data in Figs. 5.4 (b) and 5.4 (c). The agreement is good up to $x/y_c = 72.14$. The predictions deviate from the experimental data from $x/y_c = 100.3$ onwards. However, the predictions were good in the outer layer even after $x/y_c = 100.3$. The predictions were not shown beyond $x/y_c = 177.7$ because the outer edge of the outer layer was already touching the top wall at $x/y_c = 177.7$. However, the computations proceeded all the way up to $x/y_c = 360.8$ without any instabilities in the calculations. The predicted velocity profile at $x/y_c = 360.8$ was found to be a normal one, without any regions of large momentum deficit.

Figs. 7.2 (b-h) show the various predicted integral and profile parameters compared with experimental data.

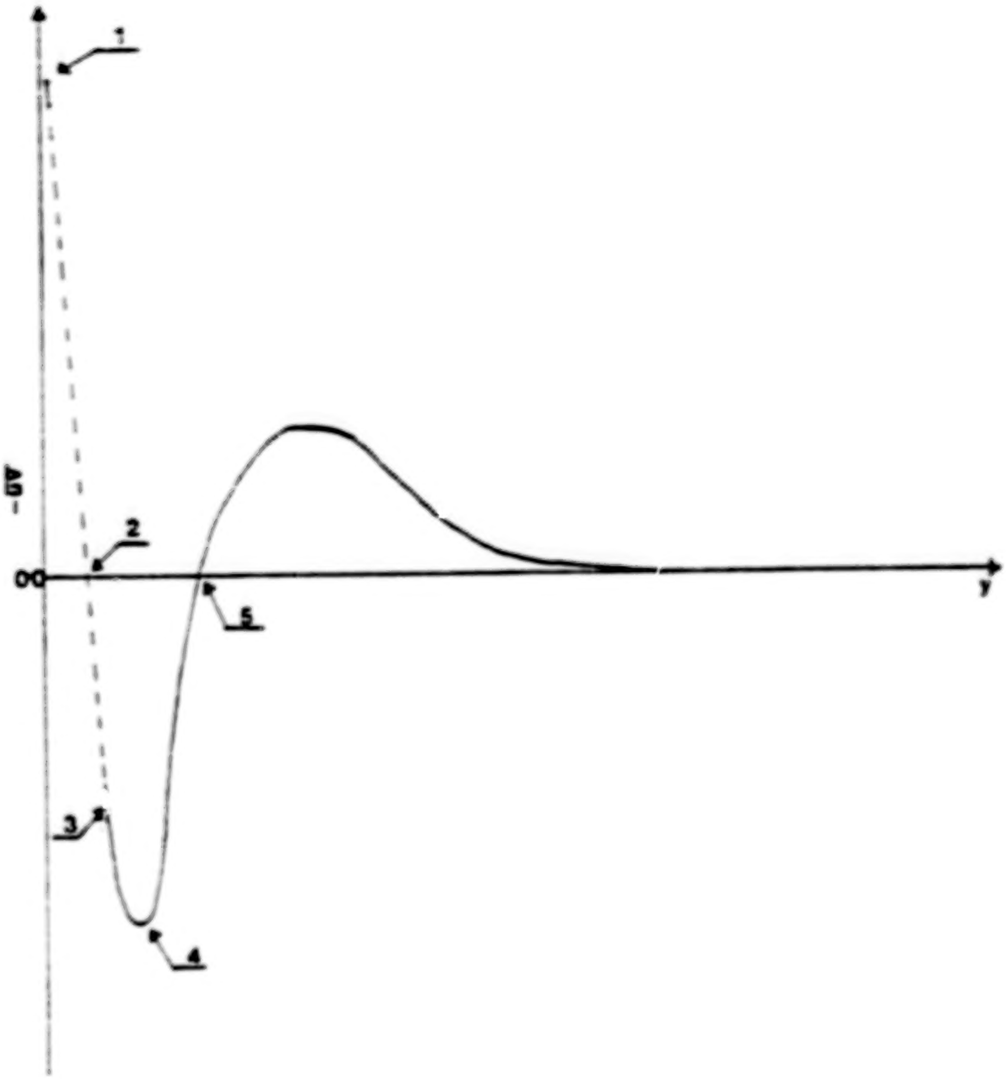

Fig. 7.2(a) Initial Profile of $-\overline{uv}$ for the Computations Using the Experimental Initial Profiles in the Case of Adverse Pressure Gradient Flow

---- Assumed distribution

—— Experimental distribution

1. First normal hot-film data point where

$$\frac{-\overline{uv}}{U_\infty^2} = \frac{C_f}{2}$$

2. Point of maximum velocity where $-\overline{uv} = 0$
3. First slant-wire data point
4. Point of maximum $|-\overline{uv}|$
5. Point of minimum velocity

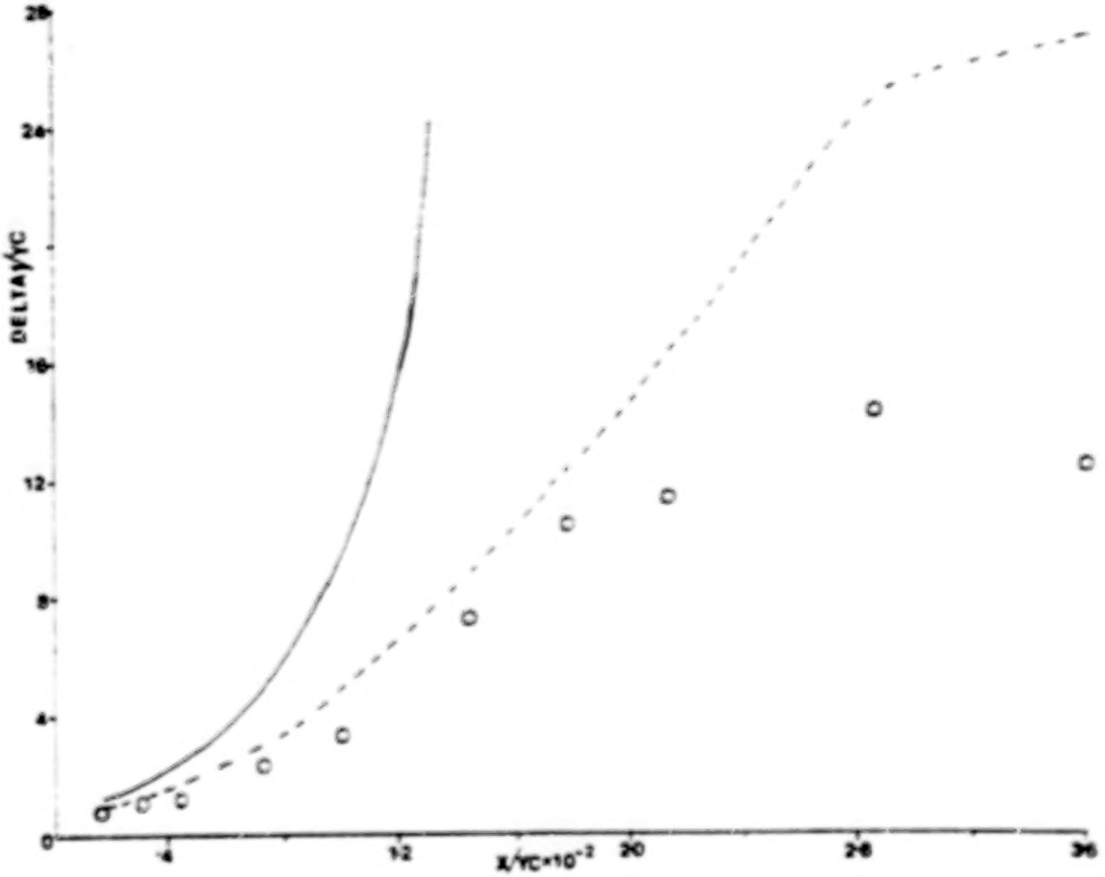

Fig. 7.2(b) Predicted Development of the Displacement Thickness for the Adverse Pressure Gradient Flow

○ Experimental Data

---- Predictions using the experimental initial profiles

—— Predictions using the automatic starting procedure

TABLE OF CONTENTS

LIST OF FIGURES . . . . .vii 1/A12

LIST OF TABLES . . . . xiv 1/B5

NOMENCLATURE . . . . xv 1/B6

Chapter

I. INTRODUCTION 1 1/B12

1.1 Previous Work 2 1/B13

1.2 Asymmetric Jet Velocity Profile 9 1/C7

1.3 Objectives of the Thesis 11 1/C10

1.4 Outline of Thesis 12 1/C11

II. EXPERIMENTAL APPARATUS 15 1/C14

2.1 Description of the Wind Tunnel Components 15 1/C14
Heat exchanger
Blower system
Plenum chamber
Transition section
Test section

2.2 Description and Performance of the Wall Jet Flow System 27 1/D13
Air supply system
Wall jet assembly
Performance of the wall jet

III. INSTRUMENTATION 49 1/F12

3.1 Pitot Probes and Preston Tubes 49 1/F12

3.2 Hot-wire probes 51 1/G1
Slant-wire rotating mechanism
Traversing mechanism

3.3 Electronic Signal Processing 56 1/G6

3.4 Calibrations 56 1/G6

3.5 Uncertainties in the Measurements . . . 57 1/G7

IV. EXPERIMENTAL RESULTS FOR THE ZERO PRESSURE GRADIENT FLOW 59 1/G9

4.1 Flow Conditions 60 1/G10

4.2 Mean Flow Data 64 2/A5
- Skin friction C_f
- Mean velocity U
- Integral parameters
- Effect of the asymmetric jet velocity profile on the mean flow
- Profile parameters

4.3 Turbulence Data 89 2/C5
- Turbulence intensity u_t/U_∞
- Turbulence intensities v_t/U_∞, w_t/U_∞ and shear stress $-\overline{uv}$
- Effect of the asymmetric jet velocity profile on the turbulent quantities
- Turbulent kinetic energy k
- Correlation functions R_{uv} and a_1
- Eddy viscosity ν_{eff}
- Length scales L_{mix} and L_k
- Production of turbulent kinetic energy
- Spectra and dissipation measurements

V. EXPERIMENTAL RESULTS FOR THE ADVERSE PRESSURE GRADIENT FLOW 140 3/A8

5.1 Flow Conditions 141 3/A9

5.2 Mean Flow Data 147 3/B2
- Skin friction C_f
- Mean Velocity U
- Integral parameters
- Effect of the asymmetric jet velocity profile on the mean flow
- Profile parameters

5.3 Turbulence Data 167 3/C12
Turbulence intensity u_t/U_∞
Turbulence intensities v_t/U_∞, w_t/U_∞ and the shear stress $-\overline{uv}$
Turbulent kinetic energy k
Correlation functions R_{uv} and a_1
Eddy viscosity
Mixing length L_{mix} and Prandtl-Kolmogorov length scale L_k
Production of turbulent kinetic energy

VI. PREDICTION METHOD 192 3/F1

6.1 Selection of the Prediction Method 192 3/F1

6.2 Description of the Theoretical Method 194 3/F3
Turbulence model
Computational procedure
Starting procedure

VII. COMPUTED RESULTS 205 3/F14

7.1 Prediction of the Zero Pressure Gradient Flow 206 3/G1
Computations using the experimental initial velocity and turbulence profiles
Computations using the automatic starting procedure

7.2 Predictions of the Adverse Pressure Gradient Flow 216 3/G11
Computations using experimental initial profiles of velocity and turbulence
Computations using the automatic starting procedure

7.3 Comparison of the Performance of Linear and Uniform Jet Velocity Profiles 232 4/B3
Selection of the parameter a
Starting turbulence profiles
Prediction results

VIII. CONCLUSIONS 249 4/C8

APPENDIX A. MEASUREMENTS ON A WALL JET BY BOWLES (1977) 252 4/C11

APPENDIX B. ESTIMATION OF THE FRICTIONAL LOSSES IN THE WALL JET NOZZLE 255 4/C14

APPENDIX C. MEASUREMENT OF THE TURBULENCE INTENSITIES AND THE REYNOLDS SHEAR STRESS 258 4/D4

APPENDIX D. NORMAL HOT-FILM DATA FOR THE ZERO PRESSURE GRADIENT FLOW 272 4/E4

APPENDIX E. SLANT-WIRE DATA FOR ZERO PRESSURE GRADIENT FLOW 279 4/E14

APPENDIX F. NORMAL HOT-FILM DATA FOR ADVERSE PRESSURE GRADIENT FLOW 286 4/F13

APPENDIX G. SLANT-WIRE DATA FOR ADVERSE PRESSURE GRADIENT FLOW 291 4/G9

LIST OF REFERENCES 294 4/G14

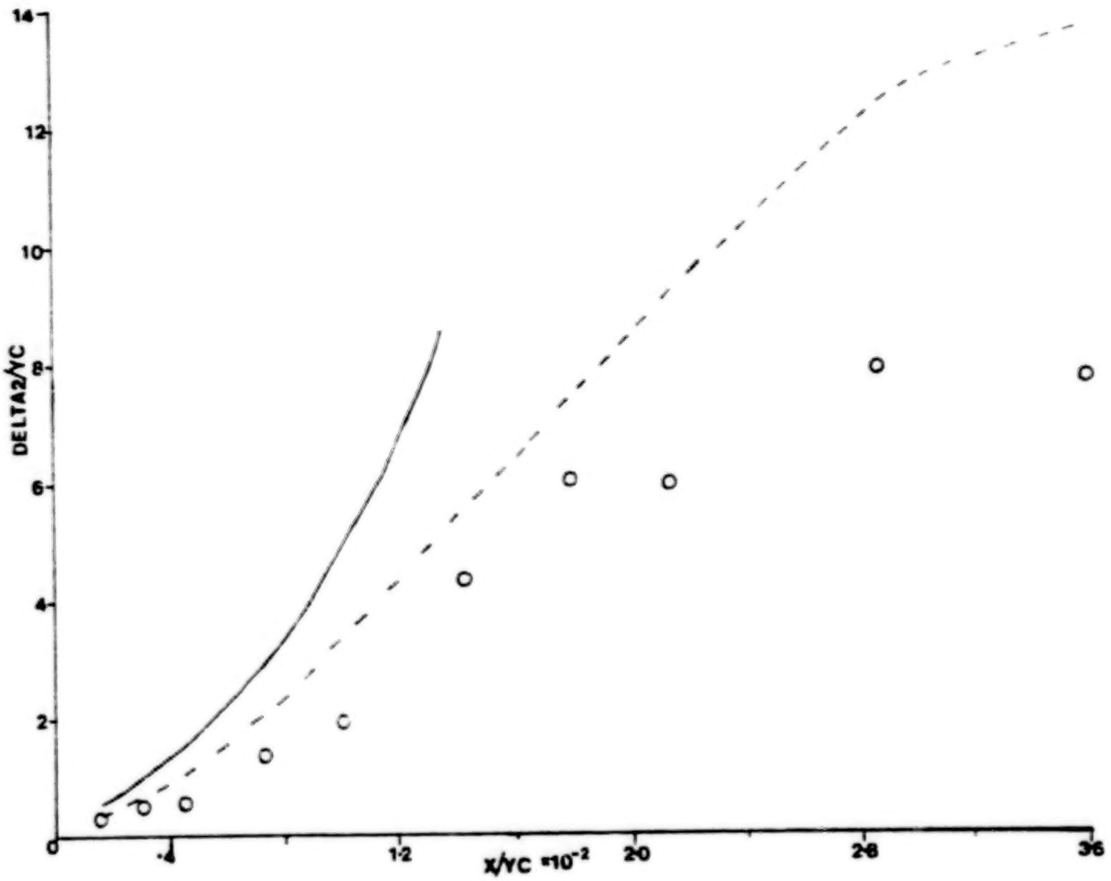

Fig. 7.2(c) Predicted Development of the Momentum Thickness for the Adverse Pressure Gradient Flow

- ● Experimental Data
- ---- Predictions using the experimental initial profiles
- —— Predictions using the automatic starting procedure

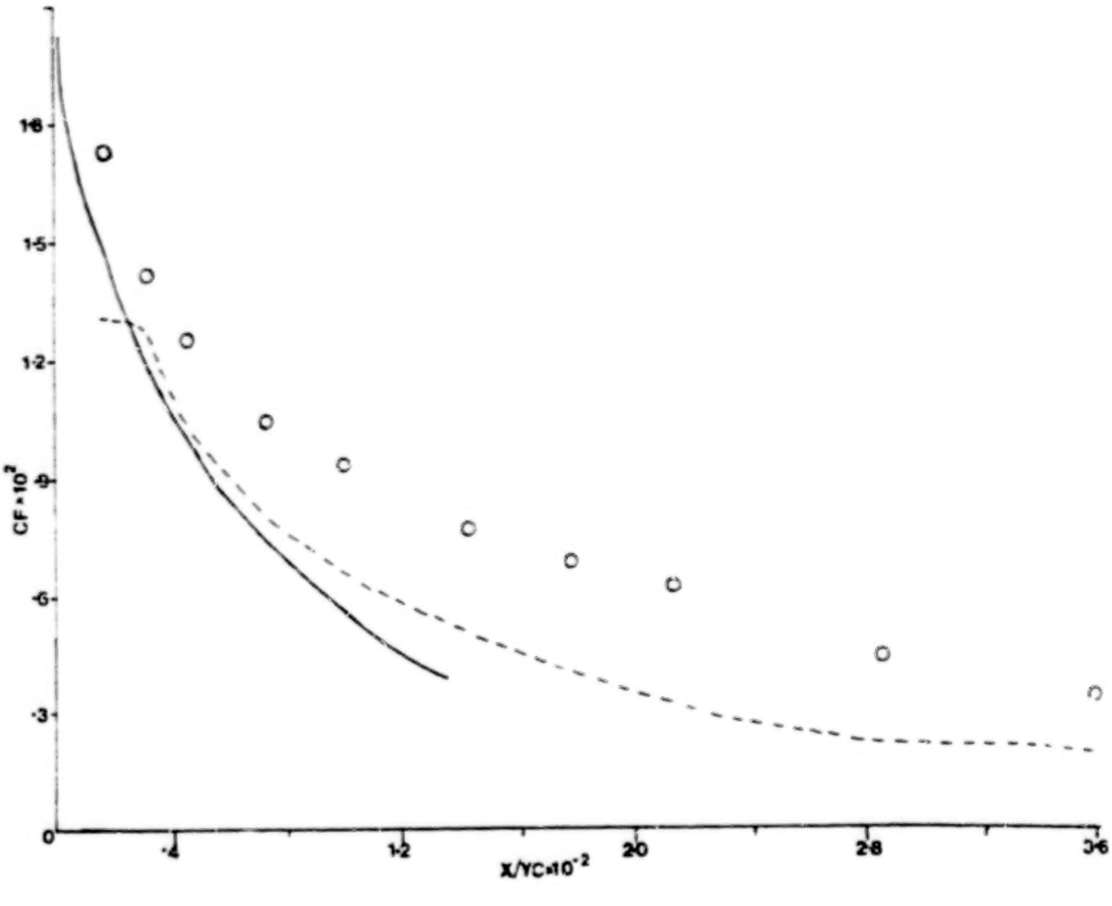

Fig. 7.2(d) Predicted Variation of Skin Friction for the Adverse Pressure Gradient Flow

○ Experimental Data

---- Predictions using the experimental initial profiles

—— Predictions using the automatic starting procedure

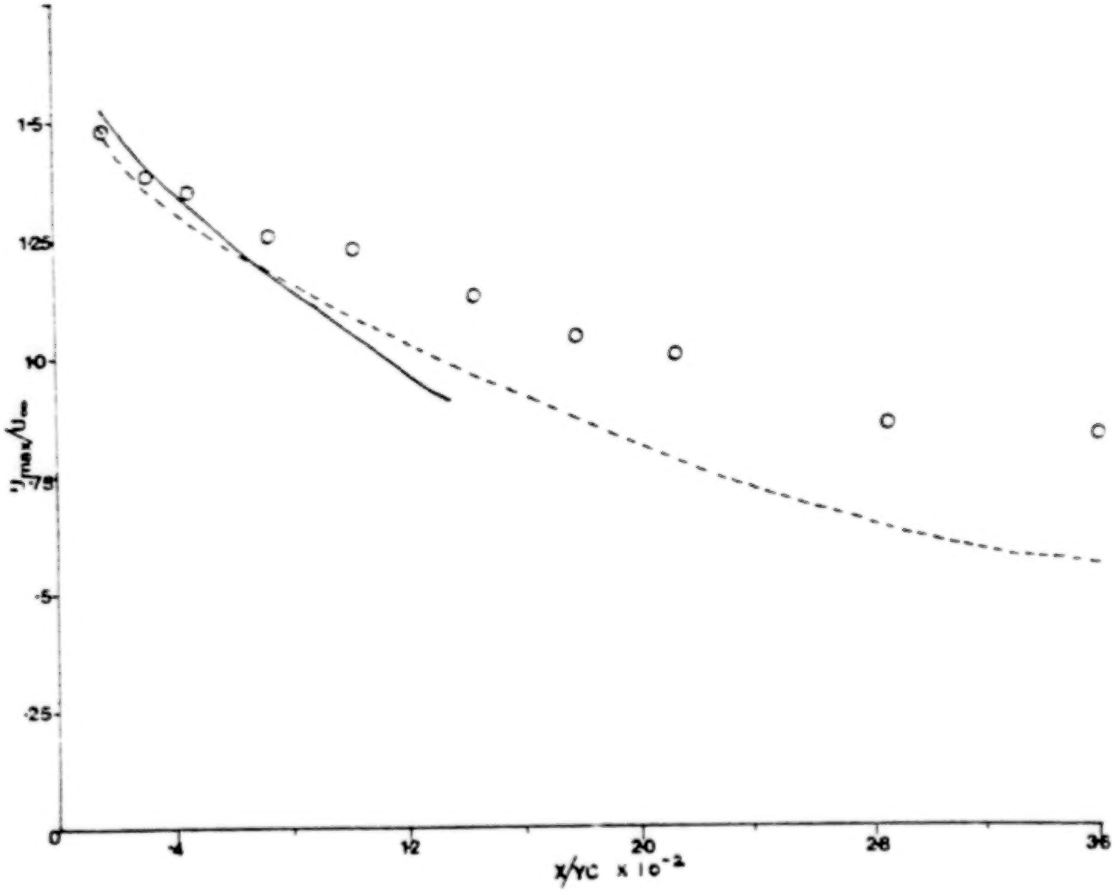

Fig. 7.2(e) Predicted Variation of U_{max} for the Adverse Pressure Gradient Flow

○ Experimental Data

---- Predictions using the experimental initial profiles

—— Predictions using the automatic starting procedure

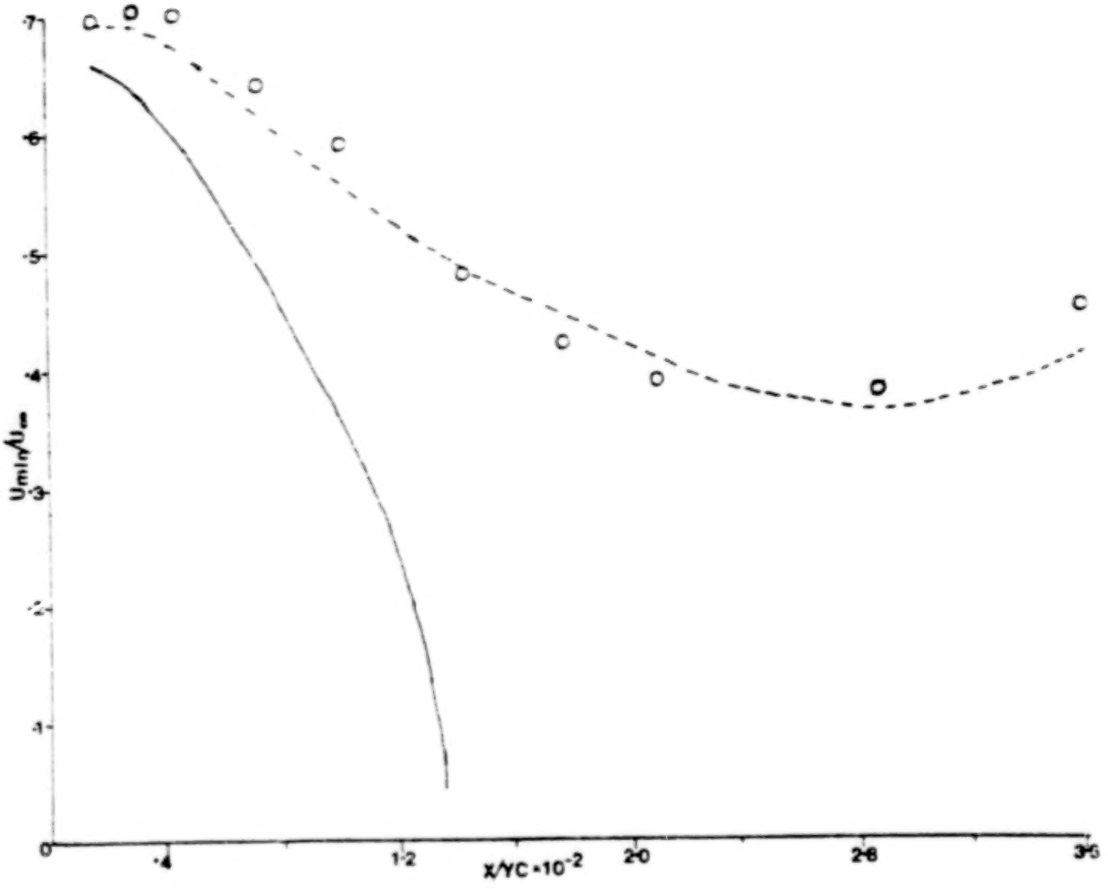

Fig. 7.2(f) Predicted Variation of U_{min} for the Adverse Pressure Gradient Flow

O Experimental Data

---- Predictions using the experimental initial profiles

—— Predictions using the automatic starting procedure

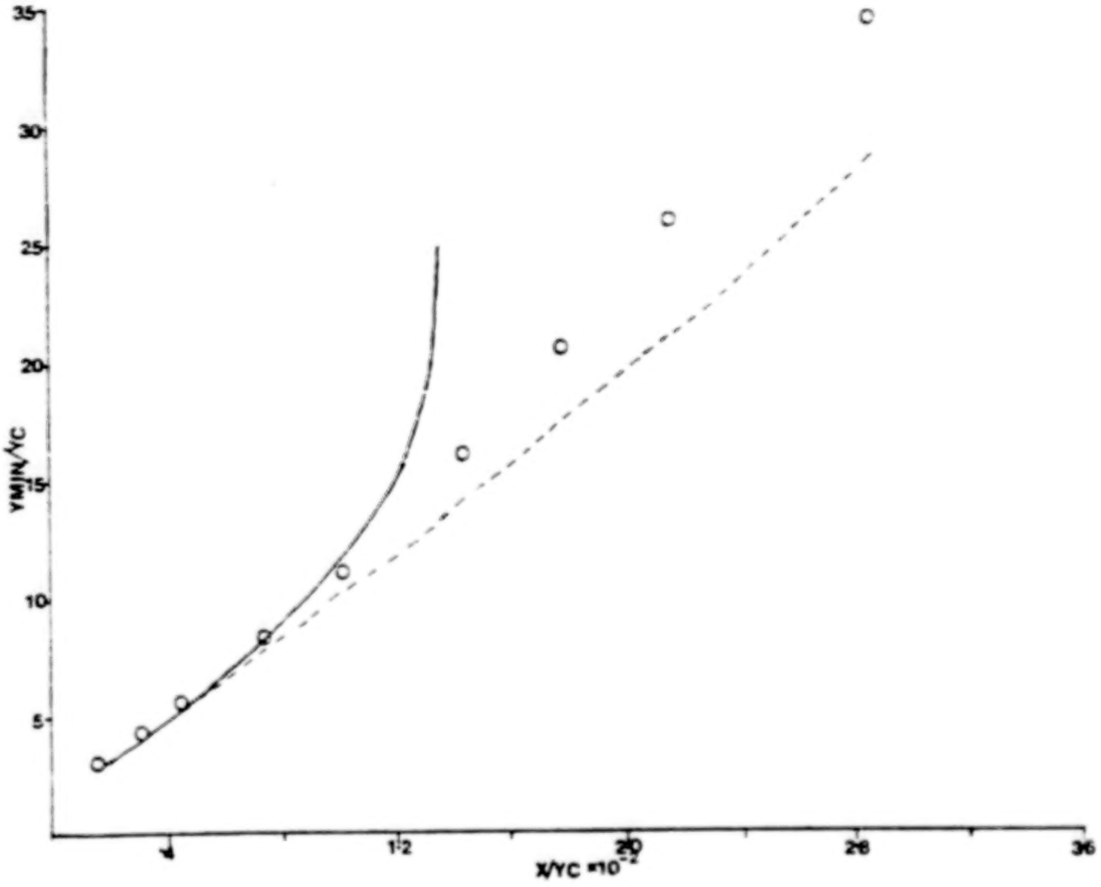

Fig. 7.2(g) Predicted Variation of Y_{min} for the Adverse Pressure Gradient Flow

● Experimental Data

---- Predictions using the experimental initial profiles

—— Predictions using the automatic starting procedure

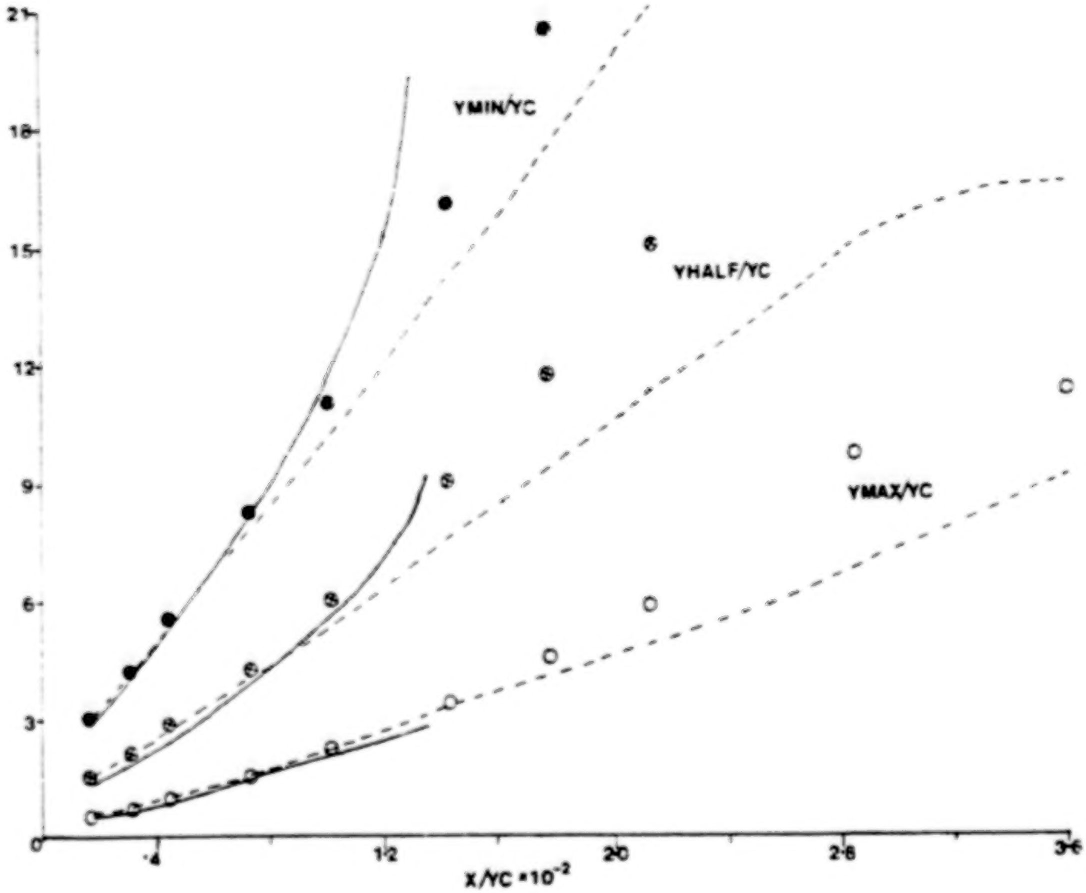

Fig. 7.2(h) Predicted Development of the Profile Length Scales for the Adverse Pressure Gradient Flow

●, ⊗, ○ Experimental Data

---- Predictions using the experimental initial profiles

—— Predictions using the automatic starting procedure

Here it should be noted again that the experimental data beyond $x/y_c = 177.7$ must be treated with caution because the entire tunnel height was filled with the shear layer beyond $x/y_c = 177.7$. δ_1 and δ_2 were predicted well up to $x/y_c = 177.7$. The predictions of C_f are lower than the experiments. The predicted U_{max} decay is faster than the experiments. However, the decay of U_{min} and the growth rate of Y_{min} are predicted well. The agreement between the predicted and experimental growth rates of Y_{max} and Y_{half} is good up to $x/y_c = 143.0$.

The disagreement between the predictions and the experiemntal data at far downstream stations is mainly due to the fact that beyond $x/y_c = 177.7$, the entire tunnel height was filled with the shear layer and hence the full thickness of the shear layer has not been taken into account in the experiments.

7.2.1 (d) Convergence or Divergence Correction

Irwin (1974) suggested that for flows under severe adverse pressure gradients, a correction term involving $\partial W/\partial z$ has to be applied to the mean momentum equation to account for the flow convergence or divergence in the lateral direction. Here z is the lateral coordinate and W is the lateral component of velocity. The flow convergence or divergence is caused by the rapid growth of the side wall boundary layers and their bleed off by means of false side walls. The fact that the flow converges or diverges in the lateral direction depends on whether too little or too much of the side wall boundary layer flow was being bled.

Sufficient care was taken in the present experiments to maintain two-dimensionality. The slant-wire measurements (Appendix C) show that the magnitude of W is very small even at far downstream stations. This implies that the magnitudes of $\partial W/\partial z$ may not be significant to apply any convergence or divergence correction. Also, it was shown in Chapter 5 (section 5.2.3) that the experimental data closely satisfy the two-dimensional integral momentum equation up to $x/y_c = 177.7$. The failure of the experimental data to satisfy the two-dimensional integral momentum equation beyond $x/y_c = 177.7$ is mainly due to the fact that the entire tunnel height is filled by the shear layer beyond $x/y_c = 177.7$. Because of the above arguments, no convergence or divergence correction has been applied to the predictions presented in this thesis. Also, one of the main objectives of the predictions is to compare the performance of the asymmetric jet velocity profile with that of a uniform jet velocity profile. Since it is only a relative comparison, the flow convergence or divergence correction should not influence the conclusions regarding the asymmetric jet velocity profile.

7.2.2 Computations Using the Automatic Starting Procedure

Predictions of the adverse pressure gradient flow were made using the automatic starting procedure described in Chapter 6. As mentioned before, the velocity profile (Fig. 6.1 (b)) used in the automatic starting procedure was assumed to represent the case of the uniform jet velocity profile. The step size was chosen as .015 times flow width up to x/y_c = 15.0 and .03 times the flow width beyond x/y_c = 15.0. The number of grid points was taken to be 60. The value of "a" was taken as 0.6.

The computations using the automatic starting procedure predicted reverse flow near the minimum velocity point in the wake region at x/y_c = 130.0. The computations broke down after the reverse flow was observed since the computing method cannot handle regions of reverse flow. In comparison, the computations using the experimental starting conditions representing the asymmetric jet velocity profile proceeded all the way up to x/y_c = 360.8. Fig. 5.4 (b) shows the predicted velocity profile at x/y_c = 100.3 using the automatic starting procedure in comparison with the predicted profile using experimental starting conditions. A large momentum deficit can be found in the minimum velocity region of the predicted velocity profile using the automatic starting conditions. Fig. 7.4 (a) shows a representative predicted velocity profile using the automatic starting procedure with uniform jet velocity profile just before the occurrence of reverse flow in the minimum velocity region.

Figs. 7.2 (b-h) show the predicted development of different integral and profile parameters using the automatic starting procedure in comparison with the predictions using the experimental starting conditions. The momentum and displacement thicknesses shown in Figs. 7.2 (b) and (c) increase very rapidly near the point where the computations broke down. One can see that the increase of δ_1 and δ_2 starts from the beginning of the computations, even though the increment is more rapid near the point of breakdown. The skin friction near the point of breakdown of the computations shows a trend that the flow might encounter separation at the bottom wall, if one proceeds further downstream.

Figs. 7.2 (e-g) show the decay of U_{max} and U_{min} and the growth rate of Y_{min} respectively. U_{min} increases rapidly from the start of the computations and eventually goes to zero near the point of breakdown. Y_{min} increases rapidly as compared to the predictions using experimental starting conditions. Fig. 7.2 (h) shows the development of Y_{max}, Y_{min}, and Y_{half}. Y_{min} and Y_{half} increase very rapidly for the case of automatic starting conditions. Y_{max} growth rate is lower than that for the experimental starting conditions.

The above predicted results using the automatic starting procedure can be explained in the following way. When a pressure gradient is imposed on the flow, the region around the junction of the upstream boundary layer and the jet needs a considerable amount of momentum to overcome the pressure gradient. If sufficient momentum is not supplied to that region by the jet, the result is a highly momentum deficient region near the minimum velocity point at the downstream stations. In the case of uniform jet velocity profile used in automatic starting procedure, considerable part of the jet momentum is concentrated near the wall and not close to the minimum velocity region. Hence the outer layer spreads more rapidly into the free-stream in search of momentum as indicated by the rapid increase of Y_{min}. However, because of the severe adverse pressure gradient, the entrainment of the free-stream momentum does not occur rapidly enough to supply momentum to the momentum deficient region near the point of velocity minimum. Hence, the velocity in the minimum velocity region decreases rapidly as indicated by the rapid decay of U_{min} and eventual reverse flow there. Because of the existence of a large momentum deficient region near the point of minimum velocity, the momentum and displacement thicknesses increase very rapidly. The relative concentration of the jet momentum near the wall causes increased frictional losses, resulting in the rapid decrease of C_f. The relatively large momentum and displacement thicknesses, the lower values of C_f, and reverse flow in the minimum velocity region are all unwanted effects and they might lead to eventual flow separation at the bottom wall.

In comparison, the flow development in the case of the experimental asymmetric jet velocity profile is different. Given the same total jet momentum, the asymmetric jet velocity profile will have a higher concentration of momentum in the upper half of the jet. Hence, the momentum requirements of the minimum velocity region is more readily met by the higher momentum in the upper half of the jet. The outer layer does not grow very rapidly as indicated by the slower growth rates of Y_{half} and Y_{min} shown in Fig. 7.2 (h). Y_{max} increases rapidly because of the tendency of the inner layer to grow faster to supply momentum to the outer layer. The decay of U_{min} shown in Fig. 7.2 (f) is more gradual in comparison to the rapid decrease of U_{min} to zero in the case of predictions using automatic starting procedure. The growth of displacement and momentum thicknesses is also gradual. In essence, the asymmetric jet velocity profile tries to distribute the momentum evenly across the layer, thereby preventing the possibility of separation of the inner layer near the wall. The asymmetric velocity profile also results in lower frictional losses at the wall by keeping the jet momentum away from the wall as indicated by the lower values of C_f in the region near to the jet.

Here it should be mentioned that Irwin (1974) has documented one case of flow prediction where the computations predicted reverse flow in the minimum velocity region with the experimental starting conditions, even though the experiments did not show any flow reversal in the minimum velocity region. Irwin gave the explanation that the predicted flow reversal in the minimum velocity region may be due to either experimental inaccuracy or the failure of the boundary layer assumption because of the very low velocities reached in the region of velocity minimum. It was further indicated that the application of flow convergence-divergence correction, along with the accurate specification of the experimental starting conditions has carried the computations farther than without them. But, the prediction method still predicts the reverse flow. In the present case, it is true that the flow velocities are considerably smaller, at far downstream stations. However, the difference in flow development between the uniform velocity profile and asymmetric velocity profile can be observed from the beginning of the computations. Therefore, the breakdown of computations in the present predictions using the automatic starting procedure is not a local effect of low velocities, but it is a result of a gradual process which starts at the slot because of the uniform jet velocity profile.

7.3 Comparison of the Performance of Linear and Uniform Jet Velocity Profiles

This part of the predictions has been made to isolate the effect of the shape of the jet velocity profile on the flow development. Predictions were made with two different types of jet velocity profiles in the case of an adverse pressure gradient flow by keeping the other initial conditions the same.

The two jet velocity profiles considered are given below. A uniform jet velocity profile shown in Fig. 7.3 (a), which is the same as the profile shown in Fig. 6.1 (b), was generated by the automatic starting procedure and has the same jet momentum as the experimental case. A linear jet velocity profile shown in Fig. 7.3 (b) was the second profile. This linear jet velocity profile was assumed to represent the ideal case of an asymmetric jet velocity profile. It was obtained by replacing the profile shown in Fig. 7.3 (a) below the velocity minimum point by two linear segments with the following constraints:

1. U_{min} is the same for the profiles shown in Fig. 7.3 (a) and 7.3 (b)

2. $U = 0$ at $y = 0$

3. $U = U_{Jmax}$ at $y/y_c = a$, where a is the fraction of the slot height over which the flow is uniform

4. The momentum below the minimum velocity point is the same for both cases.

Referring to Fig. 7.3 (b), U_{Jmax} is greater than U_j. However, for the particular case where a = 1.0 and there is no mixing layer, $U_{Jmax} = \sqrt{3}\, U_J$ as shown in Fig. 7.3 (c).

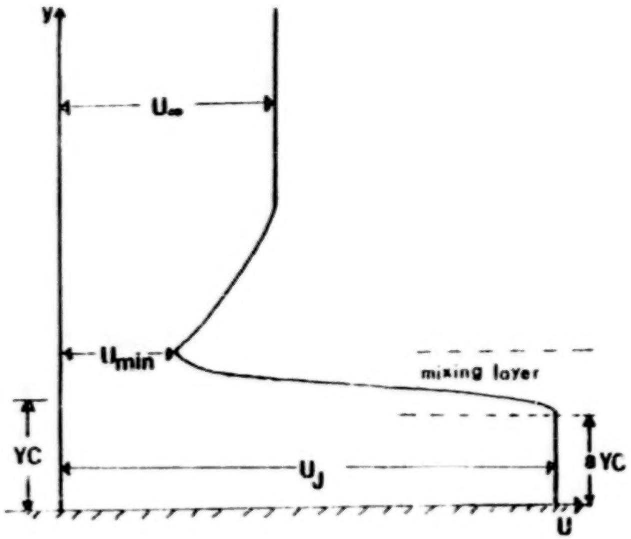
y
U∞
Umin
mixing layer
YC
U_J
a YC
U

Fig. 7.3(a) Starting Velocity Profile for the Predictions with Uniform Jet Velocity Profile using the Automatic Starting Procedure

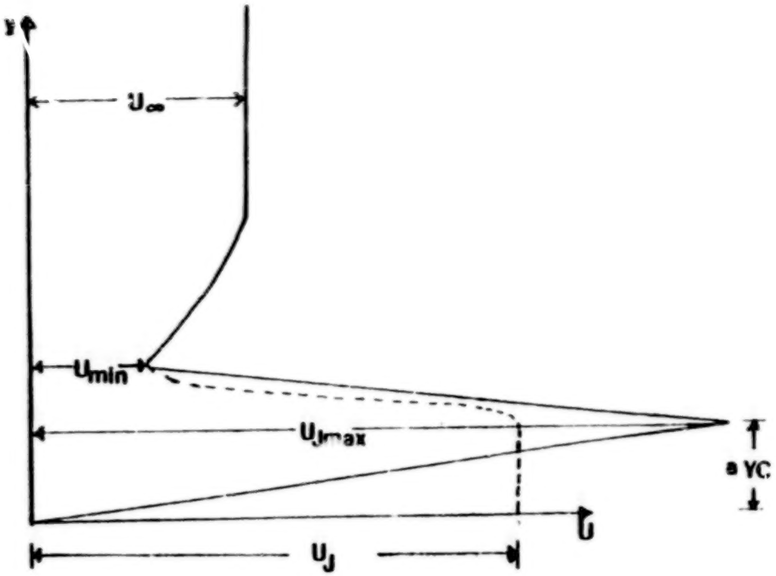
y
U∞
Umin
U_Jmax
a YC
U
U_J

Fig. 7.3(b) Starting Velocity Profile for the Predictions with Linear Jet Velocity Profile using the Automatic Starting Procedure

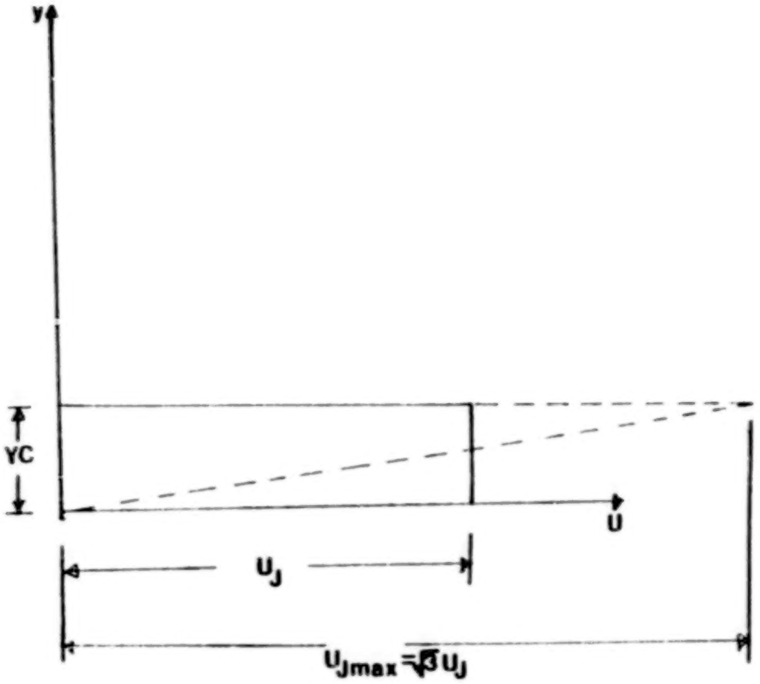
y
YC
U
U_J
$U_{Jmax} = \sqrt{3}\, U_J$

Fig. 7.3(c) Comparison of Uniform and Linear Jet Velocity Profiles Without the Mixing Layer

Here, U_{Jmax} is the maximum jet velocity in the linear profile and U_J is the jet velocity in the case of uniform profile for the same jet momentum in both cases. The above mentioned velocity profiles shown in Figs. 7.3 (a) and 7.3 (b) were used as the starting velocity profiles in the predictions.

7.3.1 Selection of the Parameter a

a is the fraction of the slot height over which the flow is uniform with reference to Fig. 7.3 (a). Irwin recommends a value of a = 0.6. When a = 0.6 was used, the resulting linear profile was such that the velocity gradients in the mixing layer were lower than the velocity gradients in the jet region below the point of maximum velocity. This results in greater momentum transfer towards the wall than towards the region of minimum velocity. However, in an actual situation of an asymmetric profile, the region near the slot can be expected to have higher velocity gradients in the mixing layer than in the jet region below the point of maximum velocity. Therefore, the value of "a" was taken as 0.95 in generating the profiles shown in Figs. 7.3 (a) and (b). The higher value of "a" makes the width of the mixing layer very thin thereby increasing the velocity gradients in the mixing layer and simulating the actual conditions that might be expected in the case of an asymmetric jet velocity profile.

7.3.2 Starting Turbulence Profiles

The starting profiles of $\overline{u^2}$, $\overline{v^2}$, $\overline{w^2}$, $-\overline{uv}$ and ε used in the predictions for the uniform jet velocity profile were kept the same as for the automatic starting procedure. The starting profiles of $\overline{u^2}$, $\overline{v^2}$, $\overline{w^2}$ used in the predictions for the linear jet velocity profile were also kept the same as for the automatic starting procedure.

The starting profile of $-\overline{uv}$ for the linear velocity profile was chosen in the following way. The $-\overline{uv}$ distribution above the point of minimum velocity was kept the same as for the automatic starting procedure. The shear stress in the mixing layer was obtained from the shear stress distribution in the mixing layer for the automatic starting procedure by multiplying with a factor equal to $(U_{Jmax} - U_{min})_{linear} / (U_J - U_{min})_{uniform}$. The shear stress distribution below the point of maximum velocity was taken as linear with $-\overline{uv} = 0$ at the point of maximum velocity and $-\overline{uv} = \nu(\partial U/\partial y)_{linear}$ at the first grid point.

The number of grid points was taken to be 80 to accommodate the details of the linear velocity profile. The step size was taken as 0.015 times the flow width up to $x/y_c = 15.0$ and 0.03 times the flow width after $x/y_c = 15.0$.

7.3.3 Prediction Results

As mentioned earlier, the predictions using linear and uniform profiles were made only for the case of adverse pressure gradient flow. The theoretical method predicts flow reversal in the minimum velocity region for the case of uniform profile at $x/y_c = 102.0$. In comparison, the computations for the case of linear profile proceeded all the way up to $x/y_c = 360.8$ without any problem. Fig. 7.4 (a) shows a comparison of the predicted velocity profiles for the uniform and linear cases at $x/y_c = 100.3$. One can see a large momentum deficient region near the minimum velocity point for the case of uniform profile.

The predicted development of the different integral and profile parameters is shown in Figs. 7.4 (b-g) for both the uniform and linear cases. Most of the predictions made in the case of uniform profile are in agreement with the results obtained in Section 7.2.2. The momentum and displacement thicknesses increase very rapidly for the uniform profile in comparison with the linear profile. The skin friction shown in Fig. 7.4 (d) decreases very rapidly indicating higher momentum loss due to friction at the wall for the uniform case. In fact, the area between the two skin friction curves up to the point where the C_f for both cases become equal indicates an increased loss of momentum due to friction for the case of uniform profile.

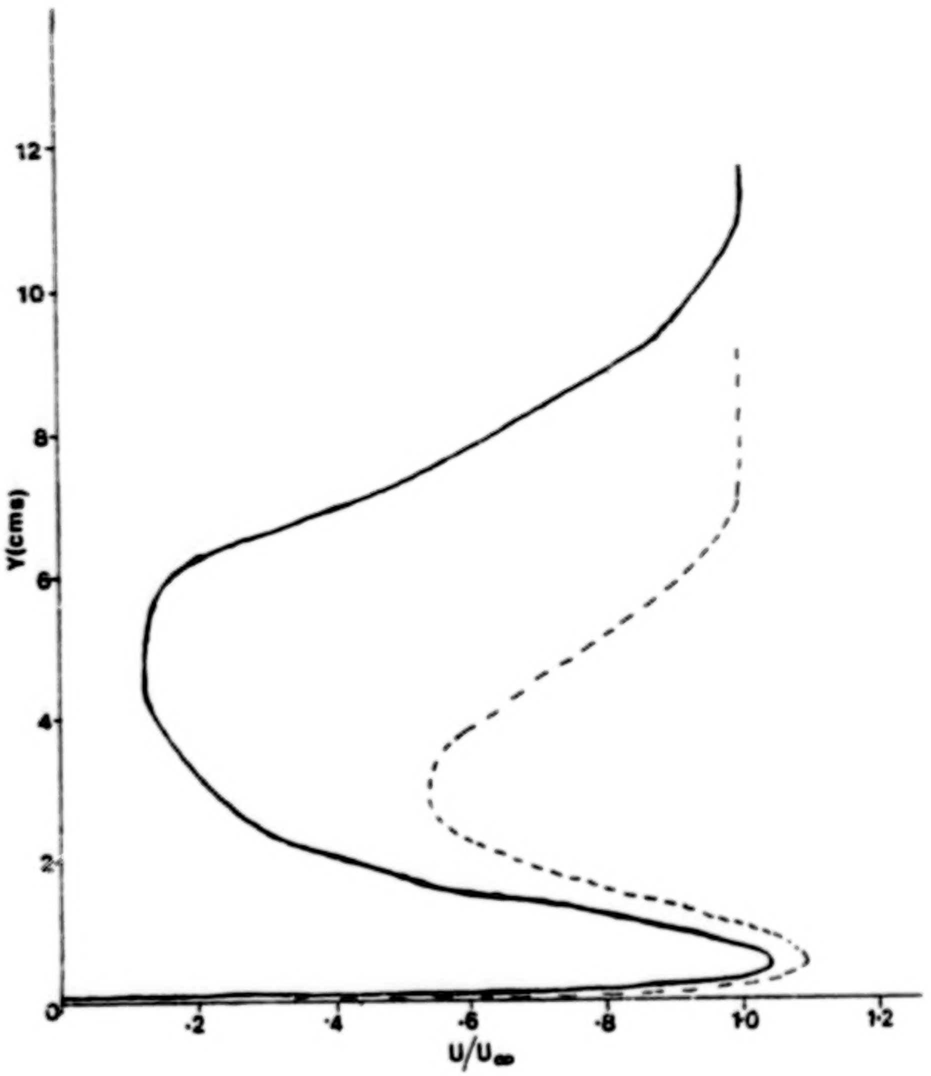

Fig. 7.4(a) Predicted Velocity Profiles at x/y_c = 100.3 for the Adverse Pressure Gradient Flow

---- Predictions with linear jet velocity profile

—— Predictions with uniform jet velocity profile

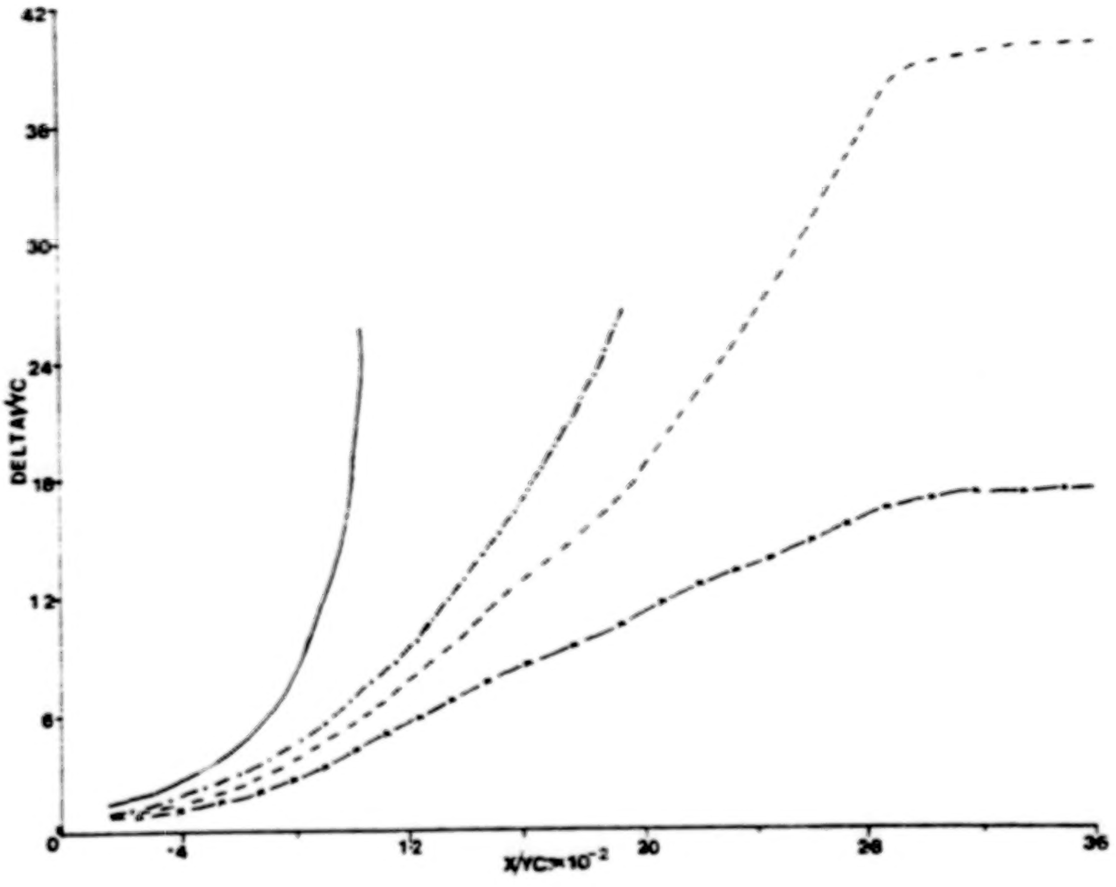

Fig. 7.4(b) Predicted Development of the Displacement Thickness for the Adverse Pressure Gradient Flow

---- Predictions with linear jet velocity profile

—— Predictions with uniform jet velocity profile and with the same momentum as in the experiments

— • — • — Predictions with uniform jet velocity profile and with 20% excess momentum than in the experiments

— x — x — Predictions with uniform jet velocity profile and with 30% excess momentum than in the experiments

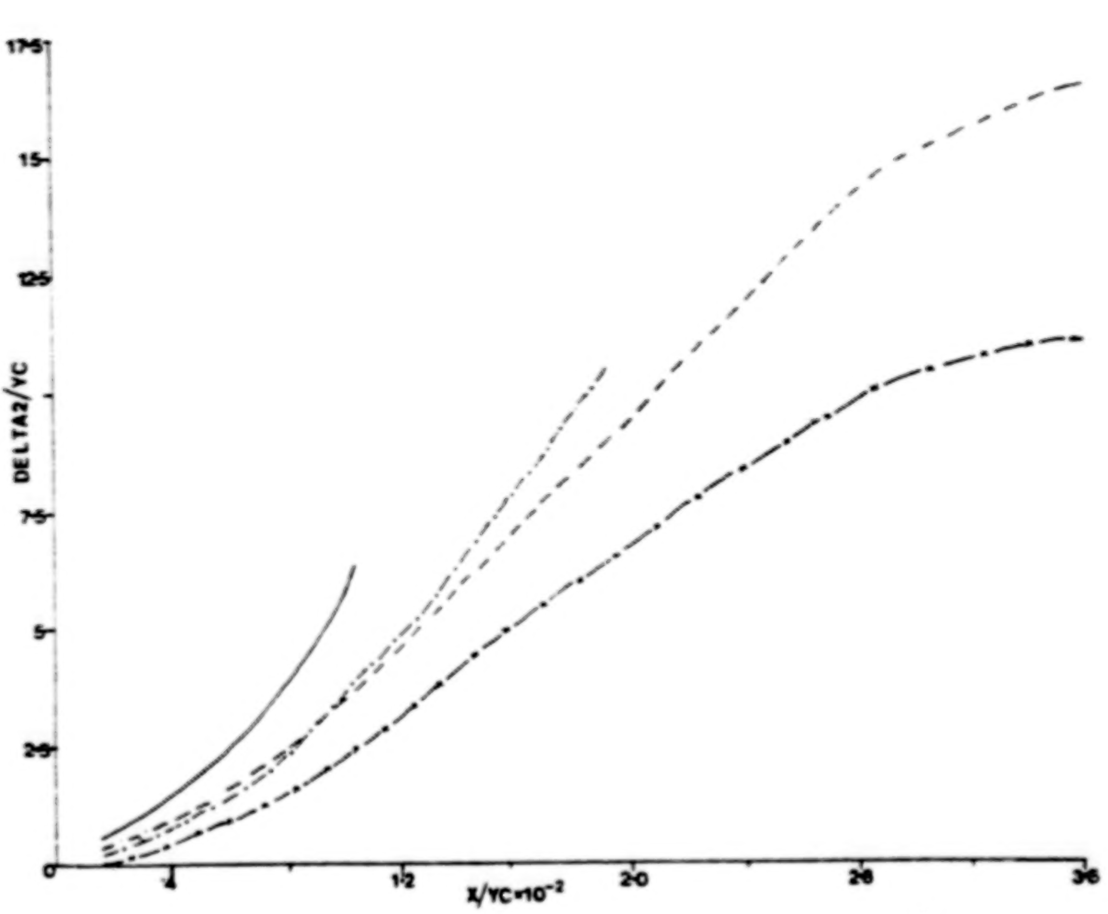

Fig. 7.4(c) Predicted Growth of the Momentum Thickness in the Case of Adverse Pressure Gradient Flow

---- Predictions with linear jet velocity profile

—— Predictions with uniform jet velocity profile and with the same momentum as in the experiments

— · — · — Predictions with uniform jet velocity profile and with 20% excess momentum than in the experiments

— x — x — Predictions with uniform jet velocity profile and with 30% excess momentum than in the experiments

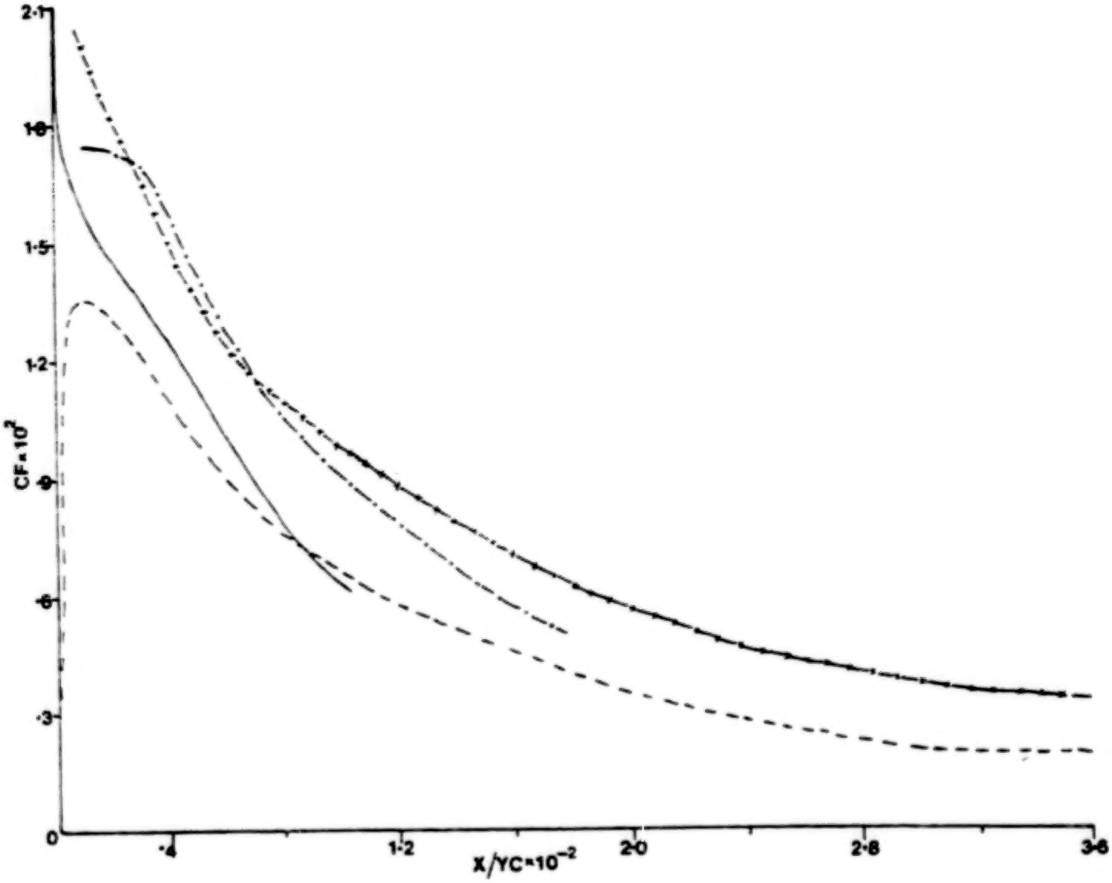

Fig. 7.4(d) Predicted Variation of Skin Friction for the Adverse Pressure Gradient Flow

- - - - Predictions with linear jet velocity profile

—— Predictions with uniform jet velocity profile and with the same momentum as in the experiments

— · — · — Predictions with uniform jet velocity profile and with 20% excess momentum than in the experiments

— x — x — Predictions with uniform jet velocity profile and with 30% excess momentum than in the experiments

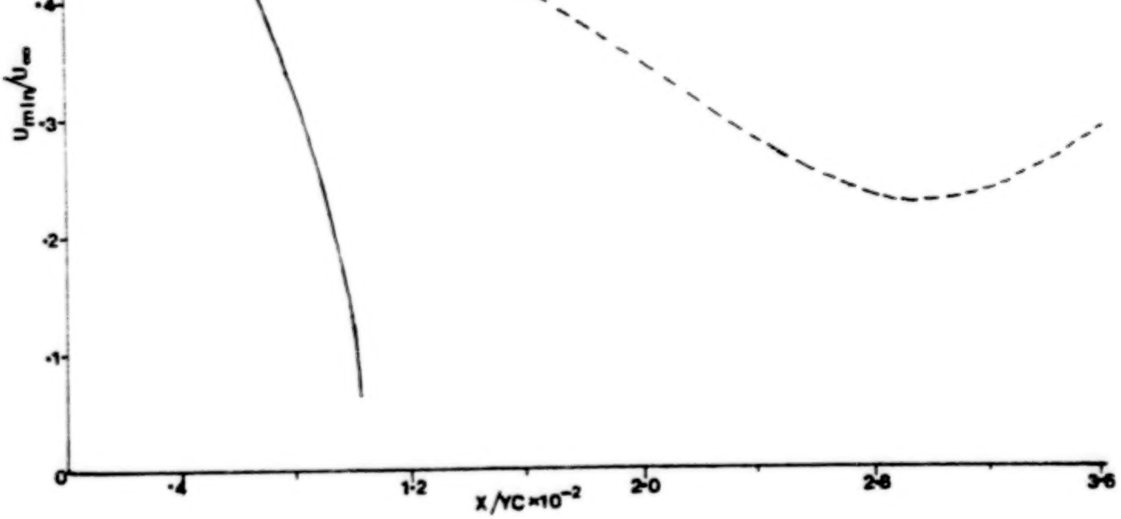

Fig. 7.4 (e) Predicted Variation of U_{min} for the Adverse Pressure Gradient Flow

---- Predictions with linear jet velocity profile

—— Predictions with uniform jet velocity profile

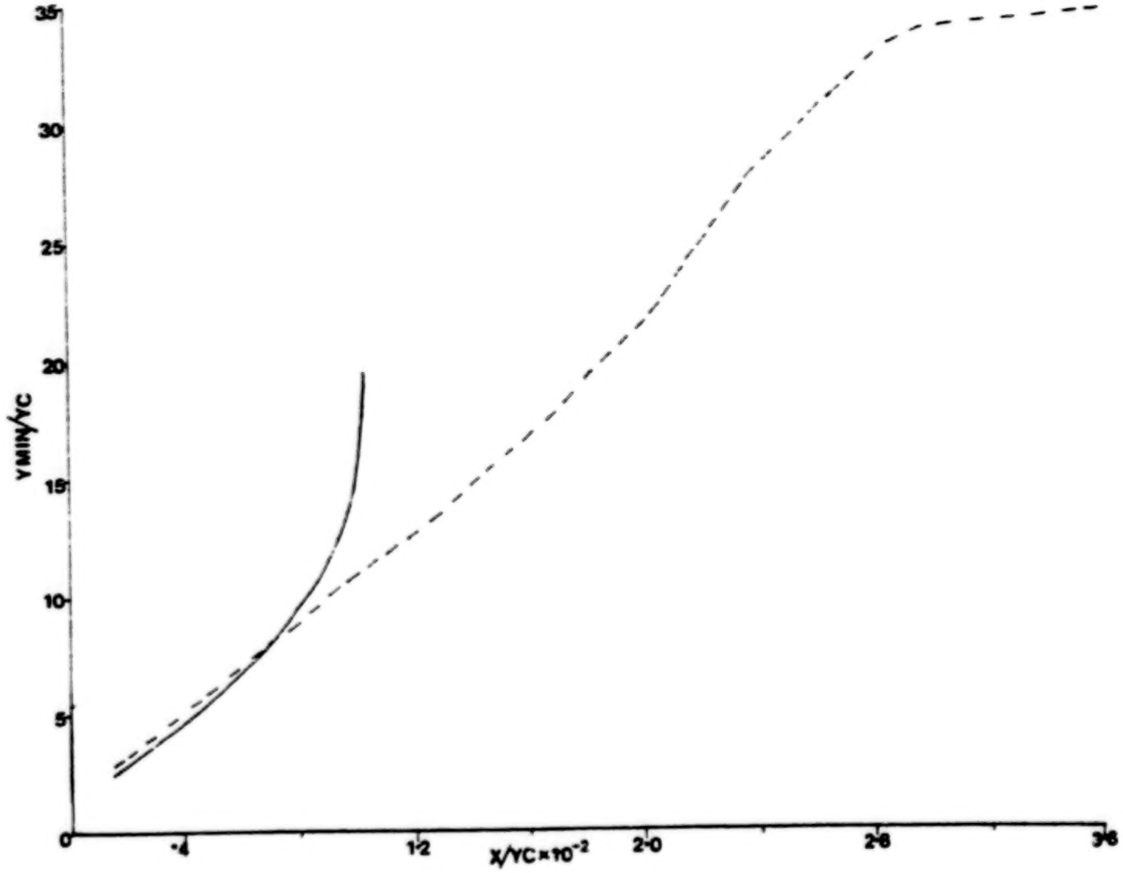

Fig. 7.4(f) Predicted Variation of Y_{min} for the Adverse Pressure Gradient Flow

---- Predictions with linear jet velocity profile

—— Predictions with uniform jet velocity profile

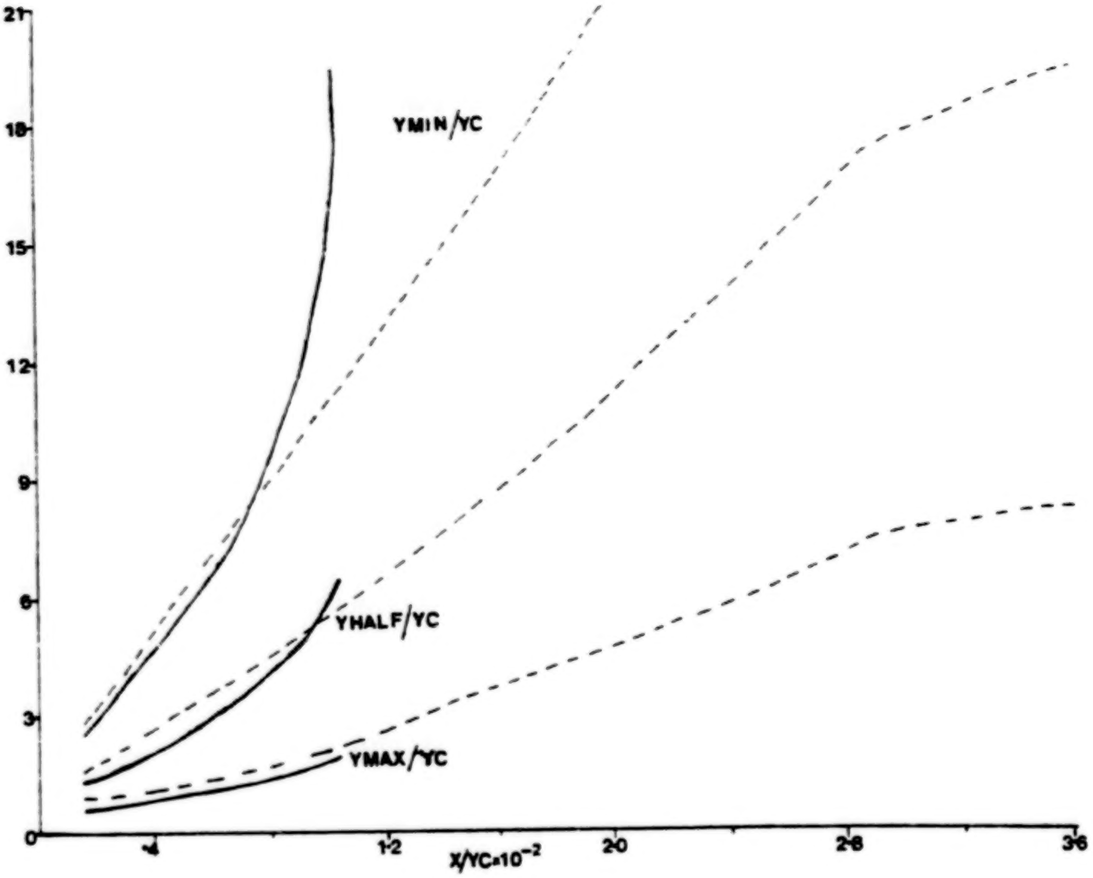

Fig. 7.4(g) Predicted Variation of the Profile Length Scales for the Adverse Pressure Gradient Flow

---- Predictions with linear jet velocity profile

—— Predictions with uniform jet velocity profile

The decay of U_{min} and the growth of Y_{min} are shown in Figs. 7.4 (e) and 7.4 (f). U_{min} decreases very rapidly to zero and Y_{min} increases considerably in the case of uniform profile. In comparison, the decay of U_{min} and the growth of Y_{min} are gradual for the linear profile. Fig. 7.4 (g) shows the relative development of the profile length scales Y_{max}, Y_{half}, and Y_{min}. Once again Y_{half} and Y_{min} develop much faster for the uniform case than for the linear case. However, the growth rate of Y_{max} is almost the same for both cases even though the absolute value of Y_{max} is lower in the case of uniform profile.

The mechanism of flow development in the case of uniform jet velocity profile in comparison with that for the asymmetric jet velocity profile is given in detail under Section 7.2.2 and the same thing is applicable when a comparison is made between the uniform and linear jet velocity profiles. However, the flow development with a linear profile and with the same starting conditions as the uniform profile reveals more clearly the distinct advantages of having an asymmetric velocity profile in the jet.

At this point, it is reasonable to ask the question of how much extra jet momentum is needed in the case of uniform profile to achieve a similar flow development as in the case of the linear profile indicated by the development of different integral and profile parameters. To investigate it, predictions were made with different values of jet momentum higher than the experimental value. The flow development was compared on the basis of development of δ_1 and δ_2. Figs. 7.4 (b) and 7.4 (c) show the predicted development of δ_1 and δ_2 using the automatic starting procedure with 20% excess momentum and 30% excess momentum. With 20% excess momentum, the predictions broke down at about $x/y_c = 177.70$. Reverse flow was predicted in the minimum velocity region near $x/y_c = 177.7$. With 30% excess momentum, the flow was predicted all the way up to $x/y_c = 360.84$ without any reverse flow. Therefore, an approximately 30% increase in jet momentum is necessary in the case of an uniform profile to achieve similar flow development as in the case of a linear velocity profile. Also, it should be noted that for a given jet momentum, the mass flow rate in the case of asymmetric profile is less than the uniform case. This is evident from the mass flow calculations for the linear and uniform cases shown in Fig. 7.3 (c). The mass flow for the linear case is $\sqrt{3}/2$ times the mass flow for the uniform case with the same momentum. However, for a similar flow development, the momentum of the uniform jet has to be increased by 30%. Therefore the actual savings in mass flow in the case of a linear profile for a similar flow development is $(1 - \frac{\sqrt{3}}{2}\frac{1}{\sqrt{1.3}}) \times 100$ or 24% along with a jet momentum savings of 30%. Fig. 7.4 (d) shows the predicted skin friction using the automatic starting procedure with 20% excess momentum and 30% excess momentum. The increased momentum loss due to friction in these cases can be observed as indicated by the high values of skin friction.

CHAPTER VIII

CONCLUSIONS

Conclusions

1. Measurements have been made in a zero pressure gradient two-dimensional wall jet with a low jet excess velocity and a thick upstream boundary layer. The quantities measured are the mean velocity, turbulence intensities, Reynolds shear stress, spectra and skin friction. The derived quantities included turbulent kinetic energy, eddy viscosity, mixing length, Prandtl-Kolmogorov length scale, correlation coefficients, dissipation and production rates of turbulent kinetic energy and bursting periods.

2. Measurements have also been made in an adverse pressure gradient two-dimensional wall jet with a low jet excess velocity and thick upstream boundary layer. The quantities measured and derived included all those listed under (1) with the exceptions of spectra, dissipation rate and bursting period.

3. The mean velocity profiles show a defined logarithmic region which followed the conventional logarithmic law of the wall with the same constants as applicable to normal boundary layers.

4. The point of zero shear stress was generally found to be closer to the wall than that of zero velocity gradient.

5. The profiles of effective viscosity, Prandtl mixing length and the Prandtl-Kolmogorov length scale do not exhibit an obvious similarity and consequently prediction procedures which depend on these concepts are unlikely to be wholly satisfactory for blown boundary layers.

6. Tchen's mean vorticity theory with $\alpha = 0.8$ estimates the dissipation rates which are in good agreement with -5/3 law in the logarithmic region of the velocity profile.

7. It is possible to produce an asymmetric jet velocity profile and it is a unique feature of the present wall jet design.

8. The asymmetric jet velocity profile affects the downstream development of the flow considerably. It causes the effect of the jet to be carried to a much longer distance as compared to a uniform jet velocity profile. The asymmetric profile tries to supply more momentum to the momentum deficient upstream boundary layer instead of wasting it as friction at the wall, resulting in a more even distribution of momentum across the whole layer.

9. The prediction method of Irwin (1974) gave satisfactory predictions of the present class of blown boundary layers using experimental starting conditions.

10. The prediction method used was able to show theoretically the advantages of asymmetric jet velocity profile over uniform jet velocity profile more clearly in the case of adverse pressure gradient flow.

11. Blown boundary layers under adverse pressure gradients with an asymmetric jet velocity profile result in much lower values (or more accurately lower growth rates) of momentum and displacement thicknesses and prevent the development of large momentum deficient region downstream of the slot as compared to a uniform jet velocity profile. It is well known that large displacement and momentum thicknesses result in a situation approaching separation and cause lower lift on aerofoils.

Suggestions for Future Work

There is a need for more detailed and accurate turbulence measurements taking proper account of high flow inclination angles for the present class of flows under adverse pressure gradients. A parametric study of the effect of asymmetric velocity profile for different slot heights and jet velocities can be made. Also, there is a need for comparison of measurements with a uniform and an asymmetric jet velocity profile under similar conditions with the same jet momentum in each case. The skewness of the asymmetric jet velocity profile can be enhanced further and its effect can be studied on the downstream flow development.

APPENDIX A

MEASUREMENTS ON A WALL JET BY BOWLES (1977)

Bowles (1977) took hot wire measurements of U and u_t at the exit of a wall jet with a similar design as in the present experiments. The slot height in his case was 6.35 mm. Fig. A.1 shows the velocity and turbulence profiles at the exit of the jet for the Bowles case. The asymmetric velocity profile typical of the present wall jet design can be observed in this case also. However, the turbulence profile is different as compared with the turbulence profile at the jet exit in the present experiments shown in Fig. 2.11. The turbulence profile shown in Fig. A.1 shows a maximum near the wall at about $0.2y_c$ which is well above the outer limit of the thin sublayer for this high speed flow (U_{Jmax} = 35 m/sec). The cross sectional area of the nozzle around the corner in the case of Bowles' jet was kept constant as compared to a reduction in the cross-sectional area in the present case. As discussed in Chapter 2, this feature gives rise to the possibility of separation around the corner and the consequent re-attachment downstream. Therefore, the maxima in u_t near the wall shown in Fig. A.1 may be the remainder

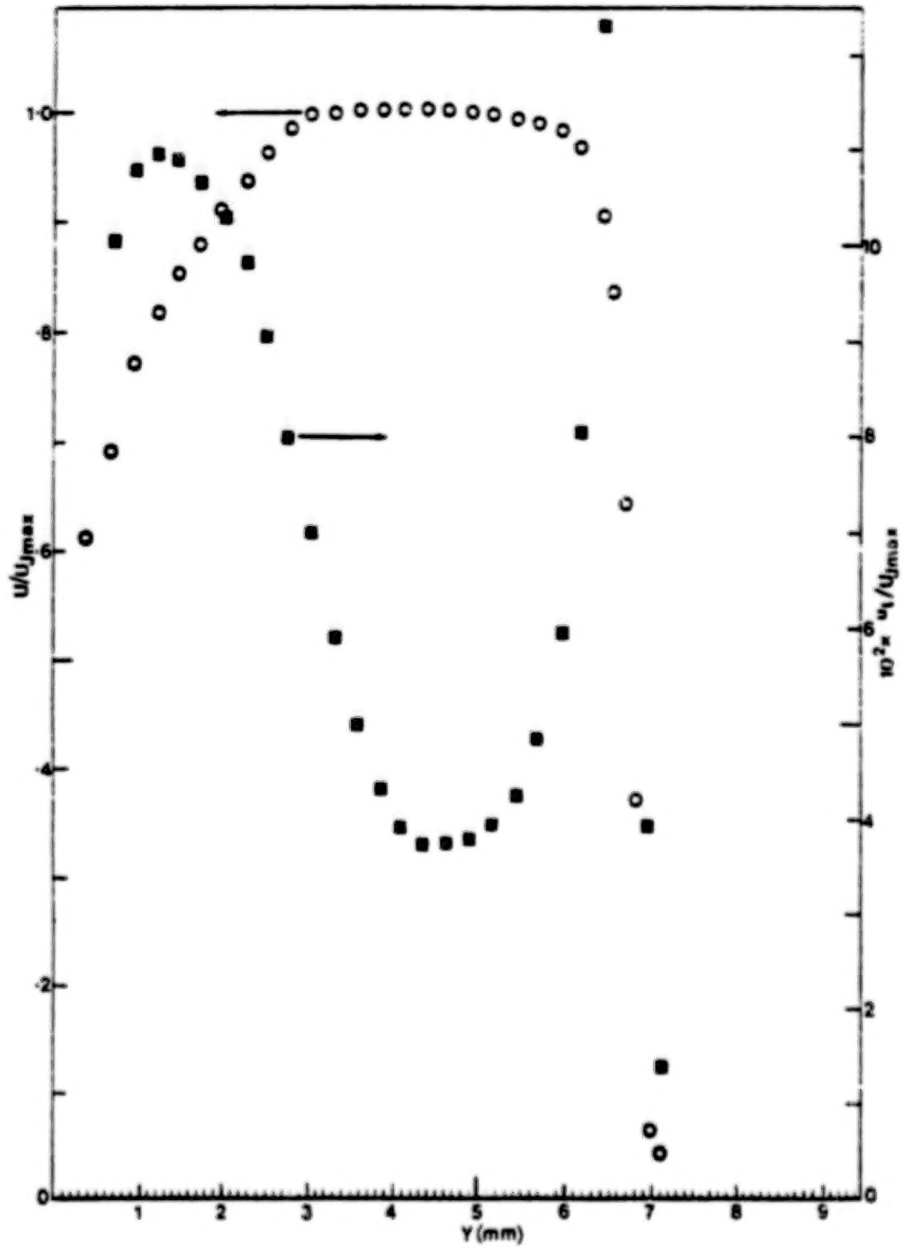

Fig. A-1 Mean Velocity and Turbulence Profiles at the Exit of the Jet (Bowles) from separation around the corner of the nozzle. The u_t values in Fig. A.1 are non-dimensionalized with U_{Jmax}, the maximum velocity at the jet exit. The hot wire measurements of Bowles were taken at 0.8 mm from the lip.

APPENDIX B

ESTIMATION OF THE FRICTIONAL LOSSES IN THE WALL JET NOZZLE

The details on the estimation of frictional losses in the present wall jet nozzle are given in this appendix. The frictional losses are estimated by making an energy balance on the control volume surrounding the wall jet nozzle. The measured jet exit velocity profile and the measured static pressure inside the nozzle are used in the estimation of frictional losses.

Fig. B.1 shows the close-up view of the wall jet nozzle. The section (1) corresponds to the position where the static pressure connection was made in the wall jet nozzle as described in Chapter 2. Section (1) is located 1.27 cm below the surface of the wind tunnel as shown in Fig. 2.5. The Section (2) corresponds to the exit of the wall jet. Since most of the frictional losses in the nozzle occur between Sections (1) and (2), an attempt has been made to estimate those losses.

Let U_2 be the velocity at any given y location at Section (2)

U_1 be the uniform average velocity at Section (1)

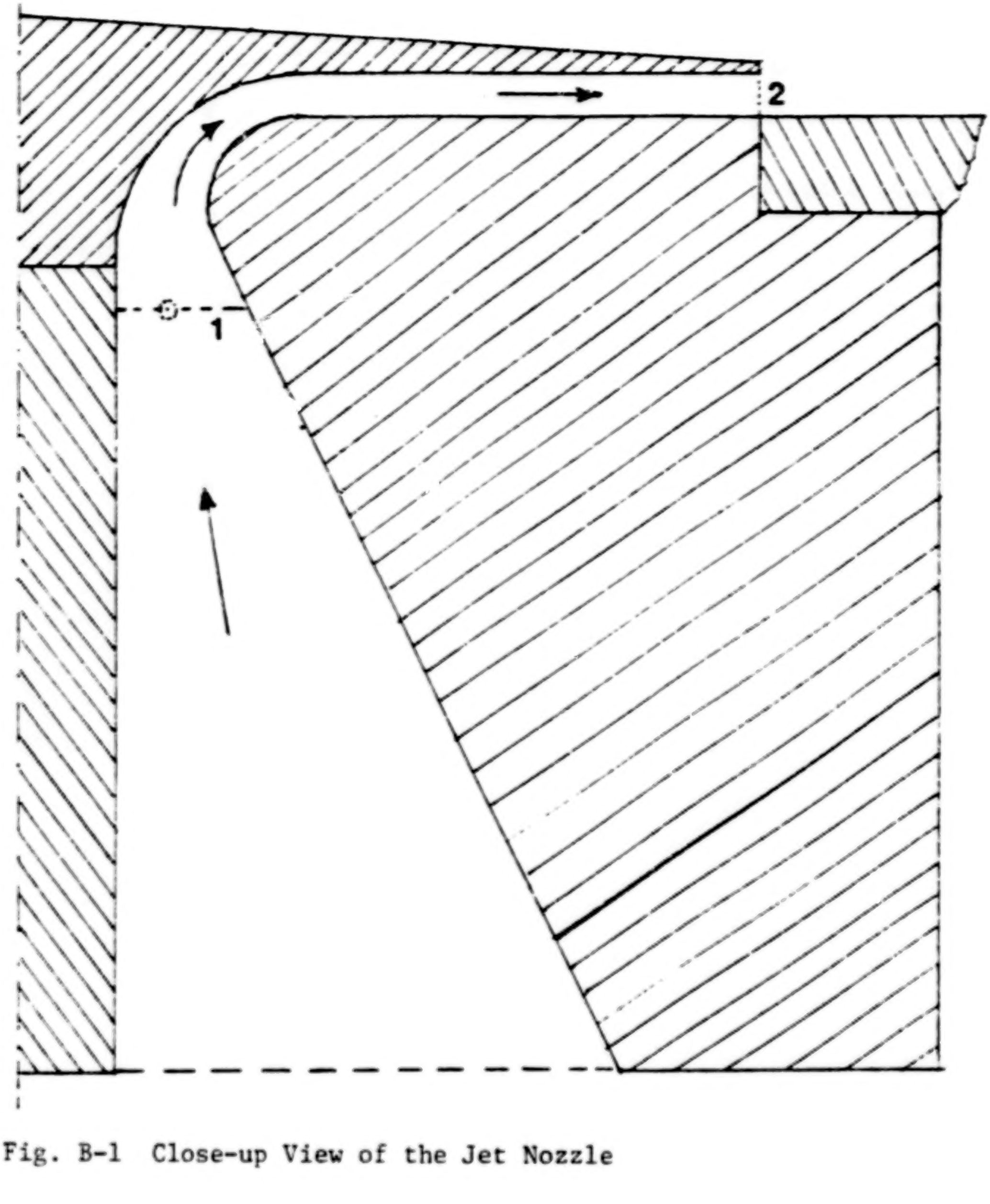

Fig. B-1 Close-up View of the Jet Nozzle

b_1 be the width of the nozzle at Section (1)

P_1 be the static pressure at Section (1)
above the static pressure at Section (2)

ρ be the density of the fluid

For the unit length of the nozzle:

Kinetic energy going out at Section (2) =

$$\frac{\rho}{2} \int_0^{y_c} U_2^3 \, dy$$

Kinetic energy coming in at Section (1) =

$$\frac{\rho}{2} U_1^3 b_1$$

Flow work input at Section (1) =

$$P_1 b_1 U_1$$

Let the frictional losses between the Sections (1) and (2) = F.L.

An energy balance on the control volume surrounding the Sections (1) and (2) and the portion of the nozzle in between them gives

$$\text{F.L.} + \frac{\rho}{2} \int_0^{y_c} U_2^3 \, dy = \frac{\rho}{2} U_1^3 b_1 + P_1 b_1 U_1 \quad \text{(B.1)}$$

In the equation (B.1), U_2 can be obtained from the measured velocity profile at the jet exit, and the corresponding value of P_1 can be measured directly. The velocity U_1 at Section (1) is obtained by making a mass balance between the sections (1) and (2) as follows:

Let M_1 and M_2 be the mass flow rates per unit length of the nozzle at Sections (1) and (2) respectively.

Then

$$M_1 = \rho U_1 b_1$$

$$M_2 = \rho \int_0^{y_c} U_2 dy \qquad (B.2)$$

U_1 can be calculated from the measured distribution of U_2 and the mass balance $M_1 = M_2$. Therefore, the frictional losses (F.L) in the equation (B.3) can be calculated from the measured velocity distribution U_2 at the jet exit and the corresponding measured static pressure (P_1) at Section (1).

In the present nozzle design, the frictional losses between the Sections (1) and (2) were found to be about 15% of the total energy input at Section (1). These frictional losses between Sections (1) and (2) form a significant part of the total frictional losses in the nozzle.

APPENDIX C

MEASUREMENT OF TURBULENCE INTENSITIES AND THE REYNOLDS SHEAR STRESS

This appendix gives the details regarding the measurement of turbulence intensities v_t/U_∞ and w_t/U_∞ and the Reynolds shear stress $-\overline{uv}$ using the slant-wire. A brief description of the probe alignment procedures, and the estimation of mean V and W are also given.

The directional sensitivity of the slant-wire makes possible the use of it for the measurement of individual components of the velocity vector. Several investigators, e.g., Andersen, et al. (1972), have used the slant wire successfully to obtain different components of the turbulent fluctuations and the Reynolds shear stress $-\overline{uv}$. A similar method was used in the present experiments for the determination of v_t, w_t, and $-\overline{uv}$. A general outline of the method of obtaining these turbulent quantities will be given here and for greater details one may refer to the work of Andersen et al. (1972). The method of obtaining $\overline{v^2}$, $\overline{w^2}$ and $-\overline{uv}$ is given below. v_t and w_t can be obtained using the relations $v_t^2 = \overline{v^2}$ and $w_t^2 = \overline{w^2}$.

C.1 Theory of the Directional Sensitivity of the Hot-Wire

As shown by Jorgensen (1971), the effective cooling velocity $\widetilde{U}_i$ for a hot-wire may be approximated by

$$\widetilde{U}_i^{\,2} = (\widetilde{U}_2)^2 + (K_1)^2(\widetilde{V}_2)^2 + (K_2)(\widetilde{W}_2)^2 \qquad (C.1)$$

where $\widetilde{U}_2$ is the velocity component perpendicular to the wire and lies in the plane of wire supports, $\widetilde{V}_2$ is parallel to the wire and $\widetilde{W}_2$ is perpendicular to the wire and the wire supports. K_1 and K_2 are constants which depend on the hot wire probe design and the velocity. These constants are experimentally determined for the given probe and the range of velocities under consideration.

Fig. C.1 shows the probe geometry and position for a slant hot-wire probe. The slant wire makes an angle ϕ with a plane perpendicular to the probe axis. (x_1, y_1, z_1) is the mean flow co-ordinate system in which the mean velocity vector has the components $(U_1, 0, 0)$. This co-ordinate system is in general not completely coincident with the laboratory co-ordinate system (x, y, z) in which the mean velocity vector is (U, V, W). The measured values of $\overline{v^2}$, $\overline{w^2}$, and $-\overline{uv}$ will strictly speaking be expressed in the (x_1, y_1, z_1) co-ordinate system. However, for the flow under consideration V and W are small compared with U and the measured turbulent quantities can be considered as measured in laboratory co-ordinates (x, y, z) with negligible error. The hot-wire probe axis will be assumed to be

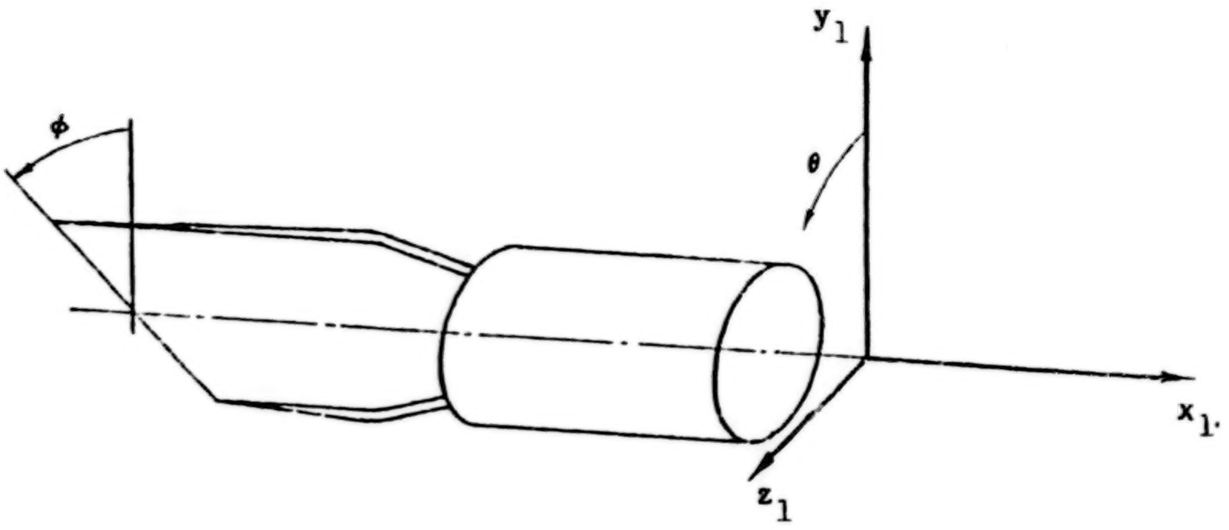
ϕ
y_1
θ
x_1.
z_1

Fig. C-1 Geometry and Position of the Slant-Wire Probe (schematic). Probe shown for $\theta = 0$.

aligned with the mean velocity vector, i.e., the probe axis is in the direction of x_1. θ is the angle of rotation of the probe about its own axis and it is zero when the plane of wire supports coincides with the x_1, y_1 plane.

Referring to Fig. C.1, the relationship between the velocity components ($\tilde{U}_1$, $\tilde{V}_1$, $\tilde{W}_1$) in the mean flow reference system (x_1, y_1, z_1) and the components ($\tilde{U}_2$, $\tilde{V}_2$, $\tilde{W}_2$) in the wire co-ordinates is given by

$$\begin{bmatrix} \tilde{U}_2 \\ \tilde{V}_2 \\ \tilde{W}_2 \end{bmatrix} = \begin{bmatrix} \cos\phi & \sin\phi\cos\theta & \sin\phi\sin\theta \\ -\sin\phi & \cos\phi\cos\theta & \cos\phi\sin\theta \\ 0 & -\sin\theta & \cos\theta \end{bmatrix} \begin{bmatrix} \tilde{U}_1 \\ \tilde{V}_1 \\ \tilde{W}_1 \end{bmatrix} \qquad (C.2)$$

Equation (C.3) is obtained by performing the following steps.

1. Inserting equation C.2 into C.1.

2. Resolving the velocity components U_i, U_1, V_1, W_1 as

$$\tilde{U}_i = U_i + u_i$$

$$\tilde{U}_1 = U_1 + u_1$$

$$\tilde{V}_1 = v_1$$

$$\tilde{W}_1 = w_1$$

3. Recognizing that the mean flow reference ($\tilde{U}_1$, $\tilde{V}_1$, $\tilde{W}_1$) is the same as the laboratory frame of reference ($\tilde{U}$, $\tilde{V}$, $\tilde{W}$) for the flow under consideration where V and W are small compared to U.

4. Simple mathematical manipulation of the resulting equations.

5. Neglecting the higher order terms.

$$\overline{u_i^2} = A\overline{u^2} + \frac{D^2}{4A}\overline{v^2} + \frac{F^2}{4A}\overline{w^2} + D\,\overline{uv} \qquad \text{(C.3)}$$

Where $\overline{u^2}$, $\overline{v^2}$, $\overline{w^2}$, and $-\overline{uv}$ are the normal stresses and shear stress in the laboratory frame of reference and $\overline{u_i^2}$ is the indicated or measured normal stress at any given position of the probe. A, D, F are the coefficients given by

$$A = \cos^2\phi + K_1{}^2\sin^2\phi$$

$$D = (1-K_1{}^2)\ \sin2\phi\cos\theta$$

$$F = (1-K_1{}^2)\ \sin2\phi\sin\theta$$

For the slant wire used in the present measurements $\phi = 45°$.

C.2 Determination of $\overline{v^2}$, $\overline{w^2}$, and $-\overline{uv}$

Equation (C.3) contains four unknowns, i.e., $\overline{u^2}$, $\overline{v^2}$, $\overline{w^2}$, and $-\overline{uv}$. Therefore, a minimum of four measurements of $\overline{u_i^2}$ are required with the rotatable slant-wire at four different values of θ for the determination of $\overline{u^2}$, $\overline{v^2}$, $\overline{w^2}$, and $-\overline{uv}$. However, the nature of the coefficient A does not permit the evaluation of $\overline{u^2}$ from equation C.3. This is because the value of A does not change with different values of θ for a given value of ϕ, when the probe axis is aligned with the mean flow direction. Hence, the normal-hot film data of $\overline{u^2}$ were used in the equation (C.3) to obtain $\overline{v^2}$, $\overline{w^2}$ and $-\overline{uv}$. The $\overline{u^2}$ at the slant wire location was obtained from the normal hot-film data by interpolating a five point quadratic curve fit. With $\overline{u^2}$ being known, a minimum of three measurements of $\overline{u_i^2}$ are required with the rotatable slant wire at three different values of θ for the determination of $\overline{v^2}$, $\overline{w^2}$, and $-\overline{uv}$. Measurements of $\overline{u_i^2}$ were made at seven different values of $\theta = (m-1)\pi/6$ ($m = 1,2,3, \ldots 7$). Seven measurements were made instead of the minimum required three, to make a redundancy check on the quantities $\overline{v^2}$, $\overline{w^2}$, and $-\overline{uv}$.

C.2.1 Techniques of Obtaining v_t, w_t, and $-\overline{uv}$

The basic principle used in the calculation of the turbulence quantities was to obtain them in a way involving a minimum amount of mathematical manipulation of the direct measurements in order to reduce the errors to a minimum.

$-\overline{uv}$ was obtained from equation C.3 in three different ways from six different measurements of $\overline{u_i^2}$ as follows:

1. $(\overline{u_i^2})_{\theta=0°} - (\overline{u_i^2})_{\theta=180°}$
2. $(\overline{u_i^2})_{\theta=30°} - (\overline{u_i^2})_{\theta=150°}$
3. $(\overline{u_i^2})_{\theta=60°} - (\overline{u_i^2})_{\theta=120°}$

All three values of $-\overline{uv}$ agreed very well within a maximum of 10% variation. The average of the three values of $-\overline{uv}$ was finally taken.

$\overline{v^2}$ was obtained from the measurements of $(\overline{u_i^2})_{\theta=0°}$ and $(\overline{u_i^2})_{\theta=180°}$. This set of measurements eliminates the effect of $\overline{w^2}$ on $\overline{v^2}$ data. A comparison of $\overline{v^2}$ obtained in this manner with the $\overline{v^2}$ obtained from measurements at other values of θ gave good agreement between them with a maximum variation of about 15%.

$\overline{w^2}$ was obtained from the measurement of $(\overline{u_i^2})_{\theta=90°}$. This measurement eliminates the effect of $\overline{v^2}$ and $-\overline{uv}$ on $\overline{w^2}$ data. A comparison of $\overline{w^2}$ obtained in this manner with the $\overline{w^2}$ obtained from measurements at other values of θ gave good agreement between them with a maximum variation of about 15%.

The variations in $\overline{v^2}$, $\overline{w^2}$, and $-\overline{uv}$ obtained from different sets of measurements are mainly due to the mean velocity gradients present within the finite space occupied by the slant wire and they cannot be calibrated. It should be noted here that the uncertainties in the measurement of $\overline{v^2}$, $\overline{w^2}$, and $-\overline{uv}$ given in Chapter 3 are smaller than the variations due to velocity gradients mentioned above.

C.3 Determination of Constants K_1 and K_2 in the Equation C.1

Knowledge of K_1 is necessary to obtain the turbulence quantities from equation C.3. However, an attempt has been made to determine the value of K_2 also. The method of Jorgensen (1971) was used for the determination of K_1 and K_2. It essentially involves the use of equation C.1 and the calibration of the slant wire at three different positions in the calibrator. The flow in the calibrator described in Chapter 2 has the components of velocity (U,0,0) in the coordinate system (x_1, y_1, z_1) shown in Fig. C.1. The relationship between the non-linearized anemometer output Voltage E and the effective velocity U_i can be written as

$$E^2 = A + B\,U_i^{\,n} \qquad \text{(C.4)}$$

Where n is the exponent of the order of 0.45 and A, B are constants. Calibration of the slant wire was done at three different positions given below:

1. The wire is perpendicular the flow and faces it with the plane of the wire supports in line with the flow, with the corresponding non-linearized anemometer voltage output being E_0.

2. The axis of the probe is in line with the flow and the wire faces the flow, with the corresponding output being E_2.

3. The plane of the wire supports, the wire and the probe axis are all perpendicular to the flow with the corresponding output being E_3.

K_1 and K_2 were evaluated from the following equations obtained from the equation (C.4).

$$K_1 = \frac{1}{\sin\phi}\left[\left(\frac{E_2^2-A}{E_0^2-A}\right)^{2/n} - \cos^2\phi\right]^{1/2} \qquad \text{(C.5)} \quad \text{With } \phi = 45°$$

$$K_2 = \frac{1}{\sin\theta}\left[\left(\frac{E_3^2-A}{E_0^2-A}\right)^{2/n} - \cos^2\theta\right]^{1/2} \qquad \text{(C.6)} \quad \text{With } \theta = 90°$$

The determination of K_1 and K_2 was done at different flow velocities covering the range of velocities encountered in the wind tunnel. The value of K_1 used in the equation (C.3) was chosen according to the magnitude of the mean velocity at the data point under consideration. The value of

K_1 for the present slant wire was between 0.3 to 0.39 and the value of K_2 was almost constant around 1.05 for the velocities ranging between 3 and 41 m/sec. K_1 was generally found to increase slowly with the velocity and K_2 was found to vary within a maximum of 1% for the range of velocities mentioned above.

C.4 Alignment of the Probe

In order to use equation (C.3) for the determination of turbulent quantities, the probe axis has to be aligned with the mean flow vector.

C.4 (a) Probe Alignment for Zero Pressure Gradient Flow

In the case of zero pressure gradient flow, the alignment was done in the free-stream. To do the alignment, the probe was held in the free-stream and then the pitch and yaw of the probe were adjusted so that the mean anemometer output remained the same at any angular position of the probe when rotated about its own axis. Afterwards, the probe position was not disturbed during the process of taking data for that streamwise station. This alignment procedure gave rise to a probe position where the probe axis was parallel to the free-stream velocity.

It was not possible to precisely adjust the probe alignment with the mean flow vector in the boundary layer and to preci[illegible] measure the angular change with respect to the free-stream alignment. Hence the mean anemometer outputs were different at different values of θ. The misalignment of the probe axis with the mean flow in the vertical and horizontal planes can be calculated from the mean anemometer outputs at $\theta = 0°$, 90° and 180° using the misalignment analysis of Andersen et al. (1972). In the region of large velocity gradients, part of the difference in anemometer output at different values of θ should be attributed to velocity gradients and finite size of the wire. However, in the present case, it was assumed that the difference in the anemometer outputs at $\theta = 0°$, 90° and 180° is entirely due to the misalignment of the probe. The misalignment angle was never greater than 0.8° in the vertical plane, and was never greater than 1° in the horizontal plane for the majority of the slant wire data in the case of zero pressure gradient flow at x/y_c = 16.5 and beyond. As given by Andersen et al. (1972), the error introduced in the measured turbulence quantities due to these small misalignment angles is very small. The misalignment angles for stations x/y_c = 0.292 and -16.4 were relatively higher because the flow near the wall jet body is inclined at these stations. This is due to the special shape of the wall jet body and no attempt has been made to correct the data at these stations for the flow inclination.

C.4 (b) Probe Alignment for the Adverse Pressure Gradient Flow

In the case of the adverse pressure gradient flow, the stream-lines were inclined towards the top wall since the fluid was escaping through the perforations in the top wall. The flow inclination was maximum near the top wall and it decreased gradually towards the bottom wall. It is not possible to precisely adjust the alignment of the probe with the flow at each vertical location. Therefore, for reference, the probe was aligned with its axis parallel to the bottom wall.

The misalignment of the probe axis with the flow in the horizontal and vertical planes was calculated in the same way as for the zero pressure gradient flow. The misalignment angle in the horizontal plane was found to be small and of the order of 1°. However, the misalignment angle in the vertical plane which is also equal to the flow inclination angle was found to be large when compared to the zero pressure gradient flow.

For points near the free-stream, where the shear stress was very small, the flow inclination angle reached values up to 13°. However, in the region where the turbulence quantities were significantly large, the flow inclination was less than 5°.

Here, it should be noted that the constant K_1 varies with the angle of inclination of the flow vector with the probe axis. Littlefield (1978) indicated that good measurements of $\overline{v^2}$ within about 10% error can be made by neglecting higher order terms and using constant values of K_1 in the equation (C.3) for flow inclination angles up to 5°. The error in the $-\overline{uv}$ measurements is relatively higher. In the present measurements the flow inclination was less than 5° points where the shear stress is significant.

For points where the flow inclination was about 5°, the shear stress was relatively smaller. Hence, the error in the present measurements of $-\overline{uv}$ at points where the shear stress is significant should not be more than 10%. However, no attempt has been made to correct the present data for the flow inclination.

C.5 Mean Velocities V and W

An attempt has been made to estimate the magnitudes of mean V and W with respect to the probe to a first order approximation using equations (C.1) and (C.2). The principle applied in the calculation of V and W was that inside the boundary layer the difference in mean anemometer outputs at different angular positions of the probe about its axis gives an indication of the magnitudes of V and W. The same principle was also applied in the calculation of misalignment angles. It is easier to conceive that the misalignment of the probe in the vertical and horizontal planes is a measure of mean V and W respectively.

A redundancy check was also made on the V and W by calculating them from three independent measurements. In the case of the zero pressure gradient flow, for stations x/y_c = 16.5 and beyond, the values of W were found to vary at random within a maximum of ±.02U and the values of V were found to be within a maximum of +.02U.

In the case of adverse pressure gradient flow, the flow was inclined towards the top wall and hence resulted in a larger V as compared to the zero pressure gradient flow. However, the nature and magnitude of W variation were comparable with that of the zero pressure gradient flow.

APPENDIX D

In this appendix the normal hot-film data for the zero pressure gradient flow are tabulated. The data consist of mean velocity U/U_∞ and the turbulence intensity u_t/U_∞. The skin friction data are also presented at each station.

TABLE D

NORMAL HOT-FILM DATA OF U/U_∞ AND u_t/U_∞ FOR THE ZERO PRESSURE GRADIENT FLOW

X/YC = -77.100   UINF = 25.67 M/SEC
CF = .003303   DELTA = 1.529 CMS

Y(CMS)	U/UINF	UT/UINF
.015	.338	.0837
.018	.369	.0882
.020	.405	.0902
.023	.429	.0924
.025	.451	.0921
.028	.478	.0915
.033	.500	.0887
.038	.522	.0869
.043	.543	.0841
.048	.557	.0814
.053	.570	.0801
.058	.579	.0783
.063	.591	.0771
.076	.608	.0747
.089	.624	.0737
.102	.636	.0728
.114	.645	.0732
.127	.655	.0727
.140	.665	.0738
.165	.679	.0733
.191	.692	.0739
.216	.704	.0738
.241	.716	.0739
.267	.726	.0732
.320	.747	.0723
.394	.769	.0708
.457	.787	.0696
.521	.805	.0679
.584	.821	.0664
.711	.850	.0636
.838	.882	.0594
.965	.908	.0550
1.092	.933	.0497
1.219	.956	.0404
1.346	.973	.0304
1.473	.986	.0199
1.600	.994	.0119
1.854	1.000	.0063
2.108	1.000	.0041
2.362	1.000	.0032
2.616	.999	.0024
2.870	.999	.0020
3.378	.999	.0016
3.886	.998	.0014
4.394	.998	.0013
4.902	.998	.0012
5.410	.997	.0012
5.918	.997	.0012
6.426	.997	.0013
6.680	.999	.0016

X/YC = -16.300   UINF = 28.21 M/SEC
DELTA = 1.130 CMS

Y(CMS)	U/UINF	UT/UINF
.010	.481	.0654
.013	.579	.0761
.015	.655	.0851
.018	.718	.0850
.020	.758	.0822
.023	.794	.0787
.028	.838	.0724
.033	.863	.0678
.038	.879	.0645
.043	.891	.0622
.048	.897	.0602
.053	.903	.0586
.061	.909	.0564
.074	.914	.0545
.086	.918	.0537
.099	.919	.0525
.112	.921	.0522
.137	.920	.0526
.163	.922	.0524
.201	.922	.0526
.264	.924	.0527
.328	.929	.0519
.391	.933	.0505
.455	.939	.0488
.518	.944	.0474
.645	.953	.0463
.772	.963	.0444
.899	.972	.0415
1.026	.981	.0377
1.280	.995	.0253
1.534	1.000	.0132
1.788	.995	.0069
2.042	.989	.0041
2.296	.982	.0029
2.550	.978	.0023
2.804	.974	.0019
3.058	.970	.0016
3.185	.968	.0016
3.312	.966	.0015
3.820	.961	.0012
4.328	.957	.0011
4.836	.954	.0010
5.344	.952	.0012
5.852	.950	.0016

X/YC = .292   UINF = 27.14 M/SEC
DELTA = 2.174 CMS
U/UINF : 1.281

Y(CMS)	U/UINF	UT/UINF
.020	1.205	.0909
.023	1.225	.0890
.025	1.239	.0871
.028	1.253	.0847
.030	1.263	.0825
.033	1.276	.0797
.038	1.293	.0754
.043	1.306	.0716
.048	1.312	.0673
.053	1.320	.0643
.061	1.331	.0627
.066	1.337	.0587
.079	1.347	.0548
.091	1.360	.0522
.104	1.367	.0500
.117	1.372	.0479
.142	1.383	.0459
.168	1.392	.0454
.193	1.397	.0495
.206	1.393	.0546
.218	1.385	.0646
.231	1.359	.0831
.244	1.262	.1103
.249	1.168	.1178
.254	1.000	.1267
.259	.743	.1573
.264	.393	.1263
.269	.168	.0543
.274	.119	.0369
.284	.136	.0360
.292	.088	.0341
.300	.046	.0183
.307	.045	.0152
.315	.072	.0303
.323	.159	.0509
.328	.236	.0775
.333	.301	.0801
.338	.379	.0842
.345	.427	.0850
.353	.449	.0854
.358	.465	.0858
.366	.483	.0864
.371	.496	.0863
.384	.521	.0859
.396	.541	.0854
.409	.557	.0846
.434	.587	.0834
.460	.614	.0818
.485	.639	.0807
.511	.661	.0790
.549	.681	.0761
.561	.702	.0752
.625	.737	.0712
.688	.762	.0687
.752	.780	.0673
.815	.795	.0661
.942	.821	.0652
1.069	.849	.0616
1.196	.876	.0580
1.323	.896	.0537
1.577	.934	.0452
1.831	.965	.0315
2.085	.985	.0173
2.342	.996	.0081
2.596	.999	.0049
2.847	1.000	.0036
3.101	.999	.0027
3.609	.999	.0019
4.117	.996	.0016
4.625	.995	.0013
5.133	.995	.0011
5.641	.993	.0011
6.150	.993	.0014

TABLE D (Cont.)

X/YC = 7.400 UINF = 27.99 M/SEC

CF = .013294 DELTA = 2.298 CMS

Y(CMS)	U/UINF	UT/UINF
.010	.715	.1443
.013	.769	.1520
.015	.851	.1591
.018	.916	.1579
.020	.970	.1550
.023	1.017	.1490
.028	1.083	.1410
.033	1.129	.1324
.038	1.167	.1252
.043	1.197	.1178
.048	1.219	.1120
.053	1.237	.1073
.066	1.270	.0997
.079	1.290	.0950
.091	1.301	.0919
.104	1.306	.0912
.117	1.306	.0912
.130	1.301	.0930
.142	1.293	.0951
.155	1.283	.0974
.168	1.269	.1002
.180	1.251	.1021
.193	1.231	.1047
.218	1.183	.1112
.244	1.127	.1187
.269	1.064	.1253
.295	1.001	.1286
.320	.937	.1275
.345	.870	.1209
.371	.829	.1100
.396	.788	.0988
.422	.758	.0875
.447	.736	.0787
.472	.725	.0735
.498	.721	.0712
.523	.722	.0702
.549	.726	.0703
.574	.732	.0702
.599	.741	.0690
.625	.748	.0681
.688	.768	.0665
.752	.784	.0653
.815	.795	.0642
.879	.808	.0637
1.006	.835	.0614
1.133	.859	.0582
1.260	.881	.0556
1.387	.902	.0515
1.514	.922	.0463
1.641	.940	.0410
1.768	.955	.0340
1.895	.967	.0267
2.022	.978	.0195
2.149	.985	.0131
2.276	.989	.0094
2.403	.993	.0071
2.530	.995	.0057
2.657	.996	.0043
2.784	.996	.0038
3.038	.997	.0029
3.292	.998	.0023
3.546	.999	.0018
3.800	.999	.0016
4.308	1.000	.0013
4.816	1.000	.0011
5.324	1.000	.0010
5.832	1.000	.0011
6.340	1.000	.0016

X/YC = 16.300 UINF = 26.67 M/SEC

CF = .010956 DELTA = 2.222 CMS

Y(CMS)	U/UINF	UT/UINF
.010	.796	.1262
.013	.842	.1263
.015	.888	.1236
.018	.924	.1206
.020	.950	.1173
.023	.983	.1130
.028	1.026	.1078
.033	1.056	.1036
.041	1.092	.0988
.048	1.119	.0958
.056	1.137	.0933
.069	1.163	.0904
.081	1.181	.0888
.094	1.194	.0881
.107	1.202	.0877
.119	1.205	.0874
.132	1.206	.0880
.145	1.204	.0887
.157	1.200	.0896
.170	1.195	.0908
.183	1.185	.0919
.208	1.163	.0951
.234	1.140	.0982
.259	1.111	.1010
.310	1.049	.1048
.373	.967	.1021
.437	.897	.0925
.500	.843	.0794
.564	.807	.0693
.627	.791	.0653
.691	.794	.0657
.754	.802	.0655
.818	.814	.0655
.881	.825	.0639
1.008	.847	.0607
1.135	.870	.0574
1.262	.892	.0544
1.522	.929	.0455
1.776	.960	.0341
2.030	.981	.0205
2.284	.993	.0102
2.538	.997	.0058
2.792	1.000	.0041
3.046	1.000	.0031
3.363	1.000	.0025
3.681	1.000	.0020
3.998	1.000	.0018
4.252	1.000	.0017
4.760	.999	.0015
5.268	1.002	.0014
5.776	1.003	.0014
6.284	1.002	.0010

X/YC = 35.050 UINF = 26.64 M/SEC

CF = .007797 DELTA = 2.192 CMS

Y(CMS)	U/UINF	UT/UINF
.010	.576	.1050
.013	.636	.1069
.015	.676	.1080
.018	.719	.1085
.020	.754	.1091
.023	.783	.1081
.028	.826	.1040
.033	.859	.0992
.043	.907	.0904
.056	.950	.0819
.069	.980	.0756
.081	1.003	.0710
.107	1.036	.0638
.132	1.058	.0589
.157	1.069	.0555
.183	1.075	.0547
.196	1.076	.0550
.208	1.077	.0557
.221	1.076	.0570
.234	1.073	.0583
.259	1.068	.0601
.284	1.060	.0630
.310	1.049	.0652
.361	1.028	.0686
.424	.997	.0716
.488	.965	.0713
.551	.934	.0685
.615	.906	.0636
.678	.883	.0582
.742	.866	.0548
.805	.856	.0532
.869	.854	.0521
.932	.857	.0544
.996	.862	.0552
1.059	.867	.0558
1.186	.884	.0540
1.313	.902	.0523
1.440	.917	.0482
1.567	.937	.0429
1.694	.952	.0392
1.948	.976	.0272
2.202	.990	.0143
2.456	.999	.0076
2.710	1.000	.0048
2.964	1.000	.0035
3.472	1.000	.0023
3.980	.999	.0018
4.488	.999	.0017
4.996	.998	.0015
5.504	.998	.0015
6.013	.999	.0017

TABLE D (Cont.)

X/YC = 53.740 UINF = 26.87 M/SEC

CF = .006276 DELTA = 2.262 CMS

Y(CMS)	U/UINF	UT/UINF
.010	.535	.1036
.013	.574	.1035
.015	.618	.1024
.018	.652	.1004
.020	.677	.0987
.023	.699	.0970
.028	.736	.0950
.033	.764	.0936
.041	.796	.0899
.048	.820	.0871
.061	.853	.0816
.074	.881	.0768
.099	.922	.0692
.124	.954	.0624
.150	.977	.0572
.175	.994	.0529
.201	1.007	.0495
.226	1.015	.0476
.251	1.020	.0470
.277	1.021	.0470
.302	1.021	.0478
.328	1.018	.0492
.356	1.014	.0504
.404	1.004	.0530
.455	.991	.0549
.493	.980	.0554
.556	.962	.0560
.620	.945	.0552
.683	.930	.0530
.747	.913	.0505
.810	.902	.0482
.874	.894	.0465
.937	.888	.0455
1.001	.886	.0453
1.064	.886	.0461
1.128	.888	.0470
1.191	.892	.0470
1.255	.897	.0481
1.382	.910	.0484
1.509	.924	.0466
1.636	.938	.0476
1.763	.953	.0392
2.017	.975	.0282
2.271	.991	.0153
2.525	.998	.0082
2.779	1.000	.0049
3.033	1.000	.0035
3.287	1.000	.0028
3.541	.999	.0024
3.795	.999	.0020
4.303	.999	.0017
4.811	.998	.0015
5.319	.997	.0014
5.827	.997	.0017
6.081	.998	.0018

X/YC = 74.480 UINF = 26.74 M/SEC

CF = .005286 DELTA = 2.411 CMS

Y(CMS)	U/UINF	UT/UINF
.010	.464	.0945
.013	.510	.0965
.015	.547	.0958
.018	.576	.0933
.020	.605	.0914
.025	.637	.0879
.030	.670	.0848
.036	.692	.0830
.046	.726	.0813
.059	.756	.0788
.071	.779	.0763
.084	.799	.0741
.109	.836	.0698
.135	.866	.0647
.173	.902	.0574
.211	.929	.0506
.249	.947	.0449
.287	.960	.0412
.325	.966	.0392
.363	.969	.0386
.401	.970	.0388
.439	.968	.0390
.503	.962	.0414
.566	.953	.0426
.630	.943	.0429
.757	.926	.0421
.884	.911	.0390
1.011	.900	.0381
1.138	.896	.0384
1.265	.899	.0402
1.392	.907	.0417
1.519	.917	.0422
1.646	.932	.0413
1.900	.956	.0355
2.154	.977	.0253
2.408	.990	.0137
2.662	.997	.0075
2.916	.999	.0047
3.170	1.000	.0035
3.424	1.000	.0027
3.678	1.000	.0023
3.932	.999	.0021
4.186	.999	.0019
4.440	.999	.0017
4.694	.998	.0016
5.202	.999	.0015
5.456	.999	.0016
5.710	.999	.0017
5.964	.999	.0017

X/YC = 92.290 UINF = 26.72 M/SEC

CF = .004706 DELTA = 2.532 CMS

Y(CMS)	U/UINF	UT/UINF
.010	.432	.0921
.013	.476	.0951
.015	.509	.0949
.018	.536	.0933
.020	.562	.0913
.023	.584	.0887
.028	.618	.0850
.033	.640	.0828
.038	.657	.0807
.048	.687	.0780
.061	.713	.0769
.074	.739	.0753
.086	.757	.0741
.099	.774	.0722
.124	.805	.0680
.150	.830	.0632
.175	.852	.0610
.201	.872	.0572
.226	.889	.0533
.277	.918	.0457
.328	.936	.0394
.378	.947	.0356
.417	.952	.0339
.480	.955	.0333
.544	.953	.0339
.607	.949	.0347
.671	.941	.0340
.734	.936	.0349
.798	.931	.0349
.861	.924	.0344
.925	.922	.0341
.988	.917	.0338
1.052	.914	.0332
1.115	.911	.0331
1.179	.910	.0334
1.242	.910	.0337
1.369	.913	.0350
1.496	.921	.0364
1.623	.927	.0375
1.750	.937	.0374
1.877	.947	.0358
2.131	.968	.0292
2.385	.983	.0191
2.639	.995	.0102
2.893	.998	.0058
3.147	1.000	.0040
3.401	1.000	.0030
3.655	.999	.0025
4.163	.999	.0018
4.671	.998	.0016
5.179	.998	.0015
5.687	.998	.0016
5.941	.998	.0018

TABLE D (Cont.)

X/YC = 108.360 UINF = 26.72 M/SEC

CF = .004430 DELTA = 2.575 CMS

Y(CMS)	U/UINF	UT/UINF
.013	.450	.0921
.015	.482	.0933
.018	.511	.0923
.020	.530	.0905
.023	.561	.0881
.025	.581	.0853
.030	.611	.0812
.036	.630	.0786
.041	.647	.0770
.046	.660	.0756
.051	.673	.0752
.058	.689	.0741
.071	.709	.0730
.084	.727	.0724
.097	.743	.0716
.122	.772	.0693
.147	.797	.0671
.185	.830	.0623
.249	.873	.0539
.312	.905	.0450
.376	.927	.0378
.439	.941	.0326
.503	.947	.0302
.566	.949	.0294
.630	.948	.0297
.696	.945	.0300
.757	.942	.0301
.884	.935	.0303
.947	.931	.0300
1.011	.928	.0297
1.074	.926	.0296
1.138	.924	.0295
1.201	.923	.0296
1.265	.923	.0298
1.328	.924	.0302
1.455	.926	.0316
1.582	.931	.0330
1.836	.946	.0330
2.091	.964	.0309
2.345	.980	.0227
2.599	.991	.0136
2.853	.997	.0077
3.107	.999	.0048
3.361	1.000	.0035
3.678	1.000	.0027
4.186	.999	.0020
4.694	.998	.0016
5.202	.998	.0015
5.710	.998	.0016
6.218	.998	.0020

X/YC = 146.100 UINF = 26.70 M/SEC

CF = .003855 DELTA = 2.796 CMS

Y(CMS)	U/UINF	UT/UINF
.013	.422	.0892
.015	.453	.0909
.018	.477	.0906
.020	.500	.0889
.023	.518	.0880
.025	.533	.0852
.030	.561	.0813
.036	.581	.0770
.041	.597	.0755
.046	.611	.0735
.056	.633	.0704
.069	.653	.0692
.081	.670	.0687
.094	.687	.0686
.119	.711	.0684
.145	.733	.0673
.170	.752	.0657
.196	.771	.0640
.234	.796	.0607
.297	.831	.0555
.361	.861	.0490
.424	.888	.0435
.488	.903	.0378
.551	.917	.0314
.615	.927	.0273
.678	.933	.0248
.742	.936	.0234
.805	.937	.0226
.869	.937	.0226
.932	.936	.0226
.996	.935	.0228
1.059	.935	.0227
1.123	.934	.0229
1.186	.933	.0231
1.250	.933	.0234
1.377	.933	.0241
1.504	.935	.0249
1.631	.938	.0260
1.885	.947	.0279
2.139	.960	.0279
2.393	.974	.0243
2.647	.985	.0176
2.901	.993	.0106
3.155	.997	.0064
3.409	1.000	.0041
3.688	1.000	.0032
4.196	1.000	.0021
4.704	.999	.0017
5.212	.998	.0016
5.720	.998	.0017
6.228	.999	.0021

X/YC = 182.830 UINF = 26.51 M/SEC

CF = .003485 DELTA = 2.911 CMS

Y(CMS)	U/UINF	UT/UINF
.013	.435	.0898
.015	.458	.0894
.018	.476	.0882
.020	.494	.0869
.023	.508	.0850
.025	.521	.0830
.030	.546	.0790
.036	.559	.0763
.041	.573	.0743
.046	.583	.0724
.051	.593	.0711
.058	.607	.0695
.071	.625	.0683
.084	.641	.0681
.097	.654	.0681
.109	.665	.0676
.122	.676	.0677
.135	.686	.0676
.160	.706	.0667
.185	.723	.0659
.211	.739	.0643
.236	.755	.0630
.262	.768	.0610
.312	.794	.0573
.376	.822	.0534
.439	.848	.0490
.503	.868	.0445
.566	.886	.0394
.630	.901	.0341
.693	.913	.0294
.820	.927	.0225
.947	.934	.0198
1.074	.936	.0192
1.201	.937	.0192
1.328	.938	.0198
1.455	.939	.0204
1.582	.941	.0213
1.709	.943	.0223
1.963	.951	.0241
2.217	.962	.0245
2.472	.972	.0226
2.726	.983	.0182
2.980	.993	.0125
3.234	.997	.0077
3.488	1.000	.0051
3.742	1.000	.0036
3.996	1.000	.0029
4.504	1.000	.0020
5.012	1.000	.0017
5.520	.999	.0017
6.028	.999	.0020
6.282	.999	.0023

TABLE D (Cont.)

X/YC = 220.650 UINF = 26.65 M/SEC

CF = .003244 DELTA = 3.095 CMS

Y(CMS)	U/UINF	UT/UINF
.013	.377	.0850
.015	.405	.0876
.018	.429	.0876
.020	.451	.0874
.023	.468	.0854
.025	.483	.0841
.030	.507	.0811
.036	.527	.0777
.041	.544	.0750
.046	.555	.0732
.053	.570	.0701
.066	.592	.0673
.079	.607	.0658
.091	.620	.0653
.104	.632	.0656
.117	.644	.0650
.142	.662	.0660
.168	.678	.0663
.193	.694	.0656
.218	.709	.0653
.244	.722	.0642
.307	.733	.0612
.371	.761	.0582
.434	.804	.0545
.498	.826	.0521
.561	.847	.0476
.625	.864	.0437
.688	.877	.0397
.752	.893	.0354
.815	.904	.0309
.942	.922	.0239
1.069	.931	.0178
1.196	.936	.0181
1.323	.938	.0178
1.450	.941	.0130
1.577	.942	.0186
1.704	.945	.0193
1.958	.952	.0211
2.212	.960	.0223
2.466	.969	.0213
2.720	.978	.0194
2.974	.986	.0162
3.228	.991	.0108
3.482	.997	.0072
3.736	.999	.0046
3.991	1.000	.0035
4.499	.999	.0024
5.007	.999	.0019
5.515	.998	.0018
6.023	.998	.0021
6.277	.999	.0023

X/YC = 237.060 UINF = 26.55 M/SEC

CF = .003036 DELTA = 3.279 CMS

Y(CMS)	U/UINF	UT/UINF
.013	.345	.0810
.015	.367	.0837
.018	.394	.0851
.020	.417	.0857
.023	.430	.0850
.025	.452	.0849
.028	.479	.0830
.036	.501	.0794
.041	.510	.0766
.046	.531	.0739
.051	.543	.0715
.056	.553	.0700
.061	.560	.0686
.066	.569	.0670
.079	.584	.0646
.091	.596	.0631
.104	.608	.0624
.117	.610	.0620
.130	.627	.0619
.155	.644	.0625
.180	.650	.0630
.206	.672	.0635
.231	.684	.0639
.257	.697	.0646
.320	.725	.0629
.384	.748	.0611
.447	.772	.0584
.511	.792	.0554
.574	.813	.0524
.638	.830	.0502
.765	.861	.0435
.892	.886	.0360
1.019	.907	.0296
1.146	.921	.0236
1.273	.931	.0190
1.400	.936	.0181
1.654	.943	.0179
1.908	.949	.0189
2.162	.956	.0200
2.416	.964	.0204
2.670	.972	.0190
2.924	.980	.0177
3.178	.988	.0145
3.432	.993	.0102
3.686	.997	.0071
3.940	.999	.0051
4.448	1.000	.0030
4.956	1.000	.0023
5.464	1.000	.0020
5.972	1.000	.0021
6.480	.999	.0029

X/YC = 253.470 UINF = 26.24 M/SEC

CF = .002760 DELTA = 3.620 CMS

Y(CMS)	U/UINF	UT/UINF
.008	.220	.0576
.010	.274	.0681
.013	.306	.0740
.015	.335	.0786
.018	.366	.0805
.020	.388	.0817
.025	.423	.0806
.030	.457	.0796
.036	.470	.0777
.043	.493	.0759
.056	.521	.0727
.069	.541	.0700
.081	.554	.0683
.094	.567	.0664
.107	.575	.0654
.132	.593	.0635
.157	.608	.0616
.183	.620	.0602
.208	.631	.0590
.246	.647	.0577
.310	.660	.0556
.373	.683	.0549
.437	.704	.0523
.500	.721	.0539
.627	.751	.0537
.754	.779	.0534
.881	.806	.0530
1.008	.830	.0501
1.135	.854	.0461
1.262	.875	.0417
1.389	.895	.0360
1.516	.909	.0314
1.643	.923	.0267
1.897	.940	.0215
2.151	.949	.0203
2.405	.956	.0201
2.659	.964	.0201
2.913	.972	.0193
3.167	.980	.0180
3.421	.986	.0159
3.675	.992	.0131
3.929	.995	.0078
4.183	.999	.0073
4.437	1.000	.0056
4.691	1.000	.0044
4.945	1.000	.0036
5.199	1.000	.0032
5.707	1.000	.0029
6.215	.999	.0031

TABLE D (Cont.)

X/TC = 395.440 UINF = 26.34 M/SEC

CF = .002662 DELTA = 3.781 CMS

Y(CMS)	U/UINF	UT/UINF
.013	.314	.0784
.015	.340	.0802
.018	.361	.0820
.020	.385	.0831
.021	.402	.0829
.025	.422	.0827
.028	.433	.0828
.030	.444	.0824
.036	.465	.0797
.041	.482	.0776
.046	.495	.0755
.051	.507	.0732
.056	.515	.0713
.061	.524	.0701
.071	.537	.0672
.084	.552	.0655
.097	.562	.0631
.109	.571	.0621
.122	.580	.0612
.135	.587	.0608
.160	.602	.0606
.185	.615	.0611
.211	.625	.0610
.236	.635	.0611
.262	.642	.0616
.287	.655	.0626
.351	.673	.0626
.414	.693	.0626
.478	.709	.0619
.541	.727	.0608
.605	.742	.0594
.732	.772	.0558
.859	.798	.0526
.986	.823	.0509
1.113	.843	.0469
1.240	.864	.0434
1.367	.881	.0391
1.494	.896	.0351
1.621	.910	.0316
1.875	.933	.0239
2.129	.947	.0191
2.383	.957	.0175
2.637	.964	.0169
2.891	.970	.0167
3.145	.977	.0160
3.399	.983	.0153
3.653	.987	.0129
3.907	.992	.0103
4.161	.995	.0079
4.669	.999	.0045
5.177	1.000	.0032
5.685	1.000	.0028
6.193	1.000	.0031
6.701	.999	.0042

X/TC = 435.160 UINF = 26.35 M/SEC

CF = .002624 DELTA = 3.866 CMS

Y(CMS)	U/UINF	UT/UINF
.010	.298	.0760
.013	.324	.0794
.015	.349	.0805
.018	.372	.0817
.020	.396	.0824
.023	.412	.0824
.025	.427	.0823
.028	.438	.0812
.033	.459	.0799
.038	.476	.0772
.043	.491	.0755
.051	.506	.0721
.063	.526	.0684
.076	.542	.0657
.089	.553	.0635
.102	.563	.0624
.114	.572	.0612
.140	.587	.0606
.165	.601	.0604
.190	.613	.0604
.216	.622	.0604
.241	.632	.0608
.267	.640	.0609
.330	.662	.0617
.394	.679	.0620
.457	.697	.0622
.521	.712	.0613
.584	.727	.0599
.711	.756	.0573
.838	.780	.0548
.965	.803	.0515
1.092	.824	.0501
1.219	.843	.0467
1.346	.861	.0442
1.600	.893	.0370
1.854	.921	.0299
2.108	.940	.0233
2.362	.953	.0191
2.616	.962	.0174
2.870	.969	.0165
3.124	.975	.0158
3.632	.987	.0135
4.140	.995	.0079
4.648	.999	.0053
5.156	1.000	.0036
5.664	1.000	.0031
6.172	1.000	.0034
6.426	1.000	.0039
6.680	.999	.0046
6.934	.998	.0062

APPENDIX E

In this appendix the slant-wire data for the zero pressure gradient flow are tabulated. The data consist of turbulence intensities v_t/U_∞, w_t/U_∞ and the shear stress $-\overline{uv}/U_\infty^2$. The interpolated data of $\frac{u_t}{U_\infty}$ and $\partial(U/U_\infty)/\partial(y/\delta)$ at each slant-wire location were also tabulated. They were obtained from the normal hot-film data by interpolating a five point quadratic curve fit.

TABLE E

SLANT-WIRE DATA FOR THE ZERO PRESSURE GRADIENT FLOW

X/YC = -16.400   UINF = 26.80 M/SEC

DELTA = 1.213 CMS

Y(CMS)	DUDY X10	UT/UINF X100	-UV/(UINF)^2 X10000	VT/UINF X100	WT/UINF X100
.165	.332	5.250	10.700	5.080	5.830
.216	.352	5.200	12.000	5.240	5.890
.267	.530	5.270	12.800	5.390	5.870
.318	.709	5.220	12.900	5.230	5.710
.368	.815	5.140	12.400	5.100	5.520
.419	.887	5.020	12.400	5.050	5.320
.521	.877	4.810	11.200	4.740	4.920
.571	.873	4.730	10.800	4.580	4.850
.673	.876	4.630	9.920	4.100	4.290
.800	.864	4.450	8.660	3.660	3.710
.927	.833	4.190	7.110	3.050	2.980
1.054	.731	3.750	5.430	2.690	2.530
1.181	.616	3.320	3.080	2.090	1.780
1.308	.433	2.680	2.260	1.520	.923
1.435	.290	2.160	1.150	.411	0.000
1.562	.113	1.600	.487	.352	0.000
1.689	-.007	1.020	.133	.770	.274
1.816	-.130	.814	.065	.670	.305
1.943	-.206	.042	.028	1.010	.066
2.197	-.269	.218	.008	.727	.632
2.705	-.208	.211	.005	.525	.459
3.213	-.163	.161	.004	.481	.154
3.721	-.122	.137	.005	.472	.447
4.229	-.096	.117	-.001	.500	.450

X/YC = .292   UINF = 25.59 M/SEC

DELTA = 2.337 CMS

Y(CMS)	DUDY X10	UT/(UINF) X100	-UV/(UINF)^2 X10000	VT/UINF X100	WT/UINF X100
.340	170.667	4.910	22.500	10.200	10.400
.356	252.804	7.400	21.400	7.430	7.550
.368	177.720	8.360	19.350	5.410	6.100
.381	93.750	8.550	19.200	4.420	5.440
.394	55.026	6.600	18.900	3.970	5.520
.419	37.745	9.550	20.400	4.300	5.790
.445	30.093	8.430	21.500	4.980	6.480
.470	24.242	8.310	23.100	5.050	6.600
.508	21.083	8.130	21.300	4.780	7.210
.571	17.059	7.740	15.300	4.290	6.290
.635	12.708	7.320	10.400	3.470	5.680
.698	7.394	7.010	8.750	2.640	4.840
.762	7.131	6.810	7.710	1.940	4.350
.889	5.271	6.650	9.290	1.360	3.530
1.016	4.639	6.470	9.140	0.000	3.060
1.270	4.116	5.830	10.200	1.760	2.380
1.534	3.349	5.060	9.470	2.490	2.970
1.788	2.618	4.070	6.380	2.580	2.670
2.042	1.932	2.900	2.210	1.310	1.130
2.296	1.255	1.550	.533	1.380	.733
2.550	.666	.557	.070	1.320	1.100
2.804	.273	.312	.006	1.030	.895
3.058	.091	.361	.003	.762	.614
3.566	-.052	.212	.009	.660	.570
5.027	-.054	.124	-.000	.641	.579

TABLE E (Cont.)

X/YC = 16.500 UINF = 25.70 M/SEC

DELTA = 2.260 CMS

Y(CMS)	DUDY X10	UT/UINF X100	-UV/(UINF)^2 X10000	VT/UINF X100	WT/UINF X100
.346	-26.884	10.400	-58.400	9.260	8.820
.368	-25.919	10.200	-57.100	9.670	9.240
.432	-22.232	9.380	-47.700	9.620	9.610
.521	-14.277	7.780	-32.500	9.070	9.490
.584	-7.911	6.820	-15.800	7.300	7.710
.648	-2.466	6.490	-4.380	5.490	5.720
.711	1.358	6.510	3.300	4.380	4.530
.775	3.293	6.570	7.500	4.300	4.610
.902	3.939	6.370	11.400	4.580	5.070
1.029	3.926	6.040	12.200	4.870	5.370
1.156	3.777	8.740	12.100	4.780	5.230
1.410	3.248	4.980	10.100	4.450	4.870
1.664	2.609	4.060	6.630	3.830	3.980
1.918	1.892	2.890	3.510	2.880	2.850
2.172	1.193	1.600	.939	1.900	1.760
2.426	.635	.321	.110	1.510	1.340
2.934	.098	.260	-.003	.699	.584
3.442	-.003	.237	-.006	.429	.350
3.950	-.004	.187	-.014	.359	.312

X/YC = 35.050 UINF = 24.84 M/SEC

DELTA = 2.170 CMS

Y(CMS)	DUDY X10	UT/(UINF) X100	-UV/(UINF)^2 X10000	VT/UINF X100	WT/UINF X100
.340	-9.461	6.800	-20.400	6.040	5.980
.404	-10.445	7.110	-24.700	6.630	6.510
.467	-10.608	7.150	-26.300	6.940	6.950
.531	-10.083	6.910	-24.000	6.770	6.700
.594	-8.916	6.460	-20.300	6.550	6.520
.658	-7.143	5.940	-14.760	6.220	6.200
.721	-4.952	5.540	-8.360	5.450	5.610
.785	-2.627	5.340	-3.000	4.930	5.210
.848	-.628	5.320	1.160	4.450	4.760
.912	.794	5.410	4.850	4.260	4.700
1.039	2.206	5.560	9.430	4.270	4.710
1.102	2.633	5.560	10.900	3.990	4.620
1.356	3.044	5.070	9.100	3.340	3.710
1.610	2.596	4.180	5.700	2.710	2.790
1.864	1.850	3.000	2.660	1.990	1.590
2.118	1.162	1.840	.815	1.050	.619
2.499	.418	.199	.051	1.170	1.010
3.007	.042	.329	.003	.554	.383
3.515	-.020	.214	-.004	.448	.396
4.023	-.019	.167	-.001	.412	.384

TABLE E (Cont.)

X/YC = 53.740 UINF = 25.61 M/SEC

DELTA = 2.298 CMS

Y(CMS)	DUDY X10	UT/UINF X100	-UV/(UINF)^2 X10000	VT/UINF X100	WT/UINF X100
.366	-3.940	5.080	-9.320	4.770	4.930
.399	-4.920	5.250	-11.100	5.030	5.290
.462	-5.941	5.480	-13.500	5.270	5.280
.526	-6.275	5.580	-14.900	5.415	5.560
.653	-5.704	5.460	-13.500	5.240	5.280
.716	-5.150	5.240	-11.300	5.040	5.250
.780	-4.379	4.980	-8.450	4.800	4.950
.843	-3.327	4.770	-5.080	4.490	4.710
.907	-2.183	4.610	-2.290	4.210	4.330
.970	-1.127	4.540	.409	4.020	4.290
1.034	-.256	4.540	2.860	4.040	4.210
1.097	.502	4.620	4.060	4.070	4.190
1.161	1.115	4.720	6.500	4.140	4.200
1.224	1.600	4.780	7.960	4.160	4.140
1.288	1.960	4.840	8.640	4.010	4.140
1.415	2.366	4.820	9.170	3.910	4.000
1.542	2.491	4.650	8.550	3.650	3.680
1.669	2.427	4.320	7.500	3.430	3.330
1.796	2.238	3.870	5.010	3.220	3.080
2.050	1.674	2.770	2.700	2.353	2.050
2.306	1.057	1.660	.087	1.410	1.080
2.558	.536	.763	.175	1.210	.979
2.812	.191	.459	.023	.847	.440
3.320	-.025	.287	.002	.506	.363
3.828	-.023	.211	.000	.393	.321

X/YC = 74.480 UINF = 25.93 M/SEC

DELTA = 2.404 CMS

Y(CMS)	DUDY X10	UT/(UINF) X100	-UV/(UINF)^2 X10000	VT/UINF X100	WT/UINF X100
.391	.101	3.880	-2.640	3.830	3.950
.455	-1.021	4.020	-5.090	4.120	4.160
.518	-2.848	4.170	-6.530	4.280	4.410
.582	-3.303	4.260	-7.660	4.450	4.530
.645	-3.321	4.280	-8.420	4.590	4.730
.709	-3.157	4.220	-8.330	4.650	4.770
.765	-2.893	4.160	-7.570	4.480	4.740
.848	-2.492	4.020	-6.140	4.370	4.570
.899	-2.167	3.970	-5.030	4.230	4.480
.963	-1.648	3.850	-3.520	4.100	4.300
1.026	-1.160	3.820	-1.880	3.900	4.140
1.090	-.567	3.840	-.277	3.760	3.940
1.153	-.057	3.860	1.290	3.600	3.830
1.217	.534	3.970	2.620	3.540	3.690
1.280	.985	4.030	3.990	3.580	3.670
1.407	1.743	4.180	6.080	3.690	3.670
1.534	2.187	4.210	7.180	3.790	3.600
1.661	2.302	4.070	7.210	3.790	3.810
1.788	2.180	3.750	6.560	3.780	3.770
1.915	2.062	3.440	5.480	3.440	3.280
2.169	1.541	2.490	2.810	2.770	2.630
2.423	.965	1.390	.946	2.130	1.980
2.677	.507	.553	.211	1.690	1.560
2.931	.195	.371	.038	1.360	1.240
3.185	.043	.307	.024	1.200	1.090
3.693	-.021	.226	.001	1.060	1.040
4.201	-.021	.184	.012	1.040	1.020
4.709	-.015	.162	-.001	1.040	1.030

TABLE E (Cont.)

X/YC = 100.400   UINF = 25.73 M/SEC

DELTA = 3.694 CMS

Y(CMS)	DUDY X10	UT/UINF X100	-UV/(UINF)^2 X10000	VT/UINF X100	WT/UINF X100
.423	6.031	3.320	1.940	2.940	3.130
.473	3.071	3.200	.589	2.950	3.170
.536	1.764	2.980	-.606	3.060	3.220
.599	.322	2.940	-1.690	3.210	3.280
.663	-.566	2.960	-2.560	3.330	3.420
.726	-1.042	3.000	-3.120	3.440	3.490
.853	-1.472	3.020	-3.520	3.500	3.500
.917	-1.437	3.020	-3.320	3.560	3.530
1.044	-1.126	2.980	-2.610	3.490	3.520
1.171	-.637	2.950	-1.110	3.400	3.420
1.298	-.057	2.970	.463	3.350	3.330
1.425	.643	3.060	2.030	3.360	3.300
1.552	.855	3.200	3.500	3.430	3.340
1.692	1.211	3.330	4.830	3.500	3.490
1.819	1.426	3.400	5.210	3.320	3.270
1.946	1.565	3.370	5.380	3.330	3.250
2.200	1.567	3.020	3.950	2.690	2.730
2.454	1.294	2.310	1.870	1.910	1.710
2.708	.896	1.460	.654	1.460	1.270
2.962	.519	.806	.112	1.300	1.160
3.216	.253	.513	.030	1.180	1.090
3.470	.113	.394	.003	1.050	.989
3.978	-.016	.240	-.001	.970	.981
4.486	-.040	.185	.002	.968	.942

X/YC = 146.200   UINF = 25.77 M/SEC

DELTA = 2.937 CMS

Y(CMS)	DUDY X10	UT/(UINF) X100	-UV/(UINF)^2 X10000	VT/UINF X100	WT/UINF X100
.335	13.525	5.350	9.760	3.700	4.390
.386	11.505	4.910	8.040	3.500	3.960
.450	9.245	4.310	6.090	3.200	3.560
.513	7.201	3.700	3.930	2.890	3.120
.577	5.394	3.170	2.410	2.680	2.900
.640	3.762	2.760	1.260	2.580	2.840
.703	2.331	2.510	.370	2.500	2.750
.767	1.199	2.360	-.231	2.500	2.760
.831	.443	2.290	-.654	2.610	2.790
.894	.010	2.260	-.927	2.690	2.780
.970	-.240	2.260	-1.190	2.720	2.800
1.097	-.343	2.280	-1.170	2.820	2.850
1.224	-.231	2.310	-.700	2.810	2.850
1.351	-.003	2.360	-.013	2.830	2.820
1.478	.287	2.430	.762	2.850	2.810
1.605	.585	2.520	1.690	2.970	2.840
1.732	.839	2.640	2.540	3.010	2.840
1.859	1.033	2.760	3.320	3.060	2.850
1.986	1.183	2.810	3.890	3.080	2.940
2.113	1.278	2.810	4.060	2.990	2.940
2.431	1.298	2.570	3.190	2.610	2.540
2.621	1.204	2.250	2.110	1.960	1.790
2.875	.932	1.600	.877	1.440	1.210
3.129	.608	.910	.311	1.330	1.150
3.383	.342	.460	.059	1.220	1.100
3.891	.082	.316	-.002	.970	.938
4.399	-.088	.229	-.013	.927	.900

TABLE E (Cont.)

X/YC = 220.700   UINF = 25.36 M/SEC

DELTA = 3.307 CMS

Y(CMS)	DUDY X10	UT/UINF X100	-UV/(UINF)^2 X10000	VT/UINF X100	WT/UINF X100
.340	14.170	6.120	11.500	3.000	4.710
.391	12.902	5.860	11.400	4.070	4.880
.442	11.869	5.650	10.700	3.960	4.590
.493	11.021	5.410	9.890	3.810	4.480
.544	10.203	5.170	8.870	3.620	4.080
.594	9.420	4.900	8.160	3.390	3.720
.645	8.431	4.520	7.010	3.240	3.610
.721	7.473	4.150	5.620	2.890	3.090
.848	5.745	3.370	3.290	2.300	2.490
.975	4.024	2.600	1.670	1.900	1.980
1.102	2.602	2.190	.757	1.840	1.940
1.229	1.354	1.830	.360	2.060	2.100
1.356	.910	1.760	.345	2.030	2.050
1.610	.341	1.610	.615	2.160	2.160
1.864	.679	1.950	1.250	2.370	2.100
2.118	.864	2.100	1.980	2.470	2.300
2.372	1.004	2.190	2.510	2.520	2.260
2.626	1.070	2.170	2.450	2.320	2.000
2.880	1.057	2.030	1.940	1.900	1.680
3.388	.776	1.410	.500	.736	.870
3.896	.340	.574	.054	.948	.839
4.404	.072	.348	.007	.834	.792
4.912	-.014	.246	.004	.844	.819
5.547	-.030	.104	-.002	.659	.854

X/YC = 257.900   UINF = 25.77 M/SEC

DELTA = 3.328 CMS

Y(CMS)	DUDY X10	UT/(UINF) X100	-UV/(UINF)^2 X10000	VT/UINF X100	WT/UINF X100
.376	12.613	6.150	11.100	2.150	2.920
.414	11.887	6.010	10.600	2.790	3.350
.478	10.882	5.740	10.200	3.440	3.900
.541	10.074	5.440	9.460	3.830	4.260
.605	9.201	5.170	9.040	3.920	4.330
.668	8.561	4.890	8.130	3.850	4.190
.731	7.865	4.580	7.260	3.730	3.900
.795	7.152	4.270	5.970	3.400	3.630
.859	6.441	3.900	5.310	3.290	3.120
.922	5.762	3.570	4.530	3.170	3.130
.986	5.014	3.220	3.570	2.930	3.130
1.112	3.675	2.590	1.970	2.490	2.350
1.240	2.535	2.160	1.140	2.230	2.300
1.367	1.789	1.930	.760	2.130	2.230
1.621	1.052	1.810	.675	2.210	2.220
1.874	.874	1.800	1.190	2.390	2.200
2.128	.913	1.900	1.720	2.550	2.120
2.383	.986	2.040	2.190	2.620	2.400
2.637	1.030	2.000	2.300	2.600	2.240
2.890	1.010	1.840	2.040	2.450	2.100
3.145	.882	1.550	1.440	2.140	1.900
3.399	.685	1.190	.745	1.780	1.500
3.652	.458	.852	.312	1.570	1.450
4.161	.154	.402	.052	1.270	1.100
4.668	.020	.244	.005	1.100	1.030
5.685	-.014	.196	-.004	1.050	1.030

TABLE E (Cont.)

X/YC = 4?3.200   UINF = 26.07 M/SEC

DELTA = 4.004 CMS

Y(CMS)	DUDY X10	UT/UINF X100	$-UV/(UINF)^2$ X10000	VT/UINF X100	WT/UINF X100
.371	11.346	6.100	10.400	2.790	3.990
.434	10.340	6.310	9.760	1.030	3.060
.498	9.627	6.190	9.970	.771	2.600
.561	9.133	6.100	9.090	0.000	1.930
.625	8.775	5.970	8.900	0.000	1.700
.752	7.900	5.730	8.330	0.000	1.910
.879	7.254	5.450	7.940	.792	1.000
1.006	6.610	5.220	7.050	.005	2.350
1.133	6.003	4.900	7.250	2.200	3.090
1.387	5.326	4.470	5.020	3.240	3.710
1.641	4.534	3.810	4.030	3.410	3.700
1.895	3.669	3.120	3.370	3.100	3.360
2.149	2.770	2.500	2.390	2.640	2.790
2.403	1.994	2.040	1.700	2.350	2.490
2.657	1.450	1.800	1.490	2.230	2.330
2.911	1.160	1.700	1.350	2.220	2.230
3.165	1.000	1.620	1.640	2.170	2.090
3.419	.864	1.530	1.320	1.970	1.800
3.673	.759	1.380	1.140	1.810	1.660
3.927	.647	1.250	.829	1.530	1.370
4.435	.421	.884	.273	[illegible]	.489
4.689	.304	.670	.139	.804	.400
4.943	.216	.492	.071	.673	.430
5.451	.002	.324	.011	.535	.443
5.959	.000	.301	-.011	.564	.440
6.467	-.039	.342	-.020	.707	.354

APPENDIX F

In this appendix the normal hot-film data for the adverse pressure gradient flow are tabulated. The data consist of mean velocity U/U_∞ and the turbulence intensity u_t/U_∞. The skin friction data are also presented at each station.

BLANK PAGE

BLANK PAGE

TABLE F

NORMAL HOT-FILM DATA OF U/U_∞ AND u_t/U_∞ FOR THE ADVERSE PRESSURE GRADIENT FLOW

X/YC = -16.360 UINF = 19.50 M/SEC

DELTA = 1.270 CMS

Y(CMS)	U/UINF	UT/UINF
.015	.662	.0799
.018	.707	.0833
.020	.741	.0845
.023	.763	.0848
.025	.789	.0823
.030	.823	.0783
.036	.845	.0743
.043	.865	.0737
.056	.884	.0682
.069	.892	.0634
.081	.897	.0604
.107	.898	.0594
.145	.897	.0598
.200	.898	.0620
.272	.902	.0630
.399	.913	.0593
.526	.927	.0551
.653	.941	.0520
.780	.954	.0485
.907	.965	.0447
1.034	.976	.0402
1.293	.996	.0290
1.542	1.005	.0161
1.796	1.007	.0079
2.050	1.004	.0050
2.304	1.008	.0037
2.812	.993	.0026
3.320	.988	.0020
3.828	.986	.0017
4.844	.983	.0016
5.860	.984	.0020
6.368	.986	.0026
6.876	.987	.0050
7.384	.985	.0107

X/YC = .292 UINF = 18.50 M/SEC

DELTA = 3.490 CMS

U_{J-E} = 1.563

Y(CMS)	U/UINF	UT/UINF
.015	1.132	.1304
.018	1.215	.1416
.020	1.289	.1380
.023	1.343	.1303
.025	1.387	.1208
.028	1.417	.1140
.030	1.443	.1068
.036	1.480	.0951
.041	1.506	.0859
.048	1.531	.0767
.061	1.557	.0663
.074	1.575	.0600
.086	1.588	.0555
.099	1.598	.0518
.124	1.614	.0476
.150	1.626	.0447
.175	1.636	.0434
.201	1.642	.0438
.226	1.643	.0498
.251	1.607	.0744
.264	1.527	.1076
.277	1.182	.1505
.290	.278	.0778
.302	.076	.0099
.315	.071	.0116
.328	.048	.0063
.340	.055	.0079
.353	.122	.0429
.366	.268	.0770
.378	.358	.0890
.391	.403	.0868
.404	.435	.0876
.429	.473	.0987
.455	.501	.0895
.480	.528	.0898
.505	.565	.0903
.569	.600	.0876
.632	.646	.0823
.696	.680	.0769
.759	.704	.0774
.823	.722	.0759
.886	.737	.0750
.950	.749	.0758
1.077	.776	.0747
1.204	.800	.0711
1.331	.826	.0683
1.458	.851	.0635
1.585	.873	.0566
1.712	.893	.0539
1.966	.931	.0562
2.220	.959	.0265
2.474	.975	.0142
2.728	.983	.0076
2.982	.986	.0051
3.490	.990	.0033
3.998	.994	.0031
4.760	1.002	.0019
5.776	1.013	.0019
6.792	1.024	.0020
7.808	1.059	.0051
8.316	1.074	.0105

X/YC = 15.920 UINF = 16.60 M/SEC

CF = .017342 DELTA = 2.769 CMS

Y(CMS)	U/UINF	UT/UINF
.018	.925	.1630
.020	.997	.1635
.023	1.062	.1608
.025	1.116	.1585
.028	1.157	.1566
.030	1.188	.1555
.033	1.217	.1548
.038	1.269	.1544
.043	1.300	.1540
.048	1.326	.1524
.053	1.362	.1505
.064	1.402	.1470
.076	1.432	.1414
.089	1.455	.1375
.102	1.471	.1344
.127	1.487	.1329
.152	1.485	.1349
.178	1.473	.1410
.203	1.450	.1482
.229	1.431	.1567
.292	1.320	.1690
.356	1.204	.1691
.419	1.086	.1637
.483	.974	.1555
.546	.874	.1376
.610	.792	.1104
.673	.736	.0990
.737	.705	.0940
.800	.698	.0917
.864	.698	.0831
.927	.712	.0821
.991	.722	.0822
1.054	.732	.0815
1.118	.745	.0793
1.245	.770	.0764
1.372	.794	.0756
1.499	.820	.0736
1.626	.843	.0710
1.753	.865	.0677
1.880	.887	.0651
2.007	.909	.0583
2.261	.946	.0444
2.515	.973	.0284
2.769	.990	.0166
3.023	.998	.0097
3.277	1.001	.0060
3.531	1.005	.0054
3.785	1.007	.0045
4.039	1.010	.0040
4.293	1.014	.0037
4.547	1.016	.0032
4.801	1.020	.0028
5.309	1.025	.0025
5.817	1.032	.0023
6.833	1.050	.0023
7.849	1.069	.0029
8.865	1.096	.0041

TABLE F (Cont.)

X/YC = 30.000 UINF = 14.08 M/SEC

CF = .014155 DELTA = 3.185 CMS

Y(CMS)	U/UINF	UT/UINF
.018	.771	.1513
.020	.840	.1535
.023	.891	.1561
.025	.937	.1572
.028	.979	.1563
.033	1.047	.1509
.038	1.098	.1446
.043	1.134	.1382
.048	1.166	.1325
.058	1.209	.1249
.071	1.252	.1174
.084	1.283	.1126
.097	1.309	.1096
.109	1.329	.1075
.135	1.359	.1069
.160	1.373	.1068
.185	1.380	.1085
.249	1.366	.1156
.312	1.327	.1264
.376	1.271	.1366
.439	1.209	.1454
.503	1.143	.1509
.566	1.074	.1533
.630	1.000	.1484
.693	.933	.1407
.757	.873	.1276
.820	.820	.1119
.884	.776	.0999
.947	.743	.0956
1.011	.722	.0858
1.074	.710	.0849
1.138	.707	.0855
1.201	.709	.0860
1.265	.712	.0868
1.392	.733	.0887
1.519	.756	.0884
1.646	.778	.0838
1.773	.799	.0826
1.900	.823	.0781
2.027	.844	.0738
2.281	.887	.0651
2.535	.922	.0565
2.789	.950	.0425
3.043	.973	.0292
3.297	.985	.0165
3.551	.990	.0110
3.805	.991	.0078
4.059	.990	.0061
4.313	.990	.0050
4.821	.990	.0040
5.329	.990	.0034
5.837	.989	.0030
6.599	.988	.0029
7.615	.986	.0028
8.631	.994	.0027
9.139	1.001	.0028

X/YC = 44.390 UINF = 13.24 M/SEC

CF = .012385 DELTA = 3.675 CMS

Y(CMS)	U/UINF	UT/UINF
.018	.570	.1307
.020	.643	.1434
.023	.708	.1520
.025	.767	.1559
.028	.818	.1564
.033	.897	.1533
.038	.959	.1504
.043	1.005	.1480
.051	1.056	.1436
.064	1.118	.1368
.076	1.162	.1311
.089	1.197	.1259
.102	1.226	.1214
.127	1.269	.1150
.152	1.302	.1103
.178	1.324	.1058
.229	1.349	.1047
.292	1.352	.1099
.356	1.330	.1226
.419	1.298	.1283
.483	1.256	.1380
.546	1.211	.1454
.610	1.164	.1499
.673	1.112	.1522
.737	1.062	.1513
.800	1.012	.1455
.864	.964	.1408
.927	.915	.1341
.991	.873	.1292
1.054	.830	.1203
1.118	.794	.1123
1.181	.765	.1042
1.245	.740	.1024
1.308	.723	.0959
1.435	.703	.0912
1.562	.705	.0924
1.689	.719	.0952
1.816	.738	.0975
1.943	.755	.0992
2.197	.800	.0948
2.451	.839	.0807
2.705	.884	.0753
2.959	.919	.0625
3.213	.946	.0497
3.467	.968	.0331
3.721	.982	.0229
3.975	.988	.0135
4.229	.989	.0092
4.483	.989	.0068
4.737	.989	.0052
5.245	.986	.0039
5.753	.981	.0030
6.261	.977	.0027
6.769	.970	.0026
7.277	.963	.0024
7.785	.956	.0023
8.801	.947	.0022
9.309	.952	.0023

X/YC = 72.140 UINF = 11.38 M/SEC

CF = .010405 DELTA = 4.976 CMS

Y(CMS)	U/UINF	UT/UINF
.018	.505	.1272
.020	.556	.1380
.023	.609	.1467
.025	.659	.1455
.028	.700	.1481
.030	.732	.1488
.036	.789	.1502
.041	.842	.1479
.048	.891	.1435
.061	.950	.1343
.074	.991	.1267
.086	1.022	.1238
.099	1.048	.1199
.112	1.074	.1173
.137	1.111	.1131
.163	1.142	.1107
.188	1.169	.1093
.239	1.208	.1079
.302	1.240	.1061
.366	1.257	.1073
.429	1.258	.1114
.493	1.252	.1167
.556	1.236	.1242
.683	1.190	.1328
.810	1.134	.1393
.937	1.072	.1443
1.064	1.013	.1386
1.191	.949	.1397
1.445	.827	.1301
1.699	.723	.1133
1.953	.660	.0925
2.207	.642	.0859
2.461	.657	.0903
2.715	.692	.0961
2.969	.728	.0958
3.223	.768	.0975
3.477	.812	.0940
3.731	.852	.0896
3.985	.891	.0775
4.239	.925	.0624
4.493	.956	.0446
4.747	.974	.0341
5.001	.986	.0211
5.255	.993	.0133
5.509	.995	.0101
5.763	.996	.0081
6.271	.997	.0055
6.779	.996	.0043
7.287	.976	.0037
7.795	.996	.0034
8.303	.995	.0032
8.811	1.001	.0030
9.319	.993	.0030
9.827	.960	.0046

TABLE F (Cont.)

X/YC = 100.320 UINF = 10.01 M/SEC

CF = .009314 DELTA = 6.299 CMS

Y(CMS)	U/UINF	UT/UINF
.015	.347	.0945
.018	.370	.1031
.020	.413	.1133
.023	.453	.1222
.025	.493	.1316
.030	.574	.1449
.036	.639	.1526
.041	.696	.1554
.051	.772	.1501
.061	.834	.1426
.071	.873	.1398
.081	.906	.1343
.094	.937	.1317
.107	.963	.1294
.132	1.005	.1256
.157	1.038	.1220
.183	1.065	.1196
.246	1.122	.1131
.310	1.165	.1058
.373	1.194	.1014
.437	1.217	.0978
.564	1.235	.0974
.691	1.228	.1050
.818	1.204	.1172
.945	1.167	.1303
1.072	1.126	.1363
1.199	1.084	.1459
1.326	1.038	.1479
1.580	.939	.1497
1.834	.846	.1441
2.088	.757	.1324
2.342	.678	.1194
2.596	.621	.1033
2.850	.595	.0915
3.104	.594	.0927
3.358	.616	.0966
3.612	.649	.1006
3.866	.682	.1039
4.120	.721	.1023
4.374	.759	.0997
4.628	.804	.0926
5.136	.881	.0805
5.644	.945	.0575
6.152	.987	.0342
6.660	1.000	.0169
7.170	1.002	.0110
7.676	1.002	.0082
8.184	1.000	.0078
8.692	1.000	.0060
9.200	1.004	.0058
9.708	.999	.0055

X/YC = 142.960 UINF = 8.91 M/SEC

CF = .007701 DELTA = 9.062 CMS

Y(CMS)	U/UINF	UT/UINF
.013	.284	.0769
.017	.331	.0954
.019	.371	.1006
.022	.412	.1180
.024	.442	.1242
.027	.475	.1295
.032	.527	.1340
.037	.576	.1369
.042	.612	.1387
.050	.650	.1399
.057	.695	.1390
.070	.738	.1338
.083	.772	.1284
.095	.797	.1231
.121	.837	.1153
.146	.866	.1116
.171	.890	.1084
.210	.919	.1048
.273	.959	.1042
.337	.996	.1033
.400	1.027	.1025
.464	1.050	.1031
.591	1.088	.1011
.718	1.114	.0986
.845	1.127	.0996
.972	1.125	.1049
1.099	1.114	.1091
1.226	1.094	.1162
1.353	1.072	.1232
1.480	1.046	.1252
1.734	.989	.1317
1.988	.931	.1366
2.242	.866	.1397
2.496	.800	.1413
2.750	.738	.1399
3.004	.677	.1327
3.258	.615	.1224
3.512	.566	.1094
3.766	.526	.1011
4.020	.493	.0914
4.274	.482	.0859
4.528	.486	.0862
5.036	.530	.0958
5.544	.591	.1019
6.052	.663	.1060
6.560	.738	.1042
7.068	.813	.0958
7.576	.880	.0791
8.084	.931	.0503
8.592	.963	.0302
9.100	.979	.0180
9.608	.975	.0140
9.862	.967	.0120

X/YC = 177.720 UINF = 8.43 M/SEC

CF = .006777 DELTA = 9.929 CMS

Y(CMS)	U/UINF	UT/UINF
.015	.240	.0559
.018	.264	.0683
.020	.295	.0814
.023	.317	.0933
.028	.370	.1109
.033	.431	.1205
.038	.477	.1274
.043	.510	.1281
.048	.543	.1269
.061	.603	.1273
.074	.643	.1228
.086	.676	.1197
.099	.701	.1188
.124	.735	.1123
.150	.762	.1094
.175	.784	.1064
.213	.815	.1042
.277	.848	.0996
.340	.875	.0985
.404	.900	.0964
.467	.923	.0935
.531	.943	.0923
.658	.978	.0919
.785	1.005	.0888
.912	1.022	.0896
1.039	1.035	.0899
1.293	1.042	.0928
1.547	1.027	.1019
1.801	.995	.1148
2.055	.956	.1230
2.309	.900	.1286
2.563	.858	.1357
2.817	.812	.1369
3.071	.760	.1401
3.325	.713	.1372
3.579	.667	.1334
3.833	.617	.1262
4.087	.575	.1227
4.341	.530	.1133
4.595	.492	.1085
4.849	.467	.1021
5.103	.442	.0956
5.357	.434	.0901
5.611	.423	.0910
5.865	.433	.0893
6.119	.448	.0957
6.373	.474	.1000
6.881	.532	.1060
7.391	.595	.1065
7.897	.657	.1085
8.405	.736	.1089
8.926	.816	.0978
9.421	.884	.0775
9.675	.916	.0636
9.929	.940	.0543

TABLE F (Cont.)

X/YC = 213.350 UINF = 7.91 M/SEC
CF = .004222 DELTA = 9.314 CMS

Y(CMS)	U/UINF	UT/UINF
.010	.253	.0637
.020	.275	.0736
.023	.303	.0847
.025	.329	.0951
.030	.375	.1082
.036	.410	.1174
.043	.464	.1237
.051	.504	.1235
.056	.527	.1211
.069	.573	.1196
.081	.607	.1153
.094	.633	.1126
.119	.669	.1090
.145	.697	.1051
.170	.718	.1046
.234	.737	.1030
.297	.790	.1034
.361	.815	.1020
.424	.842	.1000
.551	.879	.0970
.678	.909	.0939
.805	.935	.0932
.932	.961	.0898
1.186	.991	.0848
1.440	1.006	.0874
1.694	1.010	.0918
1.948	.998	.0978
2.202	.977	.1051
2.456	.950	.1169
2.710	.916	.1221
2.964	.875	.1333
3.218	.840	.1344
3.472	.798	.1377
3.980	.719	.1346
4.234	.679	.1301
4.488	.646	.1302
4.742	.605	.1298
4.996	.562	.1275
5.250	.533	.1232
5.504	.499	.1222
5.758	.472	.1109
6.012	.443	.1086
6.266	.421	.1039
6.520	.405	.0954
6.774	.390	.0920
7.282	.391	.0909
7.790	.423	.0966
8.298	.465	.1071
8.806	.517	.1113
9.314	.599	.1120

X/YC = 285.920 UINF = 7.37 M/SEC
CF = .004416 DELTA = 10.396 CMS

Y(CMS)	U/UINF	UT/UINF
.010	.190	.0353
.013	.203	.0430
.015	.214	.0476
.018	.227	.0553
.020	.246	.0628
.025	.272	.0680
.030	.297	.0770
.036	.320	.0839
.046	.365	.0956
.058	.410	.1014
.071	.442	.1045
.084	.464	.1047
.109	.496	.1009
.135	.521	.0944
.173	.543	.0897
.236	.577	.0875
.300	.596	.0891
.363	.613	.0862
.490	.641	.0850
.617	.663	.0873
.744	.682	.0865
.998	.722	.0905
1.252	.757	.0914
1.506	.785	.0942
1.760	.810	.0920
2.014	.831	.0936
2.268	.843	.0921
2.522	.848	.0936
2.776	.851	.0970
3.030	.842	.1033
3.284	.833	.1037
3.792	.802	.1150
4.300	.770	.1158
4.808	.719	.1198
5.316	.673	.1206
5.824	.636	.1233
6.332	.590	.1237
6.840	.548	.1183
7.348	.502	.1166
7.856	.461	.1196
8.364	.423	.1031
8.872	.387	.0919
9.380	.382	.0837
9.888	.389	.0770
10.396	.430	.0716

X/YC = 360.040 UINF = 7.37 M/SEC
CF = .003373 DELTA = 10.356 CMS

Y(CMS)	U/UINF	UT/UINF
.010	.183	.0332
.013	.192	.0403
.015	.205	.0464
.018	.217	.0538
.020	.228	.0583
.025	.261	.0680
.030	.287	.0771
.043	.342	.0945
.056	.389	.1083
.069	.421	.1105
.081	.447	.1131
.107	.487	.1167
.132	.520	.1128
.157	.531	.1086
.196	.553	.1025
.259	.583	.1038
.323	.598	.1037
.450	.629	.1045
.577	.654	.1067
.704	.666	.1085
.831	.687	.1035
.958	.707	.1048
1.212	.735	.1052
1.466	.759	.1071
1.720	.777	.1080
1.974	.796	.1019
2.228	.814	.1070
2.736	.829	.1114
3.244	.829	.1101
3.752	.819	.1260
4.260	.797	.1293
4.768	.763	.1307
5.276	739	.1441
5.784	.700	.1300
6.292	.675	.1392
6.800	.650	.1284
7.308	.619	.1227
7.816	.586	.1170
8.324	.560	.1206
8.832	.520	.1081
9.340	.496	.1050
9.848	.472	.0988
10.356	.454	.0871

APPENDIX G

In this appendix the slant-wire data for adverse pressure gradient flow are tabulated. The data consist of turbulence intensities v_t/U_∞ , w_t/U_∞ and the shear stress $\frac{-\overline{uv}}{U_\infty^2}$. The interpolated data of u_t/U_∞ and $\partial(U/U_\infty)/\partial(y/\delta)$ at each slant-wire location were also tabulated. They were obtained from the normal hot-film data by interpolating a five point quadratic curve fit.

TABLE G

SLANT-WIRE DATA FOR THE ADVERSE PRESSURE GRADIENT FLOW

X/TC = 13.920 UINF = 16.60 M/SEC

DELTA = 2.769 CMS

Y(CMS)	DUDY X10	UT/UINF X100	$-UV/UINF^2$ X10000	VT/UINF X100	WT/UINF X100
.315	-48.571	17.000	-140.000	11.700	13.200
.330	-49.149	16.900	-141.000	12.500	13.000
.376	-50.605	16.900	-146.000	13.400	14.000
.439	-48.209	16.200	-134.000	14.700	14.100
.566	-35.867	13.100	-72.000	12.000	11.100
.693	-16.477	8.650	-17.600	8.470	7.940
.820	-.836	8.100	5.400	4.730	5.030
.947	4.602	8.250	12.900	3.930	5.060
1.074	5.145	8.070	15.200	3.620	5.580
1.201	5.304	7.770	16.400	3.710	5.670
1.455	5.259	7.430	16.200	4.770	6.050
1.712	4.900	6.930	13.100	4.360	5.950
1.966	4.454	6.010	9.990	4.330	5.420
2.220	3.594	4.610	6.900	4.330	4.050
2.474	2.567	3.170	3.060	3.300	3.110
2.720	1.611	1.066	1.440	2.340	1.600
3.236	.500	.700	.114	1.110	.730
3.744	.316	.464	.026	.573	.352
4.252	.331	.370	.067	.334	.108
5.260	.150	.256	.001	.263	.150

X/TC = 44.398 UINF = 13.24 M/SEC

DELTA = 3.675 CMS

Y(CMS)	DUDY X10	UT/UINF X100	$-UV/UINF^2$ X10000	VT/UINF X100	WT/UINF X100
.204	-1.091	11.100	-21.100	7.000	10.100
.323	-9.336	11.500	-20.600	8.870	11.300
.386	-17.645	12.500	-48.400	9.690	12.000
.450	-22.866	13.400	-65.600	11.000	13.600
.513	-25.864	14.[illegible]	-78.100	11.600	13.700
.640	-28.774	15.100	-98.700	12.000	15.000
.767	-28.773	14.900	-99.400	12.200	13.000
.894	-26.000	13.800	-87.400	12.600	13.700
1.021	-23.465	12.500	-73.500	11.200	11.800
1.275	-10.563	9.860	-21.300	6.420	6.950
1.529	.244	9.210	2.570	2.020	3.490
1.783	4.020	9.750	9.460	0.000	3.410
2.037	6.007	9.770	14.700	0.000	4.460
2.545	5.753	8.420	16.600	5.210	6.330
3.053	4.220	5.760	8.910	4.690	4.050
3.561	2.155	2.990	2.260	2.040	2.110
4.069	.531	1.070	.226	1.030	1.170
4.577	-.065	.576	.039	1.020	.615
5.085	-.262	.437	.012	.624	.337

TABLE G (Cont.)

X/YC = 100.320   UINF = 10.01 M/SEC

DELTA = 6.299 CMS

Y(CMS)	DUDY X10	UT/UINF X100	-UV/UINF² X10000	VT/UINF X100	WT/UINF X100
.261	28.614	10.200	20.200	7.980	8.360
.301	25.487	10.100	17.200	7.720	7.900
.445	16.030	9.770	9.210	8.640	8.670
.500	9.640	9.690	1.990	8.910	9.010
.572	3.142	9.790	-7.060	9.040	8.020
.699	-6.996	10.600	-23.300	10.000	10.100
.826	-14.132	11.000	-30.000	9.140	9.330
.953	-18.443	12.900	-48.000	9.140	10.100
1.080	-20.026	13.900	-60.500	8.660	10.100
1.334	-22.920	14.900	-73.300	8.720	10.300
1.588	-23.397	14.900	-84.200	8.730	10.500
1.842	-22.342	14.400	-74.300	8.710	10.100
2.096	-19.799	13.300	-59.600	9.020	9.750
2.350	-15.634	11.000	-42.600	8.020	9.590
2.858	-3.595	9.200	-19.000	9.100	9.300
3.366	5.779	9.660	4.000	8.090	7.710
3.874	9.032	10.300	15.500	8.900	9.490
4.382	9.959	9.050	24.100	9.170	9.120
4.890	9.211	8.600	19.000	8.630	9.110
5.398	7.255	6.700	6.740	8.260	7.360
5.906	4.770	4.600	-.610	5.090	5.050

X/YC = 177.720   UINF = 8.43 M/SEC

DELTA = 9.929 CMS

Y(CMS)	DUDY X10	UT/UINF X100	-UV/UINF² X10000	VT/UINF X100	WT/UINF X100
.325	44.110	9.870	27.200	6.620	7.870
.363	39.313	9.720	26.200	6.230	8.230
.427	35.444	9.550	27.000	6.250	7.535
.554	29.001	9.250	21.000	6.190	7.460
.681	22.786	9.070	17.000	5.710	6.330
.808	16.789	8.970	10.900	5.520	6.000
.935	11.379	8.920	3.730	5.670	5.060
1.189	2.215	9.090	-6.500	6.140	5.910
1.443	-5.361	9.900	-19.600	6.970	6.210
1.697	-11.645	11.000	-37.700	8.020	8.310
1.951	-15.644	11.900	-50.500	8.050	8.080
2.205	-17.754	12.700	-65.900	10.100	10.600
2.459	-18.417	13.300	-51.000	6.820	7.260
2.967	-18.063	13.900	-63.200	8.270	9.140
3.475	-18.606	13.400	-70.400	9.290	11.800
3.983	-17.149	12.400	-83.100	13.700	13.400
4.999	-7.874	9.750	-46.100	11.200	9.060
6.015	6.172	9.400	-6.040	6.320	1.830

LIST OF REFERENCES

1. Andersen, P.S., Kays, W.M. and Moffat, R.J. 1972. The turbulent boundary layer on a porous plate: An experimental study of the fluid mechanics for adverse free-stream pressure gradients. Report No. HMT-15, Thermosciences Division, Dept. of Mech. Engrg., Stanford University.

2. Bradshaw, P. 1967a. The turbulent structure of equilibrium boundary layers. J. Fluid Mech. 29: 625-645.

3. ________. 1967b. Conditions for the existence of an inertial subrange in turbulent flow. Nat. Phys. Lab., Aero. Rept. No. 1220.

4. ________, and Gee, M.T. 1962. Turbulent wall jets with and without an external stream. Aero. Res. Counc. R and M No. 3252.

5. Bradshaw, P. and Pankhurst, R.C. 1964. The design of low speed wind tunnels. Progress in aeronautical sciences. vol. 5, pp. 1-69. New York: Manmillan.

6. Carrière, P., Eichelbrenner, E., and Poisson-Quinton. 1959. Contribution théoretique et experimentale a l'étude du contrôle de la couche limite par soufflage. Advances in Aeronautical Sciences, vol. 2. New York: Macmillan.

7. Coles, D.E. 1962. The turbulent boundary layer in a compressible fluid. Rand Corporation Report R-403-PR.

8. Corrsin, S. 1964. Further generalizations of Onsager's Cascade Model for Turbulent Spectra. Phys. of Fluids 7: 1156

TABLE OF CONTENTS

LIST OF FIGURES . . . . vii 1/A12

LIST OF TABLES . . . . xiv 1/B5

NOMENCLATURE . . . . xv 1/B6

Chapter

I. INTRODUCTION 1 1/B12

1.1 Previous Work 2 1/B13

1.2 Asymmetric Jet Velocity Profile 9 1/C7

1.3 Objectives of the Thesis 11 1/C10

1.4 Outline of Thesis 12 1/C11

II. EXPERIMENTAL APPARATUS 15 1/C14

2.1 Description of the Wind Tunnel Components 15 1/C14
Heat exchanger
Blower system
Plenum chamber
Transition section
Test section

2.2 Description and Performance of the Wall Jet Flow System 27 1/D13
Air supply system
Wall jet assembly
Performance of the wall jet

III. INSTRUMENTATION 49 1/F12

3.1 Pitot Probes and Preston Tubes 49 1/F12

3.2 Hot-wire probes 51 1/G1
Slant-wire rotating mechanism
Traversing mechanism

3.3 Electronic Signal Processing 56 1/G6

3.4 Calibrations 56 1/G6

3.5 Uncertainties in the Measurements . . . 57 1/G7

IV. EXPERIMENTAL RESULTS FOR THE ZERO PRESSURE GRADIENT FLOW 59 1/G9

4.1 Flow Conditions 60 1/G10

4.2 Mean Flow Data 64 2/A5
  - Skin friction C_f
  - Mean velocity U
  - Integral parameters
  - Effect of the asymmetric jet velocity profile on the mean flow
  - Profile parameters

4.3 Turbulence Data 89 2/C5
  - Turbulence intensity u_t/U_∞
  - Turbulence intensities v_t/U_∞, w_t/U_∞ and shear stress $-\overline{uv}$
  - Effect of the asymmetric jet velocity profile on the turbulent quantities
  - Turbulent kinetic energy k
  - Correlation functions R_{uv} and a_1
  - Eddy viscosity ν_{eff}
  - Length scales L_{mix} and L_k
  - Production of turbulent kinetic energy
  - Spectra and dissipation measurements

V. EXPERIMENTAL RESULTS FOR THE ADVERSE PRESSURE GRADIENT FLOW 140 3/A8

5.1 Flow Conditions 141 3/A9

5.2 Mean Flow Data 147 3/B2
  - Skin friction C_f
  - Mean Velocity U
  - Integral parameters
  - Effect of the asymmetric jet velocity profile on the mean flow
  - Profile parameters

5.3 Turbulence Data 167 3/C12
  Turbulence intensity u_t/U_∞
  Turbulence intensities v_t/U_∞, w_t/U_∞ and the shear stress $-\overline{uv}$
  Turbulent kinetic energy k
  Correlation functions R_{uv} and a_1
  Eddy viscosity
  Mixing length L_{mix} and Prandtl-Kolmogorov length scale L_k
  Production of turbulent kinetic energy

VI. PREDICTION METHOD 192 3/F1

6.1 Selection of the Prediction Method 192 3/F1

6.2 Description of the Theoretical Method 194 3/F3
  Turbulence model
  Computational procedure
  Starting procedure

VII. COMPUTED RESULTS 205 3/F14

7.1 Prediction of the Zero Pressure Gradient Flow 206 3/G1
  Computations using the experimental initial velocity and turbulence profiles
  Computations using the automatic starting procedure

7.2 Predictions of the Adverse Pressure Gradient Flow 216 3/G11
  Computations using experimental initial profiles of velocity and turbulence
  Computations using the automatic starting procedure

7.3 Comparison of the Performance of Linear and Uniform Jet Velocity Profiles 232 4/B3
  Selection of the parameter a
  Starting turbulence profiles
  Prediction results

VIII. CONCLUSIONS 249 4/C8

APPENDIX A. MEASUREMENTS ON A WALL JET BY BOWLES (1977) 252 4/C11

APPENDIX B. ESTIMATION OF THE FRICTIONAL LOSSES IN THE WALL JET NOZZLE 255 4/C14

APPENDIX C. MEASUREMENT OF THE TURBULENCE INTENSITIES AND THE REYNOLDS SHEAR STRESS 259 4/D4

APPENDIX D. NORMAL HOT-FILM DATA FOR THE ZERO PRESSURE GRADIENT FLOW 272 4/E4

APPENDIX E. SLANT-WIRE DATA FOR ZERO PRESSURE GRADIENT FLOW 279 4/E14

APPENDIX F. NORMAL HOT-FILM DATA FOR ADVERSE PRESSURE GRADIENT FLOW 286 4/F13

APPENDIX G. SLANT-WIRE DATA FOR ADVERSE PRESSURE GRADIENT FLOW 291 4/G9

LIST OF REFERENCES 294 4/G14

9. English, E.C. 1970. Ph.D. dissertation, Cambridge University.

10. Gartshore, I.S., and Newman, B.G. 1969. The turbulent wall jet in an arbitrary pressure gradient. Aeronautical Quarterly 20: 25.

11. Goradia, S.H. and Colwell, G.I. 1971. Parametric study of a two-dimensional turbulent wall jet in moving stream with arbitrary pressure gradient. AIAA Journal 9: 2156.

12. Guitton, D.E. 1970. Some contributions to the study of equilibrium and non-equilibrium turbulent wall jets over curved surfaces. Ph.D. dissertation, McGill University.

13. Hanjalic, K., and Launder, B.E. 1972. A Reynolds stress model of turbulence and its application to thin shear flows. J. Fluid Mech. 52: 609.

14. Hinze, J.O. 1959. Turbulence, First Edition. New York: McGraw-Hill Book Co.

15. ________. 1975. Turbulence, Second Edition. New York: McGraw-Hill Book Co.

16. Irwin, H.P.A.H. 1973. Measurements in a self-preserving plane wall jet in a positive pressure gradient. J. Fluid Mech. 61: 33.

17. ________. 1974 Measurements in blown boundary layers and their prediction by Reynolds stress modelling. Ph.D. dissertation, McGill University.

18. Jordinson, R. 1961. Design of wind tunnel contractions. Aircraft Engrg. October: 294.

19. Jorgensen, F.E. 1971. Directional sensitivity of wire and fiber-film probes. DISA Information, No.11, May.

20. Kacker, S.C., and Whitelaw, J.H. 1968. Some properties of the two-dimensional turbulent wall jet in a moving stream. Trans. ASME, J. Applied Mechanics, December: 641.

21. ________. 1971. The turbulence characteristics of two-dimensional wall-jet and wall-wake flows. Trans. ASME, J. Applied Mechanics, March: 239.

22. Kind, R.J. 1971. A calculation method for boundary layer control by tangential blowing. C.A.S.I. Trans. 4: 88.

23. Klebanoff, P.S. 1954. Characteristics of turbulence in a boundary layer with zero pressure gradient. NACA Tech. Notes No. 3178.

24. ________. 1955. Characteristics of turbulence in a boundary layer with zero pressure gradient. NACA Rep. 1247, 1135-1153.

25. Kline, S.J., and McClintock, F.A. 1953. Describing uncertainties in single-sample experiments. Mech. Eng. 75: 3-8.

26. Kruka, V., and Eskinazi, S. 1964. The wall jet in a moving stream. J. Fluid Mech. 20: 555.

27. Launder, B.E. 1969. The Prandtl-Kolmogorov Model of Turbulence with the inclusion of second-order terms. Trans. ASME, Journal of Basic Engineering, December: 855.

28. Launder, B.E., Reece, G.J., and Rodi, W. 1973. Development and application of a Reynolds stress turbulence closure. Imperial College, Mech. Eng. Dept., HTS/73/31.

29. ________. 1975. Progress in the development of a Reynolds stress turbulence closure. J. Fluid Mech. 68: 537.

30. Launder, B.E., and Spalding, D.B. 1972. Lectures in Mathematical Models of Turbulence. New York: Academic Press.

31. Littlefield, M.T. 1978. Investigation of hot-wire response characteristics in skewed mean flow. M.S. thesis, Dept. Mech. Eng., University of Washington.

32. McGahan, W.A. 1965. The incompressible turbulent wall jet in an adverse pressure gradient. Gas Turbine Lab. Rep. No. 82, Mass. Inst. of Technology.

33. Narayan, K.Y., and Narasimha, R. 1973. Parametric analysis of turbulent wall jets. Aeronautical Quarterly 24: 207.

34. Newman, B.G., and Irwin, H.P.A.H. 1975. The prevention of separation by blowing in two-dimensional flow. AGARD Conference on Flow Separation, Conference Pre-Print No. 168.

35. Ng, K.H., and Spalding, D.B. 1969. Some applications of a model of turbulence for boundary layers near walls. Imperial College of Science and Technology, Dept. of Mech. Eng. Rep. BL/TN/A/14.

36. Nicoll, W.B., and Ramaprian, B.R. 1970. Performance of conical diffusers with annular injection at inlet. Trans. ASME, Ser. D., Journal of Basic Engineering 92: 827.

37. Papell, S.S., and Trout, A.M. 1959. Experimental investigation of air film cooling applied to an adiabatic wall by means of an axially discharging slot. NASA TN D-9, August.

38. Patel, R.P. 1962. Self-preserving, two-dimensional turbulent jets and wall jets in a moving stream. M.Sc. Thesis; McGill University.

39. Patel, V.C. 1965. Calibration of the preston tube and limitations on its use in pressure gradients. J. Fluid Mech. 23: 185.

40. Ramaprian, B.R. 1969. Concial diffusers with annular injection at inlet. Ph.D. dissertation, Mech. Eng. Dept., Univ. of Waterloo, Canada.

41. ________, 1973. Turbulent wall jets in conical diffusers. AIAA Journal 11: 1684.

42. ________. 1975. Turbulence measurements in an equilibrium axisymmetric wall jet. J. Fluid Mech. 71: 317.

43. Rotta, J.C. 1951. Statistiche Theorie Nichthomogener Turbulenz. Z. Phys. 129: 547.

44. ________. 1962. Turbulent boundary layers in incompressible flow. Progress in Aeronautical Sciences, vol. 2. New York: Pergamon Press.

45. Samuel, A.E., and Joubert, P.N. 1964. Film cooling of an adiabatic flat plate in zero pressure gradient in the presence of a hot mainstream and cold tangential secondary injection. ASME Paper No. 64-WA/HT-48.

46. Seban, R.A. 1960. Heat transfer and effectiveness for a turbulent boundary layer with tangential fluid injection. Trans. ASME, J. of Heat Transfer, Series C, 82: 303.

47. Simpson, R.L., and Wyatt, W.G. 1972. The behavior of hot-film anemometers in gas mixtures. Internal report, Dept. of Civil and Mech. Eng., Southern Methodist University.

48. Spalding. D.B., and Patankar, S.V. (1967, 1969) Heat and mass transfer in boundary layers. London: Morgan-Grampain, Parts I and II. Part III: Imperial College, Dept. Mech Eng., Report No. BL/TN/G/15.

49. Strickland, J.H., and Simpson, R.L. 1973. The separating turbulent boundary layer: An experimental study of an airfoil type flow. Rept. WT-2, Thermal and Fluid Sciences Center, Southern Methodist University. Available from NTIS as AD - 771170/8GA.

50. ________. 1975. Bursting frequencies obtained from wall shear stress fluctuations in a turbulent boundary layer. *Phys. Fluids* 18: 306.

51. Thomas, F. 1962. Untersuchungen über die Erhöhung des Auftriebes von Tragflügeln mittels Grenzschichtbeeinflussung durch Ausblason. *Z. Flugwiss* 10: 46.

52. ________. 1965. Boundary layer control for increased lift by blowing. *AIAA J.* 3: 967.

53. Ueda, H., and Hinze, J.O. 1975. Fine structure turbulence in the wall region of a turbulent boundary layer. *J. Fluid Mech.* 67: 125.

54. Wieghardt, K. 1946. Hot Air Discharge for De-Icing. AAF Translation No. F-TS-919-RE.

55. Williams, J., and Alexander, A.J. 1958. Pressure plotting measurements on a 8 per cent thick aerofoil with trailing edge flap blowing. A.R.C., R and M 3087.

1. Report No. NASA CR-3340	2. Government Accession No.	3. Recipient's Catalog No.

4. Title and Subtitle

INVESTIGATION OF BLOWN BOUNDARY LAYERS WITH AN IMPROVED WALL JET SYSTEM

5. Report Date
November 1980

6. Performing Organization Code

7. Author(s)
K. R. Saripalli and R. L. Simpson

8. Performing Organization Report No.

9. Performing Organization Name and Address
Department of Civil and Mechanical Engineering
Southern Methodist University
Dallas, Texas 75275

10. Work Unit No.

11. Contract or Grant No.
NSG-1548

12. Sponsoring Agency Name and Address
National Aeronautics and Space Administration
Washington, DC 20546

13. Type of Report and Period Covered
Contractor Report
(7/1/78 - 12/31/79)

14. Sponsoring Agency Code

15. Supplementary Notes
Langley Technical Monitor: Dennis M. Bushnell
Final Report

16. Abstract

Measurements were made in a two-dimensional incompressible wall jet submerged under a thick upstream boundary layer with a zero pressure gradient and an adverse pressure gradient. The measurements included mean velocity and Reynolds stresses profiles, skin friction, and turbulence spectra. The measurements were confined to practical ratios (less than 2) of the jet velocity to the free-stream velocity. The wall jet used in the present experiments has an asymmetric velocity profile with a relatively higher concentration of momentum away from the wall. It was shown that an asymmetric jet velocity profile has distinct advantages over an uniform jet velocity profile, especially in the control of separation. Predictions were made using Irwin's (1974) method for blown boundary layers. The predictions clearly show the difference in flow development between an asymmetric jet velocity profile and an uniform jet velocity profile.

17. Key Words (Suggested by Author(s))
Turbulent boundary layers
Wall jets
Boundary layer control
Turbulence structure

18. Distribution Statement
Unclassified - Unlimited

Subject Category 34

19. Security Classif. (of this report) Unclassified	20. Security Classif. (of this page) Unclassified	21. No. of Pages 316	22. Price A14

For sale by the National Technical Information Service, Springfield, Virginia 22161

NASA-Langley, 1980

299

END

February 23 1981